Technische Universität München
Fakultät für Elektrotechnik und Informationstechnik
Lehrstuhl für Informationstechnische Regelung

Human Impedance Control during Physical Interaction

Hendrik Börner

Vollständiger Abdruck der von der Fakultät für Elektrotechnik und Informationstechnik der Technischen Universität München zur Erlangung des akademischen Grades eines

Doktor-Ingenieurs (Dr.-Ing.)

genehmigten Dissertation.

Vorsitzende/-r: Prof. Gordon Cheng, Ph.D.

Prüfende der Dissertation:

1. Prof. Dr.-Ing. Sandra Hirche

2. Prof. Etienne Burdet, Ph.D.

Die Dissertation wurde am 16.11.2020 bei der Technischen Universität München eingereicht und durch die Fakultät für Elektrotechnik und Informationstechnik am 28.04.2021 angenommen.

Preamble

This thesis summarizes the results of the research conducted during my time at the Chair of Information-Oriented Control (ITR) at the Technical University of Munich. Completing this work would not have been possible without the support and advice of a number of people, to whom I would like to express my gratitude.

First and foremost, I would like to sincerely thank my doctoral advisor and head of the chair, Prof. Sandra Hirche, for giving me the opportunity to pursue this goal, for allowing me the freedom to follow my interests, and for the continuous support and stimulating discussions along the way. Likewise, I would like to thank Prof. Etienne Burdet of the Human Robotics Group of the Imperial College London for inviting me to conduct research with him and for many motivating and inspiring scientific discussions.

I would also like to express my gratitude towards all my colleagues for many hours of challenging scientific exchange, countless words of support and encouragement, and providing help and advice at any time. Many thanks as well to the administration and technical staff for providing support whenever needed.

I am deeply grateful to my family and friends for their never-ending support and enduring patience, their open ears and helpful advice, and for cheering me on every step of the way. Without them, writing these words would never have been possible. Thank you.

Acknowledgments

The research leading to these results has received funding from the ERC Starting Grant "Control based on Human Models (con-humo)" under grant agreement no. 337654 and the European Union's Horizon 2020 research and innovation programme "REHYB" under grant agreement no. 87176.

Abstract

Physical human-robot interaction plays a key role in many envisioned future applications, e.g., in industrial and medical domains. In industrial domains, it can facilitate cooperative manipulation tasks, in which humans and robots cooperate in the joint manipulation of heavy objects. In the medical domain, robotic assistance can reduce the effort of strenuous and repetitive activities during rehabilitation and care. Not only does this decrease the physical stress of the physiotherapist or the caretaker, systematic variation of the effort distribution can provide assist-as-needed support to facilitate learning. Immediate human feedback behavior in response to unknown dynamics, e.g., due to physical interaction with a robotic partner, is embodied by human impedance control. The respective feedback dynamics are defined by the linear impedance components of inertia, damping, and stiffness, which guide the limbs back towards the unperturbed states. Knowledge of impedance components is crucial for stability assessment, based on which the robot behavior can be defined to guarantee safety and comfort of the human. Furthermore, it allows for the approximation of the desired kinematic state, which can be used to define anticipatory control strategies that provide intuitive and efficient physical human-robot interaction.

The present thesis provides a comprehensive composition of instruments and insights to facilitate the inclusion of human impedance characteristics in the control design process for physical human-robot interaction. It focuses on three relevant open challenges in regard to impedance information. First, it addresses the information exploitation, which requires a model that is able to utilize a priori impedance knowledge to produce reliable predictions of the interaction dynamics. Second, it approaches the information acquisition, which requires an impedance estimation method that is compatible with constraints common to realistic physical human-robot interaction scenarios. Third, it investigates the information alteration by analyzing impedance modulation strategies of physically interacting individuals in human dyads that cooperate in the execution of a shared task.

The major contributions of this thesis address the mentioned challenges. Regarding the information exploitation, we derive a human motor behavior model that explicitly includes an impedance control structure. By assuming Gaussian Process priors for the underlying desired trajectory and the impedance components, we are able to construct compound kernels of a multi-layered Bayesian model that allow for exploitation of a priori knowledge of human impedance characteristics for regression of human motor behavior based on inference of human motor intention. Regarding the information acquisition, we apply dynamic regressor representation and a limited estimation interval duration to obtain an impedance estimation method that does not include voluntary feedback behavior common to realistic physical human-robot interaction scenarios. We apply force perturbations that are designed such that the respective unperturbed states can be estimated through isolation of the evoked feedback jerk frequency content with a high pass filter. With respect to the information alteration, we demonstrate that physically interacting individuals that cooperate in the execution of a shared task modulate muscle coactivation based on their respective levels of uncertainty regarding the shared task and the partner. We describe the motor behaviors of the two individuals, both during individual and dyadic task execution, with a neuromechanical model that includes a coactivation modulation model. In this thesis, all derived methods and models are validated in simulations and experiments carried out with human participants.

Zusammenfassung

Physische Mensch-Roboter Interaktion spielt in vielen zukunftsrelevanten Anwendungen eine essentiell wichtige Rolle, z.B. im industriellen und im medizinischen Bereich. Im industriellen Bereich können kooperative Manipulationsaufgaben, welche die gemeinsame Manipulation von Objekten durch Mensch und Roboter beinhalten, ermöglicht werden. Im medizinischen Bereich kann der Aufwand für körperlich anstrengende, repetitive Tätigkeiten im Kontext von Rehabilitation und Pflege reduziert werden. Hierdurch wird nicht nur die körperliche Beanspruchung des Physiotherapeuten bzw. der Pflegekraft reduziert, durch systematische Variation der Aufwandsverteilung kann zusätzlich bedarfsgerechte Patientenunterstützung ermöglicht werden. Die unmittelbare menschliche Reaktion auf unbekanntes Verhalten, z.B. aufgrund von physischer Interaktion mit einem Roboter, wird durch menschliche Impedanzregelung verkörpert. Die zugehörigen linearen Impedanzkomponenten Masse, Dämpfung und Steifigkeit bewirken, dass die Bewegung zurück in Richtung des ungestörten Zustands gelenkt wird. Die Kenntnis dieser Komponenten ist Voraussetzung für Stabilitätsanalysen, auf Basis welcher das Roboterverhalten so definiert werden kann, dass die Sicherheit des Menschen garantiert wird. Zusätzlich kann der gewünschte kinematische Zustand approximiert werden, welcher mit antizipierenden Roboterregelungen kombiniert werden kann, um intuitive und effiziente physische Mensch-Roboter Interaktion zu gewährleisten.

Diese Thesis beinhaltet Methoden und Erkenntnisse, die die Inklusion von menschlichen Impedanzeigenschaften im Kontext der Reglerentwicklung für physische Mensch-Roboter Interaktion ermöglichen. Es werden drei relevante offene Herausforderungen in Bezug auf die Impedanzeigenschaften behandelt. Zunächst wird die Informationsverwertung thematisiert, für die ein Modell benötigt wird, welches mittels a priori Impedanzkenntnissen zuverlässige Prädiktionen der Interaktionsdynamik liefern kann. Anschließend wird die Informationsgewinnung behandelt, für die eine Impedanzschätzungsmethode benötigt wird, die mit den Randbedingungen von realistischer physischer Mensch-Roboter Interaktion kompatibel ist. Zuletzt wird die Veränderung der Informationen anhand der Impedanzmodulation während physischer Interaktion von kooperierenden menschlichen Dyaden untersucht.

Die Hauptbeiträge dieser Thesis beziehen sich auf die drei genannten Herausforderungen. Für die Informationsverwertung wird ein Verhaltensmodell inklusive expliziter Impedanzregelungsstruktur entwickelt. Die Impedanzkomponenten und die Wunschtrajektorie werden durch Gaußprozesse modelliert, welche die Grundlage für ein mehrschichtiges Bayes'sches Modell bilden. Dieses Modell integriert a priori Impedanzkenntnisse um Verhaltensregression basierend auf Intentionsinferenz zu ermöglichen. Für die Informationsgewinnung wird mittels dynamischem Regressor und begrenztem Schätzintervall eine Impedanzschätzungsmethode entwickelt, welche den Ausschluss von freiwilligem Feedbackverhalten garantiert. Es werden Kraftstörungen verwendet, die so konzipiert sind, dass die zugehörigen ungestörten Zustände durch Isolation der resultierenden Feedback Jerk Frequenzinhalte geschätzt werden können. Bezüglich der Informationsveränderung wird gezeigt, dass physisch kooperierende Menschen ihre Muskelkokontraktionen entsprechend der Unsicherheit hinsichtlich der gemeinsam zu bewältigenden Aufgabe und des Partners modulieren. Das Verhalten der Kooperierenden, sowohl während einzelner als auch gemeinsamer Ausführung der Aufgabe, wird mittels eines neuromechanischen Modells beschrieben, welches ein Modell der Kokontraktionsmodulation enthält. Alle in dieser Thesis entwickelten Methoden und Modelle werden in Simulationen validiert und in Experimenten mit menschlichen Teilnehmern evaluiert.

Contents

Notation

In this work, explicit function dependencies are omitted whenever clear from the context in order to improve readability.

Acronyms and Abbreviations

AIC	Akaike information criterion
BIC	Bayesian information criterion
BIP	base inertial parameter
CNS	central nervous system
DoF	degrees of freedom
ECRL	extensor carpi radialis longus
EMG	electromyography
EMV	expected mean value
ERD	Erden and Billard
ESD	energy spectral density
FCR	flexor carpi radialis
FJI	feedback jerk isolation
GOM	Gomi and Kawato
GP	Gaussian process
HHI	human-human interaction
HRI	human-robot interaction
LQR	linear quadratic regulator
MSLL	mean standardized log loss
NAE	normalized absolute error
NRMSE	normalized root mean square error
PD	proportional derivative

RMSE root mean square error

RSS residual sum of squares

SD standard deviation

SE squared exponential

SEM standard error of the mean

SMSE standardized mean square error

Experimental Conditions

CC subject clean - partner clean condition

CN subject clean - partner noisy condition

NC subject noisy - partner clean condition

NN subject noisy - partner noisy condition

S1 solo condition before interaction trials

S2 solo condition after interaction trials

SC solo clean condition

SN solo noisy condition

Mathematical Conventions

Indices as well as scalar variables and functions are denoted by lower case italic characters, while vector-valued variables and functions are denoted by lower case bold italic characters. Matrices are denoted by capital italic characters.

Operators

$\hat{(\cdot)}$ estimated value

$\tilde{(\cdot)}$ partner value

$\dot{(\cdot)}$ first time derivative

$\ddot{(\cdot)}$ second time derivative

$\dddot{(\cdot)}$ third time derivative

$(\cdot)^{-1}$	inverse
$(\cdot)^{\mathsf{T}}$	transpose
$(\cdot)^{*}$	unperturbed value
$(\cdot)_{*}$	test value
$\|A\|$	absolute value
$\|\|A\|\|$	norm
$\mathsf{Cov}[\cdot]$	covariance
$\Delta(\cdot)$	variational variable
$\mathrm{diag}\{\cdot\}$	diagonal matrix
$\mathsf{E}[\cdot]$	expectation
$\mathcal{GP}(\cdot)$	Gaussian process
$\mathcal{N}(\cdot)$	Gaussian distribution
$\mathcal{O}(\cdot)$	complexity
$\mathsf{P}(\cdot)$	probability
$\mathsf{Var}[\cdot]$	variance

Subscripts

$(\cdot)_{0}$	initial value
$(\cdot)_{\mathrm{adm}}$	associated with admittance control
$(\cdot)_{\mathrm{CA}}$	associated with muscle coactivation
$(\cdot)_{\mathrm{d}}$	desired value
$(\cdot)_{\mathrm{ext}}$	associated with external dynamics
$(\cdot)_{\mathrm{FB}}$	associated with feedback behavior
$(\cdot)_{\mathrm{FBi}}$	associated with involuntary feedback behavior
$(\cdot)_{\mathrm{FBm}}$	associated with mechanical feedback behavior
$(\cdot)_{\mathrm{FBr}}$	associated with reflexive feedback behavior
$(\cdot)_{\mathrm{FBv}}$	associated with voluntary feedback behavior
$(\cdot)_{\mathrm{FF}}$	associated with feedforward behavior

$(\cdot)_{\mathrm{h}}$	associated with haptic information
$(\cdot)_{\mathrm{HP}}$	associated with high pass filter
$(\cdot)_{\mathrm{hu}}$	associated with human dynamics
$(\cdot)_{\mathrm{imp}}$	associated with impedance control
$(\cdot)_{\mathrm{int}}$	associated with interaction dynamics
$(\cdot)_{\lambda}$	variable in muscle space
$(\cdot)_{\mathrm{max}}$	maximum value
$(\cdot)_{\mathrm{n}}$	normalized value
$(\cdot)_{\mathrm{pert}}$	associated with perturbation
$(\cdot)_{q}$	variable in joint space
$(\cdot)_{\mathrm{RA}}$	associated with reciprocal muscle activation
$(\cdot)_{\mathrm{SE}}$	associated with squared exponential kernel
$(\cdot)_{\mathrm{sim}}$	associated with simulation implementation
$(\cdot)_{\mathrm{t}}$	associated with target dynamics
$(\cdot)_{\mathrm{v}}$	associated with visual information
$(\cdot)_{\mathrm{VC}}$	associated with virtual coupling
$(\cdot)_{\mathrm{w}}$	associated with wrist dynamics
$(\cdot)_{x}$	variable in Cartesian space

Sets

Γ	set of task-specific input parameters
Φ	set of perturbation angles
Ψ	set of energy spectral densities
$\mathcal{U}_{\mathrm{int}}$	set of interaction force observations
$\Xi, \overline{\Xi}$	set of input points
$\mathcal{Y}$	set of noisy output observations
$\mathbb{N}^{+}$	set of positive natural numbers
$\mathbb{R}$	set of real numbers

Variables and Functions

$\boldsymbol{a}$	muscle activations
A	regression matrix (Chapter 4), state matrix (Chapter 5)
α	parameter
$\boldsymbol{b}$	input vector
β	parameter
C	Coriolis/centrifugal matrix
d	damping
D	damping matrix
$\overline{D}$	damping parameter matrix
δ	delay
$\boldsymbol{e}$	error
$\boldsymbol{\varepsilon}_{\text{est}}$	estimation discrepancies
$\boldsymbol{\varepsilon}_{\text{dyn}}$	dynamic discrepancies
f	frequency
f_{c}	cut-off frequency
f_{s}	sample frequency
G	Kalman gain matrix
$\boldsymbol{\gamma}$	task-specific input parameters
h	number of points / samples
H	observation matrix
η_{err}	kinematic error function
η_{int}	physical interaction function
θ	tracking task angle
i	index
I	identity matrix
ι	moment of inertia
$\overline{\iota}$	moment of inertia with parallel axis component

j	index
J	Jacobian matrix
k	stiffness
K	stiffness matrix
$\overline{K}$	stiffness parameter matrix
κ	covariance function (Chapter 3), sample index (Chapter 5)
l	length of limb
l_{c}	length to center of gravity of limb
L	lower triangular matrix
$\boldsymbol{\lambda}$	muscle lengths (Chapters 3 and 4), control gain vector (Chapter 5)
Λ	length scale matrix
m	inertia
M	inertia matrix
μ	mean function / expected mean value
n	number of dimensions
N	observation noise covariance matrix
ν	observation noise
$\boldsymbol{\xi}$, $\overline{\boldsymbol{\xi}}$	input states
p	number of parameters
$\boldsymbol{p}$, $\overline{\boldsymbol{p}}$	unknown parameter vector for linear least squares
$\boldsymbol{p}_{\mathrm{nl}}$, $\overline{\boldsymbol{p}}_{\mathrm{nl}}$	unknown parameter vector for non-linear least squares
P	estimate covariance matrix
$\boldsymbol{\pi}$	standard inertial parameter vector
$\overline{\boldsymbol{\pi}}$	base inertial parameter vector
$\boldsymbol{\pi}_{\mathrm{r}}$	reduced inertial parameter vector
$\boldsymbol{q}$	arm configuration in joint space
Q	state weight matrix
r	input weight

$\boldsymbol{r}, \overline{\boldsymbol{r}}$	output vector
ρ	perturbation function (Chapter 4), cost function (Chapter 5)
σ	standard deviation
σ^2	variance
t	time
t_s	sample time
T_est	duration of estimation interval
T_mov	duration of movement
T_pert	duration of perturbation
$\boldsymbol{\tau}$	torques
$\boldsymbol{u}$	forces
$\boldsymbol{\upsilon}$	neural noise
$\boldsymbol{\omega}$	process noise
Ω	process noise covariance matrix
ϕ	perturbation angle
$\boldsymbol{x}$	arm configuration in Cartesian space
$X, \overline{X}$	independent variable matrix
$\boldsymbol{\chi}$	muscle tensions (Chapters 3 and 4), state vector (Chapter 5)
y	noisy output observation
Y	standard regressor matrix
$\overline{Y}$	base regressor matrix
Y_r	reduced regressor matrix
$\boldsymbol{\psi}$	energy spectral densities
$\boldsymbol{\psi}_\mathrm{FB}$	energy spectral densities of feedback behavior
$\boldsymbol{\psi}_\mathrm{P}$	energy spectral densities of perturbed movements
$\boldsymbol{\psi}_\mathrm{UP}$	energy spectral densities of unperturbed movements
z	noisy state observation

1. Introduction

Technological advancements and current developments in robotics research can provide direct assistance through the physical interaction of humans and robotic systems. Due to the versatile characteristics and capabilities of state-of-the-art robotic systems, the incorporation of physical human-robot interaction (HRI) can have beneficial implications on a multitude of application domains, ranging from agricultural and industrial manufacturing domains to medical and domestic service domains. In industrial manufacturing domains, the advantages of physical HRI can be exploited in cooperative manipulation tasks, in which humans and robots cooperate in the joint manipulation of an object, e.g., large construction equipment or heavy cargo material. In this type of application, the robot can account for the bulk of the necessary effort, allowing the human to focus on his cognitive capabilities and adopt a guiding role within the human-robot team [1, 2]. In the medical domain, the incorporation of physical HRI in rehabilitation and physical training results in similar scenarios. In these types of applications, systematic variations of the effort distribution between the human and the robot can be used to adapt the amount of assistance during rehabilitation routines and to execute individual configurations of physical training protocols [3, 4]. Furthermore, with the robot accounting for the effort of assistance in strenuous and repetitive activities, physical stress and fatigue of the physiotherapist or the trainer are substantially decreased. In domestic service domains, the advantages of physical HRI can be exploited in a variety of applications, e.g., in the form of mobility assistance robots that facilitate movements of elderly and physically impaired individuals [5, 6] or in the form of personal support robots that execute routine tasks and mundane chores in domestic environments [7, 8]. All of these examples of physical HRI have in common that the respective control strategies are designed to provide efficient and intuitive interaction, during which instabilities must be avoided to guarantee safety and comfort of the human. Due to the physical coupling, fulfillment of these objectives requires consideration of human motor control, especially the immediate feedback response to the robot behavior, in the control design process.

In general, human motor behavior is controlled by the central nervous system (CNS), which instantiates desired motor behavior through neural signals that regulate muscle activations at the limb joints [9]. During execution of a desired motor task, the joint torques produced by the neuromuscular system are composed of a feedforward and a feedback component [10]. A commonly accepted theory of sensory-motor control proposes that the motor commands responsible for the generation of the feedforward component are appropriately scaled by the CNS using internal models [11]. These internal models are acquired through experience and contain inverse dynamics representations of the musculoskeletal system and the interaction with the external environment [12]. As the feedforward component is calculated a priori, i.e., before the initialization of the desired motor behavior, it cannot account for unknown dynamics that arise during the execution of the desired motor task, e.g., due to incomplete or

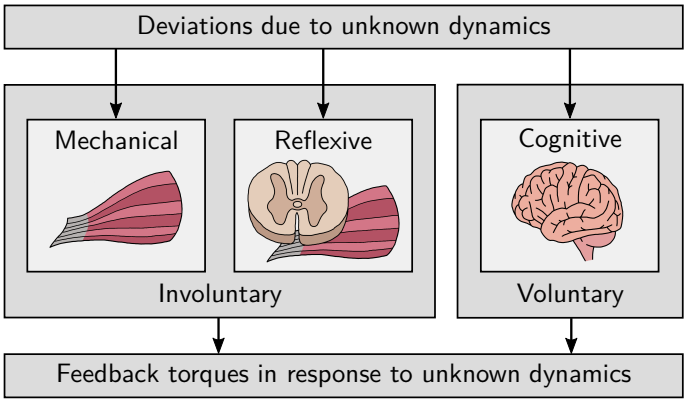

Figure 1.1.: Classification of mechanical, reflexive, and cognitive feedback in response to deviations due to unknown dynamics in involuntary and voluntary feedback.

incorrect internal models [13, 14], inherent neural noise in the sensory-motor system [15, 16], or unexpected external perturbations [17, 18]. Therefore, the occurrence of such unknown dynamics results in deviations from the desired kinematic state [19]. In addition to effects of the inertial properties of the limbs, these deviations are accompanied by restoring torques that are directed towards the unperturbed trajectory and are generated by a combination of peripheral neuromuscular properties of the limbs and motor commands from the CNS [20]. These restoring torques represent the previously mentioned feedback component and can be separated into effects of mechanical viscoelastic properties of the muscles (mechanical feedback), reflexive feedback, and cognitive feedback [21]. Apart from mechanical feedback, the respective torques are produced at different task-dependent delays. As cognitive feedback possesses the longest delays (in the order of 100 ms [22]), it may be too slow to ensure proper compensation of unknown dynamics [23]. Therefore, in unknown or unpredictable situations such as the physical interaction with a robotic system or a human partner, the CNS relies on mechanical and reflexive feedback to guarantee stable and accurate execution of the desired motor task [24]. In this work, all cognitive feedback at supraspinal level is referred to as *voluntary feedback* and the combined effects of all feedbacks that possess shorter delays than voluntary feedback are grouped into *involuntary feedback* (see Fig. 1.1).

A large body of evidence suggests that the restoring torques due to involuntary feedback are well-described by a linear system composed of joint damping and joint stiffness [25–27]. The dynamics defined by these two components combined with the inertial properties of the limbs represent those of an impedance control model, in which an impedance that consists of inertia, damping, and stiffness elements tracks the unperturbed trajectory [28]. Due to cross-bridge muscle mechanics, both joint damping and stiffness depend on joint angles and angular velocities. In addition to these two kinematic dependencies, the CNS is able to actively modulate the viscoelasticity of the limb through coactivation of antagonistic pairs of muscles at the respective limb joints [29, 30]. Multiple studies show that kinematic errors due to unknown dynamics that are not accounted for by the feedforward component are counteracted by increases in joint stiffness, which are achieved through suitable increases in agonist-antagonist muscle coactivation [31, 32]. If these unknown dynamics are predictable and therefore also learnable, they can be incorporated in the inverse dynamics representations of the internal models and the corresponding motor commands that are responsible for the generation of the feedforward component [33, 34]. As this continuous adaptation of the

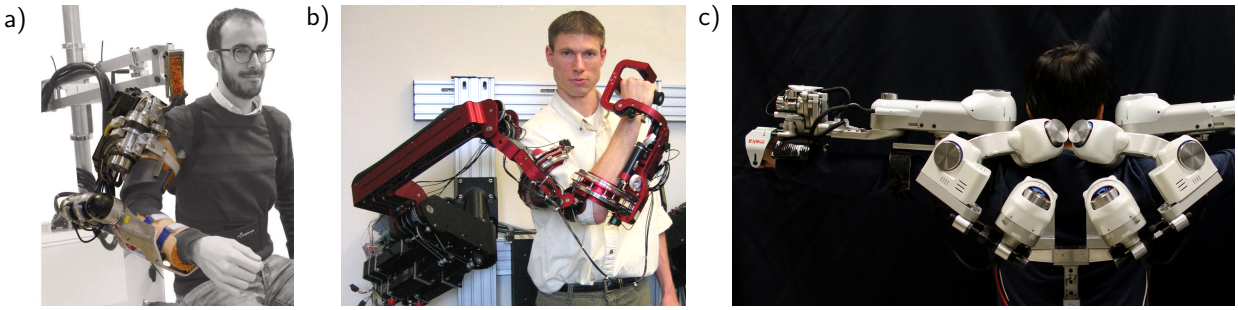

Figure 1.2.: Examples of active exoskeletons: a) shoulder-elbow exoskeleton for upper-limb neurological rehabilitation in [43], b) anthropomorphic, seven degrees of freedom, powered arm exoskeleton in [44], c) upper-body rehabilitation exoskeleton with an anatomical shoulder mechanism in [45].

internal models progresses and kinematic errors due to unknown dynamics decrease, muscle coactivation is gradually decreased to minimize metabolic cost [35, 36]. If the unknown dynamics are unpredictable and therefore also unlearnable, muscle coactivation remains at an increased level [37,38]. This correlation also applies to the unpredictable effects of inherent neural noise in the sensory-motor system [39, 40]. As the increase in muscle coactivation is positively correlated with the kinematic error, desired motor behaviors with higher accuracy requirements are accompanied by larger increases in muscle coactivation [41, 42].

Human impedance control plays a key part in the control of human motor behavior, as it defines the immediate feedback behavior to dynamics that cannot be explicitly considered in the a priori optimization of the desired motor behavior. During physical HRI, the impedance components define the immediate feedback behavior to unknown or unpredictable robot behavior and therefore represent an essential element for the control design process.

Knowledge of the impedance components is crucial for the assessment of stability, based on which the robot behavior can be adapted to guarantee safety and comfort of the human. Assessment of stability is especially relevant for active exoskeletons, which can be used for neuromuscular rehabilitation as well as general assistance in the performance of strenuous, physically demanding tasks. Figure 1.2 shows three examples of the multitude of active exoskeletons that are currently in development. As these systems are directly connected to the limbs, instabilities and ill-matched movements must be avoided at all costs. Due to the direct physical coupling, the necessary assessment of stability must take into account both the dynamics of the active exoskeleton as well as the interaction behavior of the limbs, which includes the immediate feedback behavior defined by the impedance components.

In addition to this important aspect for HRI control design, knowledge of the impedance components also enables the approximation of the desired kinematic state, which represents the human motor intention. Based on this information, the performance of the interaction can be improved through the calculation of anticipatory control signals. Figure 1.3 shows two examples of physical HRI scenarios, which would greatly benefit from such anticipatory control signals. Both during the joint manipulation of an object as well as during the joint employment of a tool, planning the robot behavior in accordance with the desired movement of the human partner can lead to substantial improvements in efficiency and intuitiveness of the interaction. Thus, the estimation of the human motor intention based on the impedance components would represent a great step towards seamless physical HRI.

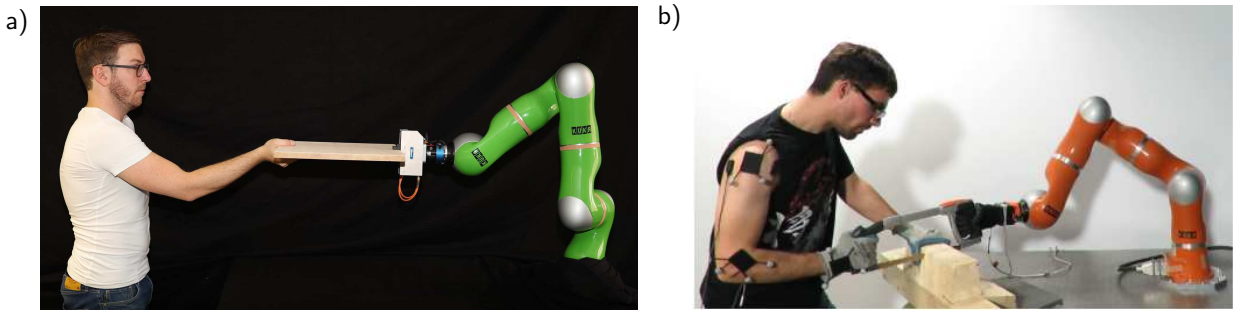

Figure 1.3.: Examples of physical collaboration of human and robot: a) joint manipulation of an object b) joint employment of a tool in a dyadic sawing task in [46].

The CNS is able to simultaneously modulate the impedance components joint damping and stiffness through appropriate coactivation of antagonistic pairs of muscles at the respective limb joints. By exploiting this capability, humans are able to adapt their motor behavior during physical cooperation to efficiently achieve shared objectives, independent of whether they are interacting with an inferior or a superior partner. Therefore, the investigation of impedance modulation strategies during physical human-human interaction (HHI) can provide novel insights for optimal control of impedance components during physical HRI. When transferred to the development of impedance control schemes for robotic end-effectors, these insights are valuable in two regards. Firstly, they will allow for anticipation of changes in impedance components on the side of the human partner. Secondly, they will allow for an interpretation of what this change in impedance means in terms of the understanding that the human partner has of his/her contribution to the interaction with the robot.

The advantageous aspects of the consideration of human impedance characteristics in the control design process for physical HRI are accompanied by multiple relevant open challenges, some of which are addressed in this thesis and introduced in detail in the following section.

1.1. Challenges

In the present thesis, we address three crucial open challenges in regard to the consideration of human impedance characteristics in the control design process for physical HRI. First of all, we focus on the information exploitation, i.e, the development of a means to enable effective utilization of a priori impedance knowledge and exploitation of its advantageous aspects. Secondly, we approach the information acquisition, i.e., the development of a method that can provide us with suitable impedance knowledge for realistic physical HRI scenarios. Lastly, we analyze the information alteration by investigating the open research question of how humans naturally modulate their impedance when interacting with a partner in a shared cooperative task. The novelties and open problems that characterize each of these three challenges are discussed in detail in the following paragraphs.

Effective exploitation of impedance information

Due to the complexity of human motor behavior, i.a., caused by the ambiguity in sensory processing, the redundancy of the musculoskeletal system, and the inherent neural noise, in human motor behavior modeling for HRI applications, sensory-motor control is generally

treated as a "black box" system [47]. For this system, inputs (e.g., limb configurations and task-specific parameters) and outputs (e.g., interaction torques) are deterministically or stochastically mapped onto a model without additional constraints. Due to the lack of system structure, the resulting models cannot provide information on intrinsic states. The incorporation of impedance knowledge could provide insights on such an intrinsic state. Specifically, it could allow for approximation of the human motor intention in the form of the desired kinematic state. Despite this immense potential, the exploitation of a priori knowledge about the impedance control model and the corresponding impedance components in human motor behavior modeling as well as the approximation of the desired kinematic state remains a significant open challenge.

Acquisition of suitable impedance information

While the involuntary feedback torques are well-described by a linear system composed of the impedance components joint damping and stiffness [26], the voluntary feedback torques, which are generated based on higher-order cognitive processes, may take on more complex task-specific forms that cannot be accurately represented by such a general formulation [22]. Consequently, accurate estimation of the impedance components requires separation of involuntary and voluntary feedback. Furthermore, a suitable estimation method must also provide accurate isolation of feedback behavior from feedforward behavior, as estimation errors in the feedback behavior directly influence the estimation accuracy. To the best of the author's knowledge, existing estimation methods are not suitable for the estimation of impedance components in experiments that emulate realistic physical HRI scenarios, either due to inappropriate assumptions or methodological limitations. Thus, the development of a suitable impedance estimation method remains a significant open challenge.

Investigation of impedance information alteration

Humans are capable of adapting their motor behavior during physical HHI to efficiently achieve shared objectives. From carefully supporting a child in its first steps to seamlessly coordinating such complex interactions as acrobatics, humans precisely regulate exchanged forces and skillfully modulate limb dynamics to enable intuitive and efficient cooperation. Modulation of limb dynamics, more specifically, modulation of the impedance component joint stiffness, is achieved through modulation of muscle coactivation [25, 29]. Despite the existence of comprehensive insights concerning non-physical and physical interaction with the environment [35, 48], little is currently known about modulation of muscle coactivation during physical HHI. A previous study investigated muscle effort adaptation to modified connection rigidity between two physically interacting partners, but did not study how muscle effort changes with the sensory information perceived by each partner. Furthermore, it did not differentiate between reciprocal muscle activation and muscle coactivation [49]. Thus, the analysis of muscle coactivation modulation strategies during physical HHI remains an open and challenging research question.

1.2. Main Contributions and Outline

The present thesis provides essential instruments and insights for systematic and efficient inclusion of human impedance characteristics in the control design process for physical HRI. The structure of the thesis is as follows:

Chapter 2 introduces related background information and establishes relevant correlations of neuromechanics and motor control by deriving a general model of human motor behavior that incorporates an impedance control model. In order to optimally tailor the introduction of this related background information to the contents of the following chapters, this general model is formulated for the multi-joint human arm, which consists of the complete upper limb including the shoulder joint. The following three chapters each individually address one of the three challenges discussed in Section 1.1. In Chapter 3, we present a novel method for modeling human motor behavior of the multi-joint human arm that explicitly incorporates an impedance control model. By adopting a Bayesian setting and assuming Gaussian process (GP) priors for the impedance components and the desired trajectory, we are able to exploit a priori impedance knowledge for the regression of human motor behavior and the estimation of human motor intention. In Chapter 4, we present a novel method for the estimation of the impedance components of the multi-joint human arm during movement. By limiting the duration of the estimation interval to guarantee the exclusion of voluntary feedback and estimating the feedback behavior via feedback jerk isolation, we ensure that the method can be applied to realistic physical HRI scenarios. In Chapter 5, we analyze muscle coactivation modulation strategies in cooperative physical HHI. We conduct an experiment to observe how different levels of tracking performance affect modulation of muscle coactivation in two physically coupled individuals that cooperate on a shared tracking task and evaluate multiple variations of a muscle coactivation modulation model. Chapter 6 concludes this thesis and discusses possible future works and research directions.

At the beginning of each chapter, the related work and open problems are presented. At the end of each chapter, the obtained results and developed methods are discussed and summarized. In the remainder of this section, the contributions of each individual chapter, with respect to the challenges presented in Section 1.1, are outlined in more detail.

Chapter 3: Bayesian Impedance Model for Human Motor Behavior Prediction

In this chapter, we present a method for modeling human motor behavior in physical and non-physical HRI that explicitly incorporates an impedance control model. Without loss of generality, particular focus is placed on the derivation of a model for physical HRI, as it represents the more challenging problem. We consider complex movements of the multi-joint human arm along a given trajectory and approximate the lower dimensional manifolds of human motor behavior by an impedance control model that counteracts deviations from a desired trajectory. We adopt a Bayesian setting by assuming GP priors for the impedance components and the desired trajectory. This enables the exploitation of a priori human arm impedance knowledge for the regression of human motor behavior. Moreover, it enables the estimation of human motor intention in the form of a desired trajectory and corresponding confidence levels. We present an overview of estimated human arm impedance characteristics in the literature and discuss proper parameterization of the GP priors. The model is validated with simulated data of a neuromechanical model of the human arm. The direct control over simulated intrinsic states, namely the impedance components and the desired trajectory,

enables both validation of intention estimation capabilities as well as assessment of effects of GP prior parameterization. Superior prediction performance is demonstrated with respect to a naive GP prior. An experiment with human participants is conducted to analyze effects of training data sparsity and demonstrate generalization capabilities.

The results in this chapter have partially been published in [50, 51]. The contents of [50], which was authored by J.R. Medina, S. Endo, and S. Hirche, represent a preliminary and particulate variation of the more comprehensive results in [51], which was authored by J.R. Medina, H. Börner, S. Endo, and S. Hirche, and to which J.R. Medina and H. Börner contributed equally. In [51] and in this thesis, we demonstrate advanced theory by refining the derivation of the general model of human motor behavior, elaborating the construction of the compound kernels of the Bayesian model, and generalizing the obtained results to non-physical HRI. We facilitate proper application of the model by presenting application guidelines, which include an overview of estimated human arm impedance characteristics in the literature, implications for the parameterization of the GP priors, and pseudocode application instructions. In order to consider the highly task-specific nature of human motor behavior, we complement a validation of a time-dependent desired trajectory. Furthermore, an experiment with human participants is performed to assess the applicability to real data, the generalization capabilities of the model, and the effects of training data sparsity.

Chapter 4: Impedance Estimation for physical HRI via Feedback Jerk Isolation

In this chapter, we present a method for the estimation of the impedance components of the multi-joint human arm during movement. We apply force perturbations in order to evoke deviations during two-dimensional point to point arm movements. These perturbations are designed such that the dominant frequencies of the jerk in the evoked feedback behavior lie above those of the unperturbed movements. Thus, the feedback behavior can be isolated by a high pass filter. The duration of the estimation interval is limited to guarantee the exclusion of voluntary feedback. Dynamic regressor representation of the rigid body dynamics yields a model that is linear in the impedance components in joint space. The constant values of the inertial parameters are estimated in a static posture maintenance task and subsequently used in order to estimate the remaining impedance components in a dynamic movement task. Both the feedback jerk isolation and the impedance estimation are validated with simulated data of a neuromechanical model of the human arm. We compare the validation results to those obtained by application of the methods presented in [52] and [53]. In the validation of the feedback jerk isolation, we additionally analyze the effects of different movement velocities as well as different frequencies and amplitudes of neural noise. Finally, we perform an extensive evaluation of the applicability of the method to real data based on an experiment with human participants. It includes an analysis of the effects of different durations of the estimation interval. The results in this chapter have partially been published in [54, 55].

Chapter 5: Coactivation Modulation Model for Cooperative Physical HHI

In this chapter, we reveal novel insights regarding modulation of muscle coactivation in cooperative physical HHI. We perform an experiment, in which two individuals use wrist movements to track pseudo-random movements of a shared target, while physically coupled by a virtual spring. Each individual is provided with distinct visual feedback and cannot see the visual feedback of the partner. During the course of the experiment, the individuals each experience two different levels of visual noise in their respective visual feedback. Thus, we are able to observe how different levels of tracking performance due to different levels of visual noise, affect modulation of muscle coactivation. In order to describe the motor behavior adaptation of the individuals, both during individual and dyadic task execution, we extend the physiological representativeness of the neuromechanical goal sharing model of [49] and propose three different variations of a muscle coactivation modulation model. We compare the functionality of the three different variations by implementing a simulation of the conditions in our experiment. The evaluation of the experiment shows that, when the individual experiences low quality visual feedback with visual noise, there is little difference in muscle coactivation between the interactions with different partners. In contrast, when the individual experiences high quality visual feedback without visual noise, muscle coactivation is significantly larger in the interaction with an inferior partner than in the interaction with an equal partner. The evaluation of the simulated data demonstrates that the coactivation modulation model is able to accurately reproduce modulation of coactivation, both during individual as well as dyadic task execution. Furthermore, the analysis of the interaction trials demonstrates that proper functionality of the model requires the inclusion of an interaction function that models the explicit change in coactivation due to physical interaction with the partner. Correlation of this interaction function with the amount of visual noise in the visual feedback of the individual, i.e., the uncertainty with respect to the tracking task, allows for accurate representation of the experimental results. The results in this chapter were partially elaborated in cooperation with S. Endo and S. Hirche (Chair of Information-oriented Control, Department of Electrical and Computer Engineering, Technical University of Munich, Munich, Germany), G. Carboni, X. Cheng, and E. Burdet (Human Robotics Group, Department of Bioengineering, Imperial College London, London, United Kingdom), and A. Takagi (NTT Communication Science Laboratories, Kyoto, Japan). A publication that includes the results in this chapter has recently been submitted [56].

Human Motor Behavior and Impedance Control Models

2.

The provision of a comprehensive composition of instruments and insights that facilitate systematic and efficient consideration of human impedance characteristics in the control design process for physical HRI requires suitable models of human motor behavior that place specific emphasis on the impedance control model and the associated impedance components. This chapter introduces the necessary background information and establishes the relevant neuromechanical correlations for the development of such models of human motor behavior. In order to optimally tailor the presentation of the necessary background information and the relevant neuromechanical correlations to the contents of the subsequent chapters, the developed models are derived for the multi-joint human arm, which consists of the complete upper limb including the shoulder joint. Moreover, it is assumed that during physical HRI the robot directly assists the human as he/she tightly grasps the robot end-effector and executes a desired motor behavior, e.g., for upper limb rehabilitation [57–59].

This chapter is structured as follows: In Section 2.1, we present the neuromuscular rigid body dynamics of the multi-joint human arm. Specific focus is placed on the composition of the muscle activities and the internally generated joint torques that instantiate the desired motor behavior. In Section 2.2, we focus on the involuntary feedback torques and derive an impedance control model that explicitly contains the impedance components joint damping and joint stiffness. This model serves as the basis for the estimation of impedance components for realistic physical HRI in Chapter 4. In Section 2.3, we shift focus towards the feedforward torques and use internal models to obtain a general model of human motor behavior during physical HRI. Additionally, we describe adjustments for non-physical HRI. In Section 2.4, we transform the two model variations to Cartesian space. The resulting Cartesian space representations serve as the basis for the inclusion of impedance knowledge in human motor behavior modeling in Chapter 3. The necessary background information and the relevant neuromechanical correlations for the analysis of impedance modulation strategies during physical HHI in Chapter 5 are presented within the respective chapter, as the developed model specifically describes the human motor behavior during an experiment, in which two individuals use wrist flexion/extension movements to track pseudo-random movements of a shared target, and is thus only pertinent to the contents of the respective chapter.

2.1. Neuromuscular Rigid Body Dynamics

The human arm is modeled as a two-joint two-link system. In order to reduce complexity and neglect gravity, possible movements are constrained to the horizontal plane. Thus, the rigid body dynamics, when tightly grasping the robot end-effector, is given by

$$\boldsymbol{\tau}_{\text{hu}} + \boldsymbol{\tau}_{\text{ext}} = M_q(\boldsymbol{q})\ddot{\boldsymbol{q}} + C_q(\boldsymbol{q}, \dot{\boldsymbol{q}})\dot{\boldsymbol{q}} \ , \tag{2.1}$$

where $\boldsymbol{q} = [q_1, q_2]^\mathsf{T}$ is the 2 degree of freedom (DoF) configuration of the human arm in joint space, in which q_1 is the shoulder angle and q_2 is the elbow angle, M_q is the positive definite and symmetric inertia matrix [25], C_q is the Coriolis/centrifugal matrix, $\boldsymbol{\tau}_{\text{hu}}$ are the internally generated joint torques, and $\boldsymbol{\tau}_{\text{ext}}$ are the external torques [52].

The internally generated joint torques $\boldsymbol{\tau}_{\text{hu}}$ that evoke the desired motor behavior are produced by the muscle tensions $\boldsymbol{\chi}$ that act on the musculoskeletal system:

$$\boldsymbol{\tau}_{\text{hu}} = J_\lambda^\mathsf{T}(\boldsymbol{\lambda})\boldsymbol{\chi}(\boldsymbol{\lambda}, \dot{\boldsymbol{\lambda}}, \boldsymbol{a}) \ , \tag{2.2}$$

where $\boldsymbol{\lambda}$ are the muscle lengths, $\dot{\boldsymbol{\lambda}}$ are the respective derivatives, $\boldsymbol{a}$ are the muscle activations, and J_λ is the muscle Jacobian that contains the muscle moment arms for the transformation to joint space [60]. During execution of a desired motor task, the muscle activations $\boldsymbol{a}$ consist of a feedforward term $\boldsymbol{a}_{\text{FF}}$, a feedback term $\boldsymbol{a}_{\text{FB}}$, and a neural noise term $\boldsymbol{\upsilon}_\lambda$ [35]:

$$\boldsymbol{a} = \boldsymbol{a}_{\text{FF}} + \boldsymbol{a}_{\text{FB}} + \boldsymbol{\upsilon}_\lambda \ . \tag{2.3}$$

The feedforward term $\boldsymbol{a}_{\text{FF}}$ is calculated by the CNS through a priori optimization of the statistics of the desired motor behavior with respect to costs defined by the task-specific input parameters $\boldsymbol{\gamma}$, which depend on factors such as environmental constraints and task requirements [15]. The neural noise term $\boldsymbol{\upsilon}_\lambda$ represents the effects of inherent neural noise within the sensory-motor system [61]. Deviations caused by unpredictable dynamics are compensated by the feedback term $\boldsymbol{a}_{\text{FB}}$, which consists of multiple components that depend on delayed afferent sensory information and are produced at different delays [22]:

$$\boldsymbol{a}_{\text{FB}} = \begin{cases} 0 & \forall\ t_{\text{FB}} \in [0, \delta_{\text{FBr}}] \\ \boldsymbol{a}_{\text{FBr}}(\boldsymbol{\lambda}, \dot{\boldsymbol{\lambda}}) & \forall\ t_{\text{FB}} \in \,]\delta_{\text{FBr}}, \delta_{\text{FBv}}] \\ \boldsymbol{a}_{\text{FBr}}(\boldsymbol{\lambda}, \dot{\boldsymbol{\lambda}}) + \boldsymbol{a}_{\text{FBv}}(\boldsymbol{\gamma}) & \forall\ t_{\text{FB}} > \delta_{\text{FBv}} \end{cases} \ , \tag{2.4}$$

where $\boldsymbol{a}_{\text{FBr}}$ and $\boldsymbol{a}_{\text{FBv}}$ are reflexive and voluntary feedback muscle activations, respectively. The variables δ_{FBr} and δ_{FBv} are the associated delays and $t_{\text{FB}} = t - t_{\text{FB},0}$ is the time after the onset of the unpredictable dynamics at $t_{\text{FB},0}$. During the interval $[0, \delta_{\text{FBr}}]$, immediately after the onset of the unpredictable dynamics, the feedback behavior is governed exclusively by effects of muscle mechanical viscoelastic properties. Consequently, the feedback muscle activations $\boldsymbol{a}_{\text{FB}}$ in response to the unpredictable dynamics are zero. During the subsequent interval $]\delta_{\text{FBr}}, \delta_{\text{FBv}}]$, the feedback muscle activations $\boldsymbol{a}_{\text{FB}}$ only consist of reflexive feedback muscle activations $\boldsymbol{a}_{\text{FBr}}$, which are affected by neural conduction delays that depend on the length and type of the nerve fiber. As the feedback behavior in this interval does not recruit higher-order cognitive processes at supraspinal level, the reflexive feedback muscle activations $\boldsymbol{a}_{\text{FBr}}$ only depend on the muscle lengths $\boldsymbol{\lambda}$ and the respective derivatives $\dot{\boldsymbol{\lambda}}$.

Remark 2.1. The fastest reflexive feedback is produced by the short-latency monosynaptic stretch reflex, with a delay in the order of $10 - 40$ ms [62]. Slightly slower reflexive feedback is produced by the cortical component of the long-latency stretch reflex, with a delay in the order of $30 - 70$ ms [63].

For all $t_{\text{FB}} > \delta_{\text{FBv}}$, the voluntary feedback muscle activations $\boldsymbol{a}_{\text{FBv}}$, which are, analogous to the feedforward muscle activations $\boldsymbol{a}_{\text{FF}}$, also defined by the task-specific input parameters $\boldsymbol{\gamma}$, additionally contribute to the feedback muscle activations $\boldsymbol{a}_{\text{FB}}$.

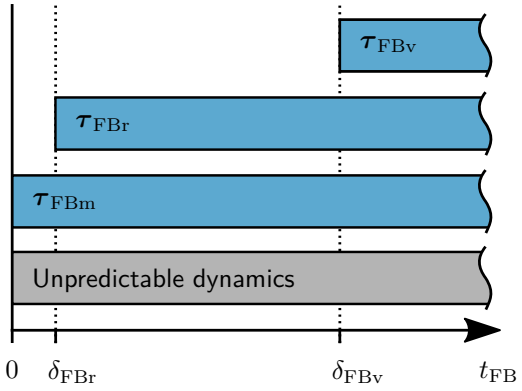

Figure 2.1.: Feedback torques $\boldsymbol{\tau}_{\mathrm{FB}}$ elicited by deviations due to unpredictable dynamics.

Remark 2.2. For voluntary feedback due to haptic motion perception, the transmission of proprioceptive sensory information to the CNS is subject to delays in the order of 100 ms. Conduction delays of descending motor commands from the motor cortex to the muscles of the upper arm and the forearm are approximately 15 ms [64]. Consequently, the minimum delay δ_{FBv} of the voluntary feedback muscle activations $\boldsymbol{a}_{\mathrm{FBv}}$ is in the order of 115 ms.

Replacing the feedback muscle activations $\boldsymbol{a}_{\mathrm{FB}}$ in (2.3) by the reflexive and voluntary contributions in (2.4) yields the muscle activations $\boldsymbol{a}$ for all $t > \delta_{\mathrm{FBv}}$:

$$\boldsymbol{a}(\boldsymbol{\lambda}, \dot{\boldsymbol{\lambda}}, \boldsymbol{\gamma}) = \boldsymbol{a}_{\mathrm{FF}}(\boldsymbol{\gamma}) + \boldsymbol{a}_{\mathrm{FBr}}(\boldsymbol{\lambda}, \dot{\boldsymbol{\lambda}}) + \boldsymbol{a}_{\mathrm{FBv}}(\boldsymbol{\gamma}) + \boldsymbol{\upsilon}_{\lambda} \ . \tag{2.5}$$

During execution of a desired motor task, the internal torques $\boldsymbol{\tau}_{\mathrm{hu}}$ are also composed of a feedforward term $\boldsymbol{\tau}_{\mathrm{FF}}$, a feedback term $\boldsymbol{\tau}_{\mathrm{FB}}$, and a neural noise term $\boldsymbol{\upsilon}_q$, which represent the joint torque equivalents to the respective muscle activation terms in (2.3):

$$\boldsymbol{\tau}_{\mathrm{hu}} = \boldsymbol{\tau}_{\mathrm{FF}} + \boldsymbol{\tau}_{\mathrm{FB}} + \boldsymbol{\upsilon}_q \ . \tag{2.6}$$

Analogous to the feedback muscle activations $\boldsymbol{a}_{\mathrm{FB}}$ in (2.4), the feedback torques $\boldsymbol{\tau}_{\mathrm{FB}}$ are composed of multiple components that are produced at different delays [65]:

$$\begin{aligned} \boldsymbol{\tau}_{\mathrm{FB}} = \boldsymbol{\tau}_{\mathrm{FBm}}(\boldsymbol{\lambda}, \dot{\boldsymbol{\lambda}}, \boldsymbol{a}(\boldsymbol{\lambda}, \dot{\boldsymbol{\lambda}}, \boldsymbol{\gamma})) \\ + \begin{cases} 0 & \forall\ t_{\mathrm{FB}} \in [0, \delta_{\mathrm{FBr}}] \\ \boldsymbol{\tau}_{\mathrm{FBr}}(\boldsymbol{a}_{\mathrm{FBr}}(\boldsymbol{\lambda}, \dot{\boldsymbol{\lambda}})) & \forall\ t_{\mathrm{FB}} \in \,]\delta_{\mathrm{FBr}}, \delta_{\mathrm{FBv}}] \\ \boldsymbol{\tau}_{\mathrm{FBr}}(\boldsymbol{a}_{\mathrm{FBr}}(\boldsymbol{\lambda}, \dot{\boldsymbol{\lambda}})) + \boldsymbol{\tau}_{\mathrm{FBv}}(\boldsymbol{a}_{\mathrm{FBv}}(\boldsymbol{\gamma})) & \forall\ t_{\mathrm{FB}} > \delta_{\mathrm{FBv}} \end{cases} , \end{aligned} \tag{2.7}$$

where $\boldsymbol{\tau}_{\mathrm{FBm}}$, $\boldsymbol{\tau}_{\mathrm{FBr}}$, and $\boldsymbol{\tau}_{\mathrm{FBv}}$ are the mechanical, reflexive, and voluntary contributions to the feedback torques $\boldsymbol{\tau}_{\mathrm{FB}}$, respectively. The consecutive occurrences of these feedback torque contributions after the respective delays are illustrated schematically in Fig. 2.1. In the interval $[0, \delta_{\mathrm{FBr}}]$, the feedback torques $\boldsymbol{\tau}_{\mathrm{FB}}$ only consist of mechanical feedback torques $\boldsymbol{\tau}_{\mathrm{FBm}}$, which result from muscle mechanical viscoelastic properties and are thus not affected by any delays [10]. Due to cross-bridge muscle mechanics, the mechanical feedback torques $\boldsymbol{\tau}_{\mathrm{FBm}}$ depend on the muscle lengths $\boldsymbol{\lambda}$ and the respective derivatives $\dot{\boldsymbol{\lambda}}$. Furthermore, the muscle mechanical viscoelastic properties also depend on the muscle activations $\boldsymbol{a}$, both in terms of

reciprocal muscle activation [66,67] as well as muscle coactivation [39,40]. In the subsequent interval $]\delta_{\mathrm{FBr}}, \delta_{\mathrm{FBv}}]$ and for all $t_{\mathrm{FB}} > \delta_{\mathrm{FBv}}$, the feedback torques $\boldsymbol{\tau}_{\mathrm{FB}}$ additionally consist of reflexive feedback torques $\boldsymbol{\tau}_{\mathrm{FBr}}$ and voluntary feedback torques $\boldsymbol{\tau}_{\mathrm{FBv}}$, which represent the joint torque equivalents to the respective feedback muscle activations in (2.4).

Replacing the feedback torques $\boldsymbol{\tau}_{\mathrm{FB}}$ in (2.6) by the mechanical, reflexive, and voluntary contributions in (2.7) yields the internal torques $\boldsymbol{\tau}_{\mathrm{hu}}$ for all $t > \delta_{\mathrm{FBv}}$:

$$\begin{aligned}\boldsymbol{\tau}_{\mathrm{hu}}(\boldsymbol{\lambda}, \dot{\boldsymbol{\lambda}}, \boldsymbol{a}(\boldsymbol{\lambda}, \dot{\boldsymbol{\lambda}}, \boldsymbol{\gamma})) = \boldsymbol{\tau}_{\mathrm{FF}}(\boldsymbol{a}_{\mathrm{FF}}(\boldsymbol{\gamma})) + \boldsymbol{\tau}_{\mathrm{FBm}}(\boldsymbol{\lambda}, \dot{\boldsymbol{\lambda}}, \boldsymbol{a}(\boldsymbol{\lambda}, \dot{\boldsymbol{\lambda}}, \boldsymbol{\gamma})) \\ + \boldsymbol{\tau}_{\mathrm{FBr}}(\boldsymbol{a}_{\mathrm{FBr}}(\boldsymbol{\lambda}, \dot{\boldsymbol{\lambda}})) + \boldsymbol{\tau}_{\mathrm{FBv}}(\boldsymbol{a}_{\mathrm{FBv}}(\boldsymbol{\gamma})) + \boldsymbol{\upsilon}_q \ . \end{aligned} \tag{2.8}$$

This compositional model of the internal torques $\boldsymbol{\tau}_{\mathrm{hu}}$ for all $t > \delta_{\mathrm{FBv}}$ in combination with the rigid body dynamics (2.1) represents the basis for the derivation of the impedance control model as well as the general model of human motor behavior during physical HRI.

2.2. Feedback Torques and Impedance Components

While the combination of the mechanical feedback torques $\boldsymbol{\tau}_{\mathrm{FBm}}$ and the reflexive feedback torques $\boldsymbol{\tau}_{\mathrm{FBr}}$ is well-described by a linear system composed of the impedance components joint damping and stiffness [26], the voluntary feedback torques $\boldsymbol{\tau}_{\mathrm{FBv}}$, which are generated based on higher-order cognitive processes, may take on more complex task-specific forms that cannot be accurately represented by such a general formulation [22]. Thus, in the following derivation of the impedance control model, we only consider the interval $[0, \delta_{\mathrm{FBv}}]$ after the onset of the unpredictable dynamics, i.e., we only consider those feedback torques $\boldsymbol{\tau}_{\mathrm{FB}}$ that are generated before the occurrence of voluntary feedback torques $\boldsymbol{\tau}_{\mathrm{FBv}}$.

Due to the short latency and the variable delays of the reflexive feedback, separation of the mechanical and the reflexive contributions in the feedback torques $\boldsymbol{\tau}_{\mathrm{FB}}$ is difficult [24]. Thus, we summate the contributions in the involuntary feedback torques

$$\boldsymbol{\tau}_{\mathrm{FBi}} = \boldsymbol{\tau}_{\mathrm{FBm}}(\boldsymbol{\lambda}, \dot{\boldsymbol{\lambda}}, \boldsymbol{a}(\boldsymbol{\lambda}, \dot{\boldsymbol{\lambda}}, \boldsymbol{\gamma})) + \begin{cases} 0 & \forall\ t_{\mathrm{FB}} \in [0, \delta_{\mathrm{FBr}}] \\ \boldsymbol{\tau}_{\mathrm{FBr}}(\boldsymbol{a}_{\mathrm{FBr}}(\boldsymbol{\lambda}, \dot{\boldsymbol{\lambda}})) & \forall\ t_{\mathrm{FB}} \in]\delta_{\mathrm{FBr}}, \delta_{\mathrm{FBv}}] \end{cases} . \tag{2.9}$$

For small deviations, the involuntary feedback behavior in the interval $[0, \delta_{\mathrm{FBv}}]$ after the onset of the unpredictable dynamics is well-described by a linearized model, which can be obtained by first order Taylor series expansion of the compositional model (2.8) about the states of the unperturbed dynamics. According to (2.8), the variations in internal torques $\boldsymbol{\tau}_{\mathrm{hu}}$ in response to the occurrence of the unpredictable dynamics depend on the muscle lengths $\boldsymbol{\lambda}$, the respective derivatives $\dot{\boldsymbol{\lambda}}$, and the muscle activations $\boldsymbol{a}$. Due to the confinement to the interval $[0, \delta_{\mathrm{FBv}}]$, according to (2.5), the variations in muscle activations $\boldsymbol{a}$ can only consist of reflexive feedback muscle activations $\boldsymbol{a}_{\mathrm{FBr}}$, which only depend on the muscle lengths $\boldsymbol{\lambda}$ and the respective derivatives $\dot{\boldsymbol{\lambda}}$. Therefore, considering that the muscle Jacobian J_λ can be used to transform the kinematic states from muscle space to joint space, i.e., $\boldsymbol{\lambda} = J_\lambda(\boldsymbol{\lambda})\boldsymbol{q}$ and $\dot{\boldsymbol{\lambda}} = J_\lambda(\boldsymbol{\lambda})\dot{\boldsymbol{q}}$, linearization of the internal torques $\boldsymbol{\tau}_{\mathrm{hu}}$ for $t_{\mathrm{FB}} \in [0, \delta_{\mathrm{FBv}}]$ yields

$$\Delta\boldsymbol{\tau}_{\mathrm{hu}} = \frac{\mathrm{d}\boldsymbol{\tau}_{\mathrm{hu}}(\boldsymbol{q}, \dot{\boldsymbol{q}}, \boldsymbol{a}(\boldsymbol{q}, \dot{\boldsymbol{q}}, \boldsymbol{\gamma}))}{\mathrm{d}\dot{\boldsymbol{q}}}\Delta\dot{\boldsymbol{q}} + \frac{\mathrm{d}\boldsymbol{\tau}_{\mathrm{hu}}(\boldsymbol{q}, \dot{\boldsymbol{q}}, \boldsymbol{a}(\boldsymbol{q}, \dot{\boldsymbol{q}}, \boldsymbol{\gamma}))}{\mathrm{d}\boldsymbol{q}}\Delta\boldsymbol{q} \ , \tag{2.10}$$

in which all variational variables $\Delta(\cdot)$ represent the evoked deviations from the respective unperturbed states $(\cdot)^*$ due to the unpredictable dynamics, e.g., $\Delta\boldsymbol{q} = \boldsymbol{q} - \boldsymbol{q}^*$. The total derivative with respect to the arm configuration $\boldsymbol{q}$ in (2.10) is defined as

$$\frac{\mathrm{d}\boldsymbol{\tau}_{\mathrm{hu}}(\boldsymbol{q}, \dot{\boldsymbol{q}}, \boldsymbol{a}(\boldsymbol{q}, \dot{\boldsymbol{q}}, \boldsymbol{\gamma}))}{\mathrm{d}\boldsymbol{q}} = \frac{\partial \boldsymbol{\tau}_{\mathrm{hu}}(\boldsymbol{q}, \dot{\boldsymbol{q}}, \boldsymbol{a}(\boldsymbol{q}, \dot{\boldsymbol{q}}, \boldsymbol{\gamma}))}{\partial \boldsymbol{q}} + \frac{\partial \boldsymbol{\tau}_{\mathrm{hu}}(\boldsymbol{q}, \dot{\boldsymbol{q}}, \boldsymbol{a}(\boldsymbol{q}, \dot{\boldsymbol{q}}, \boldsymbol{\gamma}))}{\partial \boldsymbol{a}} \frac{\partial \boldsymbol{a}(\boldsymbol{q}, \dot{\boldsymbol{q}}, \boldsymbol{\gamma})}{\partial \boldsymbol{q}} \tag{2.11}$$

and the total derivative with respect to the respective derivative $\dot{\boldsymbol{q}}$ is defined as

$$\frac{\mathrm{d}\boldsymbol{\tau}_{\mathrm{hu}}(\boldsymbol{q}, \dot{\boldsymbol{q}}, \boldsymbol{a}(\boldsymbol{q}, \dot{\boldsymbol{q}}, \boldsymbol{\gamma}))}{\mathrm{d}\dot{\boldsymbol{q}}} = \frac{\partial \boldsymbol{\tau}_{\mathrm{hu}}(\boldsymbol{q}, \dot{\boldsymbol{q}}, \boldsymbol{a}(\boldsymbol{q}, \dot{\boldsymbol{q}}, \boldsymbol{\gamma}))}{\partial \dot{\boldsymbol{q}}} + \frac{\partial \boldsymbol{\tau}_{\mathrm{hu}}(\boldsymbol{q}, \dot{\boldsymbol{q}}, \boldsymbol{a}(\boldsymbol{q}, \dot{\boldsymbol{q}}, \boldsymbol{\gamma}))}{\partial \boldsymbol{a}} \frac{\partial \boldsymbol{a}(\boldsymbol{q}, \dot{\boldsymbol{q}}, \boldsymbol{\gamma})}{\partial \dot{\boldsymbol{q}}} \ . \tag{2.12}$$

Inserting the compositional model (2.8) for $t_{\mathrm{FB}} \in [0, \delta_{\mathrm{FBv}}]$ and (2.9) into (2.10) yields

$$\Delta\boldsymbol{\tau}_{\mathrm{hu}} = -D_q(\boldsymbol{q}, \dot{\boldsymbol{q}}, \boldsymbol{a}(\boldsymbol{q}, \dot{\boldsymbol{q}}, \boldsymbol{\gamma}))\Delta\dot{\boldsymbol{q}} - K_q(\boldsymbol{q}, \dot{\boldsymbol{q}}, \boldsymbol{a}(\boldsymbol{q}, \dot{\boldsymbol{q}}, \boldsymbol{\gamma}))\Delta\boldsymbol{q} \ . \tag{2.13}$$

In this linearized model of the involuntary feedback behavior due to unpredictable dynamics, the impedance components joint damping D_q and joint stiffness K_q are defined as

$$D_q(\boldsymbol{q}, \dot{\boldsymbol{q}}, \boldsymbol{a}(\boldsymbol{q}, \dot{\boldsymbol{q}}, \boldsymbol{\gamma})) = -\frac{\mathrm{d}\boldsymbol{\tau}_{\mathrm{FBi}}(\boldsymbol{q}, \dot{\boldsymbol{q}}, \boldsymbol{a}(\boldsymbol{q}, \dot{\boldsymbol{q}}, \boldsymbol{\gamma}))}{\mathrm{d}\dot{\boldsymbol{q}}} \ , \tag{2.14}$$

$$K_q(\boldsymbol{q}, \dot{\boldsymbol{q}}, \boldsymbol{a}(\boldsymbol{q}, \dot{\boldsymbol{q}}, \boldsymbol{\gamma})) = -\frac{\mathrm{d}\boldsymbol{\tau}_{\mathrm{FBi}}(\boldsymbol{q}, \dot{\boldsymbol{q}}, \boldsymbol{a}(\boldsymbol{q}, \dot{\boldsymbol{q}}, \boldsymbol{\gamma}))}{\mathrm{d}\boldsymbol{q}} \ . \tag{2.15}$$

Remark 2.3. Due to the inclusion of reflexive feedback, according to the terminology in [68–70], the matrices D_q and K_q represent apparent impedance components. In this work, for simplicity, we refer to them simply as impedance components. Furthermore, from this point on, we refer to the individual matrices D_q and K_q simply as damping and stiffness.

In addition to the damping D_q and the stiffness K_q, the dynamics of the impedance control model are also determined by the inertial properties of the limbs. Expressing the variational internal torques $\Delta\boldsymbol{\tau}_{\mathrm{hu}}$ in terms of the rigid body dynamics (2.1) results in

$$\Delta\boldsymbol{\tau}_{\mathrm{hu}} = M_q(\boldsymbol{q})\ddot{\boldsymbol{q}} + C_q(\boldsymbol{q}, \dot{\boldsymbol{q}})\dot{\boldsymbol{q}} - M_q(\boldsymbol{q}^*)\ddot{\boldsymbol{q}}^* - C_q(\boldsymbol{q}^*, \dot{\boldsymbol{q}}^*)\dot{\boldsymbol{q}}^* - \Delta\boldsymbol{\tau}_{\mathrm{ext}} \ . \tag{2.16}$$

Combining this expression of the variational internal torques $\Delta\boldsymbol{\tau}_{\mathrm{hu}}$ with the linearized model of the involuntary feedback behavior due to unpredictable dynamics (2.13) yields

$$\begin{aligned}\Delta\boldsymbol{\tau}_{\mathrm{ext}} = {} & M_q(\boldsymbol{q})\ddot{\boldsymbol{q}} + C_q(\boldsymbol{q}, \dot{\boldsymbol{q}})\dot{\boldsymbol{q}} - M_q(\boldsymbol{q}^*)\ddot{\boldsymbol{q}}^* - C_q(\boldsymbol{q}^*, \dot{\boldsymbol{q}}^*)\dot{\boldsymbol{q}}^* \\ & + D_q(\boldsymbol{q}, \dot{\boldsymbol{q}}, \boldsymbol{\gamma})\Delta\dot{\boldsymbol{q}} - K_q(\boldsymbol{q}, \dot{\boldsymbol{q}}, \boldsymbol{\gamma})\Delta\boldsymbol{q} \ .\end{aligned} \tag{2.17}$$

This impedance control model describes the variational behavior in the interval $[0, \delta_{\mathrm{FBv}}]$ after the onset of the unpredictable dynamics and includes the impedance components damping D_q

and stiffness K_q as well as the inertial properties of the limbs in the inertia matrix M_q and the Coriolis/centrifugal matrix C_q. It represents the basis for the impedance estimation in Chapter 4, in which we apply dynamic regressor representation of the rigid body dynamics in order to express the inertial properties of the limbs with a minimal set of inertial parameters and obtain a completely linear model.

Remark 2.4. For simplicity, in the impedance control model (2.17) as well as in the remainder of this thesis, the intermediate dependency on the muscle activations $\boldsymbol{a}$ of the damping D_q and the stiffness K_q is not explicitly specified and instead replaced by the resulting dependency on the task-specific input parameters $\boldsymbol{\gamma}$.

2.3. Feedforward Torques and Internal Models

While the description of the variational behavior in the interval $[0, \delta_{\mathrm{FBv}}]$ after the onset of the unpredictable dynamics in the impedance control model (2.17) allows for the estimation of the impedance components, it does not allow for the full description and prediction of human motor behavior during physical HRI. In order to derive a more general model with these capabilities, we assume that the unperturbed states, towards which the restoring torques of the impedance control model are directed, represent the desired kinematic states of the desired motor behavior. Furthermore, we assume that these desired kinematic states are given by a desired trajectory $\boldsymbol{q}_{\mathrm{d}}$, which is a well-defined, twice differentiable (with respect to time) function $\boldsymbol{q}_{\mathrm{d}}(\boldsymbol{\gamma})$ that depends on the task-specific input parameters $\boldsymbol{\gamma}$.

Remark 2.5. The task-specific input parameters $\boldsymbol{\gamma}$ depend on factors such as environmental constraints and task requirements. Thus, they can be defined by a variety of different parameters, e.g, the arm configuration $\boldsymbol{q}$, the angular velocities $\dot{\boldsymbol{q}}$, or the time t. In order to provide a comprehensive formulation, the general model of human motor behavior during physical HRI is first derived for a general desired trajectory $\boldsymbol{q}_{\mathrm{d}}$ in this chapter and later analyzed in more detail for different parameterizations in Chapter 3.

Replacing the unperturbed arm configuration $\boldsymbol{q}^*$ in (2.13) by the desired trajectory $\boldsymbol{q}_{\mathrm{d}}$ and inserting (2.8) and (2.13) into (2.1) yields

$$\begin{aligned} -\boldsymbol{\tau}_{\mathrm{ext}}(\boldsymbol{q}, \dot{\boldsymbol{q}}, \ddot{\boldsymbol{q}}, \boldsymbol{\gamma}) = \boldsymbol{\tau}_{\mathrm{FF}}(\boldsymbol{\gamma}) + D_q(\boldsymbol{q}, \dot{\boldsymbol{q}}, \boldsymbol{\gamma})\dot{\boldsymbol{e}}_q(\boldsymbol{\gamma}) + K_q(\boldsymbol{q}, \dot{\boldsymbol{q}}, \boldsymbol{\gamma})\boldsymbol{e}_q(\boldsymbol{\gamma}) \\ + \boldsymbol{\tau}_{\mathrm{FBv}}(\boldsymbol{\gamma}) - M_q(\boldsymbol{q})\ddot{\boldsymbol{q}} - C_q(\boldsymbol{q}, \dot{\boldsymbol{q}})\dot{\boldsymbol{q}} + \boldsymbol{\upsilon}_q \ , \end{aligned} \tag{2.18}$$

where the joint error $\boldsymbol{e}_q(\boldsymbol{\gamma}) = \boldsymbol{q}_{\mathrm{d}}(\boldsymbol{\gamma}) - \boldsymbol{q}$. According to a commonly accepted theory of sensory-motor control the feedforward torques $\boldsymbol{\tau}_{\mathrm{FF}}$, which are necessary to attain the desired trajectory $\boldsymbol{q}_{\mathrm{d}}$, are appropriately scaled by the CNS using internal models [11]. These internal models are acquired through experience and contain inverse dynamics representations of the musculoskeletal system and the interaction with the external environment [12]:

$$\begin{aligned} \boldsymbol{\tau}_{\mathrm{FF}}(\boldsymbol{\gamma}) = \hat{M}_q(\boldsymbol{q}_{\mathrm{d}}(\boldsymbol{\gamma}))\ddot{\boldsymbol{q}}_{\mathrm{d}}(\boldsymbol{\gamma}) + \hat{C}_q(\boldsymbol{q}_{\mathrm{d}}(\boldsymbol{\gamma}), \dot{\boldsymbol{q}}_{\mathrm{d}}(\boldsymbol{\gamma}))\dot{\boldsymbol{q}}_{\mathrm{d}}(\boldsymbol{\gamma}) \\ - \hat{\boldsymbol{\tau}}_{\mathrm{ext}}(\boldsymbol{q}_{\mathrm{d}}(\boldsymbol{\gamma}), \dot{\boldsymbol{q}}_{\mathrm{d}}(\boldsymbol{\gamma}), \ddot{\boldsymbol{q}}_{\mathrm{d}}(\boldsymbol{\gamma})) \ , \end{aligned} \tag{2.19}$$

where the variables $\hat{\boldsymbol{\tau}}_{\text{ext}}$, $\hat{M}_q$, and $\hat{C}_q$ are the estimated internal model counterparts to the respective variables in (2.1). Inserting these feedforward torques $\boldsymbol{\tau}_{\text{FF}}$ in (2.18) yields

$$\begin{aligned}-\boldsymbol{\tau}_{\text{ext}}(\boldsymbol{q},\dot{\boldsymbol{q}},\ddot{\boldsymbol{q}},\boldsymbol{\gamma}) = \hat{M}_q(\boldsymbol{q}_{\text{d}}(\boldsymbol{\gamma}))\ddot{\boldsymbol{q}}_{\text{d}}(\boldsymbol{\gamma}) - M_q(\boldsymbol{q})\ddot{\boldsymbol{q}} + \hat{C}_q(\boldsymbol{q}_{\text{d}}(\boldsymbol{\gamma}),\dot{\boldsymbol{q}}_{\text{d}}(\boldsymbol{\gamma}))\dot{\boldsymbol{q}}_{\text{d}}(\boldsymbol{\gamma}) \\ - C_q(\boldsymbol{q},\dot{\boldsymbol{q}})\dot{\boldsymbol{q}} + D_q(\boldsymbol{q},\dot{\boldsymbol{q}},\boldsymbol{\gamma})\dot{\boldsymbol{e}}_q(\boldsymbol{\gamma}) + K_q(\boldsymbol{q},\dot{\boldsymbol{q}},\boldsymbol{\gamma})\boldsymbol{e}_q(\boldsymbol{\gamma}) \\ + \boldsymbol{\tau}_{\text{FBv}}(\boldsymbol{\gamma}) - \hat{\boldsymbol{\tau}}_{\text{ext}}(\boldsymbol{q}_{\text{d}}(\boldsymbol{\gamma}),\dot{\boldsymbol{q}}_{\text{d}}(\boldsymbol{\gamma}),\ddot{\boldsymbol{q}}_{\text{d}}(\boldsymbol{\gamma})) + \boldsymbol{\upsilon}_q\ . \end{aligned} \tag{2.20}$$

Summarizing the discrepancies between the inertia and Coriolis/centrifugal terms in (2.1) and the estimated counterparts in (2.19) in the estimation discrepancies $\boldsymbol{\varepsilon}_{\text{est},q}$ yields

$$\begin{aligned}-\boldsymbol{\tau}_{\text{ext}}(\boldsymbol{q},\dot{\boldsymbol{q}},\ddot{\boldsymbol{q}},\boldsymbol{\gamma}) = M_q(\boldsymbol{q})\ddot{\boldsymbol{e}}_q(\boldsymbol{\gamma}) + C_q(\boldsymbol{q},\dot{\boldsymbol{q}})\dot{\boldsymbol{e}}_q(\boldsymbol{\gamma}) + \boldsymbol{\varepsilon}_{\text{est},q}(\boldsymbol{q},\dot{\boldsymbol{q}},\ddot{\boldsymbol{q}},\boldsymbol{\gamma}) \\ + D_q(\boldsymbol{q},\dot{\boldsymbol{q}},\boldsymbol{\gamma})\dot{\boldsymbol{e}}_q(\boldsymbol{\gamma}) + K_q(\boldsymbol{q},\dot{\boldsymbol{q}},\boldsymbol{\gamma})\boldsymbol{e}_q(\boldsymbol{\gamma}) + \boldsymbol{\tau}_{\text{FBv}}(\boldsymbol{\gamma}) \\ - \hat{\boldsymbol{\tau}}_{\text{ext}}(\boldsymbol{q}_{\text{d}}(\boldsymbol{\gamma}),\dot{\boldsymbol{q}}_{\text{d}}(\boldsymbol{\gamma}),\ddot{\boldsymbol{q}}_{\text{d}}(\boldsymbol{\gamma})) + \boldsymbol{\upsilon}_q\ , \end{aligned} \tag{2.21}$$

As the term $C_q(\boldsymbol{q},\dot{\boldsymbol{q}})\dot{\boldsymbol{e}}_q(\boldsymbol{\gamma})$ is characterized by complexity $\mathcal{O}(\dot{\boldsymbol{q}}^2)$, its contributions are small compared to those of the other terms. Thus, we add it to the estimation discrepancies $\boldsymbol{\varepsilon}_{\text{est},q}$ and define the dynamic discrepancies $\boldsymbol{\varepsilon}_{\text{dyn},q}(\boldsymbol{q},\dot{\boldsymbol{q}},\ddot{\boldsymbol{q}},\boldsymbol{\gamma}) = C_q(\boldsymbol{q},\dot{\boldsymbol{q}})\dot{\boldsymbol{e}}_q(\boldsymbol{\gamma}) + \boldsymbol{\varepsilon}_{\text{est},q}(\boldsymbol{q},\dot{\boldsymbol{q}},\ddot{\boldsymbol{q}},\boldsymbol{\gamma})$. Furthermore, in order to limit the complexity of the derived model and place specific focus on the impedance characteristics, we assume the contributions of the voluntary feedback torques $\boldsymbol{\tau}_{\text{FBv}}$ to be small compared to those of the impedance components damping D_q and stiffness K_q. In order to consider these comparatively small contributions without the need to formulate an explicit model of voluntary feedback behavior, we replace the fully feedforward term $\hat{\boldsymbol{\tau}}_{\text{ext}}(\boldsymbol{q}_{\text{d}}(\boldsymbol{\gamma}),\dot{\boldsymbol{q}}_{\text{d}}(\boldsymbol{\gamma}),\ddot{\boldsymbol{q}}_{\text{d}}(\boldsymbol{\gamma}))$ by the term $\hat{\boldsymbol{\tau}}_{\text{ext,FBv}}(\boldsymbol{q},\dot{\boldsymbol{q}},\ddot{\boldsymbol{q}},\boldsymbol{\gamma})$, which depends on the kinematics $\{\boldsymbol{q},\dot{\boldsymbol{q}},\ddot{\boldsymbol{q}}\}$ and the task-specific input parameters $\boldsymbol{\gamma}$. With these changes, we obtain the following general model of human motor behavior during physical HRI:

$$\begin{aligned}-\boldsymbol{\tau}_{\text{ext}}(\boldsymbol{q},\dot{\boldsymbol{q}},\ddot{\boldsymbol{q}},\boldsymbol{\gamma}) = M_q(\boldsymbol{q})\ddot{\boldsymbol{e}}_q(\boldsymbol{\gamma}) + D_q(\boldsymbol{q},\dot{\boldsymbol{q}},\boldsymbol{\gamma})\dot{\boldsymbol{e}}_q(\boldsymbol{\gamma}) + K_q(\boldsymbol{q},\dot{\boldsymbol{q}},\boldsymbol{\gamma})\boldsymbol{e}_q(\boldsymbol{\gamma}) \\ - \hat{\boldsymbol{\tau}}_{\text{ext,FBv}}(\boldsymbol{q},\dot{\boldsymbol{q}},\ddot{\boldsymbol{q}},\boldsymbol{\gamma}) + \boldsymbol{\varepsilon}_{\text{dyn},q}(\boldsymbol{q},\dot{\boldsymbol{q}},\ddot{\boldsymbol{q}},\boldsymbol{\gamma}) + \boldsymbol{\upsilon}_q\ . \end{aligned} \tag{2.22}$$

In non-physical HRI, there are no external torques $\boldsymbol{\tau}_{\text{ext}}$ and consequently also no estimated external torques $\hat{\boldsymbol{\tau}}_{\text{ext}}$. Without physical interaction with the environment, the only source of unpredictable dynamics consists of the neural noise $\boldsymbol{\upsilon}_q$, which, due to its stochastic nature, cannot be compensated by voluntary feedback torques $\boldsymbol{\tau}_{\text{FBv}}$. As there are no estimated external torques $\hat{\boldsymbol{\tau}}_{\text{ext}}$ and no voluntary feedback torques $\boldsymbol{\tau}_{\text{FBv}}$, the term $\hat{\boldsymbol{\tau}}_{\text{ext,FBv}}$ is also zero. Consideration of these correlations yields a simplified variation of the general model:

$$\begin{aligned}\boldsymbol{0} = M_q(\boldsymbol{q})\ddot{\boldsymbol{e}}_q(\boldsymbol{\gamma}) + D_q(\boldsymbol{q},\dot{\boldsymbol{q}},\boldsymbol{\gamma})\dot{\boldsymbol{e}}_q(\boldsymbol{\gamma}) + K_q(\boldsymbol{q},\dot{\boldsymbol{q}},\boldsymbol{\gamma})\boldsymbol{e}_q(\boldsymbol{\gamma}) \\ + \boldsymbol{\varepsilon}_{\text{dyn},q}(\boldsymbol{q},\dot{\boldsymbol{q}},\ddot{\boldsymbol{q}},\boldsymbol{\gamma}) + \boldsymbol{\upsilon}_q\ . \end{aligned} \tag{2.23}$$

In the following section, both variations of this general model of human motor behavior, for physical HRI as well as for non-physical HRI, are transformed to Cartesian space.

2.4. Cartesian Space Representations

In most realistic physical HRI scenarios, measurements are obtained at the robot end-effector in Cartesian space. If the upper limb dimensions of the human with whom the robot is interacting are known, the arm configuration $\boldsymbol{q}$ in joint space can be calculated from the arm configuration $\boldsymbol{x}$ in Cartesian space with the inverse kinematics

$$q_1 = \tan^{-1}\left(\frac{x_2}{x_1}\right) - \tan^{-1}\left(\frac{l_2 \sin(q_2)}{l_1 + l_2 \cos(q_2)}\right) , \tag{2.24}$$

$$q_2 = \cos^{-1}\left(\frac{x_1^2 + x_2^2 - l_1^2 - l_2^2}{2 l_1 l_2}\right) , \tag{2.25}$$

where l_1 is the length of the upper arm, l_2 is the length of the forearm, and the origin of the Cartesian coordinate system is located in the shoulder joint. Furthermore, the Jacobian J_x can be used to transform the external forces $\boldsymbol{u}_{\text{ext}}$ to the external torques

$$\boldsymbol{\tau}_{\text{ext}} = J_x^{\mathsf{T}}(\boldsymbol{q}) \boldsymbol{u}_{\text{ext}} . \tag{2.26}$$

However, in many realistic physical HRI scenarios, the upper limb dimensions of the human are unknown. Therefore, in order to avoid the dependency on the lengths of the upper arm l_1 and the forearm l_2 and enable transferability to a broad selection of physical HRI scenarios, we express the general models (2.22) and (2.23) in Cartesian space representation.

Firstly, we transform the external torques $\boldsymbol{\tau}_{\text{ext}}$ and the term $\hat{\boldsymbol{\tau}}_{\text{ext,FBv}}$ to Cartesian space, including a change in algebraic sign to account for the fact that the measurements are obtained by a force sensor situated at the robot end-effector:

$$\boldsymbol{u}_{\text{int}}(\boldsymbol{x}, \dot{\boldsymbol{x}}, \ddot{\boldsymbol{x}}, \boldsymbol{\gamma}) = -J_x(\boldsymbol{q})^{-\mathsf{T}} \boldsymbol{\tau}_{\text{ext}}(\boldsymbol{q}, \dot{\boldsymbol{q}}, \ddot{\boldsymbol{q}}, \boldsymbol{\gamma}) , \tag{2.27}$$

$$\hat{\boldsymbol{u}}_{\text{int,FBv}}(\boldsymbol{x}, \dot{\boldsymbol{x}}, \ddot{\boldsymbol{x}}, \boldsymbol{\gamma}) = -J_x(\boldsymbol{q})^{-\mathsf{T}} \hat{\boldsymbol{\tau}}_{\text{ext,FBv}}(\boldsymbol{q}, \dot{\boldsymbol{q}}, \ddot{\boldsymbol{q}}, \boldsymbol{\gamma}) . \tag{2.28}$$

We refer to $\boldsymbol{u}_{\text{int}}$ as the interaction forces and $\hat{\boldsymbol{u}}_{\text{int,FBv}}$ as the estimated interaction forces. Secondly, we transform the inertia M_q, the damping D_q, and the stiffness K_q as well as the dynamic discrepancies $\boldsymbol{\varepsilon}_{\text{dyn},q}$ and the neural noise $\boldsymbol{\upsilon}_q$ to Cartesian space:

$$M_x(\boldsymbol{x}) = J_x(\boldsymbol{q})^{-\mathsf{T}} M_q(\boldsymbol{q}) J_x(\boldsymbol{q})^{-1} , \tag{2.29}$$

$$D_x(\boldsymbol{x}, \dot{\boldsymbol{x}}, \boldsymbol{\gamma}) = J_x(\boldsymbol{q})^{-\mathsf{T}} D_q(\boldsymbol{q}, \dot{\boldsymbol{q}}, \boldsymbol{\gamma}) J_x(\boldsymbol{q})^{-1} , \tag{2.30}$$

$$K_x(\boldsymbol{x}, \dot{\boldsymbol{x}}, \boldsymbol{\gamma}) = J_x(\boldsymbol{q})^{-\mathsf{T}} K_q(\boldsymbol{q}, \dot{\boldsymbol{q}}, \boldsymbol{\gamma}) J_x(\boldsymbol{q})^{-1} , \tag{2.31}$$

$$\boldsymbol{\varepsilon}_{\text{dyn},x}(\boldsymbol{x}, \dot{\boldsymbol{x}}, \ddot{\boldsymbol{x}}, \boldsymbol{\gamma}) = J_x(\boldsymbol{q})^{-\mathsf{T}} \boldsymbol{\varepsilon}_{\text{dyn},q}(\boldsymbol{q}, \dot{\boldsymbol{q}}, \ddot{\boldsymbol{q}}, \boldsymbol{\gamma}) , \tag{2.32}$$

$$\boldsymbol{\upsilon}_x = J_x(\boldsymbol{q})^{-\mathsf{T}} \boldsymbol{\upsilon}_q , \tag{2.33}$$

where M_x, D_x, K_x, $\boldsymbol{\varepsilon}_{\text{dyn},x}$, and $\boldsymbol{\upsilon}_x$ are the Cartesian space counterparts of the respective matrices and vectors. By inserting (2.27) - (2.33) into (2.22), we obtain the Cartesian space representation of the general model of human motor behavior during physical HRI:

$$\boldsymbol{u}_{\text{int}}(\overline{\boldsymbol{\xi}}) = \boldsymbol{u}_{\text{imp}}(\overline{\boldsymbol{\xi}}) + \hat{\boldsymbol{u}}_{\text{int},\varepsilon}(\overline{\boldsymbol{\xi}}) + \boldsymbol{\upsilon}_x , \tag{2.34}$$

$$\boldsymbol{u}_{\text{imp}}(\overline{\boldsymbol{\xi}}) = M_x(\boldsymbol{x}) \ddot{\boldsymbol{e}}_x(\boldsymbol{\gamma}) + D_x(\boldsymbol{\xi}) \dot{\boldsymbol{e}}_x(\boldsymbol{\gamma}) + K_x(\boldsymbol{\xi}) \boldsymbol{e}_x(\boldsymbol{\gamma}) , \tag{2.35}$$

where the error $\boldsymbol{e}_x(\boldsymbol{\gamma}) = \boldsymbol{x}_\mathrm{d}(\boldsymbol{\gamma}) - \boldsymbol{x}$, in which $\boldsymbol{x}_\mathrm{d}$ is the desired trajectory, and $\boldsymbol{\xi} = [\boldsymbol{x}^\mathsf{T}, \dot{\boldsymbol{x}}^\mathsf{T}, \boldsymbol{\gamma}^\mathsf{T}]^\mathsf{T}$, $\overline{\boldsymbol{\xi}} = [\boldsymbol{x}^\mathsf{T}, \dot{\boldsymbol{x}}^\mathsf{T}, \ddot{\boldsymbol{x}}^\mathsf{T}, \boldsymbol{\gamma}^\mathsf{T}]^\mathsf{T}$, and $\hat{\boldsymbol{u}}_{\mathrm{int},\varepsilon}(\overline{\boldsymbol{\xi}}) = \hat{\boldsymbol{u}}_{\mathrm{int,FBv}}(\overline{\boldsymbol{\xi}}) + \boldsymbol{\varepsilon}_{\mathrm{dyn},x}(\overline{\boldsymbol{\xi}})$ are defined to increase clarity. We refer to $\boldsymbol{u}_\mathrm{imp}$ as the impedance forces and, for simplicity, despite the combination with the dynamic discrepancies $\boldsymbol{\varepsilon}_{\mathrm{dyn},x}$, we still refer to $\hat{\boldsymbol{u}}_{\mathrm{int},\varepsilon}$ as the estimated interaction forces. By inserting (2.29) - (2.33) into (2.23), we obtain the Cartesian space representation of the simplified variation of the general model, which applies to non-physical HRI:

$$\mathbf{0} = \boldsymbol{u}_\mathrm{imp}(\overline{\boldsymbol{\xi}}) + \boldsymbol{\varepsilon}_{\mathrm{dyn},x}(\overline{\boldsymbol{\xi}}) + \boldsymbol{v}_x \ . \tag{2.36}$$

Remark 2.6. As there are no interaction forces $\boldsymbol{u}_\mathrm{int}$ during non-physical HRI, this simplified variation of the general model of human motor behavior is based exclusively on position measurements of the human hand in Cartesian space.

The general model (2.34) represents the basis for the derivation of the Bayesian impedance model for human motor behavior prediction in Chapter 3, in which, without loss of generality, particular focus is placed on the derivation of a Bayesian human motor behavior model for physical HRI. As (2.36) is a simplification of (2.34), the derived Bayesian model includes a simplified variation that applies to non-physical HRI.

2.5. Summary

In this chapter, we introduced the necessary background information and established the relevant neuromechanical correlations for the development of human motor behavior models that place specific emphasis on the impedance control model and the impedance components. In order to optimally preface the contents of the subsequent chapters, we focused on the multi-joint human arm, i.e., the complete upper limb including the shoulder joint. We began by presenting the neuromuscular rigid body dynamics of the multi-joint human arm, with specific focus placed on the muscle activities and the internally generated joint torques that instantiate the desired motor behavior. Subsequently, we derived an impedance control model that represents the effects of the involuntary feedback behavior in the form of the impedance components joint damping and joint stiffness. In order to obtain a more general model that allows for the full description and prediction of human motor behavior, we shifted focus towards the feedforward torques and the internal models. By assuming that the unperturbed states are representations of the desired kinematic states of the desired motor behavior, which are given by a desired trajectory, we were able to derive a general model of human motor behavior, which we formulated both for physical as well as non-physical HRI. Furthermore, we transformed both model variations to Cartesian space. The models that are derived in this chapter represent the bases for the derivation of models that facilitate consideration of human impedance characteristics in the control design process for physical HRI within the following chapters.

Bayesian Impedance Model for Human Motor Behavior Prediction

3.

In the previous chapter, we formulated a general model of human motor behavior during physical HRI. In this chapter, we address the first of the three previously summarized crucial open challenges in the consideration of human impedance characteristics in the control design process for physical HRI by focusing on the information exploitation, i.e, the inclusion of a priori impedance knowledge in human motor behavior modeling. In the derivation of the general model in the previous chapter, we incorporated an underlying behavioral structure by approximating the lower dimensional manifolds of human motor behavior by an impedance control model that counteracts deviations from a desired trajectory. In this chapter, in order to enable the integration of a priori knowledge about this underlying behavioral structure, we adopt a Bayesian setting by assuming GP priors for the impedance components and the desired trajectory. The resulting Bayesian model enables exploitation of a priori human arm impedance knowledge for the regression of human motor behavior. As the integration of the underlying behavioral structure in the form of the impedance control model guarantees that all correlations of the Bayesian model are inherently consistent with the structural constraints, it not only enables regression of human motor behavior, but also leads to superior prediction performance and generalization capabilities. Furthermore, it provides insights on otherwise unobservable intrinsic states. In the context of the impedance control model and the corresponding impedance components, it specifically enables the estimation of the human motor intention in the form of the desired trajectory and corresponding confidence levels. In this chapter, without loss of generality, we place particular focus on the derivation of a Bayesian impedance model for physical HRI, as it represents the more challenging problem. However, we additionally describe necessary adjustments for non-physical HRI.

The remainder of this chapter is structured as follows: related work and open problems are reviewed in Section 3.1. An introduction to GPs and multivariate Gaussian conditioning is presented in Section 3.2. Subsequently, in Section 3.3, we derive the GP-based Bayesian model, which addresses the considered problem of human motor behavior regression via human motor intention inference. In Section 3.4, we facilitate proper application of the model by presenting application guidelines, which include an overview of estimated human arm impedance characteristics in the literature, implications for GP prior parameterization, and pseudocode application instructions. In Section 3.5, the model is validated with simulated data of a neuromechanical model of the human arm. The direct control over the simulated intrinsic states enables both validation of the intention estimation capabilities as well as assessment of the effects of GP prior parameterization. Superior prediction performance is demonstrated with respect to a naive GP prior. In Section 3.6, an experiment with human participants is conducted to evaluate the model with experimental data, analyze effects of training data sparsity, and demonstrate generalization capabilities. The obtained results are discussed in Section 3.7 and summarized in Section 3.8.

3.1. Related Work and Open Problems

In current HRI research, human motor behavior is modeled in different ways. The authors of [71] propose a method for short-term motor behavior predictions based on observed forces and respective derivatives. Others transfer the minimum jerk principle [72] to HRI scenarios (e.g., [73] and [74]) for both short- and long-term predictions, depending on the task type. For tasks with increased complexity, methods based on the minimum jerk principle are outperformed by a combination of judiciously defined polynomials that allow for increased flexibility in the approximation of the dynamics [75]. In contrast to dynamics level methods, the programming by demonstration paradigm is applied for the derivation of long-term motor behavior predictions at task level. The required demonstrations of task-specific HRI behavior are obtained through direct physical interaction [47] or teleoperation [76] and are encoded in probabilistic models that capture the joint statistics of the observed trajectories and forces [77]. These models are naive in the sense that they do not incorporate a priori knowledge on the system. However, the inclusion of such knowledge can provide insights on unobservable intrinsic states and lead to superior prediction performance and generalization capabilities. GP-based models are a powerful, non-parametric approach that allows for the integration of a priori knowledge and only requires the definition of second-order statistics between function values to efficiently approximate continuous functions from data [78, 79]. They are well-suited for human motor behavior modeling, due to their desirable smoothness properties and their ability to accurately model non-linear correlations [80].

GP-based models for regression were first described in a machine learning context by Williams and Rasmussen in [78]. These authors were partly inspired by the work of Neal, who had shown that a Bayesian neural network converges towards a GP as the number of hidden layers within the network approaches infinity [81]. The benefits of GPs for system identification are exploited for example in [82–87]. In [83], a GP is used to approximate a non-linear state vector field. In [84], an additional GP is used to model the non-linear mapping from the observation space to a latent state space. The model is extended in [85], where human motion is modeled by explicitly incorporating an intention function into the latent state space transition function, which is also modeled by a set of GPs. Second order interaction dynamics are explored in [86], where observed trajectories are considered to be driven by latent forces. In [87], a dynamic lower-dimensional representation of human finger motion is obtained by decomposing variations in reach-and-grasp motions and modeling respective primitives with a multivariate GP model. GPs define input space correlations and derive predictions analytically by applying Bayes' rule, which yields confidence bounds of the results. These bounds are particularly interesting for control design, as they enable control adaptation according to the prediction confidence [88, 89]. The performance of GPs depends on an appropriate kernel structure. If the structure of the covariance function is not defined in accordance with the real function, the convergence rate of the former towards the latter may increase exponentially. This leads to a decrease of the generalization capabilities in previously unobserved regions of the input space. The validity of the prediction covariance as an indicator of the reliability decreases with increasing distance to the training data [90]. This dependency can be overcome by inclusion of a priori knowledge in the definition of the GP prior structure. In this chapter, we construct a GP-based human motor behavior model that incorporates an impedance control model and enable the integration of a priori knowledge by assuming GP priors for the impedance components and the desired trajectory.

3.2. Gaussian Process Priors

A GP $g(\boldsymbol{\xi}) : \mathbb{R}^n \to \mathbb{R}$ at input points $\boldsymbol{\xi} \in \mathbb{R}^n$ is a statistical distribution over function values, wherein any finite collection of samples $\{g(\boldsymbol{\xi}_1) \ \cdots \ g(\boldsymbol{\xi}_h)\}$ with sample number $h \in \mathbb{N}^+$ forms a multivariate Gaussian random variable. A GP $g(\boldsymbol{\xi}) \sim \mathcal{GP}\left(\mu(\boldsymbol{\xi}), \kappa(\boldsymbol{\xi}, \boldsymbol{\xi}')\right)$ is fully defined by its mean function $\mu(\boldsymbol{\xi}) = \mathsf{E}\left[g(\boldsymbol{\xi})\right]$ and its covariance function

$$\kappa(\boldsymbol{\xi}, \boldsymbol{\xi}') = \mathsf{Cov}\Big[g(\boldsymbol{\xi}), g(\boldsymbol{\xi}')\Big] = \mathsf{E}\left[(g(\boldsymbol{\xi}) - \mu(\boldsymbol{\xi}))(g(\boldsymbol{\xi}') - \mu(\boldsymbol{\xi}'))^{\mathsf{T}}\right] \ , \tag{3.1}$$

which represents the correlation of two input points $\boldsymbol{\xi}$ and $\boldsymbol{\xi}'$ in terms of the statistical relationship of the respective GP values $g(\boldsymbol{\xi})$ and $g(\boldsymbol{\xi}')$ and is also referred to as kernel. Selecting an appropriate mean function μ and covariance function κ is key for acquiring high generalization capabilities, as they define the overall properties of the GP.

GPs possess the desirable properties of multivariate normal distributions, which enable the computation of conditional posterior distributions from joint prior distributions. The joint prior distribution $\mathsf{P}\left(\mathcal{Y}, y_* | \Xi, \boldsymbol{\xi}_*\right)$ of a given training set of noisy observations $\mathcal{Y} = \{y_j\}_{j=1}^h$ at inputs $\Xi = \{\boldsymbol{\xi}_j\}_{j=1}^h$ and predictive output y_* at test input $\boldsymbol{\xi}_*$ is defined as

$$\mathsf{P}\left(\mathcal{Y}, y_* | \Xi, \boldsymbol{\xi}_*\right) = \mathcal{N}\left(\begin{bmatrix}\mathcal{Y} \\ y_*\end{bmatrix} \middle| \begin{bmatrix}\mu(\Xi) \\ \mu(\boldsymbol{\xi}_*)\end{bmatrix}, \begin{bmatrix}K + \sigma_\nu^2 I & \boldsymbol{\kappa}_* \\ \boldsymbol{\kappa}_*^{\mathsf{T}} & \kappa_{**} + \sigma_n^2\end{bmatrix}\right) \ , \tag{3.2}$$

where $K = \kappa(\Xi, \Xi)$, $\boldsymbol{\kappa}_* = \kappa(\boldsymbol{\xi}_*, \Xi)$, and $\kappa_{**} = \kappa(\boldsymbol{\xi}_*, \boldsymbol{\xi}_*)$ represent the covariances of the training inputs Ξ and the test input $\boldsymbol{\xi}_*$. The matrix I is the identity matrix and σ_ν^2 is the observation noise variance. By means of multivariate Gaussian conditioning, i.e., application of Bayes' rule, the conditional (predictive) posterior $\mathsf{P}\left(y_* | \mathcal{Y}, \Xi, \boldsymbol{\xi}_*\right)$ is computed as

$$\begin{aligned}\mathsf{P}\left(y_* | \mathcal{Y}, \Xi, \boldsymbol{\xi}_*\right) = \mathcal{N}(y_* | \mu(\boldsymbol{\xi}_*) + \boldsymbol{\kappa}_*^{\mathsf{T}}(K + \sigma_\nu^2 I)^{-1}(\mathcal{Y} - \mu(\Xi)), \\ \kappa_{**} + \sigma_\nu^2 - \boldsymbol{\kappa}_*^{\mathsf{T}}(K + \sigma_\nu^2 I)^{-1}\boldsymbol{\kappa}_*) \ ,\end{aligned} \tag{3.3}$$

Remark 3.1. The computation of the conditional (predictive) posterior $\mathsf{P}\left(y_* | \mathcal{Y}, \Xi, \boldsymbol{\xi}_*\right)$ is governed by matrix inversion $(K + \sigma_\nu^2 I)^{-1}$ with complexity $\mathcal{O}(h^3)$. If necessary, multi-output GPs, in which the covariance function is defined to capture the dependencies between all input points as well as non-trivial correlations across all outputs, offer output correlations, but at the cost of higher computational complexity [91].

3.3. Bayesian Impedance Model

The problem considered in this chapter consists of the prediction of human motor behavior, represented by the interaction forces $\boldsymbol{u}_{\text{int}}$ in the interaction dynamics (2.34), through the estimation of the human motor intention, represented by the desired trajectory $\boldsymbol{x}_{\text{d}}$ in the impedance dynamics (2.35). This is to be achieved by means of regression analysis, given the input-output pairs $\{\overline{\boldsymbol{\xi}}, \boldsymbol{u}_{\text{int}}(\overline{\boldsymbol{\xi}})\}$, which are obtained through sensors at the robot end-effector. Therefore, in this section, we derive a multi-layered Bayesian model, which is presented schematically in Fig. 3.1. The lowest layer of the model is composed of the latent variables

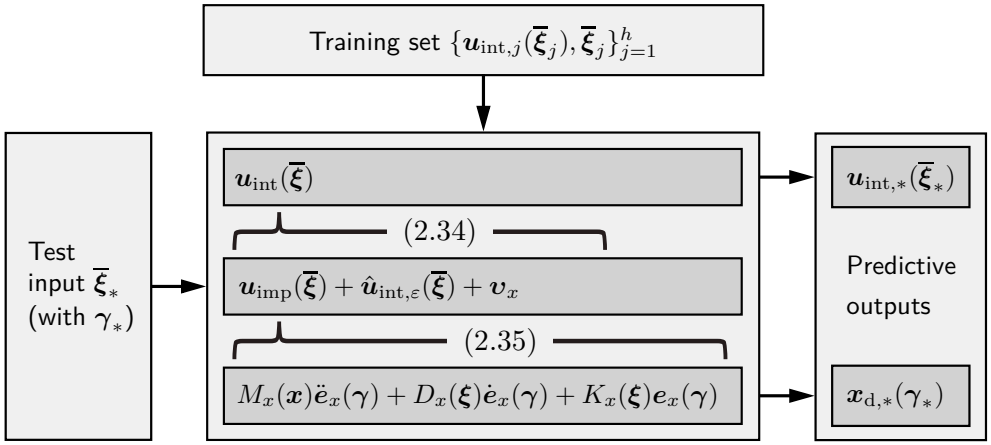

Figure 3.1.: Schematic block diagram of the Bayesian model. The transitions between the layers correspond to (2.34) and (2.35). (© 2019 IEEE)

M_x, D_x, K_x, and $\boldsymbol{x}_{\mathrm{d}}$. By assuming prior distributions on these latent variables, we construct a compound kernel for the impedance forces $\boldsymbol{u}_{\mathrm{imp}}$. It is part of the middle layer of the model, which additionally contains the neural noise $\boldsymbol{v}_x$ and the estimated interaction forces $\hat{\boldsymbol{u}}_{\mathrm{int},\varepsilon}$. By again assuming prior distributions, we combine all of the middle layer components to construct a compound kernel for the interaction forces $\boldsymbol{u}_{\mathrm{int}}$. It constitutes the top layer of the model and is able to account for predictable ($\hat{\boldsymbol{u}}_{\mathrm{int},\varepsilon}$) as well as unpredictable ($\boldsymbol{u}_{\mathrm{imp}}$) interaction dynamics. Due to dependency on $\overline{\boldsymbol{\xi}}$, both components can be adapted during task execution. Given a training set $\{\boldsymbol{u}_{\mathrm{int},j}(\overline{\boldsymbol{\xi}}_j\}), \overline{\boldsymbol{\xi}}_j\}_{j=1}^h$, the model provides predictions $\boldsymbol{u}_{\mathrm{int},*}$ at test inputs $\overline{\boldsymbol{\xi}}_*$ and infers the desired trajectory $\boldsymbol{x}_{\mathrm{d},*}$ at test input $\boldsymbol{\gamma}_*$. The inclusion of the latter requires that the desired motor behavior can be described by a twice differentiable, well-defined function $\boldsymbol{q}_{\mathrm{d}}(\boldsymbol{\gamma})$, which is defined by suitable, task-specific input parameters $\boldsymbol{\gamma}$.

In this chapter, we approximate the inertia M_x, the damping D_x, and the stiffness K_x in the impedance dynamics (2.35) by diagonal matrices. Thus, the interaction dynamics (2.34) and the impedance dynamics (2.35) in the i-th dimension can be expressed as

$$u_{\mathrm{int},i}(\overline{\boldsymbol{\xi}}) = u_{\mathrm{imp},i}(\overline{\boldsymbol{\xi}}) + \hat{u}_{\mathrm{int},\varepsilon,i}(\overline{\boldsymbol{\xi}}) + v_x \ , \tag{3.4}$$

$$u_{\mathrm{imp},i}(\overline{\boldsymbol{\xi}}) = m_{x,i}\ddot{e}_{x,i}(\boldsymbol{\gamma}) + d_{x,i}(\boldsymbol{\xi})\dot{e}_{x,i}(\boldsymbol{\gamma}) + k_{x,i}(\boldsymbol{\xi})e_{x,i}(\boldsymbol{\gamma}) \ , \tag{3.5}$$

where $m_{x,i}$ is a one-dimensional variable, $u_{\mathrm{int},i}$, $u_{\mathrm{imp},i}$, $\hat{u}_{\mathrm{int},\varepsilon,i}$, $d_{x,i}$, $k_{x,i}$, $e_{x,i}$, $x_{\mathrm{d},i}$, and x_i are one-dimensional functions, and the neural noise v_x is defined as $v_x \sim \mathcal{N}\left(v_x \,\middle|\, 0, \sigma_v^2\right)$, in which σ_v^2 is the respective neural noise variance. For notational convenience, from this point on, we omit the subscript $(\cdot)_x$ in the one-dimensional counterparts $m_{x,i}$, $d_{x,i}$, $k_{x,i}$, and $e_{x,i}$ to the respective two-dimensional variables M_x, D_x, K_x, and $\boldsymbol{e}_x$.

Remark 3.2. Veridical biomechanical modeling would require inclusion of the non-diagonal elements of the inertia M_x, the damping D_x, and the stiffness K_x. Although this would in principle be possible within the context of the Bayesian impedance model, we nonetheless approximate these three matrices by diagonal matrices. This approximation is motivated by multiple reasons: 1) Of the few quantitative Cartesian space results of human arm impedance estimation during movement, most are one-dimensional [92, 93] or assume decoupled arm

dynamics [53, 94, 95]. 2) Non-diagonal elements would require convolved multi-output GPs with output correlations, which possess substantially higher computational complexity [96]. 3) These output correlations would greatly diminish the comprehensibility of the derivations of the compound kernels as well as the analyses of the effects of GP prior parameterization. For completeness, we discuss adjustments for multi-dimensional treatment in Section 3.7.

3.3.1. Impedance Model Priors

For statistical analysis of the one-dimensional formulation of the general model of human motor behavior during physical HRI, we assume that variable m_i and functionals d_i, k_i, $x_{\mathrm{d},i}$, and $\hat{u}_{\mathrm{int},\varepsilon,i}$ are all statistically independent and possess prior distributions

$$m_i \sim \mathcal{N}\left(m_i \,\middle|\, \mu_{m,i}, \sigma^2_{m,i}\right) \ , \tag{3.6}$$

$$d_i(\boldsymbol{\xi}) \sim \mathcal{GP}\left(\mu_{d,i}, \kappa_d(\boldsymbol{\xi}, \boldsymbol{\xi}')\right) \ , \tag{3.7}$$

$$k_i(\boldsymbol{\xi}) \sim \mathcal{GP}\left(\mu_{k,i}, \kappa_k(\boldsymbol{\xi}, \boldsymbol{\xi}')\right) \ , \tag{3.8}$$

$$x_{\mathrm{d},i}(\boldsymbol{\gamma}) \sim \mathcal{GP}\left(\mu_{x_\mathrm{d},i}, \kappa_{x_\mathrm{d}}(\boldsymbol{\gamma}, \boldsymbol{\gamma}')\right) \ , \tag{3.9}$$

$$\hat{u}_{\mathrm{int},\varepsilon,i}(\overline{\boldsymbol{\xi}}) \sim \mathcal{GP}\Big(0, \kappa_{\hat{u}_{\mathrm{int},\varepsilon}}(\overline{\boldsymbol{\xi}}, \overline{\boldsymbol{\xi}}')\Big) \ , \tag{3.10}$$

where $\mu_{m,i}$, $\mu_{d,i}$, $\mu_{k,i}$, and $\mu_{x_\mathrm{d},i}$ are the expected mean values (EMVs) of inertia, damping, stiffness, and desired trajectory, respectively, and $\sigma^2_{m,i}$ is the inertia variance. The prior distributions d_i, k_i, $x_{\mathrm{d},i}$, and $\hat{u}_{\mathrm{int},\varepsilon,i}$ are defined by the covariance functions κ_d, κ_κ, κ_{x_d}, and $\kappa_{\hat{u}_{\mathrm{int},\varepsilon}}$, respectively. The covariance function of the desired trajectory κ_{x_d} is given by a twice differentiable function (with respect to the task-specific input parameters $\boldsymbol{\gamma}$).

Remark 3.3. Due to the statistical independence, positive correlation of damping d_i and stiffness k_i [10] is not directly included in the priors. However, it can be partially incorporated by suitable definition of the respective EMVs $\mu_{d,i}$ and $\mu_{k,i}$.

Remark 3.4. Positivity of damping d_i and stiffness k_i can be strictly ensured by warped GP priors [97], in which the priors are transformed to $\log(d_i(\boldsymbol{\xi})) \sim \mathcal{GP}(\log(\mu_{d,i}), \kappa_d(\boldsymbol{\xi}, \boldsymbol{\xi}'))$ and $\log(k_i(\boldsymbol{\xi})) \sim \mathcal{GP}(\log(\mu_{k,i}), \kappa_k(\boldsymbol{\xi}, \boldsymbol{\xi}'))$. Application of these warped GP priors would require all compound kernel derivations to consider the log formulations and the respective derivatives. For better comprehensibility of the derivations, we instead assume that the corresponding variances only assign high probabilities to appropriate regions within the positive domain.

3.3.2. Impedance, PD, and Interaction Kernels

Given the GP prior definitions (3.7) - (3.9), the terms $d_i(\boldsymbol{\xi})\dot{e}_i(\boldsymbol{\gamma})$ and $k_i(\boldsymbol{\xi})e_i(\boldsymbol{\gamma})$ in the impedance dynamics (3.5) are products of statistically independent Gaussian distributions. Consequently, the impedance force $u_{\mathrm{imp},i}$ is a combination of both Gaussian and chi-squared distributions and possesses non-central chi-squared terms. Nonetheless, the computation of its expected value and covariance function enables its approximation as a GP:

$$u_{\mathrm{imp},i}(\overline{\boldsymbol{\xi}}) \sim \mathcal{GP}\Big(\mathsf{E}\left[u_{\mathrm{imp},i}(\overline{\boldsymbol{\xi}})\right], \kappa_{u_\mathrm{imp}}(\overline{\boldsymbol{\xi}}, \overline{\boldsymbol{\xi}}')\Big) \ . \tag{3.11}$$

Remark 3.5. The loss of accuracy due to the negligence of the non-central chi-squared terms increases with the variances of the damping d_i and the stiffness k_i. If both functionals were deterministic, second order statistical characterization of the impedance force $u_{\mathrm{imp},i}$ would not imply any loss of accuracy. Consequently, by considering low variances due to proper parameterization, we are able to approximate the impedance force $u_{\mathrm{imp},i}$ as a GP.

The expected value of the impedance force $u_{\mathrm{imp},i}$ is calculated by insertion of the GP prior definitions (3.6) - (3.9) into the impedance dynamics (3.5), which yields

$$\mathsf{E}\left[u_{\mathrm{imp},i}(\overline{\boldsymbol{\xi}})\right] = \mu_{m,i}(\ddot{\mu}_{x_{\mathrm{d}},i} - \ddot{x}_i) + \mu_{d,i}(\dot{\mu}_{x_{\mathrm{d}},i} - \dot{x}_i) + \mu_{k,i}(\mu_{x_{\mathrm{d}},i} - x_i) \ . \tag{3.12}$$

The covariance function of the impedance force $\kappa_{u_{\mathrm{imp}}}$ is defined as

$$\begin{aligned}\kappa_{u_{\mathrm{imp}}}(\overline{\boldsymbol{\xi}}, \overline{\boldsymbol{\xi}}') = \mathsf{Cov}\Big[&m_i\ddot{e}_i(\boldsymbol{\gamma}) + d_i(\boldsymbol{\xi})\dot{e}_i(\boldsymbol{\gamma}) + k_i(\boldsymbol{\xi})e_i(\boldsymbol{\gamma}),\\ &m_i\ddot{e}_i(\boldsymbol{\gamma}') + d_i(\boldsymbol{\xi}')\dot{e}_i(\boldsymbol{\gamma}') + k_i(\boldsymbol{\xi}')e_i(\boldsymbol{\gamma}')\Big]\end{aligned} \tag{3.13}$$

and is more involved due to the correlations with the desired trajectory $x_{\mathrm{d},i}$ and the respective derivatives $\dot{x}_{\mathrm{d},i}$ and $\ddot{x}_{\mathrm{d},i}$. As differentiation is a linear operator, the derivatives $\dot{x}_{\mathrm{d},i}$ and $\ddot{x}_{\mathrm{d},i}$ are also GPs that possess derivative covariance functions [83]. Based on the covariance of sums and the covariance of products [98], the impedance kernel $\kappa_{u_{\mathrm{imp}}}$ can be derived by calculating the sum of the covariances of all possible product term combinations.

For simplicity, we first derive a partial kernel variation that only considers those terms that include the damping d_i and the stiffness k_i. From a control perspective, the limitation to these terms corresponds to proportional derivative (PD) control. Consequently, the resulting partial kernel variation represents the covariance function of the PD force

$$u_{\mathrm{PD},i}(\boldsymbol{\xi}) = d_i(\boldsymbol{\xi})\dot{e}_i(\boldsymbol{\gamma}) + k_i(\boldsymbol{\xi})e_i(\boldsymbol{\gamma}) \ . \tag{3.14}$$

Based on the impedance kernel $\kappa_{u_{\mathrm{imp}}}$ in (3.13), the PD kernel $\kappa_{u_{\mathrm{PD}}}$ is defined as

$$\kappa_{u_{\mathrm{PD}}}(\boldsymbol{\xi}, \boldsymbol{\xi}') = \mathsf{Cov}\Big[d_i(\boldsymbol{\xi})\dot{e}_i(\boldsymbol{\gamma}) + k_i(\boldsymbol{\xi})e_i(\boldsymbol{\gamma}), d_i(\boldsymbol{\xi}')\dot{e}_i(\boldsymbol{\gamma}') + k_i(\boldsymbol{\xi}')e_i(\boldsymbol{\gamma}')\Big] \ . \tag{3.15}$$

According to the covariance of sums, the definition of the PD kernel $\kappa_{u_{\mathrm{PD}}}$ can be separated into individual covariances of all possible product term combinations

$$\begin{aligned}\kappa_{u_{\mathrm{PD}}}(\boldsymbol{\xi}, \boldsymbol{\xi}') = &\ \mathsf{Cov}[d_i(\boldsymbol{\xi})\dot{e}_i(\boldsymbol{\gamma}), d_i(\boldsymbol{\xi}')\dot{e}_i(\boldsymbol{\gamma}')] + \mathsf{Cov}[d_i(\boldsymbol{\xi})\dot{e}_i(\boldsymbol{\gamma}), k_i(\boldsymbol{\xi}')e_i(\boldsymbol{\gamma}')]\\ &+ \mathsf{Cov}[k_i(\boldsymbol{\xi})e_i(\boldsymbol{\gamma}), d_i(\boldsymbol{\xi}')\dot{e}_i(\boldsymbol{\gamma}')] + \mathsf{Cov}[k_i(\boldsymbol{\xi})e_i(\boldsymbol{\gamma}), k_i(\boldsymbol{\xi}')e_i(\boldsymbol{\gamma}')] \ .\end{aligned} \tag{3.16}$$

Application of the covariance of products and omission of zero covariances yields

$$\begin{aligned}\kappa_{u_{\mathrm{PD}}}(\boldsymbol{\xi}, \boldsymbol{\xi}') = &\Big(\mathsf{E}\left[d_i(\boldsymbol{\xi})\right]\mathsf{E}\left[d_i(\boldsymbol{\xi}')\right] + \mathsf{Cov}[d_i(\boldsymbol{\xi}), d_i(\boldsymbol{\xi}')]\Big)\,\mathsf{Cov}[\dot{e}_i(\boldsymbol{\gamma}), \dot{e}_i(\boldsymbol{\gamma}')]\\ &+ \mathsf{E}\left[\dot{e}_i(\boldsymbol{\gamma})\right]\mathsf{E}\left[\dot{e}_i(\boldsymbol{\gamma}')\right]\mathsf{Cov}[d_i(\boldsymbol{\xi}), d_i(\boldsymbol{\xi}')]\\ &+ \mathsf{E}\left[d_i(\boldsymbol{\xi})\right]\mathsf{E}\left[k_i(\boldsymbol{\xi}')\right]\mathsf{Cov}[\dot{e}_i(\boldsymbol{\gamma}), e_i(\boldsymbol{\gamma}')]\\ &+ \mathsf{E}\left[k_i(\boldsymbol{\xi})\right]\mathsf{E}\left[d_i(\boldsymbol{\xi}')\right]\mathsf{Cov}[e_i(\boldsymbol{\gamma}), \dot{e}_i(\boldsymbol{\gamma}')]\\ &+ \Big(\mathsf{E}\left[k_i(\boldsymbol{\xi})\right]\mathsf{E}\left[k_i(\boldsymbol{\xi}')\right] + \mathsf{Cov}[k_i(\boldsymbol{\xi}), k_i(\boldsymbol{\xi}')]\Big)\,\mathsf{Cov}[e_i(\boldsymbol{\gamma}), e_i(\boldsymbol{\gamma}')]\\ &+ \mathsf{E}\left[e_i(\boldsymbol{\gamma})\right]\mathsf{E}\left[e_i(\boldsymbol{\gamma}')\right]\mathsf{Cov}[k_i(\boldsymbol{\xi}), k_i(\boldsymbol{\xi}')] \ .\end{aligned} \tag{3.17}$$

Finally, inclusion of the GP prior definitions in (3.7) - (3.9) and the derivative covariance function of the desired trajectory derivative $\dot{x}_{\mathrm{d},i}$ yields

$$\begin{aligned}\kappa_{u_{\mathrm{PD}}}(\boldsymbol{\xi},\boldsymbol{\xi}') &= (\mu_{d,i}^2 + \kappa_d(\boldsymbol{\xi},\boldsymbol{\xi}'))\frac{\partial^2\kappa_{x_\mathrm{d}}(\boldsymbol{\gamma},\boldsymbol{\gamma}')}{\partial t\partial t'} + (\dot{\mu}_{x_\mathrm{d},i} - \dot{x}_i)(\dot{\mu}_{x_\mathrm{d},i} - \dot{x}_i')\kappa_d(\boldsymbol{\xi},\boldsymbol{\xi}') \\ &\quad + \mu_{d,i}\mu_{k,i}\Big(\frac{\partial\kappa_{x_\mathrm{d}}(\boldsymbol{\gamma},\boldsymbol{\gamma}')}{\partial t} + \frac{\partial\kappa_{x_\mathrm{d}}(\boldsymbol{\gamma},\boldsymbol{\gamma}')}{\partial t'}\Big) + (\mu_{k,i}^2 + \kappa_k(\boldsymbol{\xi},\boldsymbol{\xi}'))\kappa_{x_\mathrm{d}}(\boldsymbol{\gamma},\boldsymbol{\gamma}') \\ &\quad + (\mu_{x_\mathrm{d},i} - x_i)(\mu_{x_\mathrm{d},i} - x_i')\kappa_k(\boldsymbol{\xi},\boldsymbol{\xi}')\ , \end{aligned} \tag{3.18}$$

where t and t' are the time variables that belong to the observations $\boldsymbol{\gamma}$ and $\boldsymbol{\gamma}'$, respectively.

Additionally including the inertia m_i yields the impedance kernel κ_{u_imp}. According to the covariance of sums, analogous to (3.16), the definition of the impedance kernel κ_{u_imp} can be separated into individual covariances of all possible product term combinations

$$\begin{aligned}\kappa_{u_\mathrm{imp}}(\overline{\boldsymbol{\xi}},\overline{\boldsymbol{\xi}}') &= \mathsf{Cov}[m_i\ddot{e}_i(\boldsymbol{\gamma}), m_i\ddot{e}_i(\boldsymbol{\gamma}')] + \mathsf{Cov}[m_i\ddot{e}_i(\boldsymbol{\gamma}), d_i(\boldsymbol{\xi}')\dot{e}_i(\boldsymbol{\gamma}')] \\ &\quad + \mathsf{Cov}[m_i\ddot{e}_i(\boldsymbol{\gamma}), k_i(\boldsymbol{\xi}')e_i(\boldsymbol{\gamma}')] + \mathsf{Cov}[d_i(\boldsymbol{\xi})\dot{e}_i(\boldsymbol{\gamma}), m_i\ddot{e}_i(\boldsymbol{\gamma}')] \\ &\quad + \mathsf{Cov}[k_i(\boldsymbol{\xi})e_i(\boldsymbol{\gamma}), m_i\ddot{e}_i(\boldsymbol{\gamma}')] + \kappa_{u_\mathrm{PD}}(\boldsymbol{\xi},\boldsymbol{\xi}')\ . \end{aligned} \tag{3.19}$$

Application of the covariance of products and omission of zero covariances yields

$$\begin{aligned}\kappa_{u_\mathrm{imp}}(\overline{\boldsymbol{\xi}},\overline{\boldsymbol{\xi}}') &= \Big(\mathsf{E}\Big[m_i\Big]\,\mathsf{E}\Big[m_i\Big] + \mathsf{Cov}[m_i, m_i]\Big)\,\mathsf{Cov}[\ddot{e}_i(\boldsymbol{\gamma}), \ddot{e}_i(\boldsymbol{\gamma}')] \\ &\quad + \mathsf{E}\Big[\ddot{e}_i(\boldsymbol{\gamma})\Big]\,\mathsf{E}\Big[\ddot{e}_i(\boldsymbol{\gamma}')\Big]\,\mathsf{Cov}[m_i, m_i] \\ &\quad + \mathsf{E}\Big[m_i\Big]\,\mathsf{E}\Big[d_i(\boldsymbol{\xi}')\Big]\,\mathsf{Cov}[\ddot{e}_i(\boldsymbol{\gamma}), \dot{e}_i(\boldsymbol{\gamma}')] \\ &\quad + \mathsf{E}\Big[m_i\Big]\,\mathsf{E}\Big[k_i(\boldsymbol{\xi}')\Big]\,\mathsf{Cov}[\ddot{e}_i(\boldsymbol{\gamma}), e_i(\boldsymbol{\gamma}')] \\ &\quad + \mathsf{E}\Big[d_i(\boldsymbol{\xi}')\Big]\,\mathsf{E}\Big[m_i\Big]\,\mathsf{Cov}[\dot{e}_i(\boldsymbol{\gamma}), \ddot{e}_i(\boldsymbol{\gamma}')] \\ &\quad + \mathsf{E}\Big[k_i(\boldsymbol{\xi}')\Big]\,\mathsf{E}\Big[m_i\Big]\,\mathsf{Cov}[e_i(\boldsymbol{\gamma}), \ddot{e}_i(\boldsymbol{\gamma}')] + \kappa_{u_\mathrm{PD}}(\boldsymbol{\xi},\boldsymbol{\xi}')\ . \end{aligned} \tag{3.20}$$

Finally, inclusion of the GP prior definitions in (3.6) - (3.9) and the derivative covariance functions of the desired trajectory derivatives $\dot{x}_{\mathrm{d},i}$ and $\ddot{x}_{\mathrm{d},i}$ yields

$$\begin{aligned}\kappa_{u_\mathrm{imp}}(\overline{\boldsymbol{\xi}},\overline{\boldsymbol{\xi}}') &= (\mu_{m,i}^2 + \sigma_{m,i}^2)\frac{\partial^4\kappa_{x_\mathrm{d}}(\boldsymbol{\gamma},\boldsymbol{\gamma}')}{\partial^2 t\partial^2 t'} + (\ddot{\mu}_{x_\mathrm{d},i} - \ddot{x}_i)(\ddot{\mu}_{x_\mathrm{d},i} - \ddot{x}_i')\sigma_{m,i}^2 \\ &\quad + \mu_{m,i}\mu_{d,i}\Big(\frac{\partial^3\kappa_{x_\mathrm{d}}(\boldsymbol{\gamma},\boldsymbol{\gamma}')}{\partial^2 t\partial t'} + \frac{\partial^3\kappa_{x_\mathrm{d}}(\boldsymbol{\gamma},\boldsymbol{\gamma}')}{\partial^2 t'\partial t}\Big) \\ &\quad + \mu_{m,i}\mu_{k,i}\Big(\frac{\partial^2\kappa_{x_\mathrm{d}}(\boldsymbol{\gamma},\boldsymbol{\gamma}')}{\partial^2 t} + \frac{\partial^2\kappa_{x_\mathrm{d}}(\boldsymbol{\gamma},\boldsymbol{\gamma}')}{\partial^2 t'}\Big) + \kappa_{u_\mathrm{PD}}(\boldsymbol{\xi},\boldsymbol{\xi}')\ . \end{aligned} \tag{3.21}$$

Remark 3.6. If the desired trajectory $x_{\mathrm{d},i}$ is a function of time ($\boldsymbol{\gamma} = t$), the computation of the derivatives of the respective covariance function κ_{x_d} is straightforward. For all remaining parameterizations, the derivatives are computed in terms of partial derivatives

$$\frac{\partial \kappa_{x_\mathrm{d}}(\boldsymbol{\gamma}, \boldsymbol{\gamma}')}{\partial t'} = \left(\frac{\partial \kappa_{x_\mathrm{d}}(\boldsymbol{\gamma}, \boldsymbol{\gamma}')}{\partial \boldsymbol{\gamma}'}\right)^\mathsf{T} \frac{\partial \boldsymbol{\gamma}'}{\partial t} \ , \tag{3.22}$$

$$\frac{\partial^2 \kappa_{x_\mathrm{d}}(\boldsymbol{\gamma}, \boldsymbol{\gamma}')}{\partial t'^2} = \left(\frac{\partial \boldsymbol{\gamma}'}{\partial t}\right)^\mathsf{T} \frac{\partial^2 \kappa_{x_\mathrm{d}}(\boldsymbol{\gamma}, \boldsymbol{\gamma}')}{\partial \boldsymbol{\gamma}'^2} \frac{\partial \boldsymbol{\gamma}'}{\partial t} + \left(\frac{\partial \kappa_{x_\mathrm{d}}(\boldsymbol{\gamma}, \boldsymbol{\gamma}')}{\partial \boldsymbol{\gamma}'}\right)^\mathsf{T} \frac{\partial^2 \boldsymbol{\gamma}'}{\partial t^2} \ . \tag{3.23}$$

Proposition 3.1. *Assume the kernels κ_d, κ_k, and κ_{x_d} in (3.7) - (3.9) are symmetric and positive semi-definite and the desired trajectory kernel κ_{x_d} is a twice differentiable function (with respect to the task-specific input parameters $\boldsymbol{\gamma}$). Then, the PD kernel κ_{u_PD} in (3.18) and the impedance kernel κ_{u_imp} in (3.21) are valid kernels.*

Proof. A symmetric, positive semi-definite function $g(\xi, \xi')$ is a valid kernel function [99]. Thus, given the assumptions in the proposition, the kernels κ_d, κ_k, and κ_{x_d} are valid kernels. Given the desired trajectory kernel κ_{x_d} is a twice differentiable function, the PD kernel κ_{u_PD} and the impedance kernel κ_{u_imp} are defined by the covariance functions (3.18) and (3.21), respectively. If a compound kernel is fully defined by affine transformations of valid kernels, it itself is also a valid kernel [100]. As the covariance functions (3.18) and (3.21) are only defined by affine transformations of the kernels κ_d, κ_k, and κ_{x_d}, the PD kernel κ_{u_PD} and the impedance kernel κ_{u_imp} are valid kernels. □

With the interaction dynamics (3.4) and the GP prior definitions (3.6) - (3.10), the a priori statistical characterization of the interaction force $u_{\mathrm{int},i}$ is given by

$$u_{\mathrm{int},i}(\overline{\boldsymbol{\xi}}) \sim \mathcal{GP}\Big(\mathsf{E}\left[u_{\mathrm{imp},i}(\overline{\boldsymbol{\xi}})\right], \kappa_{u_\mathrm{int}}(\overline{\boldsymbol{\xi}}, \overline{\boldsymbol{\xi}}')\Big) \ , \tag{3.24}$$

where $\mathsf{E}[u_{\mathrm{int},i}(\overline{\boldsymbol{\xi}})] = \mathsf{E}[u_{\mathrm{imp},i}(\overline{\boldsymbol{\xi}})]$, because the EMV of the estimated interaction force $\hat{u}_{\mathrm{int},\varepsilon,i}$ in the GP prior definition (3.10) is zero. The interaction kernel κ_{u_int} is defined as

$$\kappa_{u_\mathrm{int}}(\overline{\boldsymbol{\xi}}, \overline{\boldsymbol{\xi}}') = \kappa_{u_\mathrm{imp}}(\overline{\boldsymbol{\xi}}, \overline{\boldsymbol{\xi}}') + \kappa_{\hat{u}_{\mathrm{int},\varepsilon}}(\overline{\boldsymbol{\xi}}, \overline{\boldsymbol{\xi}}') + \sigma_v^2 \ . \tag{3.25}$$

Remark 3.7. Proper parameterization of the GP prior of the desired trajectory $x_{\mathrm{d},i}$ is key, as it affects all impedance terms. Given a priori task-specific information, its EMV $\mu_{x_\mathrm{d},i}$ may be defined as a function of time t or other task-specific input parameters $\boldsymbol{\gamma}$. As deviations from the desired trajectory $x_{\mathrm{d},i}$ are compensated by impedance control, the overall mean of the state x_i approximates the desired trajectory state $x_{\mathrm{d},i}$, i.e., the steady state, in which the human is at "equilibrium". In HRI scenarios that lack a priori task-specific information, this relationship can be included by defining the desired trajectory EMV $\mu_{x_\mathrm{d},i}$ by the state x_i. With this definition, the GP prior of the desired trajectory $x_{\mathrm{d},i}$ is given by

$$x_{\mathrm{d},i}(\boldsymbol{\gamma}) \sim \mathcal{GP}\left(x_i, \kappa_{x_\mathrm{d}}(\boldsymbol{\gamma}, \boldsymbol{\gamma}')\right) \ . \tag{3.26}$$

Inserting this equilibrium definition of the GP prior of the desired trajectory $x_{\mathrm{d},i}$ in (3.12) results in $\mathsf{E}\left[u_{\mathrm{imp},i}(\overline{\boldsymbol{\xi}})\right] = 0$, which, when inserted in (3.24), results in $\mathsf{E}\left[u_{\mathrm{int},i}(\overline{\boldsymbol{\xi}})\right] = 0$.

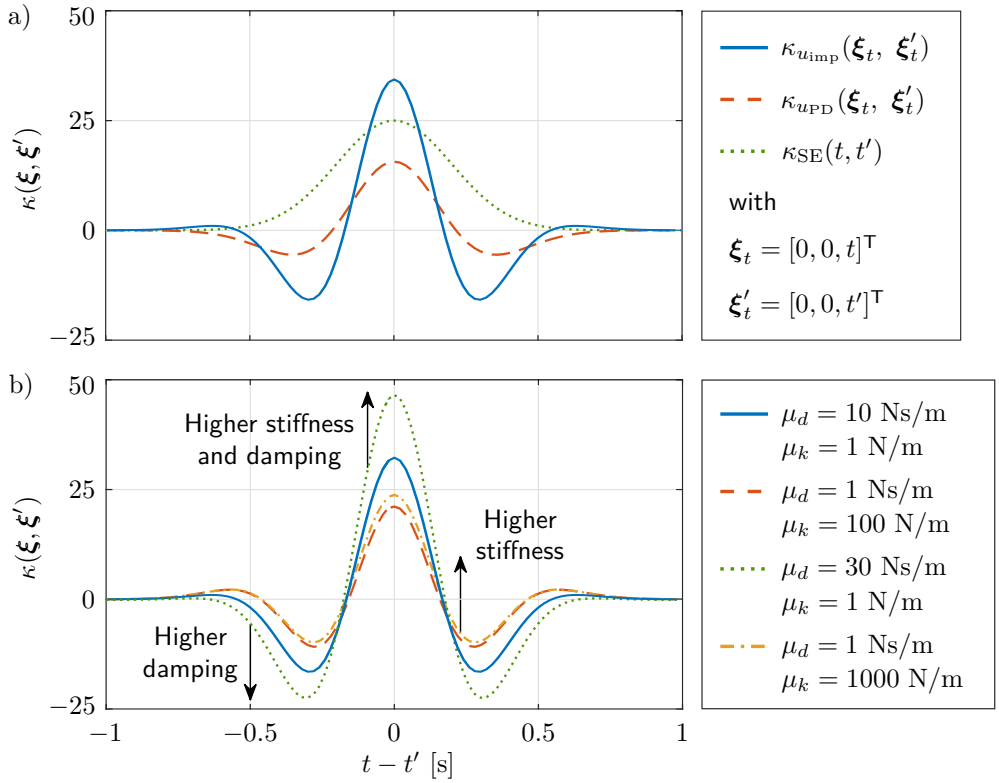

Figure 3.2.: Covariance functions for the one-dimensional case of a time-dependent desired trajectory ($\boldsymbol{\gamma} = t$). (a) Impedance, PD, and SE kernels with hyperparameters $\{0.1, (0.2)\}_{x_\text{d}}$, $\{0.1, (0.1\ 0.1)\}_d$, $\{0.1, (0.1\ 0.1)\}_k$, and $\sigma_m^2 = 0.1$. The EMVs are $\mu_m = 1$ kg, $\mu_d = 10$ Ns/m, $\mu_k = 100$ Nm, $\mu_{x_\text{d}} = 0$ m. (b) Impedance kernel with different values of the EMVs μ_d and μ_k. (© 2019 IEEE)

The derived Bayesian model includes a non-physical HRI variation that corresponds to the simplification of the general model of human motor behavior in (2.36). For this variation, the GP prior of the estimated interaction force $\hat{u}_{\text{int},\varepsilon,i}$ is not necessary and is replaced by the definition of the prior distribution of the dynamic discrepancies $\varepsilon_{\text{dyn},x} \sim \mathcal{N}\left(\varepsilon_{\text{dyn},x} \,\middle|\, 0, \sigma^2_{\varepsilon_\text{dyn}}\right)$. As a result of this substitution, the interaction kernel κ_{u_int} is replaced by

$$\overline{\kappa}_{u_\text{int}}(\overline{\boldsymbol{\xi}}, \overline{\boldsymbol{\xi}}') = \kappa_{u_\text{imp}}(\overline{\boldsymbol{\xi}}, \overline{\boldsymbol{\xi}}') + \sigma^2_{\varepsilon_\text{dyn}} + \sigma^2_\upsilon \ , \tag{3.27}$$

where $\sigma^2_{\varepsilon_\text{dyn}}$ is the dynamic discrepancy variance. Apart from these differences, all derivations, including the covariance functions (3.18) and (3.21), are identical and equally valid.

For illustrative purposes, from this point on, let the kernels κ_d, κ_k, κ_{x_d}, and $\kappa_{\hat{u}_{\text{int},\varepsilon}}$ in the GP priors (3.7) - (3.10) be defined as squared exponential (SE) kernels

$$\kappa_\text{SE}(\boldsymbol{\xi}, \boldsymbol{\xi}') = \sigma^2_{\text{SE},i} \exp\{-(\boldsymbol{\xi} - \boldsymbol{\xi}')^\mathsf{T} {\Lambda_{\text{SE},i}}^{-1} (\boldsymbol{\xi} - \boldsymbol{\xi}')\} \tag{3.28}$$

with hyperparameters $\{\sigma_i^2, \Lambda_i\}_\text{SE}$, in which $\Lambda_{\text{SE},i}$ contains the length scales of the n input dimensions and $\sigma^2_{\text{SE},i}$ is the variance. The SE kernel is the most common kernel due to its desirable smoothness and convergence properties. As it is both infinitely differentiable and a valid kernel [90], it satisfies all of the prerequisites listed in Proposition 3.1.

The most relevant characteristic of the PD and impedance kernels is the presence of terms comprising time derivatives of the desired trajectory. Thus, in the following, the effects

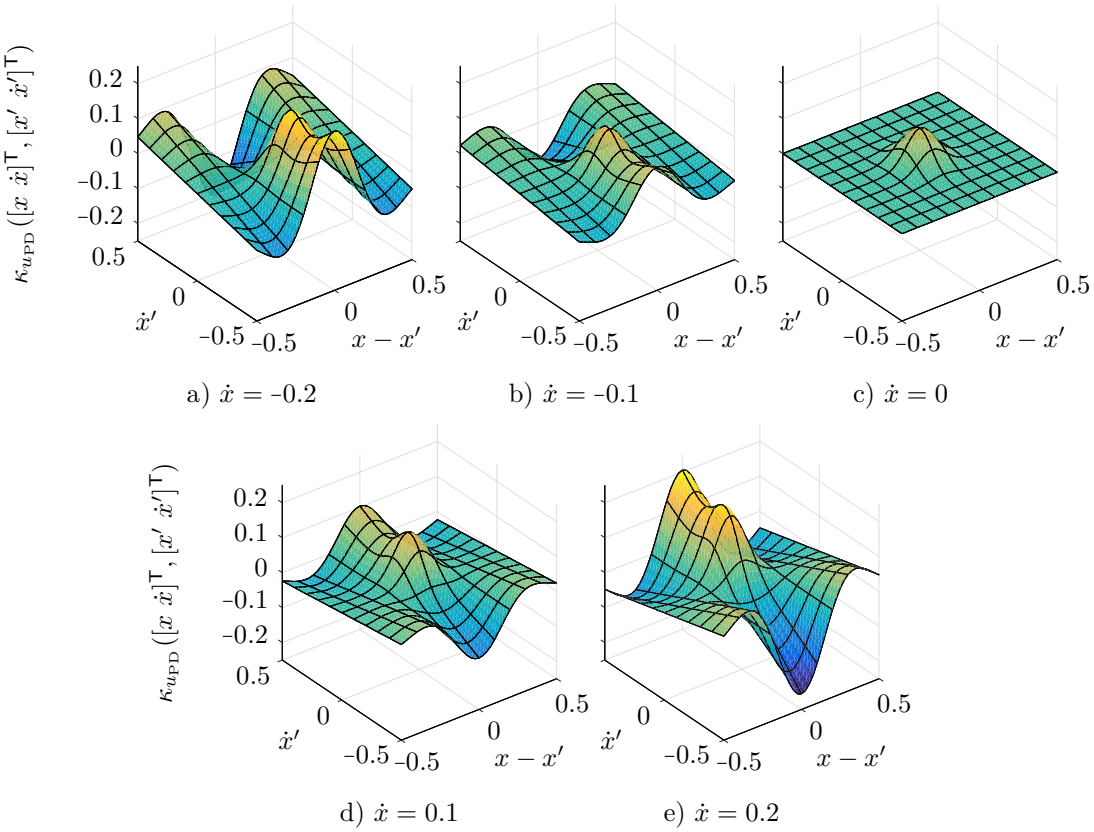

Figure 3.3.: Covariance functions for the one-dimensional case of a configuration-dependent desired trajectory ($\boldsymbol{\gamma} = x$). The PD kernel hyperparameters are $\{1, (0.2)\}_{x_{\mathrm{d}}}$, $\{0.1, (0.1\ 0.1)\}_d$, and $\{0.1, (0.1\ 0.1)\}_k$. The corresponding PD kernel EMVs are $\mu_d = 1.5$ Ns/m, $\mu_k = 1$ Nm, and $\mu_{x_{\mathrm{d}}} = 0$ m. (© 2019 IEEE)

of these terms on the correlations are analyzed for different task-specific input parameters. Fig. 3.2 shows covariance functions of a naive SE, a PD, and an impedance kernel for the one-dimensional case of a time-dependent desired trajectory, i.e., $\boldsymbol{\gamma} = t$. The PD kernel considers the derivative of the SE kernel as an additive term. Similarly, the profile of the impedance kernel is governed by the inertia term. The effects of the stiffness, damping, and inertia terms on the profiles of the respective kernels are substantially influenced by their respective EMVs. This dependency is illustrated in Fig. 3.2b, which shows several impedance covariance functions with different EMVs. As the stiffness term is governed by a SE kernel, it solely adds positive values with unnormalized Gaussian shape. Therefore, the higher the stiffness EMV, the higher the overall correlation. In contrast, increasing the damping or inertia EMVs emphasizes the profiles of the first or second derivative, respectively.

In order to illustrate these effects for a model with a desired trajectory that is not defined by time, Fig. 3.3 shows covariance functions of a PD kernel for the one-dimensional case of a configuration-dependent desired trajectory, i.e., $\boldsymbol{\gamma} = x$. When the input point velocity is zero, the damping term is nullified, as the derivative of the error is also zero. Thus, the correlation is limited to the SE kernel of the stiffness term, as illustrated in Fig. 3.3c. When the input point velocity is not zero, damping term correlations arise. Figs. 3.3a, 3.3b, and 3.3d, 3.3e show both negative and positive values of $\dot{x}$, which determine the slope of the correlation around $x - x' = 0$, as the derivative of the error is proportional to $\dot{x}$.

3.3.3. Conditional Distributions of Latent Functionals

The probabilistic nature of the derived Bayesian model, paired with the desirable properties of multivariate normal distributions, enables the computation of conditional distributions of the latent variables. In the case of multivariate normality, conditional distributions are also Gaussian distributions and computed in closed form. In this chapter and in HRI scenarios in general, the human motor intention, i.e., the desired trajectory $x_{\mathrm{d},i}$, represents especially relevant information. From (3.9) and (3.24), the joint prior distribution $\mathsf{P}\left(\mathcal{U}_{\mathrm{int}}, x_{\mathrm{d},*,i} | \overline{\Xi}, \boldsymbol{\gamma}_*\right)$ of observations of the interaction force $\mathcal{U}_{\mathrm{int}} = \{u_{\mathrm{int},i,j}(\overline{\boldsymbol{\xi}}_j)\}_{j=1}^h$ at inputs $\overline{\Xi} = \{\overline{\boldsymbol{\xi}}_j\}_{j=1}^h$ and the desired trajectory $x_{\mathrm{d},*,i}$ at test input $\boldsymbol{\gamma}_*$ is given by

$$\mathsf{P}\left(\mathcal{U}_{\mathrm{int}}, x_{\mathrm{d},*,i} | \overline{\Xi}, \boldsymbol{\gamma}_*\right) = \mathcal{N}\left(\begin{bmatrix} \mathcal{U}_{\mathrm{int}} \\ x_{\mathrm{d},*,i} \end{bmatrix} \middle| \begin{bmatrix} \mathsf{E}\left[\mathcal{U}_{\mathrm{int}}\right] \\ \mu_{x_{\mathrm{d}},i} \end{bmatrix}, \begin{bmatrix} K_{u_{\mathrm{int}}} & \boldsymbol{\kappa}_{u_{\mathrm{int}},x_{\mathrm{d}},*} \\ \boldsymbol{\kappa}_{u_{\mathrm{int}},x_{\mathrm{d}},*}^{\mathsf{T}} & \kappa_{x_{\mathrm{d}},**} \end{bmatrix}\right), \tag{3.29}$$

where $K_{u_{\mathrm{int}}} = \kappa_{u_{\mathrm{int}}}(\overline{\Xi}, \overline{\Xi}')$, $\kappa_{x_{\mathrm{d}},**} = \kappa_{x_{\mathrm{d}}}(\boldsymbol{\gamma}_*, \boldsymbol{\gamma}_*)$, and $\boldsymbol{\kappa}_{u_{\mathrm{int}},x_{\mathrm{d}},*}$ is defined as

$$\boldsymbol{\kappa}_{u_{\mathrm{int}},x_{\mathrm{d}},*} = \mathsf{Cov}[\mathcal{U}_{\mathrm{int}}, x_{\mathrm{d},*,i}] = \mathsf{Cov}[x_{\mathrm{d},*,i}, \mathcal{U}_{\mathrm{int}}]^{\mathsf{T}} \tag{3.30}$$

$$= \mu_{m,i} \frac{\partial^2 \kappa_{x_{\mathrm{d}}}(\Gamma, \boldsymbol{\gamma}_*)}{\partial t^2} + \mu_{d,i} \frac{\partial \kappa_{x_{\mathrm{d}}}(\Gamma, \boldsymbol{\gamma}_*)}{\partial t} + \mu_{k,i} \kappa_{x_{\mathrm{d}}}(\Gamma, \boldsymbol{\gamma}_*) \tag{3.31}$$

with the task-specific input parameters $\Gamma = \{\boldsymbol{\gamma}_j\}_{j=1}^h$. Multivariate Gaussian conditioning, i.e., the application of Bayes' rule, yields the conditional posterior

$$\mathsf{P}\left(x_{\mathrm{d},*,i} | \mathcal{U}_{\mathrm{int}}, \overline{\Xi}, \boldsymbol{\gamma}_*\right) = \mathcal{N}\left(x_{\mathrm{d},*,i} \,\middle|\, \mathsf{E}\left[x_{\mathrm{d},*,i}\right], \kappa_{x_{\mathrm{d}},**} - \boldsymbol{\kappa}_{u_{\mathrm{int}},x_{\mathrm{d}},*}^{\mathsf{T}} K_{u_{\mathrm{int}}}^{-1} \boldsymbol{\kappa}_{u_{\mathrm{int}},x_{\mathrm{d}},*}\right) \tag{3.32}$$

with

$$\mathsf{E}\left[x_{\mathrm{d},*,i}\right] = \mu_{x_{\mathrm{d}},i} + \boldsymbol{\kappa}_{u_{\mathrm{int}},x_{\mathrm{d}},*}^{\mathsf{T}} K_{u_{\mathrm{int}}}^{-1} (\mathcal{U}_{\mathrm{int}} - \mathsf{E}\left[\mathcal{U}_{\mathrm{int}}\right]) \ . \tag{3.33}$$

The computation of conditional posteriors of alternative latent functionals, e.g. damping d_i or stiffness k_i, is performed analogously. In the non-physical HRI variation, $K_{u_{\mathrm{int}}}$ is replaced by $\overline{K}_{u_{\mathrm{int}}} = \overline{\kappa}_{u_{\mathrm{int}}}(\overline{\Xi}, \overline{\Xi}')$ with kernel $\overline{\kappa}_{u_{\mathrm{int}}}$ of (3.27) and $\mathsf{E}\left[\mathcal{U}_{\mathrm{int}}\right] = \mathcal{U}_{\mathrm{int}} = \mathbf{0}$.

3.4. Application Guidelines

In order to facilitate proper application of the derived Bayesian human motor behavior model, in this section, we present application guidelines that include prior parameterization as well as pseudocode application instructions. The prior parameters of the priors in (3.6) - (3.10) are composed of the EMVs $\mu_{(\cdot),i}$ and the hyperparameters of the SE kernels (3.28), i.e., the variances $\sigma_{(\cdot),i}^2$ and the length scales $\Lambda_{(\cdot),i}$. Only the variable m_i poses an exception. Due to the lack of a covariance function, it is defined only by the EMV $\mu_{m,i}$ and the variance $\sigma_{m,i}^2$. The parameters of prior $\hat{u}_{\mathrm{int},\varepsilon,i}$ do not require manual definition, as its EMV is zero and its hyperparameters are trained by maximizing the log-likelihood function of a naive GP prior. In order to facilitate parameterization of the remaining priors in (3.6) - (3.9), the following section contains an overview of estimated human arm impedance characteristics as well as a discussion of implications for prior parameterization. Subsequently, the general algorithm structure of the Bayesian model is presented via pseudocode application instructions.

Table 3.1.: Human arm impedance characteristics in mean (SD). Postural: x_1, x_2, and x_3 are sagittal, transversal, and vertical axes. Non-postural: x_1, x_2, and x_3 are principal movement, lateral, and vertical axes. (© 2019 IEEE)

	Inertia [kg]					
Study description	x_1		x_2		x_3	
[101] postural	1.54	(0.07)	1.00	(0.08)	-	-
[102] postural	0.28	(0.15)	0.39	(0.21)	0.25	(0.13)
[103] postural	0.99	(0.07)	1.42	(0.20)	-	-
[104] postural	2.02	(0.39)	1.60	(0.33)	-	-
[105] postural	0.75	(0.15)	0.40	(0.10)	-	-
[53] welding - novice	0.70	(0.30)	2.40	(0.60)	0.90	(0.40)
[53] welding - expert	0.60	(0.20)	2.80	(0.80)	0.70	(0.20)
[92] catching - static	1.36	(0.09)	-	-	-	-
[92] catching - ready	1.44	(0.18)	-	-	-	-
[94] teleoperation	0.85	-	4.03	-	0.68	-
[95] stylus grasping	0.32	(0.15)	0.48	(0.15)	0.24	(0.13)
[93] tennis - static	1.79	(0.10)	-	-	-	-
[93] tennis - ready	1.84	(0.11)	-	-	-	-

	Damping [Ns/m]						**Stiffness [N/m]**					
Study description	x_1		x_2		x_3		x_1		x_2		x_3	
[101] postural	10.7	(0.9)	13.3	(1.2)	-	-	117	(14)	236	(27)	-	-
[102] postural	35.3	(23.8)	84.1	(52.2)	40.1	(21.4)	337	(190)	748	(281)	303	(209)
[103] postural	6.8	(0.8)	14.3	(1.4)	-	-	27	(4)	91	(6)	-	-
[104] postural	6.6	(1.6)	25.3	(7.3)	-	-	89	(24)	264	(92)	-	-
[105] postural	9.9	(2.6)	53.5	(8.5)	-	-	40	(16)	346	(68)	-	-
[53] welding - novice	15.0	(8.0)	32.0	(13.0)	12.0	(8.0)	341	(67)	411	(188)	280	(108)
[53] welding - expert	19.0	(5.0)	44.0	(14.0)	17.0	(5.0)	423	(232)	539	(200)	315	(150)
[92] catching - static	20.6	(2.1)	-	-	-	-	67	(34)	-	-	-	-
[92] catching - ready	23.0	(2.9)	-	-	-	-	116	(60)	-	-	-	-
[94] teleoperation	12.9	-	9.2	-	17.6	-	122	-	108	-	81	-
[95] stylus grasping	5.9	(2.2)	5.9	(1.4)	20.1	(5.1)	105	(28)	133	(29)	366	(106)
[93] tennis - static	19.8	(1.7)	-	-	-	-	116	(44)	-	-	-	-
[93] tennis - ready	21.6	(2.1)	-	-	-	-	158	(49)	-	-	-	-

3.4.1. Prior Parameterization

While there is a large body of work on estimation of human arm impedance, the results are often presented qualitatively or graphically using inertia, damping, and stiffness ellipses [72]. Of the few studies that present quantitative results, many estimate in joint space in order to address joint-specific impedance control by the CNS [21]. In this chapter, in order to enable transferability to a broad selection of realistic physical HRI scenarios, we instead focus on the Cartesian space representation. Table 3.1 shows an overview of estimated human arm impedance characteristics in postural and non-postural tasks. In the former, a desired posture is maintained and in the latter, a desired movement is performed. The stiffness, damping, and inertia values lie in the approximate ranges of $10 - 1000$ N/m, $5 - 100$ Ns/m, and $0.05 - 4$ kg, respectively. The EMVs $\mu_{m,i}$, $\mu_{d,i}$, and $\mu_{k,i}$ should be defined based on the

values in Table 3.1. While the inertia EMV $\mu_{m,i}$ only depends on the limb kinematics, for the EMVs $\mu_{d,i}$ and $\mu_{k,i}$, the task description should be considered. Furthermore, attention should be paid to correct definition of the principal movement axis.

Remark 3.8. The positive correlation between joint damping and joint stiffness is visible in the values in Table 3.1, which supports the statement that its effects can be partially incorporated by suitable definition of the EMVs $\mu_{d,i}$ and $\mu_{k,i}$.

Remark 3.9. The low standard deviations (SDs) of the non-postural values in Table 3.1 (except the values of [53], which, due to the welding accuracy requirements, is similar to a postural task) support the consideration of low variances for the approximation in (3.11).

Due to the dependence of the hyperparameters of the SE kernel on the task type and dimensions, only qualitative recommendations can be given for the length scales $\Lambda_{(\cdot),i}$ and the variances $\sigma^2_{(\cdot),i}$. In general, the larger a length scale, the smaller the variation of the mean in the GP posterior. Consequently, the expectation of a certain degree of smoothness of the desired trajectory $x_{\mathrm{d},i}$ implies comparatively large length scales $\Lambda_{x_{\mathrm{d}},i}$. As the feedback torques generated by the damping d_i and the stiffness k_i compensate deviations from the desired trajectory $x_{\mathrm{d},i}$, the respective length scales $\Lambda_{d,i}$ and $\Lambda_{k,i}$ should be smaller than $\Lambda_{x_{\mathrm{d}},i}$. Otherwise, the model would misinterpret deviations as part of the desired trajectory $x_{\mathrm{d},i}$. The hyperparameters of prior $\hat{u}_{\mathrm{int},\varepsilon,i}$, which are obtained by maximizing the log-likelihood function of a naive GP prior, can serve as reference points: length scales $\Lambda_{x_{\mathrm{d}},i}$ should be larger and length scales $\Lambda_{d,i}$ and $\Lambda_{k,i}$ should be smaller in comparison.

For the definition of the variance $\sigma^2_{x_{\mathrm{d}},i}$, it should be considered that (3.21) does not only contain the desired trajectory $x_{\mathrm{d},i}$, but also the corresponding derivatives. As the variance increases with differentiation, a large variance $\sigma^2_{x_{\mathrm{d}},i}$ would result in considerable variance for the overall model. Thus, the impedance contributions would "disappear" in the variance. In order to avoid this, the variance $\sigma^2_{x_{\mathrm{d}},i}$ should be sufficiently small. Due to similar reasons and the loss of accuracy related to the negligence of the non-central chi-squared terms in the GP approximation (3.11), the variances $\sigma^2_{d,i}$ and $\sigma^2_{k,i}$ should also be sufficiently small.

Remark 3.10. Application of GP priors with SE covariance functions allows for derivation of theory concerning upper bounds of prediction errors. In [106], a probability bound for an upper bound of the prediction error is derived using the reproducing kernel Hilbert space norm. In [107], an upper bound for the mean square prediction error of misspecified GP models is derived by solving a pseudo-concave optimization problem. As an in-depth discussion of such theories lies outside the scope of this thesis, we instead provide quantitative examples for the qualitative prior parameter recommendations. Their impact on the results can be inferred from the validation with simulated data, which is presented in Section 3.5.

3.4.2. Pseudocode Application Instructions

The pseudocode in Algorithm 3.1. shows the algorithm structure and necessary definitions. For the application of the Bayesian human motor behavior model for non-physical HRI, the inputs consist of the training set $\{\mathbf{0}, \overline{\boldsymbol{\xi}}_j\}_{j=1}^{h}$ and the test input $\boldsymbol{\gamma}_*$ and the outputs only consist of the predictive output $x_{\mathrm{d},*,i}$. Steps 1,2,3, and 7 are omitted and in step 6, the covariance function $\kappa_{u_{\mathrm{int}}}$ of (3.25) is replaced by the covariance function $\overline{\kappa}_{u_{\mathrm{int}}}$ of (3.27).

Algorithm 3.1. Bayesian model for physical HRI

Given: Suitable, task-specific input parameters $\boldsymbol{\gamma}$
Require: Training set $\{u_{\mathrm{int},i,j}(\overline{\boldsymbol{\xi}}_j), \overline{\boldsymbol{\xi}}_j\}_{j=1}^{h}$, test input $\overline{\boldsymbol{\xi}}_*$
Ensure: Predictive outputs $u_{\mathrm{int},*,i}$, $x_{\mathrm{d},*,i}$
1: Define naive GP prior $u_{\mathrm{int,naive},i}(\overline{\boldsymbol{\xi}}) \sim \mathcal{GP}(0, \kappa_{\mathrm{SE}}(\overline{\boldsymbol{\xi}}, \overline{\boldsymbol{\xi}}'))$
2: Train hyperparameters of naive GP prior $u_{\mathrm{int,naive},i}(\overline{\boldsymbol{\xi}})$ (by maximizing the log-likelihood function)
3: Copy trained hyperparameters to prior $\hat{u}_{\mathrm{int},\varepsilon,i}(\overline{\boldsymbol{\xi}})$ in (3.10)
4: Define EMV $\mu_{x_{\mathrm{d}},i}$ with a priori task-specific information or alternatively use equilibrium definition (3.26)
5: Parameterize remaining priors in (3.6) - (3.9) based on empirical values and implications in Section 3.4.1
6: Infer desired trajectory $\boldsymbol{x}_{\mathrm{d},*,i}$ with (3.32) and (3.25)
7: Predict interaction force $u_{\mathrm{int},*,i}$ with (3.24) and (3.25)

3.5. Simulation

In this section, the Bayesian model is validated using a simulated model of the human arm. The simulated desired trajectory enables validation of the intention estimation capabilities and direct control over the simulated impedance characteristics allows for assessment of the effects of prior parameterization. In order to analyze how differences between the simulated impedance characteristics and the prior parameters influence the prediction performance, the damping and stiffness EMVs are varied within plausible intervals. In order to consider the highly task-specific nature of human motor behavior during realistic physical HRI and demonstrate the versatility and adaptability of the Bayesian model, it is validated both for a time-dependent ($\boldsymbol{\gamma} = t$) and a configuration-dependent ($\boldsymbol{\gamma} = \boldsymbol{x}$) desired trajectory. All priors in (3.7) - (3.10) are defined by SE kernels. The prediction performance is assessed with the standardized mean squared error (SMSE) and the mean standardized log loss (MSLL).

In the SMSE, the squared residuals of the predicted interaction forces $u_{\mathrm{int},*,i,j}$ and the real interaction forces $u_{\mathrm{int},i,j}$ are averaged over the test inputs $\overline{\Xi}_* = \{\overline{\boldsymbol{\xi}}_{*,j}\}_{j=1}^{h}$ and normalized with the variance of the respective test outputs $\mathcal{U}_{\mathrm{int},\overline{\Xi}_*} = \{u_{\mathrm{int},i,j}(\overline{\boldsymbol{\xi}}_{*,j})\}_{j=1}^{h}$:

$$\mathrm{SMSE} = \frac{1}{n}\sum_{i=1}^{n}\left[\frac{1}{h}\sum_{j=1}^{h}\frac{(u_{\mathrm{int},*,i,j}(\overline{\boldsymbol{\xi}}_{*,j}) - u_{\mathrm{int},i,j}(\overline{\boldsymbol{\xi}}_{*,j}))^2}{\mathsf{Var}\left[\mathcal{U}_{\mathrm{int},\overline{\Xi}_*}\right]}\right]. \tag{3.34}$$

The MSLL is obtained from the negative log probability, standardized by the log probability of a Gaussian with mean and variance of the training data $\mathcal{U}_{\mathrm{int},\overline{\Xi}} = \{u_{\mathrm{int},i,j}(\overline{\boldsymbol{\xi}}_j)\}_{j=1}^{h}$:

$$\begin{aligned}\mathrm{MSLL} = \frac{1}{n}\sum_{i=1}^{n}\Bigg[\frac{1}{h}\sum_{j=1}^{h}\Bigg[&- \log \mathsf{P}\left(u_{\mathrm{int},*,i,j}(\overline{\boldsymbol{\xi}}_{*,j})|\mathcal{U}_{\mathrm{int},\overline{\Xi}}\right)\\ &- \log \mathcal{N}\Big(u_{\mathrm{int},*,i,j}(\overline{\boldsymbol{\xi}}_{*,j})|\mathsf{E}\left[\mathcal{U}_{\mathrm{int},\overline{\Xi}}\right], \mathsf{Var}\left[\mathcal{U}_{\mathrm{int},\overline{\Xi}}\right]\Big)\Bigg]\Bigg],\end{aligned} \tag{3.35}$$

in which the negative log probability $-\log \mathsf{P}\left(u_{\text{int},*,i,j}(\overline{\boldsymbol{\xi}}_{*,j})|\mathcal{U}_{\text{int},\overline{\Xi}}\right)$ is defined as

$$-\log \mathsf{P}\left(u_{\text{int},*,i,j}(\overline{\boldsymbol{\xi}}_{*,j})|\mathcal{U}_{\text{int},\overline{\Xi}}\right) = \frac{1}{2}\log\left(2\pi\,\mathsf{Var}\left[u_{\text{int},*,i,j}(\overline{\boldsymbol{\xi}}_{*,j})\right]\right) + \frac{(u_{\text{int},*,i,j}(\overline{\boldsymbol{\xi}}_{*,j}) - u_{\text{int},i,j}(\overline{\boldsymbol{\xi}}_{*,j}))^2}{2\,\mathsf{Var}\left[u_{\text{int},*,i,j}(\overline{\boldsymbol{\xi}}_{*,j})\right]} \,. \tag{3.36}$$

Analogous to the SMSE, the MSLL is determined by averaging over the test inputs $\overline{\Xi}_*$ [79].

3.5.1. Implementation

We validate the model with simulated data of a neuromechanical model of the human arm, which generates transversal movements of a two-link, six-muscle arm through calculation of muscle activities [35]. The model is selected, because it is structurally more complex than our Bayesian model and derives a two-dimensional trajectory from simulated muscle activities that provide physiologically plausible impedance characteristics.

The rigid body dynamics of the neuromechanical model are determined by (2.1) and the torque generation is determined by (2.2). The muscle tensions $\boldsymbol{\chi}$ are defined as

$$\boldsymbol{\chi} = \boldsymbol{\chi}_a + \boldsymbol{\chi}_{\text{imp}} \,, \tag{3.37}$$

where $\boldsymbol{\chi}_a$ are the muscle tensions due to muscle activation and $\boldsymbol{\chi}_{\text{imp}}$ are the muscle tensions due to impedance control. In the neuromechanical model, the muscle tensions due to muscle activation $\boldsymbol{\chi}_a$ are assumed to be identical to the muscle activations $\boldsymbol{a}$ in (2.3) and the muscle tensions due to impedance control $\boldsymbol{\chi}_{\text{imp}}$ are defined as

$$\boldsymbol{\chi}_{\text{imp}} = D_\lambda \dot{\boldsymbol{e}}_\lambda + K_\lambda \boldsymbol{e}_\lambda \,, \tag{3.38}$$

$$D_\lambda = K_\lambda/12 \,, \quad K_\lambda = \alpha_K(I + 0.035\,\text{diag}\{\boldsymbol{a}\}) \,, \tag{3.39}$$

where D_λ, K_λ, and $\boldsymbol{e}_\lambda$ represent damping, stiffness, and tracking error with respect to the desired trajectory at muscle level, respectively, and α_K is an intrinsic stiffness parameter.

The feedforward muscle activations $\boldsymbol{a}_{\text{FF}}$ are calculated a priori with the inverse kinematics and dynamics of the desired movement. The feedback muscle activations $\boldsymbol{a}_{\text{FB}}$ are modeled by PD control that is determined by the tracking error $\boldsymbol{e}_\lambda$, the respective derivative $\dot{\boldsymbol{e}}_\lambda$, and a simulated feedback delay $\delta_{\text{sim}} = 60$ ms. The signal-dependent noise $\boldsymbol{\upsilon}_\lambda$ is calculated with zero mean Brownian motion, which provides movements similar to those observed in previous experiments [37]. It is generated by a normally distributed random variable, which is amplified by a parameter $\alpha_\upsilon = 12.5$ and filtered by a fifth order low pass Butterworth filter with a cut-off frequency $f_{\text{c},\upsilon} = 2$ Hz. The simulation sample rate is set to 500 Hz.

3.5.2. Simulation Design

In the simulation, the neuromechanical model of the human arm performs two-dimensional movements along the reference trajectory displayed in Fig. 3.4. It consists of a circle with radius 0.04 m and four attached arcs that each subtend 270 degrees. The feedforward muscle activations $\boldsymbol{a}_{\text{FF}}$ are calculated a priori with the inverse kinematics and dynamics of

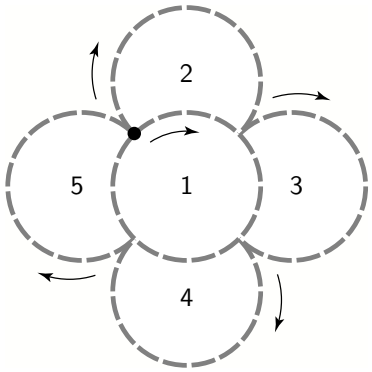

Figure 3.4.: Reference trajectory. Starting at the black dot, the arrows and numbers indicate movement direction and execution order, respectively. (© 2019 IEEE)

Table 3.2.: Simulated damping and stiffness in mean (SD). (© 2019 IEEE)

Simulation	**Damping [Ns/m]**		**Stiffness [N/m]**	
	x_1	x_2	x_1	x_2
Low stiffness	9.89 (1.47)	12.40 (0.73)	118.7 (17.6)	148.4 (20.7)
High stiffness	48.07 (6.20)	60.29 (7.55)	576.8 (74.4)	723.5 (90.6)

the positional data of the reference trajectory. In order to allow for assessment of the effects of prior parameterization, we simulate two different stiffness profiles with $\alpha_K = 3360$ for low stiffness and $\alpha_K = 16800$ for high stiffness. The resulting values of the simulated damping and stiffness are presented in mean (SD) in Table 3.2. For each of the two stiffness profiles, the same reference trajectory is repeated three times without pause at a rate of 2.618 rad/s to form the complete data set. As the reference trajectory in Fig. 3.4 does not possess a distinct principal movement axis, the coordinates x_1 and x_2 in Table 3.2 as well as in the remainder of this chapter refer to the sagittal and coronal planes, respectively. Furthermore, from this point on and without loss of generality, the impedance matrices M_x, D_x, and K_x are defined to be isotropic. For clarity, the index i of priors m_i, d_i, and k_i in (3.6) - (3.8) and the associated EMVs $\mu_{(\cdot),i}$, length scales $\Lambda_{(\cdot),i}$, and variances $\sigma^2_{(\cdot),i}$ is omitted.

3.5.3. Configuration-dependent Desired Trajectory

We consider (3.24) with a configuration-dependent desired trajectory ($\boldsymbol{\gamma} = \boldsymbol{x}$) and a priori equilibrium definition (3.26). For simplicity, priors m, d, and k are defined constant and deterministic ($\sigma_m^2 = \sigma_d^2 = \sigma_k^2 = 0$). The prediction performance of the model is evaluated with respect to a naive GP prior $u_{\text{int,naive},i}(\overline{\boldsymbol{\xi}}) \sim \mathcal{GP}(0, \kappa_{\text{SE}}(\overline{\boldsymbol{\xi}}, \overline{\boldsymbol{\xi}}'))$. The training sets are obtained by downsampling the simulated trajectories to 0.2 Hz and the validation sets are obtained by downsampling the same trajectories to 10 Hz. The hyperparameters of the naive model are trained by maximizing the log-likelihood and the resulting length scales and variances are also used to parameterize prior $\hat{u}_{\text{int},\varepsilon,i}(\overline{\boldsymbol{\xi}})$. The inertia EMV $\mu_m = 3$ kg, the damping EMVs $\mu_d \in [5, 50]$ Ns/m, and the stiffness EMVs $\mu_k \in [100, 1000]$ N/m. The hyperparameters of the desired trajectory are $\{10^{-6}, (0.2\ 0.2)\}_{x_\text{d}}$ and $\sigma_v^2 = 10^{-4}$.

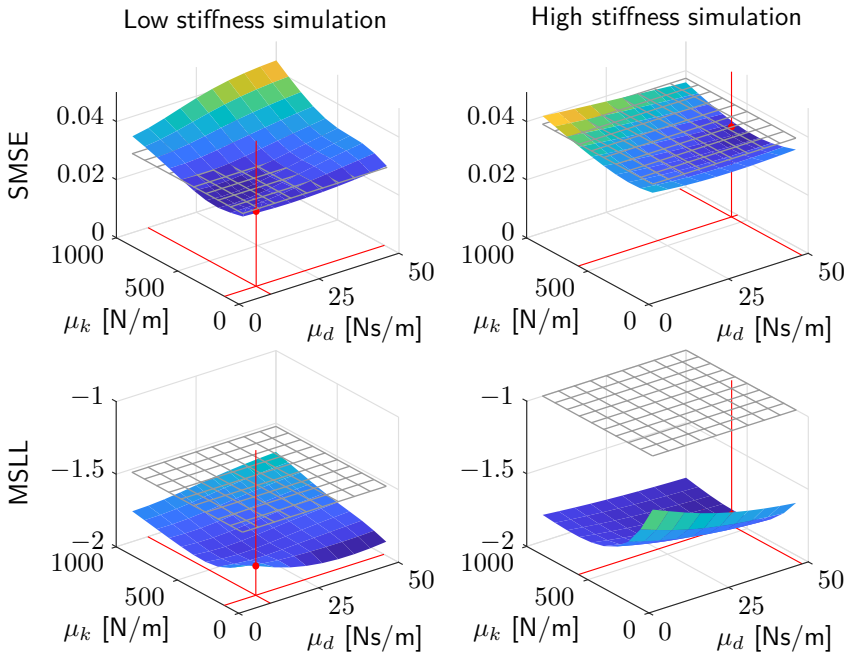

Figure 3.5.: Prediction performance with $\boldsymbol{\gamma} = \boldsymbol{x}$. The red lines indicate the mean values of the simulated x_1 impedance values and the grey grid represents the performance of the naive GP prior. (© 2019 IEEE)

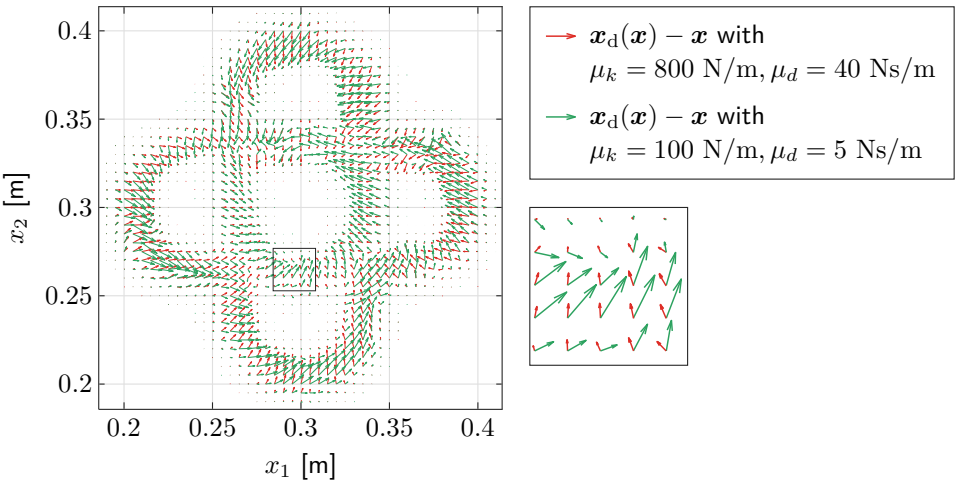

Figure 3.6.: Inference of desired trajectory $\boldsymbol{x}_\mathrm{d}$ with $\boldsymbol{\gamma} = \boldsymbol{x}$ for the high stiffness simulation. The arrows represent length and orientation of $\boldsymbol{x}_\mathrm{d} - \boldsymbol{x}$. (© 2019 IEEE)

In the second half of the analysis, the intention estimation capabilities are evaluated via the inferred desired trajectory. The evaluation is conducted for the simulated trajectory of the high stiffness simulation, downsampled to 25 Hz, and the results are presented for sets of low ($\mu_k = 100$ N/m, $\mu_d = 5$ Ns/m) and high ($\mu_k = 800$ N/m, $\mu_d = 40$ Ns/m) EMVs.

Fig. 3.5 presents the prediction performance results with respect to the naive model in terms of SMSE and MSLL. The SMSE for the low stiffness simulation shows that the Bayesian human motor behavior model outperforms the naive model over the low stiffness and low damping ranges, where the EMVs are close to the simulated values in Table 3.2. The prediction performance is decreased in the high stiffness and high damping ranges.

In terms of MSLL, the prediction performance increases throughout the whole stiffness and damping ranges and it reaches its maximum in the low stiffness and low damping ranges. The SMSE for the high stiffness simulation displays overall improved performance, especially for stiffness EMVs in the mid-range and a high damping EMV that is close to the simulated values in Table 3.2. A similar dependency is found in the MSLL. For low stiffness values, the Bayesian human motor behavior model still outperforms the naive model, but performance is reduced due to high variance, which is considered in the calculation of the MSLL.

Fig. 3.6 demonstrates the inference of the latent desired trajectory, as defined in (3.32). The arrows represent length and orientation of the differences between the input states $\boldsymbol{x}$ and the inferred states of the desired trajectory $\boldsymbol{x}_\mathrm{d}$. The model with high EMVs expects lower deviations due to higher tracking accuracy. Thus, the inferred state is persistently located in the proximity of the associated input state. In contrast, the model with low EMVs expects higher deviations due to lower tracking accuracy, which results in larger differences.

3.5.4. Time-dependent Desired Trajectory

In this section, we consider (3.24) with a time-dependent desired trajectory ($\boldsymbol{\gamma} = t$) and a priori equilibrium definition (3.26). Analogous to the configuration-dependent model in the previous section, for simplicity, priors m, d, and k are assumed constant and deterministic ($\sigma_m^2 = \sigma_d^2 = \sigma_k^2 = 0$). The error $e_i(t)$ as well as the respective derivatives $\dot{e}_i(t)$ and $\ddot{e}_i(t)$ and the estimated interaction force $\hat{u}_{\mathrm{int},\varepsilon,i}(t)$ are defined as functions of time, such that, according to (3.4), the interaction force $u_{\mathrm{int},i}(t) \sim \mathcal{GP}\left(0, \kappa_{u_\mathrm{int}}(t,t')\right)$. The prediction performance of the model is evaluated with respect to a naive GP prior $u_{\mathrm{int,naive},i}(t) \sim \mathcal{GP}\left(0, \kappa_\mathrm{SE}(t,t')\right)$. The training sets are obtained by downsampling the simulated trajectories to 3 Hz and the validation sets are identical to those in the previous section. The hyperparameters of the naive model are trained by maximizing the log-likelihood and the resulting length scales and variances are also used to parameterize prior $\hat{u}_{\mathrm{int},\varepsilon,i}(t)$. The EMVs of the impedance components are the same as in the configuration-dependent analysis. The hyperparameters of the desired trajectory are $\{10^{-6}, (0.3)\}_{x_\mathrm{d}}$ and $\sigma_\upsilon^2 = 10^{-4}$. In the second half of the analysis, the intention estimation capabilities are again evaluated via the inferred desired trajectory, based on the same simulated trajectory of the high stiffness simulation as well as the same sets of low and high stiffness and damping EMVs as in the previous section.

Fig. 3.7 presents the prediction performance results. The SMSE for the low stiffness simulation shows that the Bayesian human motor behavior model outperforms the naive model over the whole stiffness and damping ranges, with the difference in performance being especially large for low stiffness and damping EMVs, which are close to the simulated values in Table 3.2. In terms of MSLL, the prediction performance increases throughout the whole stiffness and damping ranges and it reaches its maximum in the mid-stiffness and low damping ranges. The SMSE for the high stiffness simulation displays overall improved performance, especially for the high damping and high stiffness ranges, when the EMVs are close to the simulated values in Table 3.2. A similar dependency is found in the MSLL.

Fig. 3.8 demonstrates the inference of the latent desired trajectory, as defined in (3.32). It contains the inferred desired trajectories, the corresponding confidence levels, and the reference trajectory. The model with high EMVs expects lower deviations due to higher tracking accuracy. Thus, the inferred desired trajectory possesses low variance. As the EMVs are close to the simulated values of the high stiffness simulation, the model represents

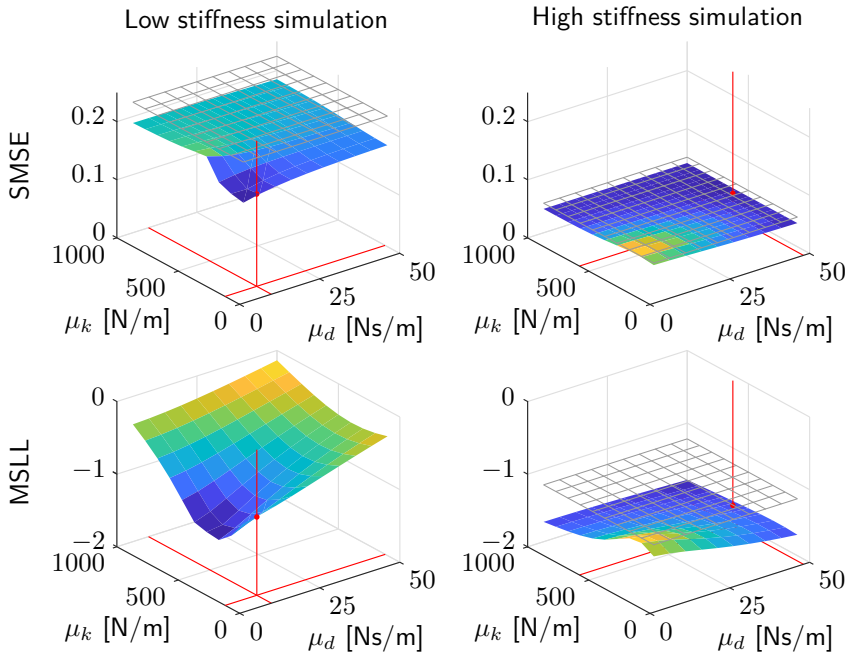

Figure 3.7.: Prediction performance with $\boldsymbol{\gamma} = t$. The red lines indicate the mean values of the simulated x_1 impedance values and the grey grid represents the performance of the naive GP prior. The naive GP prior MSLL in the low stiffness simulation is 14.14 and thus omitted for clarity. (© 2019 IEEE)

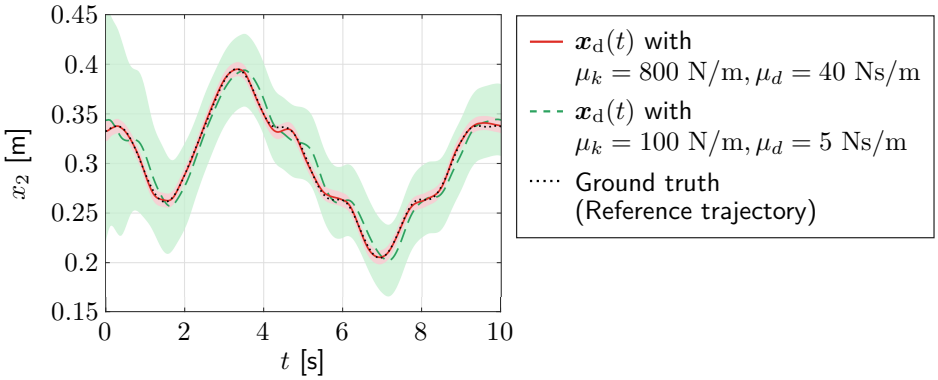

Figure 3.8.: Inference of desired trajectory $\boldsymbol{x}_\mathrm{d}$ with $\boldsymbol{\gamma} = t$ for the high stiffness simulation. The shaded areas represent the confidence levels in the form of the SDs of the desired trajectory $\boldsymbol{x}_\mathrm{d}$ and are amplified for clarity ($\pm$ 5 SD for low EMV values, $\pm$ 10 SD for high EMV values). (© 2019 IEEE)

the simulated dynamics with high accuracy. The model with low EMVs expects higher deviations due to lower tracking accuracy. As the EMVs are not close to the simulated values, the simulated dynamics are represented with less accuracy. The inferred desired trajectory possesses higher variance and deviates substantially more from the reference trajectory.

The analyses of the configuration- and time-dependent models in this section validate the intention estimation capabilities and the superior prediction performance of the model in comparison to the naive GP prior. In addition to being a positive result, the latter represents a secondary means of validation for the inferred desired trajectories. Additionally, the impact of proper prior parameterization on the prediction performance is demonstrated.

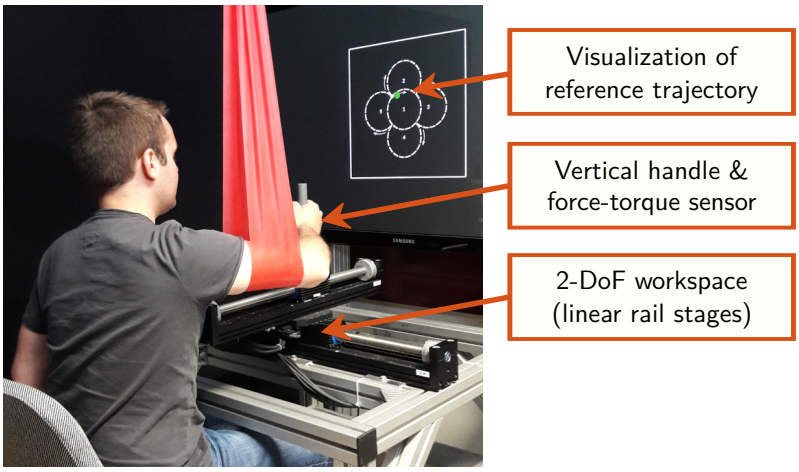

Figure 3.9.: Participant interacting with the apparatus. (© 2019 IEEE)

3.6. Experiment

In order to assess the prediction performance of the model with real data, an experiment with human participants is performed. The experiment design is based on the simulation design. However, the impedance priors are not defined constant and deterministic and the EMVs are not varied within plausible intervals. Instead, the number of training points is decreased to determine the effects of training data sparsity. In order to assess the generalization capabilities of the model, two different scenarios are evaluated, in which the training and validation sets are located in identical or different regions of the workspace. The prediction performance is quantified by the SMSE. In order to demonstrate the versatility of the model, it is evaluated for a configuration- and velocity-dependent desired trajectory.

3.6.1. Apparatus

The apparatus is presented in Fig. 3.9. It consists of two linear servo motor driven single rail stages (*Copley Controls Thrusttube Module*) that are mounted on top of each other in orthogonal orientation. The two single rail stages span a 2-DoF workspace of ±0.20 m and are each equipped with an encoder that yields position data with a precision of 1 μm. A vertical handle and a 6-DoF force-torque sensor (*JR3-67M25*) are mounted on top of the upper servo motor driven cart to measure the forces in the horizontal plane. A sling attached to the ceiling is available for limitation of participant movements to the horizontal plane. Visual feedback is provided on a screen behind the apparatus at participant eye level and implemented with the Psychophysics Toolbox [108]. The position of the cart is visualized by a dot and the workspace safety boundaries are visualized in the form of a boundary box.

Haptic interaction with the apparatus by means of participant force input is enabled by the admittance control scheme, which is defined by

$$\boldsymbol{u}_{\mathrm{adm}} = M_{x,\mathrm{adm}}\ddot{\boldsymbol{x}} + D_{x,\mathrm{adm}}\dot{\boldsymbol{x}} \ , \tag{3.40}$$

where $\boldsymbol{u}_{\mathrm{adm}}$ is the admittance force, which corresponds to the interaction force $\boldsymbol{u}_{\mathrm{int}}$ that is measured at the end-effector, and $M_{x,\mathrm{adm}} = \mathrm{diag}\{5, 5\}$ kg and $D_{x,\mathrm{adm}} = \mathrm{diag}\{15, 15\}$ Ns/m are the admittance inertia and damping, respectively. The characteristics of the admittance

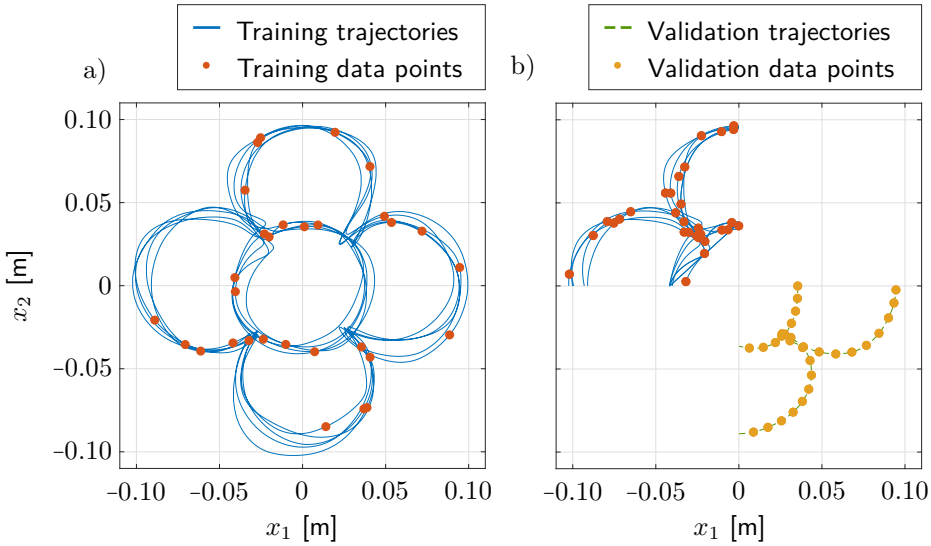

Figure 3.10.: Participant data. (a) Identical workspace regions with exemplary 30 point training set. (b) Different workspace regions with exemplary 30 point training and validation sets (validation points reduced for clarity). (© 2019 IEEE)

control scheme are chosen to guarantee natural interaction with the apparatus and sufficient attenuation of force-torque sensor noise. Precise position rendering is provided by high gain PD control, which is implemented in *Matlab/Simulink*, exported for an embedded real-time *Linux* target, and executed on an external *RT-preempt Linux* system with a real-time kernel (*Ubuntu 14.04, 3.14.3-rt4-prt*). The sample rate is set to 4 kHz and inputs to the Thrusttube Modules are downsampled to 2 kHz due to hardware limitations. The signals are filtered using a fifth order Savitzky-Golay filter with a cut-off frequency of 20 Hz [109].

3.6.2. Experiment Design

In order to consider the highly task-specific nature of human motor behavior during realistic physical HRI, in this section, we consider (3.24) with a configuration and velocity-dependent desired trajectory ($\boldsymbol{\gamma} = [\boldsymbol{x}^\mathsf{T}, \dot{\boldsymbol{x}}^\mathsf{T}]^\mathsf{T}$) and a priori equilibrium definition (3.26). For feasibility, we set all jerk-related terms in (3.21) to zero. The hyperparameters of prior $\hat{u}_{\mathrm{int},\varepsilon,i}(\overline{\boldsymbol{\xi}})$ are defined by maximum log-likelihood training of a naive GP prior. The EMVs of the impedance components are $\mu_m = 2$ kg, $\mu_d = 20$ Ns/m, and $\mu_k = 100$ N/m. They are defined based on the principal movement axis values in Table 3.1: μ_d is the approximate mean of the damping values and μ_k is based on the lower stiffness values, as they represent the most plausible values for the observed dynamics. The hyperparameters are $\{10^{-4}, (0.4\ 0.4\ 0.2\ 0.2)\}_{x_\mathrm{d}}$, $\{5^2, (0.2\ 0.2\ 0.1\ 0.1)\}_d$, and $\{50^2, (0.2\ 0.2\ 0.1\ 0.1)\}_k$, and $\sigma_v^2 = 10^{-4}$.

The training sets are obtained from data of repetitions $6-10$. It is assumed that after five repetitions the participants have had enough time to familiarize with the apparatus. The validation sets are obtained from data of repetitions $11-15$. In order to ensure sufficient coverage of the workspace, each repetition is validated separately. The number of training points is increased from 2 to 50 and there are 200 validation points. Before the evaluation, the training and validation points are uniformly distributed among the sets. In each evaluation, one of these uniformly distributed training points is randomly selected and added to the

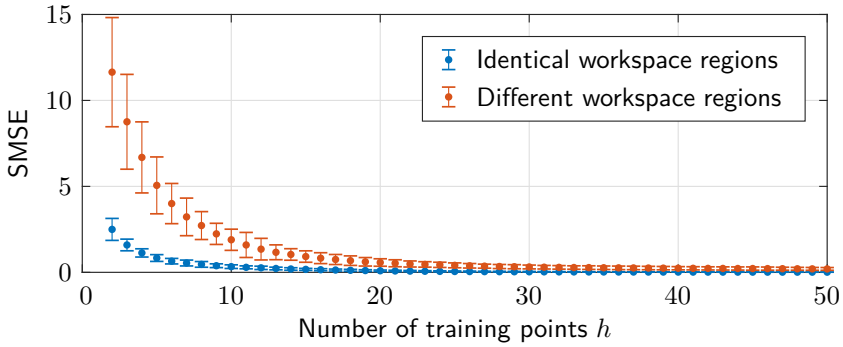

Figure 3.11.: Averaged SMSE results. The error bars indicate ±5 SD. (© 2019 IEEE)

existing training set. The evaluations are repeated 100 times for each of the five validation repetitions $(11 - 15)$ and the results are averaged. Figs. 3.10a and 3.10b show the data of a single participant for the identical and different workspace regions scenarios, respectively. In the former, all sets contain data from all workspace quadrants. In the latter, training sets contain data from Quadrant 2 and validation sets contain data from Quadrant 4.

3.6.3. Participants & Procedure

A total of 20 participants (16 male and 4 female) volunteered to take part in this experiment. The mean (SD) age at the time of the experiment was 26.95 (4.41) years. All participants had normal or corrected-to-normal vision and were right-handed. Informed written consent was obtained from all participants before the experiment. The research ethics were obtained from the ethics committee at the Technical University of Munich (project no. 205/14).

The participants were seated in front of the apparatus and instructed to grasp the handle with their right hand. Their arm was constrained to horizontal movements by a sling attached to the ceiling. The reference trajectory and the current position of the cart were visualized on the screen behind the apparatus (Fig. 3.9). The participants were instructed to move to the starting point and then follow the reference trajectory at their own pace (Fig. 3.4). Each participant completed 15 repetitions of the reference trajectory without pause.

3.6.4. Evaluation

Fig. 3.11 shows the averaged SMSE results including error bars that each indicate ±5 SD over the number of training points h. The results show that the mean SMSEs rapidly decrease with an increase of h. Although the initial value for different workspace regions is substantially increased, the values for large h are almost identical. The mean SMSE converges to zero for identical workspace regions and to a marginally larger value for different workspace regions. This difference in prediction performance is plausible, as the validation points are located in previously unobserved regions of the input space.

The results show that decreased prediction performance due to training data sparsity only arises for very small numbers of training points h. Although this difference increases with the distance between training and validation points, given a reasonable number of training points, the model nonetheless provides reliable predictions in previously unobserved regions of the input space. This reliable prediction performance of the model for real data also serves as an indirect means of validation for its intention estimation capabilities.

3.7. Discussion

In this chapter, we derive an impedance-based GP model. The model derivation is based on the assumption that the unperturbed states represent the desired kinematic states of the desired motor behavior, which can be described by a twice differentiable, well-defined function $\boldsymbol{q}_\mathrm{d}(\boldsymbol{\gamma})$. The parameters $\boldsymbol{\gamma}$ are defined by task-specific input parameters such as $\boldsymbol{\gamma} = t$ for a transient desired trajectory $\boldsymbol{q}_\mathrm{d}(t)$. We demonstrate desirable intention estimation capabilities and superior prediction performance for different parameterizations of the desired trajectory $\boldsymbol{q}_\mathrm{d}(\boldsymbol{\gamma})$. In the experiment, we consider a configuration and velocity-dependent desired trajectory with $\boldsymbol{\gamma} = [\boldsymbol{x}^\mathsf{T}, \dot{\boldsymbol{x}}^\mathsf{T}]^\mathsf{T}$. We exclude repetitions $1-5$ from the data, assuming that after five repetitions participants have had enough time to familiarize with the apparatus and possess a desired trajectory $\boldsymbol{x}_\mathrm{d}(\boldsymbol{x}, \dot{\boldsymbol{x}})$. It should be noted that this trajectory does not have to be identical to the visual reference trajectory. Nonetheless, our assumption is supported by desirable prediction performance, indicated by low averaged SMSE results, both for previously observed and unobserved regions of the input space.

The results obtained with simulated and real physical HRI data also support the general applicability of the approximation of diagonality for impedance matrices M_x, D_x, and K_x. Nonetheless, in future work, we aim to extend the methodology to physiologically accurate multi-dimensional treatment of (2.35), which would require definition of the non-diagonal elements by additional GPs. Each of these additional GPs would require suitable prior parameterization, including the respective EMVs, for which empirically determined data would need to be obtained. The additional product terms would need to be incorporated in (3.12) and (3.13). More importantly, symmetry properties of the matrices would require definition of an additional covariance function that correlates the respective GP with the interaction forces along the x_1- and x_2-axes.

The physiological plausibility of the Bayesian human motor behavior model is also slightly reduced by the omission of the positive correlation of damping d_i and stiffness k_i in the GP prior definitions in (3.7) and (3.8). It can however be partially included in the model through suitable definition of the EMVs $\mu_{d,i}$ and $\mu_{k,i}$. In the evaluation of the experiment, we define both EMVs $\mu_{d,i}$ and $\mu_{k,i}$ based on the estimated impedance characteristics for non-postural tasks in Table 3.1. Thus, if the observed behavior is in the proximity of the expected behavior, correlational characteristics of the conditional posteriors of d_i and k_i are to be expected. If the observed behavior deviates greatly from the expected behavior, the conditional posteriors may lose correlation, which may result in reduced accuracy of the inferred desired trajectory $\boldsymbol{x}_{\mathrm{d},*}$ and predicted interaction forces $\boldsymbol{u}_{\mathrm{int},*}$. Such behavioral and correlational deviations are indicated by decreased model confidence levels.

3.8. Summary

In this chapter, we present a method for modeling human motor behavior during physical and non-physical HRI that explicitly includes an impedance control model. Without loss of generality, particular focus is placed on the derivation of a human motor behavior model for physical HRI, as it represents the more challenging problem and also comprises a model for non-physical HRI. The dynamics of the human arm are modeled by an impedance control scheme that tracks a desired trajectory. We adopt a Bayesian perspective by assuming GP priors for the desired trajectory and the impedance components. By doing this, we are able to

derive covariance functions of an impedance control structure that accurately represents human motor behavior during physical and non-physical HRI through the exploitation of a priori knowledge of human impedance characteristics. Regression of the desired human motor behavior necessitates the inference of the human motor intention, which is represented by the desired trajectory. Thus, the impedance-based GP model is both a predictor of human motor behavior as well as an observer of human motor intention. The latter is validated in simulation with a neuromechanical model of the human arm. Different parameterizations of the desired trajectory are evaluated to show superior prediction performance with respect to a naive GP prior and demonstrate versatility and adaptability of the model. As the validation in simulation reveals a dependency between prediction performance and the parameters of the GP priors, an overview of estimated human arm impedance characteristics is presented and implications for proper prior parameterization are discussed. In order to evaluate the prediction performance of the model with real data similar to that of envisaged HRI scenarios, an experiment with 20 participants is performed. The effects of training data sparsity are analyzed and it is demonstrated that the generalization capabilities of the model allow for reliable motor behavior predictions in previously unobserved regions of the input space.

Impedance Estimation for Physical HRI via Feedback Jerk Isolation

4.

In the previous chapter, we addressed the information exploitation by formulating a Bayesian human motor behavior model for physical and non-physical HRI that explicitly incorporates an impedance control model and allows for the inclusion of a priori impedance knowledge. In this chapter, we focus on the information acquisition. More specifically, we enable the acquisition of comprehensive knowledge about the human arm impedance characteristics by presenting a method for the estimation of impedance components in experiments that emulate realistic physical HRI scenarios. As voluntary feedback torques may take on complex task-specific forms that require more sophisticated models than the general formulation of the impedance control model for the involuntary feedback torques, accurate estimation of the impedance components necessitates separation of involuntary and voluntary feedback. In addition to exclusion of voluntary feedback, a suitable impedance estimation method must also provide accurate isolation of feedback behavior in response to external perturbations from feedforward behavior, as estimation errors in the feedback behavior directly influence the estimation accuracy of the impedance components. In this chapter, we present a method for the estimation of the impedance components during multi-joint human arm movements. We apply force perturbations that are designed such that the feedback behavior can be isolated by a high pass filter, as the dominant frequencies of the jerks of the evoked feedback behavior lie above those of the unperturbed movements. Furthermore, we limit the duration of the estimation interval in order to guarantee the exclusion of voluntary feedback. Here, we do not require the assumption that the unperturbed states represent the desired kinematic states and thus only differentiate between perturbed and unperturbed movements. We use dynamic regressor representation of the rigid body dynamics to obtain a linear model of the impedance components in joint space. Thus, we are able to estimate the constant values of the inertial parameters in a static posture maintenance task and subsequently insert them to estimate the remaining impedance components in a dynamic movement task.

The remainder of this chapter is structured as follows: related work and open problems are reviewed in Section 4.1. The dynamic regressor representation is introduced in Section 4.2. The feedback jerk isolation and the perturbation design are presented in Section 4.3 and the impedance estimation is presented in Section 4.4. Both the feedback jerk isolation and the impedance estimation are validated with simulated data of a neuromechanical model of the human arm in Section 4.5. We compare the validation results to those obtained by application of the methods presented in [52] and [53]. In the validation of the feedback jerk isolation, we additionally analyze the effects of different movement velocities as well as different frequencies and amplitudes of neural noise. In Section 4.6, we perform an extensive evaluation of the applicability to real data based on an experiment with human participants. It also includes an analysis of the effects of different durations of the estimation interval. The obtained results are discussed in Section 4.7 and summarized in Section 4.8.

4.1. Related Work and Open Problems

Estimation of multi-joint arm impedance is generally either performed by application of a perturbation paradigm, in which perturbations evoke deviations from unperturbed states to measure variational dynamics, or by combining electromyographic (EMG) measurements with appropriate impedance models. In the latter category of approaches, multiple studies combine EMG measurements with parametric muscle models, e.g., linear models of muscle stiffness [110], quadratic models of muscle tension [60], or models of musculotendon unit forces [111]. In [112], an artificial neural network produces a mapping between EMG data and stiffness estimates, that are obtained from measured joint torques and an empirically determined linear stiffness model. In [113] and [114], similar mappings are produced by pairing stiffness estimates obtained by application of the perturbation paradigm with EMG data. All of these EMG approaches have in common that they exclusively estimate stiffness.

Estimation of multi-joint arm impedance by application of the perturbation paradigm can generally be divided into two main categories: estimation in static posture maintenance tasks and in dynamic movement tasks. In both categories, perturbations evoke deviations from unperturbed states and impedance is estimated based on the resulting variational dynamics. Impedance estimation in static posture maintenance tasks is substantially less complex, as it does not require estimation of unperturbed states of underlying movements. Furthermore, it allows for application of position perturbations, which are executed by moving the hand along a perturbation trajectory and thus enable a priori definition of the variational kinematics. Some studies exploit this advantage by using perturbation trajectories with plateau phases, during which the deviation remains constant [21, 28, 29, 115, 116]. During the plateau phase, variational velocities and accelerations are zero. Thus, the respective variational forces can be used to exclusively estimate stiffness. Some studies use position perturbations defined by third [102, 117] or fifth degree polynomials [65, 113], which are specifically designed to improve the conditioning of the estimation. Other studies use stochastic position [114, 118] or force perturbations [119] in combination with substantially longer estimation intervals to estimate frequency domain impedance transfer functions.

Impedance estimation during dynamic movement tasks is substantially more challenging than during static posture maintenance tasks, as it requires estimation of the unperturbed states of the underlying movement. In [120], impedance is solely estimated in terms of evoked feedback forces. In [121], it is represented by the ratio of frequency domain forces and velocities. In [122], position perturbations with plateau phases are used to exclusively estimate stiffness in a 60 ms interval that starts 120 ms after perturbation onset. In [123] and [124], similar methods are used to exclusively estimate stiffness in a 50 ms interval that starts 250 ms after perturbation onset. In [125], force perturbations and time-frequency analysis are used to estimate impedance 135 ms after perturbation onset. Due to reliance on vibrational energy, this method is only applicable to free, unfettered movements without any kind of physical interaction. In [52], force perturbations are used to estimate impedance during multi-joint arm movements by least squares estimation in a 280 ms interval. In [53], similar methods are used to estimate impedance in a 250 ms interval. To the best of the author's knowledge, among existing methods in the literature, only those in [52] and [53] are designed to estimate inertial characteristics, damping, and stiffness during multi-joint arm movements that include some kind of physical interaction.

In [52], participants perform transversal and longitudinal point to point movements, which are guided by a target position that moves along a reference trajectory and is displayed on a computer monitor. First order Taylor series expansion is used to obtain a linearized model of the rigid body dynamics and the feedback behavior in joint space. Inertial parameters are estimated a priori in a static posture maintenance task and subsequently inserted for the estimation of damping and stiffness in the dynamic movement task. Variational dynamics are obtained by calculating the difference to the averaged unbiased dynamics of all perturbed movements, which are calculated by subtracting the offsets at perturbation onset.

In [53], participants perform a manual tungsten inert gas welding task in cooperation with a robot. The welding movements are guided by a straight reference trajectory and the participants are instructed "to do their best to achieve a good welding". Variational behavior is described by a linear model of diagonal inertia, damping, and stiffness matrices in Cartesian space, which are estimated simultaneously during the welding task. Variational positions and forces are obtained by subtraction of the offsets at perturbation onset and variational velocities and accelerations are obtained by differentiation.

Both [52] and [53] are unable to guarantee exclusion of voluntary feedback, because the respective estimation intervals are substantially longer than the delay of voluntary feedback. In [52], this is compensated by application of the do-not-intervene-voluntarily paradigm, i.e., participants are instructed to not intervene voluntarily in response to the perturbation. While this paradigm is not able to guarantee exclusion of voluntary feedback [126], it is widely accepted as a plausible approximation [29, 110]. During static posture maintenance tasks, the avoidance of voluntary feedback does not have any major implications on the execution of desired motor behavior, as there is no underlying movement. However, during dynamic movement tasks, where there is an underlying movement, it substantially influences the successful execution of desired motor behavior. Thus, instructing the participants to not intervene voluntarily substantially limits the number of realistic physical HRI scenarios.

4.2. Dynamic Regressor Representation

The estimation of the impedance components within a limited estimation interval requires a maximally accurate formulation of the impedance control model. Thus, in this chapter, in order to avoid assumptions concerning negligibility of inertia and Coriolis terms that are necessary to obtain a linear second order system in Cartesian space, we use the impedance control model (2.17) in joint space as the basis for the impedance estimation. Furthermore, in this chapter, we do not require the assumption that the unperturbed states represent the desired kinematic states and thus only differentiate between perturbed and unperturbed movements. In the impedance control model (2.17), the inertial properties of the limbs are described by the Coriolis/centrifugal matrix C_q and the inertia matrix M_q. In order to obtain a fully linear model that allows for the estimation of the inertial characteristics of the limbs, we apply dynamic regressor representation.

The rigid body dynamics (2.1) is non-linear with respect to the arm configuration $\boldsymbol{q}$ and the respective derivatives $\dot{\boldsymbol{q}}$ and $\ddot{\boldsymbol{q}}$. For a two-joint two-link system in the horizontal plane, the inertia matrix M_q and Coriolis/centrifugal matrix C_q are defined as follows:

$$M_q(\boldsymbol{q}) = \begin{bmatrix} \overline{\iota}_1 + \overline{\iota}_2 + 2l_1 \cos(q_2) m_2 l_{c,2} + l_1^2 m_2 & \overline{\iota}_2 + l_1 \cos(q_2) m_2 l_{c,2} \\ \overline{\iota}_2 + l_1 \cos(q_2) m_2 l_{c,2} & \overline{\iota}_2 \end{bmatrix}, \tag{4.1}$$

$$C_q(\boldsymbol{q}, \dot{\boldsymbol{q}}) = \begin{bmatrix} -\dot{q}_2 l_1 \sin(q_2) m_2 l_{c,2} & -(\dot{q}_1 + \dot{q}_2)\, l_1 \sin(q_2) m_2 l_{c,2} \\ \dot{q}_1 l_1 \sin(q_2) m_2 l_{c,2} & 0 \end{bmatrix} . \tag{4.2}$$

In the definition of the inertia matrix M_q, according to the parallel axis theorem,

$$\overline{\iota}_i = \iota_i + m_i l_{c,i}^2 . \tag{4.3}$$

Thus, the inertial properties are defined by the moments of inertia ι_i, the masses m_i, the lengths l_i, and the distances from the joints to the centers of gravity $l_{c,i}$.

The Lagrangian formalism enables the derivation of the dynamic regressor representation, which is linear with respect to the standard inertial parameters of the system:

$$\boldsymbol{\tau}_{\mathrm{hu}} + \boldsymbol{\tau}_{\mathrm{ext}} = Y(\boldsymbol{q}, \dot{\boldsymbol{q}}, \ddot{\boldsymbol{q}})\boldsymbol{\pi} , \tag{4.4}$$

$$Y(\boldsymbol{q}, \dot{\boldsymbol{q}}, \ddot{\boldsymbol{q}}) = \frac{\partial(M_q(\boldsymbol{q})\ddot{\boldsymbol{q}} + C_q(\boldsymbol{q}, \dot{\boldsymbol{q}})\dot{\boldsymbol{q}})}{\partial \boldsymbol{\pi}} , \tag{4.5}$$

where Y is the regressor matrix and $\boldsymbol{\pi} = [\boldsymbol{\pi}_1^{\mathsf{T}}, \boldsymbol{\pi}_2^{\mathsf{T}}]^{\mathsf{T}}$ is the standard inertial parameter vector, which is composed of the inertial parameters of the upper arm $\boldsymbol{\pi}_1$ and the forearm $\boldsymbol{\pi}_2$ [127]. In general, the inertial parameters consist of the masses and the mass moments of first and second order [128]. However, as can be seen in the inertia matrix M_q and Coriolis/centrifugal matrix C_q in (4.1) and (4.2), some parameters do not have any effect on the system dynamics which corresponds to a zero column in the regressor matrix Y. For the multi-joint arm, omission of these parameters yields the reduced inertial parameter vector

$$\boldsymbol{\pi}_{\mathrm{r}} = [\overline{\iota}_1,\ \overline{\iota}_2,\ m_2 l_{c,2},\ m_2]^{\mathsf{T}} . \tag{4.6}$$

Comprehensive analysis of the corresponding reduced regressor matrix Y_{r} reveals that further reduction of inertial parameters is possible [129]. Application of appropriate transformations yields the base inertial parameter (BIP) vector $\overline{\boldsymbol{\pi}}$, which contains the minimal set of inertial parameters, and the corresponding base regressor matrix $\overline{Y}$ of the multi-joint arm:

$$\overline{\boldsymbol{\pi}} = \left[\overline{\iota}_1 + m_2 l_1^2,\ \overline{\iota}_2,\ m_2 l_{c,2} l_1\right]^{\mathsf{T}} , \tag{4.7}$$

$$\overline{Y}(\boldsymbol{q}, \dot{\boldsymbol{q}}, \ddot{\boldsymbol{q}}) = \begin{bmatrix} \ddot{q}_1 & \ddot{q}_1 + \ddot{q}_2 & \overline{Y}_{13} \\ 0 & \ddot{q}_1 + \ddot{q}_2 & \overline{Y}_{23} \end{bmatrix} , \tag{4.8}$$

$$\overline{Y}_{13} = (2\ddot{q}_1 + \ddot{q}_2)\cos(q_2) - (2\dot{q}_1\dot{q}_2 + \dot{q}_2^2)\sin(q_2) ,$$

$$\overline{Y}_{23} = \ddot{q}_1 \cos(q_2) + \dot{q}_1^2 \sin(q_2) .$$

Using the linear model (4.4) in combination with the BIP vector $\overline{\boldsymbol{\pi}}$ of (4.7) and the base regressor matrix $\overline{Y}$ of (4.8) to calculate the variational internal torques $\Delta\boldsymbol{\tau}_{\mathrm{hu}}$ yields

$$\begin{aligned} \Delta\boldsymbol{\tau}_{\mathrm{hu}} &= (\overline{Y}(\boldsymbol{q}, \dot{\boldsymbol{q}}, \ddot{\boldsymbol{q}}) - \overline{Y}(\boldsymbol{q}^*, \dot{\boldsymbol{q}}^*, \ddot{\boldsymbol{q}}^*))\overline{\boldsymbol{\pi}} - \Delta\boldsymbol{\tau}_{\mathrm{ext}} \\ &= \Delta\overline{Y}(\boldsymbol{q}, \boldsymbol{q}^*, \dot{\boldsymbol{q}}, \dot{\boldsymbol{q}}^*, \ddot{\boldsymbol{q}}, \ddot{\boldsymbol{q}}^*)\overline{\boldsymbol{\pi}} - \Delta\boldsymbol{\tau}_{\mathrm{ext}} . \end{aligned} \tag{4.9}$$

Subsequently inserting (2.13) in (4.9) yields the impedance estimation model

$$\Delta\boldsymbol{\tau}_{\mathrm{ext}} = \Delta\overline{Y}(\boldsymbol{q}, \boldsymbol{q}^*, \dot{\boldsymbol{q}}, \dot{\boldsymbol{q}}^*, \ddot{\boldsymbol{q}}, \ddot{\boldsymbol{q}}^*)\overline{\boldsymbol{\pi}} + D_q(\boldsymbol{q}, \dot{\boldsymbol{q}}, \boldsymbol{a})\Delta\dot{\boldsymbol{q}} + K_q(\boldsymbol{q}, \dot{\boldsymbol{q}}, \boldsymbol{a})\Delta\boldsymbol{q} , \tag{4.10}$$

which, in contrast to the formulation of the impedance control model in (2.17) is linear with respect to all impedance components, i.e., BIP vector $\overline{\boldsymbol{\pi}}$, damping D_q, and stiffness K_q.

In order to guarantee the exclusion of voluntary feedback, we limit the duration T_{est} of the estimation interval, in which we apply this impedance estimation model, to the minimum delay of voluntary feedback δ_{FBv}. Considering the delays of voluntary feedback in response to haptic motion perception as well as conduction delays of descending motor commands, this means that the duration of the estimation interval $T_{\text{est}} = \delta_{\text{FBv}} = 115$ ms (see Section 2.1). Thus, the problem considered in this chapter consists of the estimation of the impedance components, i.e, BIP vector $\overline{\boldsymbol{\pi}}$, damping D_q, and stiffness K_q, in the interval $[0, T_{\text{est}}]$ with the limited duration $T_{\text{est}} = \delta_{\text{FBv}} = 115$ ms. This is to be achieved given the perturbed observations $\{\boldsymbol{x}, \boldsymbol{u}_{\text{ext}}\}$, which result from application of force perturbations during multi-joint arm movements, and requires estimation of the unperturbed dynamics $\{\boldsymbol{q}^*, \dot{\boldsymbol{q}}^*, \ddot{\boldsymbol{q}}^*, \boldsymbol{\tau}^*_{\text{ext}}\}$.

4.3. Unperturbed Dynamics Estimation

In order to obtain the unperturbed and variational dynamics necessary for the estimation of the impedance components, we apply force perturbations that are designed such that the feedback behavior can be isolated by a high pass filter, as the dominant frequencies of the jerks of the evoked feedback behavior are located above those of the unperturbed movements. In this section, we introduce the two major elements of the estimation of the unperturbed and variational dynamics. First, we discuss the configuration and application of the feedback jerk isolation and subsequently we present the design of the external force perturbations.

4.3.1. Feedback Jerk Isolation

According to the minimum jerk principle [72], the CNS optimizes the arm endpoint trajectory in a point to point movement through minimization of the endpoint jerk. We take advantage of this by designing the perturbation such that the dominant frequencies of the jerks of the evoked feedback behavior lie above those of the unperturbed movements. Due to this design, we are able to estimate the evoked feedback behavior in the form of the variational jerks $\Delta\dddot{\boldsymbol{x}}$ through application of a high pass filter to the jerks $\dddot{\boldsymbol{x}}$ of the perturbed movement.

Remark 4.1. In order to achieve maximum pass band flatness and fast stop band roll-off, we perform the feedback jerk isolation with a Butterworth filter that is implemented as a tenth-order digital biquad filter. It is applied bi-directionally for zero phase distortion.

The cut-off frequencies $\boldsymbol{f}_{\text{c,HP}}$ of the high pass filter are defined based on the energy spectral densities (ESDs) $\boldsymbol{\psi}$ of the jerks $\dddot{\boldsymbol{x}}$ of the unperturbed and perturbed movements [130]:

$$\boldsymbol{\psi}(f) = \left| \int_{-\infty}^{\infty} e^{-2\pi i f t} \dddot{\boldsymbol{x}}(t) dt \right|^2 . \tag{4.11}$$

In order to configure the high pass filter, we use the set Ψ, which contains the ESDs $\boldsymbol{\psi}$ of the jerks $\dddot{\boldsymbol{x}}$ of all unperturbed and perturbed movements, to calculate the averaged ESDs of the unperturbed movements $\boldsymbol{\psi}_{\text{UP}}$, the averaged ESDs of the perturbed movements $\boldsymbol{\psi}_{\text{P}}$, and the averaged ESDs of the feedback behavior $\boldsymbol{\psi}_{\text{FB}} = \boldsymbol{\psi}_{\text{P}} - \boldsymbol{\psi}_{\text{UP}}$. The cut-off frequencies $\boldsymbol{f}_{\text{c,HP}}$ of the filter are defined as the frequencies $\boldsymbol{f}$ at which $\boldsymbol{\psi}_{\text{FB}} > \boldsymbol{\psi}_{\text{UP}}$, i.e., the averaged ESDs of the feedback behavior $\boldsymbol{\psi}_{\text{FB}}$ become larger than those of the unperturbed movements $\boldsymbol{\psi}_{\text{UP}}$.

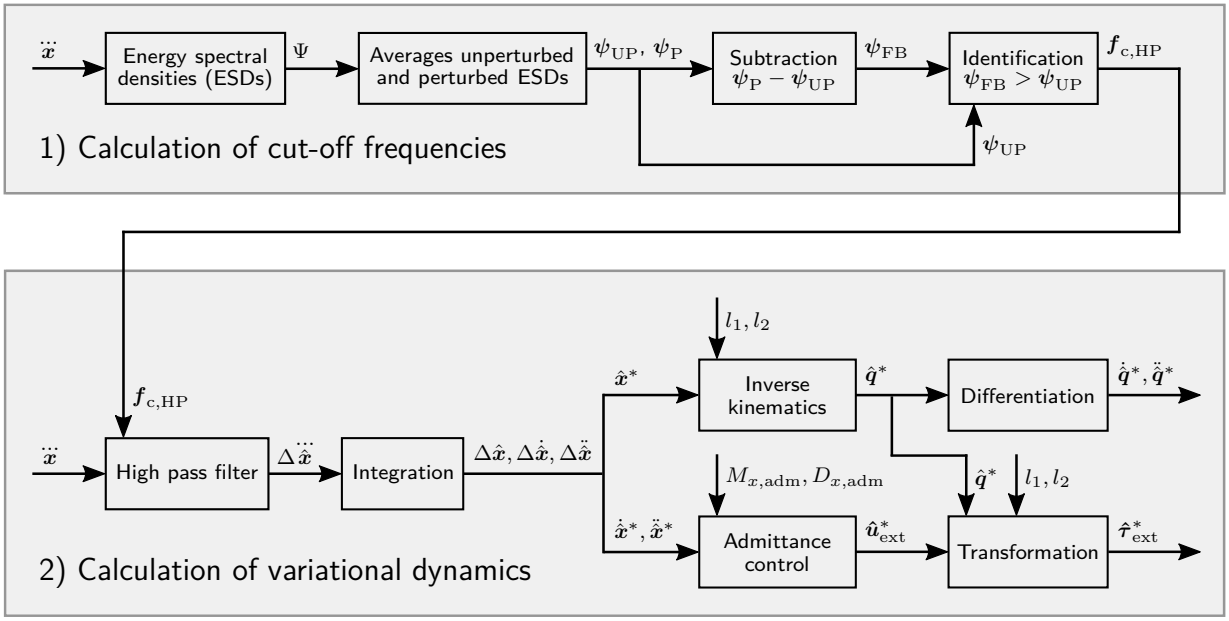

Figure 4.1.: Block diagram of the feedback jerk isolation. For every variational variable $\Delta(\cdot)$, the respective unperturbed variable $(\cdot)^* = \Delta(\cdot) + (\cdot)$ is calculated with the respective perturbed variable $(\cdot)$, and vice versa.

The high pass filtered jerks $\ddot{\boldsymbol{x}}_{\mathrm{HP}}$ provide the estimated variational jerks $\Delta\hat{\dddot{\boldsymbol{x}}}$, which yield the estimated unperturbed jerks $\hat{\dddot{\boldsymbol{x}}}^*$. Subsequently, integration yields the estimated variational kinematics $\{\Delta\hat{\boldsymbol{x}}, \Delta\hat{\dot{\boldsymbol{x}}}, \Delta\hat{\ddot{\boldsymbol{x}}}\}$ and unperturbed kinematics $\{\hat{\boldsymbol{x}}^*, \hat{\dot{\boldsymbol{x}}}^*, \hat{\ddot{\boldsymbol{x}}}^*\}$. For convenience, from this point on, we refer to the averaged ESDs $\boldsymbol{\psi}_{\mathrm{UP}}$, $\boldsymbol{\psi}_{\mathrm{P}}$, and $\boldsymbol{\psi}_{\mathrm{FB}}$ simply as ESDs.

The apparatus in our experiments is controlled by means of an admittance control scheme. Therefore, the external forces $\boldsymbol{u}_{\mathrm{ext}}$ can be calculated according to

$$\boldsymbol{u}_{\mathrm{ext}} = \boldsymbol{u}_{\mathrm{pert}} - \boldsymbol{u}_{\mathrm{adm}} - M_{x,\mathrm{handle}}\ddot{\boldsymbol{x}} \ , \tag{4.12}$$

where $\boldsymbol{u}_{\mathrm{adm}}$ is the admittance force, as defined in (3.40), $\boldsymbol{u}_{\mathrm{pert}}$ is the perturbation force, and $M_{x,\mathrm{handle}}$ is the handle inertia. Inserting the estimated unperturbed kinematics $\hat{\dot{\boldsymbol{x}}}^*$ and $\hat{\ddot{\boldsymbol{x}}}^*$ as well as $\boldsymbol{u}_{\mathrm{pert}} = \boldsymbol{0}$ in (4.12) and (3.40) yields the estimated unperturbed external forces $\hat{\boldsymbol{u}}^*_{\mathrm{ext}}$ and variational external forces $\Delta\hat{\boldsymbol{u}}_{\mathrm{ext}}$. The estimated unperturbed arm configuration $\hat{\boldsymbol{q}}^*$ and the respective derivatives $\hat{\dot{\boldsymbol{q}}}^*$ and $\hat{\ddot{\boldsymbol{q}}}^*$ are calculated using the inverse kinematics (2.24) and (2.25) and the estimated unperturbed external torques $\hat{\boldsymbol{\tau}}^*_{\mathrm{ext}}$ are calculated using the transformation (2.26). Finally, the estimated unperturbed dynamics $\{\hat{\boldsymbol{q}}^*, \hat{\dot{\boldsymbol{q}}}^*, \hat{\ddot{\boldsymbol{q}}}^*, \hat{\boldsymbol{\tau}}^*_{\mathrm{ext}}\}$ yield the estimated variational dynamics $\{\Delta\hat{\boldsymbol{q}}, \Delta\hat{\dot{\boldsymbol{q}}}, \Delta\hat{\ddot{\boldsymbol{q}}}, \Delta\hat{\boldsymbol{\tau}}_{\mathrm{ext}}\}$. Fig. 4.1 presents a block diagram that displays the procedure of the feedback jerk isolation, separated into the calculation of the cut-off frequencies $\boldsymbol{f}_{\mathrm{c,HP}}$ and the estimated variational dynamics $\{\Delta\hat{\boldsymbol{q}}, \Delta\hat{\dot{\boldsymbol{q}}}, \Delta\hat{\ddot{\boldsymbol{q}}}, \Delta\hat{\boldsymbol{\tau}}_{\mathrm{ext}}\}$.

4.3.2. Perturbation Design

The perturbation is designed to meet two essential criteria. First, the dominant frequencies of the jerks of the evoked feedback behavior should be located above those of the jerks of the unperturbed movements. Second, in order to minimize movement interference and corrective oscillations, it should not only produce deviations, but also move the hand back towards the

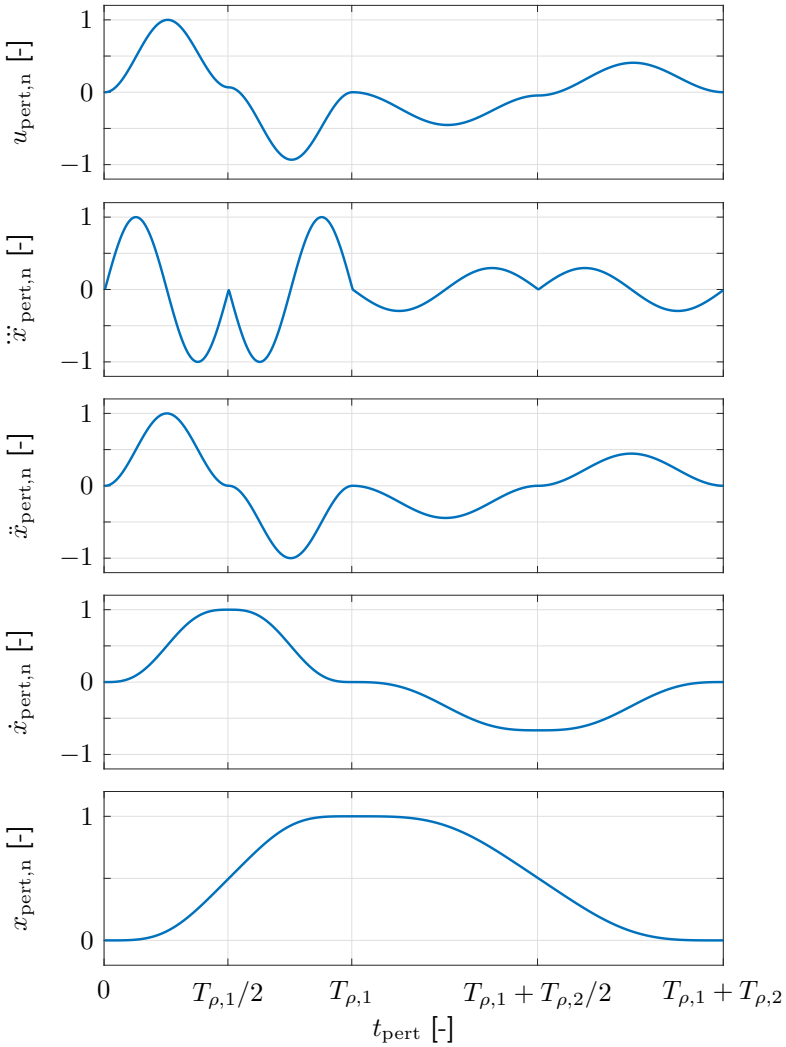

Figure 4.2.: Normalized perturbation force profile $u_{\text{pert,n}}$ and resulting kinematics profiles $\{x_{\text{pert,n}}, \dot{x}_{\text{pert,n}}, \ddot{x}_{\text{pert,n}}, \dddot{x}_{\text{pert,n}}\}$ of the dynamic movement task. The first part of the perturbation with duration $T_{\rho,1}$ is responsible for the deviation from the unperturbed states and the second part with duration $T_{\rho,2}$ supplies the retracting movement back towards the unperturbed states.

unperturbed states. In order to fulfill these two essential criteria, we design the perturbation acceleration profile $\ddot{x}_{\text{pert}}$ through concatenation of two sinusoidal functions

$$\rho = \begin{cases} \frac{1}{2}\alpha_\rho \left(\sin\left(\frac{4\pi t_{\text{pert}}}{T_\rho} + \frac{3\pi}{2}\right) + 1\right) & \forall\ t_{\text{pert}} \in [0, \frac{T_\rho}{2}] \\ -\frac{1}{2}\alpha_\rho \left(\sin\left(\frac{4\pi t_{\text{pert}}}{T_\rho} + \frac{3\pi}{2}\right) + 1\right) & \forall\ t_{\text{pert}} \in [\frac{T_\rho}{2}, T_\rho] \end{cases} . \tag{4.13}$$

The first of the two functions ρ_1 with amplitude $\alpha_{\rho,1}$ and duration $T_{\rho,1}$ is responsible for the deviation from the unperturbed states. The second function ρ_2 with amplitude $\alpha_{\rho,2}$ and duration $T_{\rho,2}$ supplies the retracting movement back towards the unperturbed states. In order to minimize hardware oscillations due to the perturbation, we define $T_{\rho,2} = (3/2)T_{\rho,1}$ and scale $\alpha_{\rho,2}$ such that all perturbation profiles are zero at the end of the perturbation.

Lastly, we combine the perturbation acceleration profile $\ddot{x}_{\text{pert}}$ and velocity profile $\dot{x}_{\text{pert}}$ with the admittance inertia $M_{x,\text{adm}}$ and damping $D_{x,\text{adm}}$ of our admittance control scheme, as defined in (3.40), in order to obtain the perturbation force profile u_{pert}. It is defined by the amplitude of its first peak α_{pert} and its combined duration $T_{\text{pert}} = T_{\rho,1} + T_{\rho,2}$.

Remark 4.2. In the dynamic movement task in this work, $\alpha_{\text{pert}} = 40$ N, $T_{\rho,1} = 70$ ms, and $T_{\text{pert}} = 175$ ms. The resulting normalized perturbation force profile $u_{\text{pert,n}}$ and the corresponding kinematics profiles $\{x_{\text{pert,n}}, \dot{x}_{\text{pert,n}}, \ddot{x}_{\text{pert,n}}, \dddot{x}_{\text{pert,n}}\}$ are illustrated in Fig. 4.2.

Given the normalized perturbation force profile $u_{\text{pert,n}}$, which is obtained by normalizing with the amplitude of the first peak α_{pert}, the perturbation force $\boldsymbol{u}_{\text{pert}}$ is given by

$$\boldsymbol{u}_{\text{pert}} = \alpha_{\text{pert}} u_{\text{pert,n}} [\cos\phi_{\text{pert}}, \sin\phi_{\text{pert}}]^{\mathsf{T}} , \tag{4.14}$$

in which the perturbation angle ϕ_{pert} is defined by the set of perturbation angles Φ_{pert}.

4.4. Impedance Estimation

In this section, we present the least squares estimation of the impedance components with the impedance estimation model (4.10), the estimated unperturbed dynamics $\{\hat{\boldsymbol{q}}^*, \dot{\hat{\boldsymbol{q}}}^*, \ddot{\hat{\boldsymbol{q}}}^*, \hat{\boldsymbol{\tau}}^*_{\text{ext}}\}$, and the estimated variational dynamics $\{\Delta\hat{\boldsymbol{q}}, \Delta\dot{\hat{\boldsymbol{q}}}, \Delta\ddot{\hat{\boldsymbol{q}}}, \Delta\hat{\boldsymbol{\tau}}_{\text{ext}}\}$. Due to the limited duration of the estimation interval T_{est}, we assume that the impedance components D_q and K_q are constant for $t_{\text{pert}} \in [0, T_{\text{est}}]$ and approximate them by the impedance parameters $\overline{D}_q$ and $\overline{K}_q$. We first introduce the linear least squares analysis of the impedance estimation in the static postural task and the dynamic movement task. Subsequently, we discuss symmetry and positive definiteness assumptions and the resulting non-linear least squares analysis.

4.4.1. Linear Least Squares Analysis

In order to calculate the linear least squares solution, we concatenate the elements of the BIP vector $\overline{\boldsymbol{\pi}}$, damping $\overline{D}_q$, and stiffness $\overline{K}_q$ in the unknown parameter vector

$$\boldsymbol{p} = \left[\overline{\pi}_1, \overline{\pi}_2, \overline{\pi}_3, \overline{D}_{q,11}, \overline{D}_{q,12}, \overline{D}_{q,21}, \overline{D}_{q,22}, \overline{K}_{q,11}, \overline{K}_{q,12}, \overline{K}_{q,21}, \overline{K}_{q,22}\right]^{\mathsf{T}} , \tag{4.15}$$

which allows for expression of (4.10) by the identification model

$$A\boldsymbol{p} = \boldsymbol{r} , \tag{4.16}$$

where A is the regression matrix and $\boldsymbol{r}$ is the output vector. For an interval with h samples, the regression matrix A and the output vector $\boldsymbol{r}$ are defined as

$$A = \left[X^{\mathsf{T}}(1), X^{\mathsf{T}}(2), \ \dots \ , X^{\mathsf{T}}(h)\right]^{\mathsf{T}} , \tag{4.17}$$

$$\boldsymbol{r} = \left[\Delta\hat{\boldsymbol{\tau}}^{\mathsf{T}}_{\text{ext}}(1), \Delta\hat{\boldsymbol{\tau}}^{\mathsf{T}}_{\text{ext}}(2), \ \dots \ , \Delta\hat{\boldsymbol{\tau}}^{\mathsf{T}}_{\text{ext}}(h)\right]^{\mathsf{T}} , \tag{4.18}$$

in which the independent variable matrix X is defined as

$$X = \frac{\partial(\Delta\overline{Y}(\boldsymbol{q}, \hat{\boldsymbol{q}}^*, \dot{\boldsymbol{q}}, \dot{\hat{\boldsymbol{q}}}^*, \ddot{\boldsymbol{q}}, \ddot{\hat{\boldsymbol{q}}}^*)\overline{\boldsymbol{\pi}} + \overline{D}_q\Delta\dot{\hat{\boldsymbol{q}}} + \overline{K}_q\Delta\hat{\boldsymbol{q}})}{\partial\boldsymbol{p}} . \tag{4.19}$$

Based on (4.15) - (4.19), minimization of the sum of squared residuals through linear least squares analysis yields a closed-form expression for the estimated parameter vector

$$\hat{\boldsymbol{p}} = (A^{\mathsf{T}}A)^{-1}A^{\mathsf{T}}\boldsymbol{r} \ . \tag{4.20}$$

Remark 4.3. Due to the limited duration of the estimation interval T_{est}, which implies the likewise limited duration of the perturbation T_{pert}, the perturbation in (4.14) does not possess sufficient richness of frequency components to guarantee persistent excitation [131]. A common approach for the compensation of such limitations is the a priori estimation of the inertial parameters [52, 123, 124, 132] which only marginally influences the overall accuracy of the estimated impedance parameters [21].

As the inertial parameters possess constant values that are independent of the dynamics, the BIP vector $\overline{\boldsymbol{\pi}}$ can be estimated a priori in a static postural task. Consequently, in the dynamic movement task, due to the insertion of the resulting estimated BIP vector $\hat{\overline{\boldsymbol{\pi}}}$ in the identification model, the unknown parameter vector $\boldsymbol{p}$ reduces to

$$\overline{\boldsymbol{p}} = \left[\overline{D}_{q,11}, \overline{D}_{q,12}, \overline{D}_{q,21}, \overline{D}_{q,22}, \overline{K}_{q,11}, \overline{K}_{q,12}, \overline{K}_{q,21}, \overline{K}_{q,22}\right]^{\mathsf{T}} \tag{4.21}$$

and the independent variable matrix X and the output vector $\boldsymbol{r}$ change to

$$\overline{X} = \frac{\partial(\overline{D}_q\Delta\dot{\hat{\boldsymbol{q}}} + \overline{K}_q\Delta\hat{\boldsymbol{q}})}{\partial \boldsymbol{p}} \ , \tag{4.22}$$

$$\overline{\boldsymbol{r}} = \Delta\hat{\boldsymbol{\tau}}_{\text{ext}} - \Delta\overline{Y}(\boldsymbol{q}, \hat{\boldsymbol{q}}^*, \dot{\boldsymbol{q}}, \dot{\hat{\boldsymbol{q}}}^*, \ddot{\boldsymbol{q}}, \ddot{\hat{\boldsymbol{q}}}^*)\hat{\overline{\boldsymbol{\pi}}} \ , \tag{4.23}$$

where, for simplicity, the dynamic output vector $\overline{\boldsymbol{r}}$ is formulated for a single data sample. Inserting the dynamic independent variable matrix $\overline{X}$ and the corresponding output vector $\overline{\boldsymbol{r}}$ in (4.17) and (4.20) yields the estimated dynamic unknown parameter vector $\overline{\boldsymbol{p}}$.

4.4.2. Non-linear Least Squares Analysis

In order to further reduce the number of unknown parameters in the impedance estimation, both for the static postural task as well as for the dynamic movement task, we examine the symmetry and positive definiteness properties of the stiffness $\overline{K}_q$.

The mechanical feedback behavior is governed by spring-like characteristics that result from the elastic properties of the individual muscles. Thus, the mechanical feedback forces possess zero curl and the mechanical stiffness is symmetric [133]. The reflexive feedback forces may possess non-zero curl which can only result from heteronymous inter-muscular reflex arcs with unequal activation gains [25]. However, as the resulting antisymmetric stiffness elements are substantially smaller than the corresponding symmetric ones, the reflexive feedback behavior is nonetheless characterized by predominantly spring-like characteristics [29, 102]. As the estimation interval in this work is substantially shorter than the ones in [29] and [102], we assume that the stiffness $\overline{K}_q$ is symmetric for $t_{\text{pert}} \in [0, T_{\text{est}}]$.

As the potential energy of the vector field of the involuntary feedback forces must increase in response to deviations from the unperturbed states, the symmetric stiffness $\overline{K}_q$ must also be positive definite. In order to incorporate both symmetry and positive definiteness of the stiffness $\overline{K}_q$ in the estimation, we apply the Cholesky decomposition $\overline{K}_q = LL^{\mathsf{T}}$, where

the stiffness $\overline{K}_q$ is expressed by the matrix product of the lower triangular matrix L [134]. With this decomposition, the unknown parameter vectors $\boldsymbol{p}$ and $\overline{\boldsymbol{p}}$ of the static postural task and the dynamic movement task, respectively, are transformed to

$$\boldsymbol{p}_{\mathrm{nl}} = \left[\overline{\pi}_1, \overline{\pi}_2, \overline{\pi}_3, \overline{D}_{q,11}, \overline{D}_{q,12}, \overline{D}_{q,21}, \overline{D}_{q,22}, L_{11}, L_{12}, L_{22}\right]^{\mathsf{T}} , \tag{4.24}$$

$$\overline{\boldsymbol{p}}_{\mathrm{nl}} = \left[\overline{D}_{q,11}, \overline{D}_{q,12}, \overline{D}_{q,21}, \overline{D}_{q,22}, L_{11}, L_{12}, L_{22}\right]^{\mathsf{T}} . \tag{4.25}$$

Due to the non-linearity of $\overline{K}_q = LL^{\mathsf{T}}$, we can no longer use the identification model (4.16). Instead, we apply non-linear least squares analysis to minimize $\|\boldsymbol{g}(\boldsymbol{p}_{\mathrm{nl}})\|^2$ and $\|\overline{\boldsymbol{g}}(\overline{\boldsymbol{p}}_{\mathrm{nl}})\|^2$ for the static postural task and the dynamic movement task, respectively:

$$\boldsymbol{g}(\boldsymbol{p}_{\mathrm{nl}}) = \Delta\overline{Y}(\boldsymbol{q}, \hat{\boldsymbol{q}}^*, \dot{\boldsymbol{q}}, \dot{\hat{\boldsymbol{q}}}^*, \ddot{\boldsymbol{q}}, \ddot{\hat{\boldsymbol{q}}}^*)\overline{\boldsymbol{\pi}} + \overline{D}_q \Delta\dot{\hat{\boldsymbol{q}}} + LL^{\mathsf{T}}\Delta\hat{\boldsymbol{q}} - \boldsymbol{r} , \tag{4.26}$$

$$\overline{\boldsymbol{g}}(\overline{\boldsymbol{p}}_{\mathrm{nl}}) = \overline{D}_q \Delta\dot{\hat{\boldsymbol{q}}} + LL^{\mathsf{T}}\Delta\hat{\boldsymbol{q}} - \overline{\boldsymbol{r}} . \tag{4.27}$$

By calculating the non-linear least squares solutions of (4.26) and (4.27) we are able to obtain the estimated impedance parameters, which consist of the individual elements of the estimated BIP vector $\hat{\overline{\boldsymbol{\pi}}}$, the estimated damping $\hat{\overline{D}}_q$ and the estimated stiffness $\hat{\overline{K}}_q$.

4.5. Simulation

Both the feedback jerk isolation and the impedance estimation are validated with simulated data of the neuromechanical model of the human arm [35], which we use in Section 3.5 to validate the Bayesian human motor behavior model. By simulating each movement twice, once with and once without perturbation, we are able to validate the estimation of the unperturbed dynamics based on the feedback jerk isolation. Furthermore, we are able to use the simulated inertial characteristics and impedance components to validate the estimation of the impedance parameters. We compare the results of the validation to those obtained by application of the methods presented in [52] and [53]. In the validation of the feedback jerk isolation, we additionally analyze the effects of different movement velocities as well as different frequencies and amplitudes of neural noise. Fig. 4.3 contains a schematic diagram that lists the major elements of the method and the validation with simulated data.

We use the neuromechanical model of the human arm to simulate a static postural task and a dynamic movement task. As the static postural task does not include any kind of underlying movement, we are able to apply the do-not-intervene-voluntarily paradigm. While the do-not-intervene-voluntarily paradigm does not guarantee exclusion of voluntary feedback or constant unperturbed states [126], it is widely used and accepted as a plausible approximation of both of these assumptions [29, 52, 110]. Thus, given the absence of an underlying movement, and the fact that the elements of the BIP vector $\overline{\boldsymbol{\pi}}$ are all constant, we are able to use an estimation interval duration T_{est} that is longer than the delay of voluntary feedback δ_{FBv} in the static postural task. As the dynamic movement task does include an underlying movement, it is performed without the do-not-intervene-voluntarily paradigm and we use the limited estimation interval duration $T_{\mathrm{est}} = \delta_{\mathrm{FBv}} = 115$ ms.

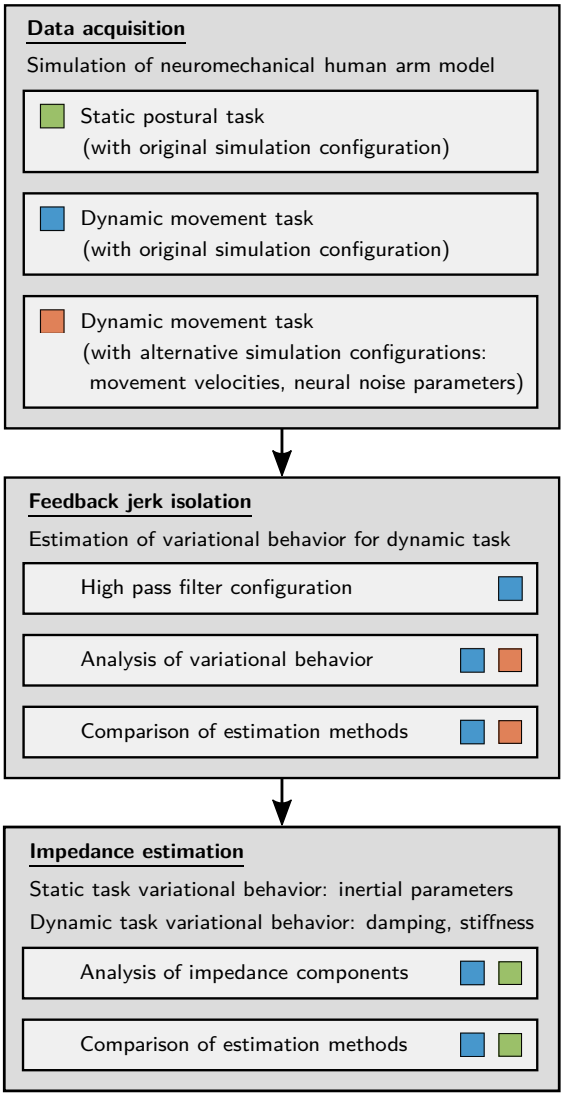

Figure 4.3.: Schematic diagram of the major elements of the method and the validation with simulated data. The colored boxes indicate which sets of simulated data are generated, applied, and analyzed in which phases of the validation.

4.5.1. Implementation

The implementation of the neuromechanical model is presented in detail in Section 3.5.1. In the implementation, there is no distinction between reflexive and voluntary feedback. Instead, both feedback mechanisms are combined and the simulated feedback delay δ_{sim} is defined to lie between the respective delays δ_{FBr} and δ_{FBv}. As the simulated feedback delay δ_{sim} is shorter than the duration of our estimation interval T_{est}, the feedback behavior within the estimation interval is influenced by voluntary contributions. In order to avoid this and enable the validation of the estimated impedance parameters $\overline{\hat{D}}_q$ and $\overline{\hat{K}}_q$ through the simulated impedance components, we use a variation of the original implementation, in which the simulated feedback delay δ_{sim} is equal to the delay δ_{FBv} of voluntary feedback, i.e., $\delta_{\text{sim}} = \delta_{\text{FBv}} = 115$ ms. In order to represent the effects of the do-not-intervene-voluntarily paradigm, voluntary feedback is removed in the simulations of the static postural task.

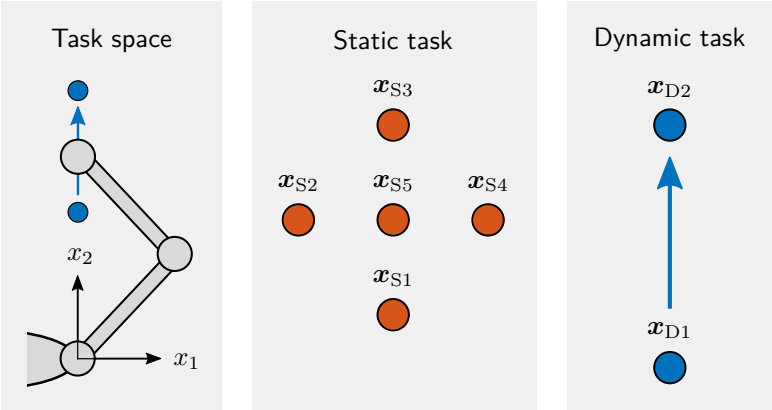

Figure 4.4.: Schematic representation of the human arm task space, the static task, and the dynamic task. In the static task, the arm maintains a total of five different positions that are spread out across the horizontal plane. In the dynamic task, it performs point to point movements along the sagittal axis.

Remark 4.4. Although the physiological correctness of the modified implementation with the simulated feedback delay $\delta_{\text{sim}} = 115$ ms is slightly reduced compared to the original implementation, it nonetheless represents a plausible simulation of human motor behavior. More importantly, it represents a means for validation of our method and for comparison of its performance to those of the existing methods presented in [52] and [53].

4.5.2. Simulation Design

As the definition of the signal-dependent noise $\boldsymbol{\upsilon}_\lambda$ in the neuromechanical model is based on a normally distributed random variable, the static task and the dynamic task are each simulated ten times and the respective results are averaged. In order to achieve maximum possible similarity of the simulated and the experimental data, the simulated manipulandum inertia and damping are defined in accordance with the inertia $M_{x,\text{adm}} = \text{diag}\{5, 5\}$ kg and damping $D_{x,\text{adm}} = \text{diag}\{20, 20\}$ Ns/m of the admittance control scheme of our apparatus.

Remark 4.5. The results of the simulation are either presented in within-, between-, or cross-simulation mean (SD). The cross-simulation mean (SD) is obtained by calculating the mean of the within-simulation means and the mean of the within-simulation SDs. As the majority of the results are cross-simulation mean (SD) results, for convenience, from this point on, the respective results are referred to simply as mean (SD) results.

Static task

In the static task, the arm maintains a total of five different positions that are spread out across the horizontal plane: $\boldsymbol{x}_{S1} = [0, 0.35]^\mathsf{T}$ m, $\boldsymbol{x}_{S2} = [-10, 0.45]^\mathsf{T}$ m, $\boldsymbol{x}_{S3} = [0, 0.55]^\mathsf{T}$ m, $\boldsymbol{x}_{S4} = [10, 0.45]^\mathsf{T}$ m, and $\boldsymbol{x}_{S5} = [0, 0.45]^\mathsf{T}$ m (see Fig. 4.4). In order to obtain perturbations that are similar to those of the static estimations in [52], we define the perturbation profile duration $T_{\rho,1} = 160$ ms which results in a total perturbation duration $T_{\text{pert}} = 400$ ms. We change the interaction mode from closed-loop to open-loop which means that applied forces do not contribute to the movement of the manipulandum. As this means that we

are essentially applying a position perturbation, we are able to define the amplitude of the perturbation position profile x_{pert}, which we set to 8 mm. The perturbation angles ϕ_{pert} are defined by the set $\Phi_{\text{pert}} = \{(\pi/12)k \mid k = 1 - 24 \setminus \{6, 12, 18, 24\}\}$, which contains a total of 20 angles. Each perturbation angle ϕ_{pert} is executed once in every position and the order of the resulting perturbations is randomized. Single execution of each of the 20 perturbation angles ϕ_{pert} in each of the five positions results in a total of 100 trials. The duration of the estimation interval $T_{\text{est}} = 400$ ms and the estimated BIP vector $\hat{\overline{\boldsymbol{\pi}}}$ is obtained by calculating the non-linear least squares solution for the complete data set of all 100 trials.

Dynamic task

In the dynamic task, the arm performs two-dimensional point to point movements along the sagittal axis from $\boldsymbol{x}_{\text{D1}} = [0, 0.30]^{\mathsf{T}}\text{m}$ to $\boldsymbol{x}_{\text{D2}} = [0, 0.55]^{\mathsf{T}}\text{m}$ (see Fig. 4.4). The duration of the movements T_{mov} is set to 2 s. The perturbations are designed to generate sufficiently large deviations in as short a time frame as possible, but nonetheless be kinesthetically renderable under hardware limitations. The perturbation amplitude $\alpha_{\text{pert}} = 40$ N and the perturbation profile duration $T_{\rho,1} = 70$ ms which yields a total perturbation duration $T_{\text{pert}} = 175$ ms. The perturbation is initiated when the hand reaches $x_2 = 0.4$ m which equals a traveled distance of 0.1 m along the axis of the principal movement. The perturbation angles ϕ_{pert} are defined by Φ_{pert}, which is identical to the static task. Each perturbation angle ϕ_{pert} is executed three times and the order of the perturbations is randomized. Three repetitions of each of the 20 perturbation angles ϕ_{pert} result in a total of 60 trials. Each of these 60 trials consists of an unperturbed and a perturbed movement. The duration of the estimation interval $T_{\text{est}} = 115$ ms and the estimated damping $\hat{\overline{D}}_q$ and stiffness $\hat{\overline{K}}_q$ are obtained by calculating the non-linear least squares solutions for data sets of 20 trials each. Grouping the complete data set of all 60 trials into smaller data sets of 20 trials each, starting from the first 20 trials, and moving the respective data set "window" along trial by trial until the last 20 trials are reached, provides a total of 41 individual non-linear least squares solutions.

Remark 4.6. The feedforward muscle activations $\boldsymbol{a}_{\text{FF}}$ for the dynamic task are calculated with the inverse kinematics and dynamics of a positional data set, which is provided by the authors of [35]. It contains positional data of 50 two-dimensional point to point arm movements, which possess identical start and goal positions as the movements in our task.

4.5.3. Feedback Jerk Isolation

We validate the estimation of the unperturbed dynamics $\{\boldsymbol{q}^*, \dot{\boldsymbol{q}}^*, \ddot{\boldsymbol{q}}^*, \boldsymbol{\tau}^*_{\text{ext}}\}$ via feedback jerk isolation by analyzing the estimated variational dynamics $\{\Delta\hat{\boldsymbol{x}}, \Delta\dot{\hat{\boldsymbol{x}}}, \Delta\ddot{\hat{\boldsymbol{x}}}, \Delta\hat{\boldsymbol{u}}_{\text{ext}}\}$ for different movement velocities and variations of neural noise. The validation is based on the normalized root mean square errors (NRMSEs) in the estimation interval $[0, T_{\text{est}}]$:

$$\text{NRMSE} = \sqrt{\frac{1}{n}\sum_{i=1}^{n}\left(\frac{\vartheta_i - \hat{\vartheta}_i}{\vartheta_{\max,i}}\right)^2}\,, \tag{4.28}$$

where $\vartheta_{\max}$ is the normalizing value, ϑ is the real value, $\hat{\vartheta}$ is the estimated value, and $n = 2$ is the dimensionality. The normalizing value $\vartheta_{\max}$ is given by the maximum real value.

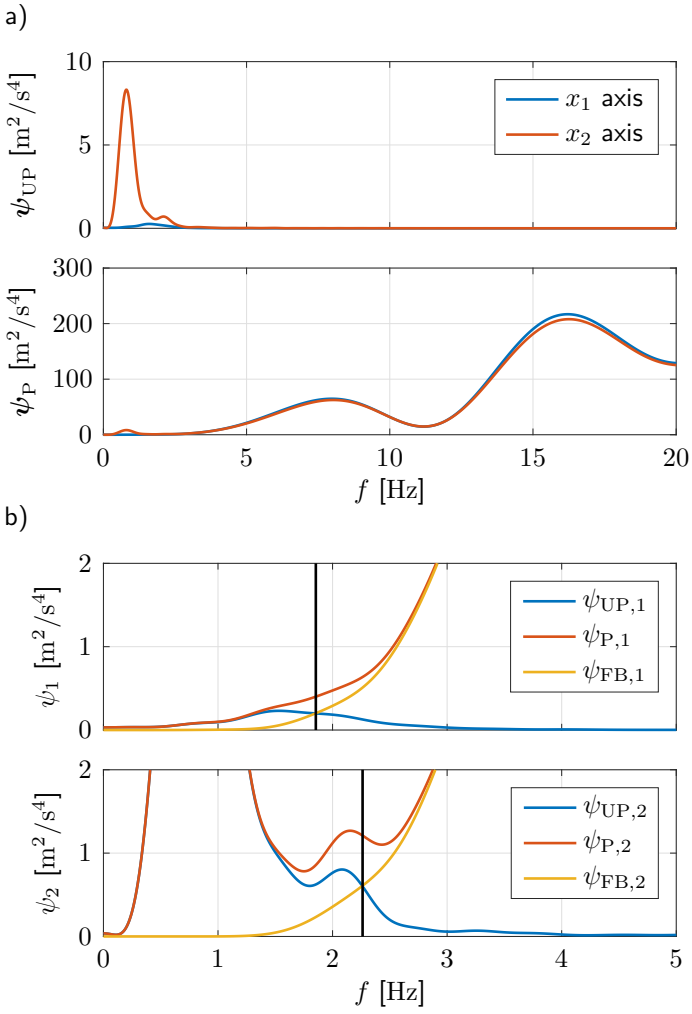

Figure 4.5.: High pass filter configuration based on simulated data. a) Mean results of the ESDs $\boldsymbol{\psi}_{\mathrm{UP}}$ and $\boldsymbol{\psi}_{\mathrm{P}}$. b) Calculation of the cut-off frequencies $\boldsymbol{f}_{\mathrm{c,HP}}$ (indicated by vertical lines). For clarity, the results are shown for a single simulation.

In order to analyze the performance for different movement velocities, the duration of the movements T_{mov} is changed (1 s, 3 s). For analysis of the performance for different variations of neural noise, the parameterization of the zero mean Brownian motion is changed in terms of the cut-off frequency $f_{\mathrm{c},\upsilon}$ (1 Hz, 3 Hz) and the amplitude α_υ (5, 20). We compare the results to those obtained with the methods in [52] and [53]. In order to enable performance comparisons without effects of voluntary feedback, all methodologies are applied to the same sets of simulated data and use the same duration of the estimation interval $T_{\mathrm{est}} = 115$ ms.

Filter configuration

Fig. 4.5a shows the mean results of the ESDs $\boldsymbol{\psi}_{\mathrm{UP}}$ and $\boldsymbol{\psi}_{\mathrm{P}}$. In the unperturbed movements, the energy of the principal movement along the x_2 axis is distinguishable by a peak in the respective ESD $\psi_{\mathrm{UP},2}$. A secondary, notably lower peak represents effects of neural noise. As the point to point movements do not require movements along the x_1 axis, the respective ESD $\psi_{\mathrm{UP},1}$ is substantially lower and represents effects of neural noise. The energy of both

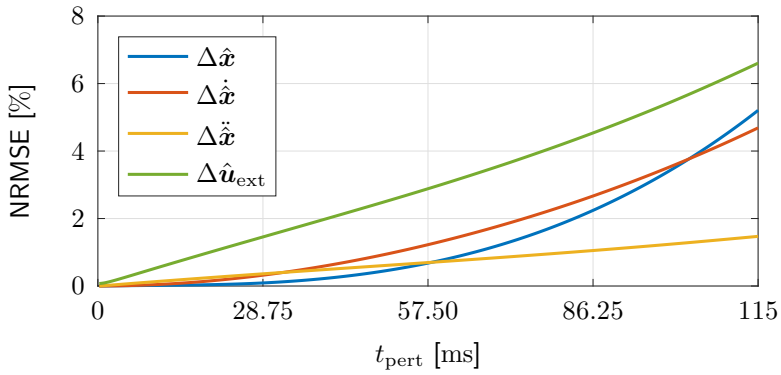

Figure 4.6.: Validation of feedback jerk isolation with simulated data. Mean results of the NRMSEs of the estimated variational dynamics $\{\Delta\hat{\boldsymbol{x}}, \Delta\dot{\hat{\boldsymbol{x}}}, \Delta\ddot{\hat{\boldsymbol{x}}}, \Delta\hat{\boldsymbol{u}}_{\text{ext}}\}$.

axes of the unperturbed movements decreases to marginally low values for high frequencies. The opposite applies for the energy of the perturbed movements, which increases to much higher values for high frequencies. The respective ESDs $\boldsymbol{\psi}_{\text{P}}$ are much higher than those of the unperturbed movements and have multiple peaks in the high frequency range.

Fig. 4.5b shows the ESDs $\boldsymbol{\psi}_{\text{UP}}$, $\boldsymbol{\psi}_{\text{P}}$, and $\boldsymbol{\psi}_{\text{FB}}$ of a single simulation in two axis-specific graphs in order to demonstrate the calculation of the cut-off frequencies $\boldsymbol{f}_{\text{c,HP}}$, defined as the frequencies $\boldsymbol{f}$ at which $\boldsymbol{\psi}_{\text{FB}} > \boldsymbol{\psi}_{\text{UP}}$. The cut-off frequency $f_{\text{c,HP},2}$ of the x_2 axis is sufficiently high to lie above the energy of the principal movement. Concurrently, it is sufficiently low to lie below the energy of the feedback behavior. Due to the absence of movements along the x_1 axis, the cut-off frequency $f_{\text{c,HP},1}$ is slightly lower. The between-simulation mean (SD) results of all ten simulations are $\boldsymbol{f}_{\text{c,HP}} = [1.89\ (0.08), 2.24\ (0.04)]$ Hz.

Results

The mean results of the NRMSEs in Fig. 4.6 show that the NRMSEs all increase with t_{pert}. The gradual increase of the NRMSEs of the estimated variational accelerations $\Delta\ddot{\hat{\boldsymbol{x}}}$ results from the integration of the estimated variational jerks $\Delta\dddot{\hat{\boldsymbol{x}}}$, which include estimation errors that originate from the calculation of the high pass filtered jerks $\dddot{\boldsymbol{x}}_{\text{HP}}$, i.e., the separation of unperturbed and variational behavior. The increases of the NRMSEs of the estimated variational velocities $\Delta\dot{\hat{\boldsymbol{x}}}$ and positions $\Delta\hat{\boldsymbol{x}}$ result from the consecutive integrations of the estimated variational accelerations $\Delta\ddot{\hat{\boldsymbol{x}}}$. The slightly increased NRMSEs of the estimated variational external forces $\Delta\hat{\boldsymbol{u}}_{\text{ext}}$ are caused by the estimation errors that are introduced into the calculation via the admittance control scheme by the estimated unperturbed velocities $\dot{\hat{\boldsymbol{x}}}^*$ and accelerations $\ddot{\hat{\boldsymbol{x}}}^*$. Despite the increase of the NRMSEs with t_{pert}, the maximum values of the estimated variational kinematics $\{\Delta\hat{\boldsymbol{x}}, \Delta\dot{\hat{\boldsymbol{x}}}, \Delta\ddot{\hat{\boldsymbol{x}}}\}$ are all below 6 % and the maximum value of the NRMSE of the estimated variational external forces $\Delta\hat{\boldsymbol{u}}_{\text{ext}}$ is below 8 %.

Remark 4.7. In order to compare the results to those of the methods in [52] and [53], we average the NRMSEs within the estimation interval $[0, T_{\text{est}}]$. For simplicity, from this point on, we refer to the resulting averaged NRMSEs simply as NRMSEs. The mean (SD) results of the NRMSEs for the original simulation are listed in Table 4.1 and those for alternative simulation configurations are listed in Tables 4.2a-c. The abbreviations FJI, GOM, and ERD represent our feedback jerk isolation and the methods in [52] and [53], respectively.

Table 4.1.: Validation of feedback jerk isolation with simulated data generated by using the original simulation. Mean (SD) results of averaged NRMSEs of estimated variational dynamics $\{\Delta\hat{\boldsymbol{x}}, \Delta\dot{\hat{\boldsymbol{x}}}, \Delta\ddot{\hat{\boldsymbol{x}}}, \Delta\hat{\boldsymbol{u}}_{\text{ext}}\}$.

Method	$\Delta\hat{\boldsymbol{x}}$ [%]		$\Delta\dot{\hat{\boldsymbol{x}}}$ [%]		$\Delta\ddot{\hat{\boldsymbol{x}}}$ [%]		$\Delta\hat{\boldsymbol{u}}_{\text{ext}}$ [%]	
FJI	1.33	(1.16)	1.60	(1.42)	0.71	(0.62)	3.04	(2.91)
GOM	29.65	(27.04)	6.47	(6.04)	1.26	(1.18)	4.96	(4.97)
ERD	911.10	(750.51)	551.24	(468.13)	5.31	(3.96)	17.77	(15.03)

Comparison - Original Simulation

The NRMSEs in Table 4.1 demonstrate that FJI achieves high estimation accuracy and outperforms both GOM and ERD. The magnitudes and differences of the NRMSEs of FJI are in accordance with those presented in Fig. 4.6. The performance difference of FJI and GOM increases from a small difference in $\Delta\ddot{\hat{\boldsymbol{x}}}$ to a large difference in $\Delta\hat{\boldsymbol{x}}$ and the performance difference in $\Delta\hat{\boldsymbol{u}}_{\text{ext}}$ is marginally larger than that of $\Delta\ddot{\hat{\boldsymbol{x}}}$. These correlations are plausible, due to the dependency on the averaged unbiased dynamics of all perturbed movements. While forces and accelerations are of similar magnitude, velocities and especially positions vary between movements. Consequently, the accuracy of the averaged unbiased dynamics decreases substantially from accelerations to positions. Similar correlations apply to the performance difference of FJI and ERD, but with substantially larger differences, especially for $\Delta\dot{\hat{\boldsymbol{x}}}$ and $\Delta\hat{\boldsymbol{x}}$. The substantially larger magnitudes of the NRMSEs of ERD are plausible, due to the dependency on the constant offset values at perturbation onset. While these constant offset values represent accurate approximations of the unperturbed states of the quasi-static movements of the manual welding task in [53], they are incapable of accurately representing the kinematics of the unperturbed states of dynamic point to point movements. For this reason, we exclude this method from the remainder of the validation.

Remark 4.8. In the discussion of the NRMSEs of the alternative simulations, the changes in configurations and results are evaluated relative to the original simulation. In order to facilitate the comparisons, Tables 4.2a-c also include the NRMSEs of the original simulation. Furthermore, the results are additionally illustrated with intermediate values in Fig. 4.7.

Comparison - Movement Durations

The NRMSEs in Table 4.2a show that the performance of FJI is decreased for a higher movement velocity (resulting from a shorter duration of the movement) and is marginally increased for a lower movement velocity (resulting from a longer duration of the movement). A higher movement velocity results in an increased cut-off frequency of the high pass filter which causes an increased information loss in the isolation of the feedback jerk. As a result, the estimation accuracy is decreased. The marginal increase in performance for a lower movement velocity suggests that the corresponding NRMSEs are in the proximity of the smallest possible errors, which are caused by unavoidable frequency overlap of unperturbed movements and feedback behavior, neural noise, and imperfect properties of a non-ideal high pass filter. The performance of GOM is slightly increased for a higher movement velocity and slightly decreased for a lower movement velocity. As the accumulated influence of the neural

Table 4.2.: Validation of feedback jerk isolation with simulated data generated using the alternative simulations. Mean (SD) results of averaged NRMSEs of estimated variational dynamics $\{\Delta\hat{\boldsymbol{x}}, \Delta\dot{\hat{\boldsymbol{x}}}, \Delta\ddot{\hat{\boldsymbol{x}}}, \Delta\hat{\boldsymbol{u}}_{\text{ext}}\}$. Alternative simulations defined by a) Movement duration T_{mov}, b) Cut-off frequency $f_{\text{c},\upsilon}$, c) Amplitude α_υ.

a)

Method	T_{mov} [s]	$\Delta\hat{\boldsymbol{x}}$ [%]	$\Delta\dot{\hat{\boldsymbol{x}}}$ [%]	$\Delta\ddot{\hat{\boldsymbol{x}}}$ [%]	$\Delta\hat{\boldsymbol{u}}_{\text{ext}}$ [%]
FJI	1.0	9.67 (6.50)	10.05 (6.56)	3.75 (2.30)	14.38 (10.12)
FJI	2.0	1.33 (1.16)	1.60 (1.42)	0.71 (0.62)	3.04 (2.91)
FJI	3.0	1.29 (1.11)	1.47 (1.32)	0.62 (0.57)	2.74 (3.04)
GOM	1.0	23.06 (20.53)	4.68 (3.93)	0.84 (0.77)	3.24 (3.31)
GOM	2.0	29.65 (27.04)	6.47 (6.04)	1.26 (1.18)	4.96 (4.97)
GOM	3.0	32.64 (29.79)	7.82 (7.36)	1.33 (1.29)	5.00 (5.24)

b)

Method	$f_{\text{c},\upsilon}$ [Hz]	$\Delta\hat{\boldsymbol{x}}$ [%]	$\Delta\dot{\hat{\boldsymbol{x}}}$ [%]	$\Delta\ddot{\hat{\boldsymbol{x}}}$ [%]	$\Delta\hat{\boldsymbol{u}}_{\text{ext}}$ [%]
FJI	1.0	2.67 (2.17)	2.92 (2.42)	1.15 (0.98)	4.51 (3.79)
FJI	2.0	1.33 (1.16)	1.60 (1.42)	0.71 (0.62)	3.04 (2.91)
FJI	3.0	3.66 (2.75)	4.12 (3.22)	1.68 (1.35)	7.68 (7.42)
GOM	1.0	11.58 (10.30)	1.52 (1.41)	0.19 (0.16)	0.84 (0.81)
GOM	2.0	29.65 (27.04)	6.47 (6.04)	1.26 (1.18)	4.96 (4.97)
GOM	3.0	34.39 (32.82)	10.37 (8.73)	2.35 (2.21)	8.80 (8.75)

c)

Method	α_υ [−]	$\Delta\hat{\boldsymbol{x}}$ [%]	$\Delta\dot{\hat{\boldsymbol{x}}}$ [%]	$\Delta\ddot{\hat{\boldsymbol{x}}}$ [%]	$\Delta\hat{\boldsymbol{u}}_{\text{ext}}$ [%]
FJI	5.0	2.54 (2.09)	2.74 (2.32)	1.07 (0.93)	4.21 (3.59)
FJI	12.5	1.33 (1.16)	1.60 (1.42)	0.71 (0.62)	3.04 (2.91)
FJI	20.0	1.79 (1.50)	2.05 (1.79)	0.85 (0.75)	3.71 (4.03)
GOM	5.0	11.14 (9.73)	2.68 (2.73)	0.48 (0.40)	1.99 (1.99)
GOM	12.5	29.65 (27.04)	6.47 (6.04)	1.26 (1.18)	4.96 (4.97)
GOM	20.0	50.18 (49.74)	10.65 (9.51)	2.18 (2.11)	8.25 (8.33)

noise at the onset of the perturbation is negatively correlated with the movement velocity, the deviations from the averaged unbiased dynamics are larger for slow movements than they are for fast movements. As the performance of GOM is directly influenced by these deviations, the estimation accuracy is positively correlated with the different movement velocities. For $T_{\text{mov}} = 1\,\text{s}$, GOM outperforms FJI in all NRMSEs except $\Delta\hat{\boldsymbol{x}}$, for which the performance difference is decreased compared to Table 4.1. For $T_{\text{mov}} = 3\,\text{s}$, FJI outperforms GOM with slightly increased performance differences compared to Table 4.1.

Comparison - Neural Noise Cut-off Frequencies

The NRMSEs in Table 4.2b show that the performance of FJI is slightly decreased for lower and higher cut-off frequencies of the noise, with the latter resulting in slightly larger performance differences than the former. It seems that the lower cut-off frequency of the noise results in such a decreased cut-off frequency of the high pass filter, that it is too close to the frequency content of the unperturbed dynamics. For the higher cut-off frequency of the noise, the increased cut-off frequency of the high pass filter results in an increased information loss in the isolation of the feedback jerk. Despite these slight decreases in

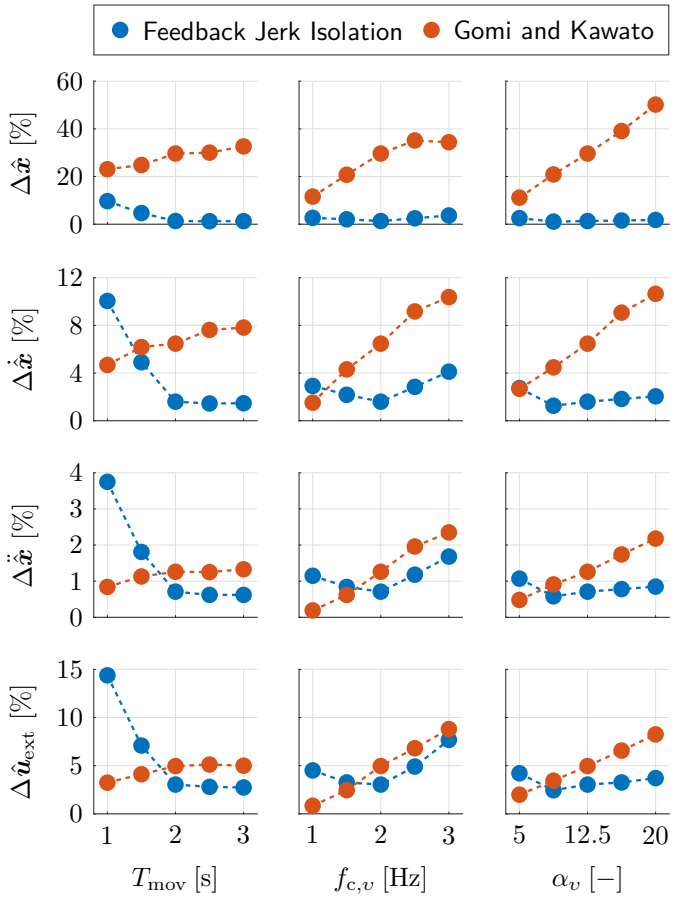

Figure 4.7.: Validation of feedback jerk isolation with simulated data. Mean results of the averaged NRMSEs of the estimated variational dynamics $\{\Delta\hat{\boldsymbol{x}}, \Delta\dot{\hat{\boldsymbol{x}}}, \Delta\ddot{\hat{\boldsymbol{x}}}, \Delta\hat{\boldsymbol{u}}_{\text{ext}}\}$ for alternative simulation configurations defined by movement durations T_{mov}, cut-off frequencies $f_{\text{c},\upsilon}$, and amplitudes α_υ.

performance, FJI still achieves high estimation accuracy for both alternative simulations. The performance of GOM is increased/decreased for lower/higher cut-off frequencies of the noise due to smaller/larger deviations from the averaged unbiased dynamics. For $f_{\text{c},\upsilon} = 1$ Hz, GOM outperforms FJI in all NRMSEs except $\Delta\hat{\boldsymbol{x}}$, for which the performance difference is decreased compared to Table 4.1. For $f_{\text{c},\upsilon} = 3$ Hz, FJI outperforms GOM with slightly increased performance differences compared to Table 4.1.

Comparison - Neural Noise Amplitudes

The NRMSEs in Table 4.2c illustrate that a lower amplitude of the noise has an almost identical effect on the performance as a lower cut-off frequency of the noise in Table 4.2b. In contrast, a higher amplitude has very different effects. For FJI, a higher amplitude only leads to a marginal performance decrease, much smaller than that in Table 4.2b. For GOM, it leads to a similar performance decrease as in Table 4.2b, except for $\Delta\hat{\boldsymbol{x}}$, for which the decrease is much larger. For $\alpha_\upsilon = 5$, the performance difference of FJI and GOM is almost identical to that of $f_{\text{c},\upsilon} = 1$ Hz in Table 4.2b. For $\alpha_\upsilon = 20$, FJI outperforms GOM with increased performance differences compared to Table 4.1, especially for $\Delta\hat{\boldsymbol{x}}$.

Table 4.3.: Validation of impedance estimation with simulated data. Mean (SD) results of the NAEs of the estimated BIP vector $\hat{\overline{\boldsymbol{\pi}}}$, damping $\hat{\overline{D}}_q$, and stiffness $\hat{\overline{K}}_q$.

Method	$\hat{\overline{\pi}}_1$ [%]	$\hat{\overline{\pi}}_2$ [%]	$\hat{\overline{\pi}}_3$ [%]	$\hat{\overline{D}}_{q,11}$ [%]	$\hat{\overline{D}}_{q,12}$ [%]	$\hat{\overline{D}}_{q,21}$ [%]	$\hat{\overline{D}}_{q,22}$ [%]
FJI	0.94	1.44	1.79	9.91 (1.48)	3.59 (1.29)	3.99 (1.03)	4.64 (0.91)
GOM	0.95	1.43	1.76	9.27 (1.99)	3.56 (1.52)	3.53 (1.43)	3.45 (1.05)

Method	$\hat{\overline{K}}_{q,11}$ [%]	$\hat{\overline{K}}_{q,12}$ [%]	$\hat{\overline{K}}_{q,21}$ [%]	$\hat{\overline{K}}_{q,22}$ [%]
FJI	10.21 (6.30)	6.23 (4.17)	6.23 (4.17)	6.21 (3.82)
GOM	20.22 (9.76)	12.53 (6.23)	11.97 (7.01)	11.94 (5.57)

Remark 4.9. The differences emphasize three issues: 1) For GOM, the estimation accuracy strongly depends on the similarity to the averaged unbiased dynamics. 2) For FJI, it depends more strongly on the frequency of the noise than it does on the amplitude, because of the influence on the cut-off frequency for the isolation of the feedback jerk by the high pass filter. 3) The performance difference in GOM due to a higher amplitude of the noise is larger than the performance difference in FJI due to a higher frequency of the noise, especially for $\Delta\hat{\boldsymbol{x}}$.

4.5.4. Impedance Estimation

The estimation accuracy of the impedance estimation is quantified using the normalized absolute errors (NAEs) of the estimated values. The normalizing values for the NAEs are either given by the real values of the elements of the BIP vector $\overline{\boldsymbol{\pi}}$ or the maximum real values of the elements of the damping $\overline{D}_q$ and stiffness $\overline{K}_q$, which are obtained by averaging the respective elements for the estimation interval $[0, T_{\text{est}}]$. For comparability of the results, we transform the inertial parameters in [52] to the elements of the BIP vector $\overline{\boldsymbol{\pi}}$.

In order to obtain additional means of comparing the overall performance of the methods, we calculate two additional performance criteria that are based on the Akaike information criterion (AIC) and the Bayesian information criterion (BIC). When comparing least squares fitted models (linear and non-linear), the AIC and the BIC are defined by the residual sum of squares (RSS) of the real values and the estimated model outputs:

$$\text{AIC} = 2p + h \ln(\text{RSS}) \ , \tag{4.29}$$

$$\text{BIC} = \ln(h)p + h \ln(\text{RSS}) \ , \tag{4.30}$$

$$\text{RSS} = \frac{1}{n} \sum_{i=1}^{n} \left(\sum_{j=1}^{h} \left(\vartheta_{i,j} - \hat{\vartheta}_{i,j} \right)^2 \right) , \tag{4.31}$$

where ϑ is the real value, $\hat{\vartheta}$ is the estimated model output, p is the number of parameters, h is the number of data points, and $n = 2$ is the dimensionality [135]. As we aim to compare the overall performance, we define the estimated model output $\hat{\vartheta}$ to be the simulation output that is obtained by inserting the estimated BIP vector $\hat{\overline{\boldsymbol{\pi}}}$, damping $\hat{\overline{D}}_q$, and stiffness $\hat{\overline{K}}_q$ into the neuromechanical model of the human arm (within the estimation interval $[0, T_{\text{est}}]$), and the real value ϑ to be the corresponding simulation output of the original simulation.

Table 4.4.: Validation of impedance estimation with simulated data. Mean (SD) results of the RSSs, AICs, and BICs of the variational external torques $\Delta\boldsymbol{\tau}_{\text{ext}}$.

Method	RSS [Nm^2]	AIC [−]	BIC [−]
FJI	8.10 (5.19)	$16.38 \cdot 10^3$ $(6.13 \cdot 10^3)$	$16.45 \cdot 10^3$ $(6.13 \cdot 10^3)$
GOM	17.31 (10.00)	$23.58 \cdot 10^3$ $(5.90 \cdot 10^3)$	$23.66 \cdot 10^3$ $(5.90 \cdot 10^3)$

Results

Table 4.3 contains the mean (SD) results of the NAEs of the estimated BIP vector $\hat{\boldsymbol{\pi}}$, damping $\hat{\overline{D}}_q$, and stiffness $\hat{\overline{K}}_q$. The NAEs of the elements of the estimated BIP vector $\hat{\boldsymbol{\pi}}$ do not possess SDs, because they are estimated with the complete data set of the static task. The NAEs of the three elements are all below 2% which indicates high estimation accuracy of the combination of the dynamic regressor representation with the data of the static task. The NAEs of the elements of the estimated damping $\hat{\overline{D}}_q$ and stiffness $\hat{\overline{K}}_q$ are approximately equal to or below 10% and demonstrate high estimation accuracy of the non-linear least squares estimation with the data of the dynamic task. The elements $\hat{\overline{D}}_{q,11}$ and $\hat{\overline{K}}_{q,11}$ possess slightly larger NAEs than the remaining elements of the respective matrices. This slight increase is plausible, as these two elements represent the contributions of the single-joint shoulder muscles, which are less involved due to less movement of the shoulder joint.

Comparison

The NAEs of the elements of the estimated BIP vector $\hat{\boldsymbol{\pi}}$ of GOM are almost identical to those of FJI. The mean NAEs of the elements of the estimated damping $\hat{\overline{D}}_q$ of GOM are marginally smaller than those of FJI and the opposite applies to the corresponding SDs which essentially makes these NAEs almost identical as well. In contrast, a considerable difference in estimation accuracy is found in the elements of the estimated stiffness $\hat{\overline{K}}_q$, for which both the mean NAEs and the SDs of GOM are larger than those of FJI, with the mean NAEs being approximately twice as large for GOM as they are for FJI. These results are plausible, as the difference in estimation accuracy of the variational dynamics $\{\Delta\boldsymbol{x}, \Delta\dot{\boldsymbol{x}}, \Delta\ddot{\boldsymbol{x}}, \Delta\boldsymbol{u}_{\text{ext}}\}$ is largest for the variational positions $\Delta\boldsymbol{x}$. Due to the correlations within the impedance estimation model (4.10), this difference directly influences the estimated stiffness $\hat{\overline{K}}_q$.

The mean (SD) results of the RSSs, AICs, and BICs are presented for the variational external torques $\Delta\boldsymbol{\tau}_{\text{ext}}$ in Table 4.4. FJI outperforms GOM in all three performance criteria. The difference in RSS is especially relevant, as it demonstrates, that the differences in AIC and BIC do not arise solely due to differences in the number of parameters p. Similar to the mean NAEs of the elements of the estimated stiffness $\hat{\overline{K}}_q$ in Table 4.3, the mean RSSs are approximately twice as large for GOM as they are for FJI.

Remark 4.10. The differences in RSSs, AICs, and BICs demonstrate that 1) the differences in the estimated BIP vector $\hat{\boldsymbol{\pi}}$, damping $\hat{\overline{D}}_q$, and stiffness $\hat{\overline{K}}_q$, represented by the respective NAEs in Table 4.3, have a substantial effect on the replicability of the real simulation output and that 2) the impedance estimation results of FJI yield a more accurate replication of the real simulation output than those of GOM.

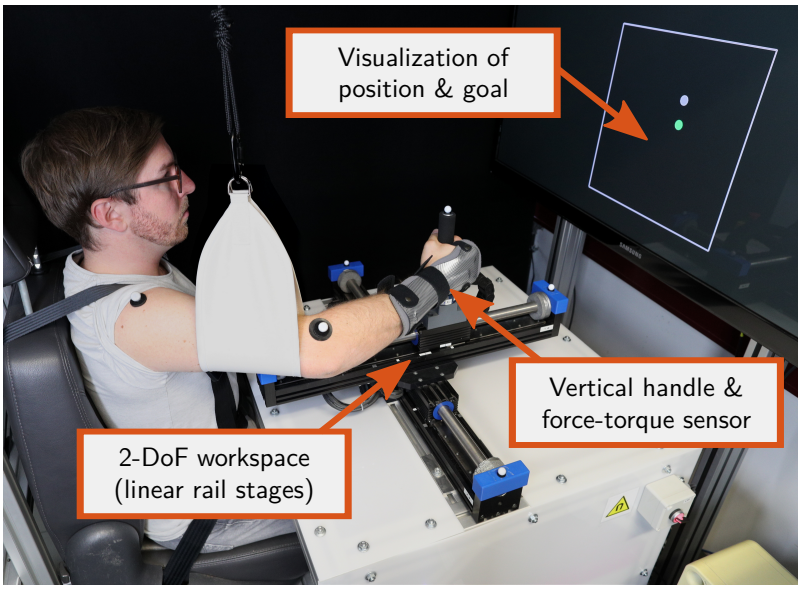

Figure 4.8.: Reenactment of an individual interacting with the apparatus during one of the three blocks of the dynamic task of the experiment. Informed written consent for the publication of this image was obtained from the individual.

4.6. Experiment

We conduct an experiment with 12 participants, in order to evaluate the performance of the proposed method on real data. The design of the experiment is almost identical to that of the simulation. However, in order to avoid predictability of the perturbations and adaptation of the participants, a randomized time interval is added before the onset of the perturbation in the static task. For the same reasons, the perturbed trials in the dynamic task are uniformly randomly distributed among the unperturbed trials. We evaluate the feedback jerk isolation in the form of the high pass filter configuration and the impedance estimation in the form of the estimated impedance components. Furthermore, we investigate the effects of different durations of the estimation interval on the estimated impedance components.

4.6.1. Apparatus

The apparatus is almost identical to the apparatus, which is presented in Section 3.6.1 and used to evaluate the Bayesian human motor behavior model in Section 3.6.4. The adapted variation of the apparatus, which is displayed in Fig. 4.8, contains multiple modifications. Six motion capture cameras (*Qualisys Miqus*) are available for tracking of passive markers. Additionally, a custom-built seat with shoulder belts, a novel sling attached to the ceiling, and a wrist orthosis are available to limit participant movements. Haptic interaction by means of participant force input is still enabled by the admittance control scheme defined in (3.40), but the values of the admittance inertia $M_{x,\mathrm{adm}}$ and damping $D_{x,\mathrm{adm}}$ are slightly adjusted to $M_{x,\mathrm{adm}} = \mathrm{diag}\{5, 5\}$ kg and $D_{x,\mathrm{adm}} = \mathrm{diag}\{20, 20\}$ Ns/m. Due to the increased high frequency precision requirements in terms of data processing, the signals are filtered using a seventh order Savitzky-Golay filter with a cut-off frequency of 50 Hz [109].

4.6.2. Experiment Design

The experiment design is almost identical to the simulation design. However, in order to avoid predictability of the perturbations, a randomized time interval with $T_{\text{random}} \in [1, 3]\,\text{s}$ is included before the onset of the perturbations in the static task. For the same reasons and to obtain both unperturbed and perturbed movements, the ratio of perturbed trials to total trials is set to 33 % and the perturbed trials are uniformly randomly distributed among the unperturbed trials in the dynamic task. In order to avoid effects of fatigue, the resulting 180 trials are performed in three consecutive blocks. Each of these blocks contains a total of 60 trials that consist of 20 perturbed and 40 unperturbed trials. In both tasks, the visual feedback of the position of the cart is deactivated during the perturbations.

Remark 4.11. Analogous to the results of the simulation, the results of the experiment are presented in within-, between-, or cross-subject mean (SD). As the majority of the results are cross-subject mean (SD) results, for simplicity, from this point on, these results are referred to simply as mean (SD) results.

4.6.3. Participants & Procedure

A total of 12 participants (9 male and 3 female) with between-subject mean (SD) age of 26.92 (3.40) years, height of 174.83 (7.38) cm, and weight of 69.43 (9.82) kg volunteered to participate in the experiment. All participants had normal or corrected-to-normal vision. All participants carried out the experiment with the right hand. One of the participants was left-handed and the remaining 11 participants were right-handed. Informed written consent was obtained from all participants before the experiment, which was conducted according to the principles in the Declaration of Helsinki. The research ethics were obtained from the ethics committee at the Technical University of Munich.

The participants were seated in front of the apparatus on a custom-built seat and their upper body was restrained by two shoulder belts in order to fix the position of the shoulder. Their upper arm was supported by a sling attached to the ceiling to constrain all motions to the horizontal plane and reduce effects of fatigue. In order to avoid wrist motions, the participants were wearing a wrist orthosis. Two passive motion capture markers were placed on shoulder and elbow to measure the lengths of the upper arm and the forearm.

In the beginning of the static task, the cart automatically moved to the first position at the bottom of the workspace. After the application of all 20 perturbations, it automatically moved to the next position, until all 100 perturbations were completed. Analogous to the simulation, each perturbation angle ϕ_{pert} was executed once in each of the positions and the order was randomized. The participants were informed about the procedure, including the perturbations and the randomized time interval before the onset of the perturbation. They were told that their objective was to naturally grasp the handle on top of the cart. Additionally, they were instructed to not voluntarily react to the perturbations in any way and not prepare for them in any kind of preemptive manner, e.g., by co-contraction.

In the beginning of the dynamic task, the cart automatically moved to the start position at the bottom of the workspace. As soon as it reached the bottom, the admittance turned on. As soon as the participants reached the goal position, represented by a dot at the top of the workspace, the admittance turned off and the cart automatically moved back down to the start position. This procedure was repeated until all 60 trials with 20 uniformly randomly

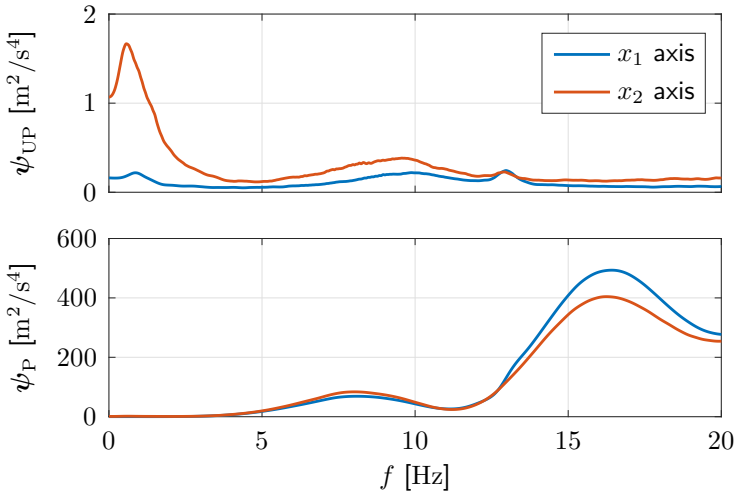

Figure 4.9.: High pass filter configuration based on experimental data. Mean results of the ESDs $\boldsymbol{\psi}_{\mathrm{UP}}$ and $\boldsymbol{\psi}_{\mathrm{P}}$ of the unperturbed and perturbed movements.

distributed perturbed trials were completed. In total, three of these blocks of trials were completed for a total of 180 trials. Analogous to the simulation, each perturbation angle ϕ_{pert} was executed three times and the order was randomized. The participants were informed about the procedure, including the perturbations and their random distribution. They were told that their objective was to naturally grasp the handle on top of the cart and move it from the start position to the goal position. They were told that the duration of the movement should be approximately 2 s. In order to help them properly adjust their movement velocity, a beep sound occurred after 2 s. The participants were informed that they were allowed to voluntarily react to the perturbations. Additionally, they were instructed to not prepare for the perturbations in any kind of preemptive manner, e.g., by co-contraction.

4.6.4. Evaluation

In the experiment, every trial is either unperturbed or perturbed. Consequently, we do not possess unperturbed ground truth for the perturbed movements and can not evaluate the estimation accuracy of the variational dynamics $\{\Delta\boldsymbol{q}, \Delta\dot{\boldsymbol{q}}, \Delta\ddot{\boldsymbol{q}}, \Delta\boldsymbol{\tau}_{\mathrm{ext}}\}$. Thus, we only evaluate the feedback jerk isolation in terms of the cut-off frequencies $\boldsymbol{f}_{\mathrm{c,HP}}$ of the high pass filter. Additionally, we evaluate the applicability to real data of the impedance estimation in terms of the estimated impedance parameters $\hat{\overline{\boldsymbol{\pi}}}$, $\hat{\overline{D}}_q$, and $\hat{\overline{K}}_q$ and analyze the effects of different durations of the estimation interval T_{est}. For simplicity, from this point on, we omit the term estimated when referring to the results of the impedance estimation.

Evaluation Feedback Jerk Isolation

Fig. 4.9 shows the mean results of the ESDs $\boldsymbol{\psi}_{\mathrm{UP}}$ and $\boldsymbol{\psi}_{\mathrm{P}}$, which look very similar to those of the simulation presented in Fig. 4.5a. In the unperturbed movements, the energy of the principal movement along the x_2 axis is more widespread than in the simulation. However, the respective ESD $\psi_{\mathrm{UP},2}$ nonetheless possesses a peak at a similar frequency. The ESD $\psi_{\mathrm{UP},1}$ is substantially lower, due to the absence of movements along the x_1 axis. Due to hardware noise, the energy of both axes of the unperturbed movements does not decrease to values

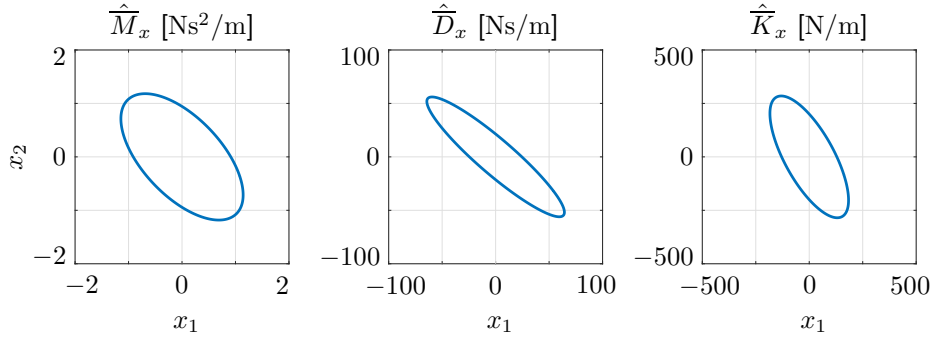

Figure 4.10.: Evaluation of impedance estimation with experimental data. Endpoint ellipses of the mean Cartesian inertia $\hat{\overline{M}}_x$, damping $\hat{\overline{D}}_x$, and stiffness $\hat{\overline{K}}_x$, derived from the mean BIP vector $\hat{\overline{\boldsymbol{\pi}}}$, damping $\hat{\overline{D}}_q$, and stiffness $\hat{\overline{K}}_q$, respectively.

as low as those of the simulation for high frequencies. However, the respective values are nonetheless substantially smaller than those of the perturbed movements, for which the energy increases to substantially higher values for high frequencies. The respective ESDs $\boldsymbol{\psi}_{\mathrm{P}}$ are substantially higher than those of the unperturbed movements and possess multiple peaks in the high frequency range. The between-subject mean (SD) results of the cut-off frequencies $\boldsymbol{f}_{\mathrm{c,HP}} = [1.45\ (0.30), 2.09\ (0.24)]$ Hz are very similar to those of the simulation. Thus, analogous to the results of the simulation, the cut-off frequency $f_{\mathrm{c,HP},2}$ is sufficiently high to lie above the energy of the principal movement.

Remark 4.12. While the overall energy of the unperturbed movements in the experiment is slightly decreased compared to the simulation, the overall energy of the perturbed movements is increased. This difference is largely caused by high frequency oscillations in the jerks $\dddot{\boldsymbol{x}}$ of the perturbed movements, which result from oscillations due to perturbations paired with sensor noise and high gain PD control.

Evaluation Impedance Estimation

Table 4.5 lists the within- and cross-subject mean (SD) results of the impedance estimation. Analogous to the estimation results with simulated data in Table 4.3, the elements of the BIP vector $\hat{\overline{\boldsymbol{\pi}}}$ do not possess SDs, because they are estimated with the complete data set of the static task. The elements of the mean BIP vector $\hat{\overline{\boldsymbol{\pi}}}$ are similar to the respective values in the simulation $\boldsymbol{\pi}_{\mathrm{sim}} = [0.1945, 0.0737, 0.0838]$. The first element $\hat{\overline{\pi}}_1$ is decreased compared to the respective value in the simulation. As this element largely depends on the inertial characteristics of the upper arm, the difference could be caused by the comparatively little movement of the shoulder joint which results in less involvement of the upper arm. As the inertial parameters in [52] are defined by the linearized rigid body dynamics, the respective estimation results can not be used for comparison. Thus, we insert the elements of the mean BIP vector $\hat{\overline{\boldsymbol{\pi}}}$ and the arm configuration $\boldsymbol{q}$ in (4.1) to calculate the mean inertia $\hat{\overline{M}}_q$. Subsequently, we transform the mean inertia $\hat{\overline{M}}_q$ to Cartesian space using (2.29) and the Jacobian matrix J_x. The elements of the resulting mean Cartesian inertia $\hat{\overline{M}}_x$ are similar to those reported in existing studies [101, 103, 104]. Consequently, the same applies to the corresponding endpoint ellipse, which is illustrated in Fig. 4.10.

Table 4.5.: Evaluation of impedance estimation with experimental data. Within-subject mean (SD) results of the BIP vector $\hat{\overline{\boldsymbol{\pi}}}$, damping $\hat{\overline{D}}_q$, and stiffness $\hat{\overline{K}}_q$.

#	$\hat{\overline{\pi}}_1$ [kgm^2]	$\hat{\overline{\pi}}_2$ [kgm^2]	$\hat{\overline{\pi}}_3$ [kgm^2]	$\hat{\overline{D}}_{q,11}$ [Nms/rad]	$\hat{\overline{D}}_{q,12}$ [Nms/rad]	$\hat{\overline{D}}_{q,21}$ [Nms/rad]	$\hat{\overline{D}}_{q,22}$ [Nms/rad]
01	0.0817	0.0582	0.0581	9.00 (0.19)	1.97 (0.08)	2.09 (0.13)	1.18 (0.16)
02	0.0890	0.0787	0.0780	8.68 (0.25)	2.19 (0.11)	2.47 (0.05)	1.92 (0.11)
03	0.1648	0.1021	0.0938	12.64 (0.23)	2.43 (0.12)	2.87 (0.06)	2.49 (0.04)
04	0.1074	0.0751	0.0714	9.08 (0.27)	2.01 (0.09)	2.10 (0.04)	1.56 (0.08)
05	0.0759	0.0877	0.0734	10.44 (1.01)	3.11 (0.36)	3.30 (0.20)	2.30 (0.14)
06	0.2099	0.0923	0.1076	12.70 (0.24)	2.14 (0.21)	2.86 (0.10)	1.98 (0.08)
07	0.1207	0.0677	0.0613	9.24 (0.21)	2.44 (0.26)	2.39 (0.10)	1.58 (0.07)
08	0.0887	0.0671	0.0692	8.07 (0.21)	2.08 (0.08)	2.13 (0.05)	1.72 (0.08)
09	0.2229	0.0838	0.1073	9.27 (0.55)	1.29 (0.19)	1.84 (0.12)	1.86 (0.05)
10	0.0777	0.0501	0.0509	6.61 (0.11)	1.28 (0.06)	1.28 (0.07)	1.03 (0.03)
11	0.1164	0.0918	0.0894	10.15 (0.35)	2.15 (0.04)	2.73 (0.02)	2.35 (0.05)
12	0.1558	0.0646	0.0702	8.15 (0.11)	1.32 (0.07)	1.74 (0.06)	1.34 (0.05)
Mean	0.1259	0.0766	0.0776	9.50 (0.31)	2.03 (0.14)	2.32 (0.08)	1.78 (0.08)

#	$\hat{\overline{K}}_{q,11}$ [Nm/rad]	$\hat{\overline{K}}_{q,12/21}$ [Nm/rad]	$\hat{\overline{K}}_{q,22}$ [Nm/rad]
01	2.77 (1.92)	4.54 (2.61)	7.75 (4.03)
02	33.66 (6.23)	1.24 (2.19)	16.34 (3.90)
03	38.30 (11.12)	6.82 (2.99)	13.88 (4.17)
04	12.46 (2.96)	13.43 (1.67)	15.40 (2.10)
05	36.84 (23.14)	14.87 (4.28)	20.00 (3.95)
06	67.15 (15.12)	18.19 (4.11)	17.62 (1.95)
07	19.02 (10.65)	11.78 (8.73)	19.06 (5.76)
08	30.30 (8.02)	1.04 (1.40)	7.60 (2.25)
09	47.23 (34.71)	0.00 (0.00)	6.63 (1.04)
10	2.50 (1.24)	4.68 (1.81)	8.96 (2.57)
11	34.84 (7.62)	1.27 (1.37)	17.24 (1.35)
12	14.58 (4.91)	7.31 (2.31)	10.55 (2.19)
Mean	28.30 (10.64)	7.10 (2.79)	13.42 (2.94)

The elements of the mean damping $\hat{\overline{D}}_q$ are similar to the respective averaged values in the simulation $D_{q,\mathrm{sim}} = [2.42, 1.20, 1.20, 1.42]$, with the exception of the element $\hat{\overline{D}}_{q,11}$, which is comparatively large. As this element represents the contributions of the single-joint shoulder muscles, which are less involved due to less movement of the shoulder joint, it is more difficult to estimate. This correlation is also visible in the increased estimation error in the validation with simulated data (see Table 4.3). As the remaining elements are decreased compared to the respective values in the simulation, it is possible that some of the contributions of these elements are allocated to the element $\hat{\overline{D}}_{q,11}$. As the damping results of [52] are not reported,

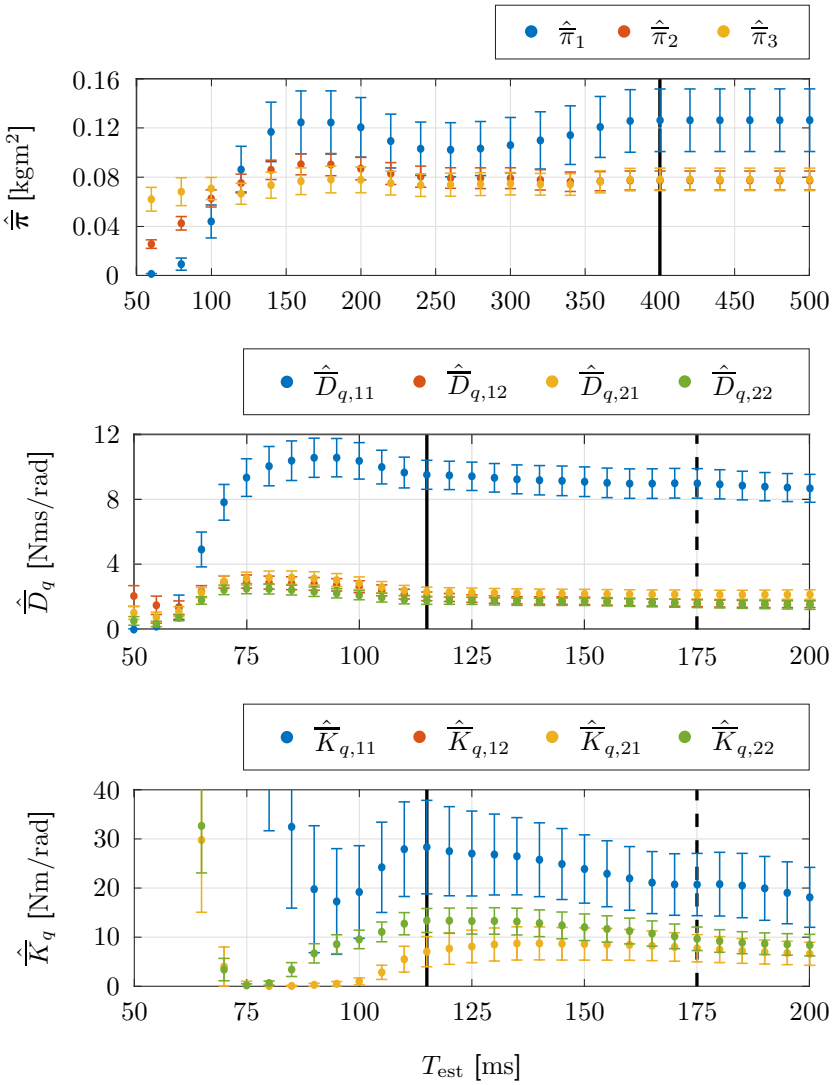

Figure 4.11.: Evaluation of impedance estimation with experimental data. Between-subject mean (SD) results of the BIP vector $\hat{\bar{\boldsymbol{\pi}}}$, damping $\hat{\bar{D}}_q$ and stiffness $\hat{\bar{K}}_q$ for different durations of the estimation interval T_{est}. The error bars represent $\pm$ 0.5 between-subject SD. The solid vertical lines indicate the durations of the estimation intervals (static task: $T_{\text{est}} = 400$ ms, dynamic task: $T_{\text{est}} = 115$ms). The dashed vertical lines represent the ends of the perturbations. For the static task, the solid and the dashed line coincide.

we can not use them for comparison. However, the elements of the mean damping $\hat{\bar{D}}_q$ are of similar order of magnitude as the estimation results reported for static tasks [65, 101]. The overall increase in magnitude compared to the estimation results of these static tasks is to be expected, as similar correlations are observed for estimates of stiffness [52].

The elements of the mean stiffness $\hat{\bar{K}}_q$ are similar to the respective averaged values in the simulation $K_{q,\text{sim}} = [29.05, 14.37, 14.37, 17.08]$, with the elements $\hat{\bar{K}}_{q,12/21}$ being slightly decreased in comparison. Consequently, the elements of the mean stiffness $\hat{\bar{K}}_q$ are also similar to those reported for comparable dynamic tasks [122–124], including those reported for the

dynamic task in [52]. The difference in SDs of the stiffness $\overline{\hat{K}}_q$ and the damping $\overline{\hat{D}}_q$ fits to the difference in estimation errors in the validation with simulated data (see Table 4.3). It could however also indicate that variations in damping during the course of the experiment are generally lower than those in stiffness or that some variations in damping are incorrectly interpreted as variations in stiffness by the non-linear least squares estimation.

Fig. 4.10 shows the endpoint ellipses of the mean Cartesian inertia $\overline{\hat{M}}_x$, damping $\overline{\hat{D}}_x$, and stiffness $\overline{\hat{K}}_x$. The shapes and orientations of the ellipses are similar to those in existing studies [21, 101, 123]. Similar to the results for the movements along the sagittal axis in [52], the major axis of the endpoint ellipse of the mean Cartesian stiffness $\overline{\hat{K}}_x$ is oriented slightly more parallel to the x_2 axis, i.e., the axis of the principal movement.

Fig. 4.11 shows the between-subject mean (SD) results of the BIP vector $\overline{\hat{\boldsymbol{\pi}}}$, damping $\overline{\hat{D}}_q$, and stiffness $\overline{\hat{K}}_q$ for different durations of the estimation interval T_{est}. In the static task, the elements of the BIP vector $\overline{\hat{\boldsymbol{\pi}}}$ converge to constant values for durations $T_{\text{est}} > 400$ ms. Similar behavior is observable in the dynamic task for the elements of the damping $\overline{\hat{D}}_q$, with a slight decrease for durations $T_{\text{est}} > 115$ ms. In comparison, the elements of the stiffness $\overline{\hat{K}}_q$ converge at a slower rate and require a longer estimation interval duration T_{est} in order to reach plausible values. Furthermore, the decrease for durations $T_{\text{est}} > 115$ ms is larger for the elements of the stiffness $\overline{\hat{K}}_q$ than for the elements of the damping $\overline{\hat{D}}_q$.

Remark 4.13. The decrease of the elements of the stiffness $\overline{\hat{K}}_q$ for durations $T_{\text{est}} > 115$ ms could be caused by the return to the unperturbed states. The longer the estimation interval, the larger the percentage of the variational data with small deviations from the unperturbed states, i.e., the more influence the respective values of the elements of the stiffness $\overline{\hat{K}}_q$ have on the non-linear least squares solution. The decrease could however also be caused by the activation of voluntary feedback contributions.

4.7. Discussion

The mean results of the impedance estimation for different durations T_{est} in Fig. 4.11 show that the elements of the damping $\overline{\hat{D}}_q$ and stiffness $\overline{\hat{K}}_q$ reach plausible values for the estimation interval with duration $T_{\text{est}} = \delta_{\text{FBv}} = 115$ ms. While the elements of the damping $\overline{\hat{D}}_q$ already reach plausible values at $T_{\text{est}} \approx 75$ ms, the information necessary for estimation of plausible values of the elements of the stiffness $\overline{\hat{K}}_q$ is not reached until $T_{\text{est}} \approx 110$ ms. The mean results in Fig. 4.11 also show that the elements of the BIP vector $\overline{\hat{\boldsymbol{\pi}}}$ converge to plausible values for the estimation interval with duration $T_{\text{est}} = 400$ ms. These results, in combination with the mean (SD) results in Table 4.5, which are similar to those reported for comparable dynamic tasks, successfully demonstrate the applicability of our method to real data.

We model the involuntary feedback behavior by a linearized model. This approximation is analogously applied in comparable studies [28, 122, 123] that include deviations of similar size or larger than the ones in this work. In our static task, the position perturbations with amplitudes of 8 mm result in mean (SD) maximum external force deviations of 4.75 (1.80) N. In our dynamic task, the force perturbations evoke mean (SD) maximum position deviations of 3.53 (0.34) mm and external force deviations of 9.48 (3.05) N. The mean (SD) results of

the NAEs in Table 4.3 show that the estimation errors of the elements of the BIP vector $\hat{\overline{\boldsymbol{\pi}}}$ are almost identical for the dynamic regressor representation and the linearized rigid body dynamics of [52]. This indicates that the variational dynamics $\{\Delta\boldsymbol{q}, \Delta\dot{\boldsymbol{q}}, \Delta\ddot{\boldsymbol{q}}, \Delta\boldsymbol{\tau}_{\text{ext}}\}$ of the static task are sufficiently small to enable linearization of the rigid body dynamics without loss of estimation accuracy and thus supports the assumption that the involuntary feedback behavior evoked by the force perturbations can be approximated by a linearized model.

The mean (SD) results of the NRMSEs in Table 4.1 show that our feedback jerk isolation achieves higher estimation accuracy for the variational dynamics $\{\Delta\hat{\boldsymbol{x}}, \Delta\hat{\dot{\boldsymbol{x}}}, \Delta\hat{\ddot{\boldsymbol{x}}}, \Delta\hat{\boldsymbol{u}}_{\text{ext}}\}$ than the methods reported in [52] and [53]. The difference in estimation accuracy is especially large for the variational positions $\Delta\hat{\boldsymbol{x}}$. As a consequence, the estimation performance of the impedance estimation is increased for the elements of the stiffness $\hat{\overline{K}}_q$, which is shown by the mean (SD) results of the NAEs in Table 4.3. The mean (SD) results of the NRMSEs for different simulation configurations in Tables 4.2a - 4.2c show that the estimation accuracy of the feedback jerk isolation is decreased for a higher movement velocity. This is plausible, as a higher movement velocity coincides with an increased cut-off frequency of the high pass filter which causes an increased information loss in the isolation of the feedback jerk. Due to similar reasons, a higher cut-off frequency of the neural noise also leads to a decrease of the estimation accuracy. For all of the remaining simulation configurations, changes in the estimation accuracy are marginal. While the estimation accuracy of the method in [52] is similarly decreased for a higher neural noise cut-off frequency, it is contrastingly increased for a higher movement velocity. As this method depends on the similarity of the movement to the averaged unbiased dynamics, an increase of the amplitude of the neural noise leads to a significant decrease of estimation accuracy, especially in the variational positions $\Delta\hat{\boldsymbol{x}}$. In summary, while the feedback jerk isolation is outperformed by the method in [52] for movements with high velocity and low movement variance, it provides superior estimation performance for movements with moderate to low velocity and moderate to high movement variability, as it is much less affected by a decrease in the similarity of the movements.

According to the main ISO safety standard DIN EN ISO 10218-1:2011 for robots and robotic devices, the maximum robot end-effector velocity during collaboration with a human must not exceed 250 mm/s [136]. Some studies on safe physical human-robot collaboration use more conservative values for the maximum robot end-effector velocity, e.g., 150 mm/s in [137] and 100 mm/s in [138]. In the original configuration simulation used to obtain the NRMSEs in Table 4.2a, the mean (SD) peak velocities $\dot{x}_{\max}$ that correspond to the different durations of the movements T_{mov} are 747.8 (6.3) mm/s for $T_{\text{mov}} = 1$ s, 377.6 (8.9) mm/s for $T_{\text{mov}} = 2$ s, and 254.0 (9.8) mm/s for $T_{\text{mov}} = 3$ s. Thus, the peak velocities $\dot{x}_{\max}$ of those movements, for which the method in [52] outperforms the feedback jerk isolation, are much higher than the current constraints for safe physical HRI. For those movements with peak velocities $\dot{x}_{\max}$ that are either similar to or moderately increased compared to the current constraints, the feedback jerk isolation achieves superior estimation performance. As the neural noise parameters in the simulation are defined to yield movement variability similar to that observed in repetitive, straight reaching movements [37] and both neural and kinematic variability are shown to be interrelated individual characteristics [139], it is unlikely that realistic physical HRI scenarios possess a lower amount of movement variability. Thus, based on these circumstances, we conclude that the feedback jerk isolation is well suited for our envisaged application in experiments that emulate realistic physical HRI.

Multiple studies present impedance estimation methods based on Kalman filters [140, 141] or extended Kalman filters [142]. The advantage of these filters is that, given continuous observations of the relevant variables, they allow for estimation of time-varying values of damping and stiffness. However, their application requires a model of the complete system dynamics, including feedforward and voluntary feedback behavior (if the respective method is used for a duration that is longer than the delay of voluntary feedback). Some studies avoid these limitations by assuming that the combination of feedforward and feedback behavior can be modeled by the sum of damping and stiffness [141] or just stiffness [142]. In [140], the authors assume that effects of feedforward and voluntary feedback behavior are neglectable due to application of pseudo-random perturbations in combination with a band pass filter. However, the plausibility of these assumptions in regard to realistic human motor behavior is not validated, as the method is only applied to a simulation that models the combination of feedforward and feedback behavior by the sum of damping and stiffness. Thus, existing impedance estimation methods based on Kalman filters are extremely limited in possible application scenarios and the application to realistic physical HRI would require substantially more complex models. While our method is not able to provide time-varying values of damping and stiffness, it is able to provide accurate estimates within a limited interval without the need for modeling feedforward and voluntary feedback behavior.

4.8. Summary

In this chapter, we present a method for the estimation of the impedance components in experiments that emulate realistic physical HRI scenarios. We apply force perturbations during multi-joint human arm movements that are designed such that the evoked feedback jerk frequency content can be isolated with a high pass filter. We limit the duration of the estimation interval to 115 ms to guarantee exclusion of voluntary feedback. We estimate the inertial parameters in a static postural task and subsequently insert them to estimate the damping and stiffness in a dynamic movement task. The evaluation of the experimental data shows that our method is able to provide plausible impedance estimates within the limited estimation interval that guarantees exclusion of voluntary feedback. Furthermore, the validation with simulated data shows that it provides superior estimation performance compared to the results obtained by application of existing impedance estimation methods within identical conditions. As the difference in estimation accuracy is especially large for the variational positions, the estimation performance is increased for the elements of the stiffness. The analysis of different movement velocities and variations of neural noise shows that the feedback jerk isolation is able to provide superior estimation performance for movements with moderate to low velocity and is much less affected by an increase in movement variability. We conclude that our method allows for impedance estimation in experiments that emulate realistic physical HRI scenarios, without the need for assumptions concerning voluntary feedback behavior or inclusion of the do-not-intervene-voluntarily paradigm or comparable constraints within the respective dynamic movement tasks. This facilitates the envisaged acquisition of comprehensive knowledge of human arm impedance characteristics.

Coactivation Modulation Model for Cooperative Physical HHI

5.

Humans are capable of adapting their motor behavior during physical interaction with a human partner to accomplish shared objectives. From carefully supporting a child in its first steps to seamlessly coordinating such complex interactions as acrobatics, humans achieve intuitive and efficient cooperation through precise regulation of exchanged forces and skillful modulation of muscle coactivation. The analysis of such muscle coactivation modulation strategies enables the design of optimal control strategies for physical HRI that maximize intuitiveness and efficiency. However, despite the availability of comprehensive knowledge concerning non-physical and physical interaction with the environment, little is currently known about modulation of muscle coactivation during physical HHI. Therefore, in this chapter, we address the third of the crucial open challenges in the consideration of human impedance characteristics in the control design process for physical HRI by focusing on the information alteration. More specifically, we analyze impedance modulation strategies of human dyads during physical interaction by investigating and modeling the modulation of muscle coactivation during cooperative physical HHI. We perform an experiment, in which two individuals track pseudo-random movements of a shared target, while being physically coupled by a virtual spring. As we aim to investigate qualitative correlations of modulation of muscle coactivation, in order to avoid confounds due to multi-joint muscle interactions, instead of focusing on the complete upper limb, we constrain the possible movements to wrist flexion/extension movements. Each individual is provided with distinct visual feedback of his/her wrist position and the target position and cannot see the visual feedback of the partner. During the course of the experiment, the individuals each experience two different levels of visual noise in their respective visual feedback of the target position. Due to this difference, we are able to observe how the resulting different levels of tracking performance affect modulation of muscle coactivation in both individuals. In order to describe the motor behavior adaptation of the individuals, both during individual and dyadic task execution, we extend the physiological representativeness of the neuromechanical goal sharing model of [49] by separating reciprocal muscle activation and muscle coactivation and proposing three different variations of a muscle coactivation modulation model. In order to evaluate the functionality of the three different variations of the muscle coactivation modulation model, we implement a simulation that emulates the conditions in our experiment.

The remainder of this chapter is structured as follows: related work and open problems are reviewed in Section 5.1. The neuromechanical modeling is performed in Section 5.2. The three variations of the coactivation modulation model are introduced in Section 5.3. The details of the experiment as well as the obtained results and the corresponding statistics are presented in Section 5.4. The details of the simulation and the obtained results are presented in Section 5.5. The plausibility and the limitations of the coactivation modulation model are discussed in Section 5.6 and the results are summarized in Section 5.7.

5.1. Related Work and Open Problems

During the execution and the simultaneous motor learning of a desired motor behavior, kinematic errors due to effects that are not accounted for by the feedforward component are counteracted by increases in limb stiffness [31, 32]. If these unaccounted effects are predictable and therefore also learnable, they can be incorporated into the internal models and the corresponding feedforward component [33, 34]. As this motor adaptation progresses and the kinematic errors decrease, muscle coactivation is gradually decreased to minimize metabolic cost [35,36]. If the effects are unpredictable and therefore also unlearnable, muscle coactivation remains at an increased level [37, 38]. As the increase in muscle coactivation is positively correlated with the kinematic error, motor behaviors with high accuracy demands result in larger increases in muscle coactivation [41, 42].

Multiple studies provide modeling approaches that characterize these motor adaptation correlations. In [35], modulation of muscle coactivation is modeled to depend on changes in muscle length, and the correlation characteristics are defined by a continuous piecewise linear function. This function depends on the kinematic error, consists of two segments with positive slopes, one for negative and one for positive kinematic errors, and includes a negative intercept to incorporate the minimization of metabolic cost. In [143], the interdependencies are modeled as a greedy optimization process that minimizes a cost function that is defined by the weighted sum of kinematic error and metabolic cost. In [48], modulation of muscle coactivation is modeled as a stochastic optimization process that minimizes internal model prediction uncertainties, in combination with kinematic error and metabolic cost demands. While providing general models for modulation of muscle coactivation during non-physical and physical interaction with the environment, these studies do not investigate how and to which extent physically interacting individuals modulate muscle coactivation.

The authors of [144] investigate motor behavior adaptation during cooperative physical HHI by performing an experiment, in which two individuals track pseudo-random movements of a shared target, both individually and while physically coupled by a virtual elastic band. The experimental data shows the motor behavior adaptations to be mutually beneficial, meaning that the tracking performance improves for both the superior and the inferior of the two individuals. The authors of [145] demonstrate that these mutual performance improvements can be explained by the interpersonal goal integration model. It assumes that physically interacting individuals are able to estimate the partner's desired position, i.e., the partner's estimate of the target position, based on a spontaneously formed internal model of the partner's motor behavior and exchanged haptic information. By exploiting the respective estimation uncertainties to optimally combine this estimate with their own estimate of the target position, both of the two individuals are able to derive an improved overall estimate of the target position that allows for improvement in tracking performance. While these two studies investigate and model behavior adaptation during cooperative physical HHI, they do not examine the corresponding modulation of muscle coactivation.

In order to examine how the compliance of the coupling mechanics influences the exchange of haptic information between the physically interacting individuals, the authors of [49] perform a variation of the previous experiment [145], in which the stiffness of the virtual band is modified. The experimental data shows the improvement in tracking performance to be negatively correlated with the compliance of the coupling mechanics. The interpersonal goal integration model is modified to obtain the neuromechanical goal sharing model, which

incorporates the additional tracking error due to the compliance of the coupling mechanics in the form of additional estimation uncertainty in the estimate of the partner's desired position. Surface EMG data from wrist flexion/extension muscle pairs is used to measure muscular effort. For a hard virtual coupling with low coupling compliance, muscular effort is increased, with the increase being larger for the superior partner than for the inferior. Similar correlations apply for medium and soft virtual couplings, with the increase being negatively correlated with the coupling compliance. The neuromechanical goal sharing model is able to reproduce these changes in muscular effort. However, both the analysis of the experimental data as well as the simulated model do not differentiate between reciprocal muscle activation and muscle coactivation and therefore do not provide explicit information regarding modulation of muscle coactivation during cooperative physical HHI. Furthermore, the study does not examine how muscular effort is modulated depending on the sensory information perceived by each partner, i.e., the level of uncertainty in each partner.

In a recent study [146], variations of the previous experiments [49, 145] are performed, in which individuals are able to exploit a novel control mechanism to modulate the stiffness of the virtual elastic band while physically interacting with a robotic partner. This control mechanism implements a negatively correlated functional dependency of muscle coactivation and the compliance of the coupling mechanics. The experiment contains multiple conditions with different levels of visual noise in the visual feedback of the tracking task and different levels of haptic noise in the haptic behavior of the robotic partner. The experimental data demonstrates that individuals learn to use the novel control mechanism to modulate the coupling compliance such that the adverse effects of perturbations are minimized and the beneficial effects of information are maximized. In conditions with visual noise, individuals increase muscle coactivation in order to decrease the coupling compliance and maximize the beneficial effects of haptic information. In conditions with haptic noise, individuals decrease muscle coactivation in order to increase the coupling compliance and minimize the adverse effects of haptic perturbations. While this study provides valuable insights on modulation of muscle coactivation when it is directly linked to the compliance of the coupling mechanics with a robotic partner, it remains unknown whether similar correlations apply during dyadic physical interaction without this control mechanism with a human partner. Therefore, in this chapter, we perform an experiment without this novel control mechanism, in which the physically interacting individuals experience two different levels of visual noise and place specific focus on analyzing and modeling modulation of muscle coactivation. Due to the difference in visual noise, we are able to observe how the resulting difference in tracking performance affects modulation of muscle coactivation in both individuals.

5.2. Tracking Task Dynamics

In this section and the following section, we present a neuromechanical model that describes the respective motor behavior adaptations of two individuals that use wrist flexion/extension movements to track random movements of a shared target, both individually and while being physically coupled by a virtual spring.

Remark 5.1. The neuromechanical model represents the motor behavior in the form of a one dimensional discrete-time system and is based on the neuromechanical goal sharing model presented in [49], with the novelty lying in the differentiation of reciprocal activation

and coactivation as well as the introduction of three different variations of the associated coactivation modulation model.

The dynamics of the tracking task are modeled as a one dimensional discrete-time system with $t = \kappa\, t_\mathrm{s},\ \kappa = 1, 2, \ldots, h$, where t is the time, t_s is the sample time, κ is the sample index, and h is the maximum number of samples. The random movements of the target are assumed to be caused by zero mean Gaussian white noise in its angular acceleration and the target dynamics are modeled as a first order system:

$$\boldsymbol{\theta}_{\mathrm{t},\kappa+1} = A\boldsymbol{\theta}_{\mathrm{t},\kappa} + \boldsymbol{\omega}_\kappa \tag{5.1}$$

with

$$\boldsymbol{\omega}_\kappa \in \mathcal{N}\left(\boldsymbol{\omega} \,\middle|\, \mathbf{0}, \Omega\right), \quad \Omega = \mathsf{E}\left[\boldsymbol{\omega}\boldsymbol{\omega}^\mathsf{T}\right] \tag{5.2}$$

and

$$A = \begin{bmatrix} 1 & t_\mathrm{s} \\ 0 & 1 \end{bmatrix}, \quad \boldsymbol{\theta}_\mathrm{t} = \begin{bmatrix} \theta_\mathrm{t} \\ \dot{\theta}_\mathrm{t} \end{bmatrix}, \tag{5.3}$$

where θ_t is the target angle and $\dot{\theta}_\mathrm{t}$ is the target angular velocity. The variables $\boldsymbol{\omega}$ and Ω are the process noise vector and covariance matrix, respectively. Given the corresponding process noise variance σ_ω^2, the process noise covariance matrix Ω is given by

$$\Omega = \sigma_\omega^2 \begin{bmatrix} t_\mathrm{s}^4/4 & t_\mathrm{s}^3/2 \\ t_\mathrm{s}^3/2 & t_\mathrm{s}^2 \end{bmatrix}. \tag{5.4}$$

Analogous to the target dynamics (5.1), the wrist dynamics of the wrist flexion/extension movements are likewise modeled as a first order system:

$$\boldsymbol{\theta}_{\mathrm{w},\kappa+1} = A\boldsymbol{\theta}_{\mathrm{w},\kappa} + \boldsymbol{b}\left(\tau_{\mathrm{RA},\kappa} + \tau_{\mathrm{CA},\kappa} + \tau_{\mathrm{VC},\kappa}\right) \tag{5.5}$$

with

$$\boldsymbol{b} = \begin{bmatrix} 0 \\ t_\mathrm{s}/\iota \end{bmatrix}, \quad \boldsymbol{\theta}_\mathrm{w} = \begin{bmatrix} \theta_\mathrm{w} \\ \dot{\theta}_\mathrm{w} \end{bmatrix}, \tag{5.6}$$

where θ_w is the wrist angle, $\dot{\theta}_\mathrm{w}$ is the wrist angular velocity, ι is the moment of inertia, and τ_VC is the torque due to the virtual coupling. In contrast to the model presented in [49], the muscle activation torques are split up into the torque due to reciprocal activation τ_RA and the torque due to coactivation τ_CA. Subtracting the target dynamics (5.1) from the wrist dynamics (5.5) yields the full state equation of the tracking dynamics:

$$\boldsymbol{\chi}_{\kappa+1} = A\boldsymbol{\chi}_\kappa + \boldsymbol{b}\left(\tau_{\mathrm{RA},\kappa} + \tau_{\mathrm{CA},\kappa} + \tau_{\mathrm{VC},\kappa}\right) - \boldsymbol{\omega}\ , \tag{5.7}$$

which is defined based on the corresponding state vector $\boldsymbol{\chi} = [\theta_\mathrm{w} - \theta_\mathrm{t}, \dot{\theta}_\mathrm{w} - \dot{\theta}_\mathrm{t}]^\mathsf{T}$.

Accurately tracking the random movements of the target by suitably scaling the reciprocal activation torque τ_RA and the coactivation torque τ_CA, requires the estimation of the state vector $\boldsymbol{\chi}$. This estimation is based on multiple noisy observations z, which are acquired

through the sensory modalities of vision, touch, and proprioception. These observations z are encompassed in the observation vector $\boldsymbol{z}$, which can be described by

$$\boldsymbol{z}_\kappa = H_\kappa \boldsymbol{\chi}_\kappa + \nu_\kappa \ , \tag{5.8}$$

where H is the observation matrix. The observation noise ν, which represents all involved sources of noise, is modeled by zero mean Gaussian white noise:

$$\nu_\kappa \in \mathcal{N}\left(\nu \,\middle|\, 0, \sigma_\nu^2\right), \quad \sigma_\nu^2 = \mathsf{E}\left[\nu^2\right] \ , \tag{5.9}$$

where σ_ν^2 is the observation noise variance. The knowledge of the full state equation (5.7) paired with the acquisition of the observation vector $\boldsymbol{z}$ allows for linear quadratic estimation of the state vector $\boldsymbol{\chi}$ by application of an iterative Kalman filter:

$$\hat{\boldsymbol{\chi}}_{\kappa+1} = \hat{\boldsymbol{\chi}}_{\kappa+1|\kappa} + G_{\kappa+1}(\boldsymbol{z}_{\kappa+1} - H\hat{\boldsymbol{\chi}}_{\kappa+1|\kappa}) \ , \tag{5.10}$$

$$G_{\kappa+1} = P_{\kappa+1|\kappa} H^\mathsf{T} (H P_{\kappa+1|\kappa} H^\mathsf{T} + N_{\kappa+1})^{-1} \ , \tag{5.11}$$

$$P_{\kappa+1} = (I - G_{\kappa+1} H) P_{\kappa+1|\kappa} \ , \tag{5.12}$$

$$\hat{\boldsymbol{\chi}}_{\kappa+1|\kappa} = A\hat{\boldsymbol{\chi}}_\kappa + \boldsymbol{b}\left(\tau_{\mathrm{RA},\kappa} + \tau_{\mathrm{CA},\kappa} + \tau_{\mathrm{VC},\kappa}\right) \ , \tag{5.13}$$

$$P_{\kappa+1|\kappa} = A P_\kappa A^\mathsf{T} + \Omega \ , \tag{5.14}$$

where $\hat{\boldsymbol{\chi}}$ is the estimated state vector, G is the Kalman gain matrix, P is the estimate covariance matrix, and I is the identity matrix. The observation vector $\boldsymbol{z}$, the observation matrix H, and the observation noise covariance matrix N for individual and dyadic task execution are introduced in Section 5.2.1 and Section 5.2.2, respectively.

Remark 5.2. The effects of sensory delay δ can be incorporated into the model by firstly obtaining the estimated state vector $\hat{\boldsymbol{\chi}}$ at time step $\kappa - \delta$ and subsequently using a forward model of the full state equation (5.7) to predict the estimated state vector $\hat{\boldsymbol{\chi}}$ at time step κ. For simplicity, we do not use such a forward model, but instead assume that the effects of sensory delay δ are sufficiently represented by the observation noise covariance matrix N.

During dyadic task execution, the two physically interacting individuals are connected by a virtual spring. Thus, the respective virtual spring torque τ_{VC} is given by

$$\tau_{\mathrm{VC},\kappa} = k_{\mathrm{VC}}(\tilde{\theta}_{\mathrm{w},\kappa} - \theta_{\mathrm{w},\kappa}) \ , \tag{5.15}$$

where $\tilde{\theta}_{\mathrm{w}}$ is the partner's wrist angle and k_{VC} is the virtual spring stiffness. When both individuals perform the tracking task individually, i.e., without being physically coupled, the virtual spring torque τ_{VC} is zero. The effects of reciprocal activation are modeled by full state feedback control. Thus, the reciprocal activation torque τ_{RA} is given by

$$\tau_{\mathrm{RA},\kappa} = -\boldsymbol{\lambda}\hat{\boldsymbol{\chi}}_\kappa \ . \tag{5.16}$$

The elements of the full state feedback control gain vector $\boldsymbol{\lambda}$ are determined by designing a linear quadratic regulator (LQR) that minimizes the cost function

$$\rho = \sum_{\kappa=0}^{\infty} \left(\boldsymbol{\chi}_\kappa^\mathsf{T} Q \boldsymbol{\chi}_\kappa + r\tau_{\mathrm{RA},\kappa}^2\right) \ , \tag{5.17}$$

where Q is the positive semi-definite state weight matrix and r is the positive input weight.

As modulation of coactivation results in modulation of impedance components, the effects of coactivation are modeled by impedance control. For simplicity, in this chapter, we only consider the stiffness component. Thus, the coactivation torque τ_{CA} is given by

$$\tau_{\mathrm{CA},\kappa} = k_{\mathrm{w},\kappa}\hat{e}_{\theta,\kappa} \ , \tag{5.18}$$

where k_{w} is the wrist stiffness and $\hat{e}_\theta$ is the estimate of the kinematic error $e_\theta = \theta_{\mathrm{t}} - \theta_{\mathrm{w}} = -\chi_1$ between the target angle θ_{t} and the wrist angle θ_{w}. The wrist stiffness k_{w} is modulated during the course of the tracking task according to the coactivation modulation model. Before we derive this model, we present the observation vector $\boldsymbol{z}$, the observation matrix H, and the observation noise covariance matrix N for individual and dyadic task execution.

5.2.1. Individual Task Execution

The estimation of the state vector $\boldsymbol{\chi}$ is based on multiple noisy observations z, which are appropriated through the sensory modalities of vision, touch, and proprioception. During individual task execution, the acquirable information consists only of the visual information that is provided by the visual feedback. Therefore, the observations z consist only of visual observations z_{v}, which are modeled as

$$z_{\mathrm{v},\kappa} = \theta_{\mathrm{w},\kappa} - \theta_{\mathrm{t},\kappa} + \nu_{\mathrm{v},\kappa} \ , \tag{5.19}$$

where ν_{v} is the visual observation noise. It includes the noise that is inherent to the visual information as well as the noise that is involved in the acquisition of the visual information and is modeled by zero mean Gaussian white noise:

$$\nu_{\mathrm{v},\kappa} \in \mathcal{N}\left(\nu_{\mathrm{v}} \,\middle|\, 0, \sigma^2_{\nu_{\mathrm{v}}}\right), \quad \sigma^2_{\nu_{\mathrm{v}}} = \mathsf{E}\left[\nu^2_{\mathrm{v}}\right] \ , \tag{5.20}$$

where $\sigma^2_{\nu_{\mathrm{v}}}$ is the visual observation noise variance. For simplicity, in this work, we assume that the visual observation noise variance $\sigma^2_{\nu_{\mathrm{v}}}$ is known from experience.

During individual task execution, based on (5.19) and (5.20), the individual observation vector $\boldsymbol{z}$ is given by $\boldsymbol{z}_\kappa = z_{\mathrm{v},\kappa}$ and the individual observation matrix H and the individual observation noise covariance matrix N are defined as

$$H = \begin{bmatrix} 1 & 0 \end{bmatrix}, \quad N = \sigma^2_{\nu_{\mathrm{v}}} \ . \tag{5.21}$$

Inclusion of these definitions in the iterative Kalman filter algorithm (5.10) - (5.14) allows for linear quadratic estimation of the state vector $\boldsymbol{\chi}$ based on visual information.

5.2.2. Dyadic Task Execution

During dyadic task execution, the physical coupling with the partner represents a second source of information that both of the individuals are able to use to improve their respective estimation of the state vector $\boldsymbol{\chi}$. Consequently, the acquirable information consists both of the visual information that is provided by the visual feedback and the haptic information that is provided by the haptic interaction. This haptic information, paired with a spontaneously formed internal model of the partner's motor behavior, can be used by each individual to obtain an estimate of the partner's estimate of the target angle θ_{t}.

Remark 5.3. The spontaneous formation and continuous adaptation of the internal model of the partner's motor behavior as well as the exploitation of this knowledge to obtain the estimate of the partner's estimate of the target angle θ_t can be accomplished by application of an iterative extended Kalman filter [145]. For simplicity, in this work, we do not include this Kalman filter, but instead directly model the resulting haptic observations z_h.

Analogous to the model presented in [49], the haptic observations z_h, which are obtained through the internal model of the partner's motor behavior, are modeled as

$$z_{\mathrm{h},\kappa} = \theta_{\mathrm{w},\kappa} - \theta_{\mathrm{t},\kappa} + \nu_{\mathrm{h},\kappa} \ , \tag{5.22}$$

where ν_h is the haptic observation noise. It includes the noise that is inherent to the haptic information, the noise that is involved in the acquisition of the haptic information, and the noise due to the internal model of the partner's motor behavior. Similar to the visual observation noise ν_v, it is modeled by zero mean Gaussian white noise:

$$\nu_{\mathrm{h},\kappa} \in \mathcal{N}\left(\nu_\mathrm{h} \,\middle|\, 0, \sigma^2_{\nu_\mathrm{h}}\right), \quad \sigma^2_{\nu_\mathrm{h}} = \mathsf{E}\left[\nu^2_\mathrm{h}\right] \ . \tag{5.23}$$

The corresponding haptic observation noise variance $\sigma^2_{\nu_\mathrm{h}}$ is modeled as

$$\sigma^2_{\nu_\mathrm{h}} = \tilde{\sigma}^2_{\nu_\mathrm{v}} + \sigma^2_\mathrm{VC} \ , \tag{5.24}$$

where $\tilde{\sigma}^2_{\nu_\mathrm{v}}$ is the partner's visual observation noise variance. The virtual spring observation noise variance σ^2_VC represents the detrimental effects that the compliance of the coupling mechanics has on the quality of the exchanged haptic information.

During dyadic task execution, based on (5.19) and (5.20) as well as (5.22) and (5.23), the dyadic observation vector $\boldsymbol{z}$ is given by $\boldsymbol{z}_\kappa = [z_{\mathrm{v},\kappa}, z_{\mathrm{h},\kappa}]^\mathsf{T}$ and the dyadic observation matrix H and the dyadic observation noise covariance matrix N are defined as

$$H = \begin{bmatrix} 1 & 0 \\ 1 & 0 \end{bmatrix}, \quad N = \begin{bmatrix} \sigma^2_{\nu_\mathrm{v}} & 0 \\ 0 & \sigma^2_{\nu_\mathrm{h}} \end{bmatrix}. \tag{5.25}$$

Inclusion of these definitions in the iterative Kalman filter algorithm (5.10) - (5.14) allows for linear quadratic estimation of the state vector $\boldsymbol{\chi}$ based on visual and haptic information.

5.3. Coactivation Modulation Model

During the course of the tracking task, the discrete-time evolution of the wrist stiffness k_w from time step κ to time step $\kappa + 1$ is described by the difference equation

$$k_{\mathrm{w},\kappa+1} = k_{\mathrm{w},\kappa} + \dot{k}_{\mathrm{w},\kappa} t_\mathrm{s} \ , \tag{5.26}$$

where $\dot{k}_\mathrm{w}$ is the respective derivative of the wrist stiffness. It characterizes the modulation of the wrist stiffness k_w and is modeled by the coactivation modulation model

$$\dot{k}_{\mathrm{w},\kappa} = \eta_{\mathrm{err},\kappa} + \eta_{\mathrm{int},\kappa} - \alpha_\mathrm{meta} \ , \tag{5.27}$$

where the functions η_err and η_int, which will be defined and explained in more detail in the following sections, represent the influences of the kinematic error e_θ and the physical interaction with the partner, respectively, and the parameter α_meta embodies the influence of the desire to reduce coactivation in order to minimize metabolic cost.

5.3.1. Kinematic Error Function

Increasing coactivation is known to serve as a means of reducing the kinematic error e_θ, with the increase being positively correlated with the respective absolute value $|e_\theta|$ [35]. The increase is also known to be positively correlated with the accuracy requirements [41]. In order to incorporate these insights, the error function η_{err} is modeled as

$$\eta_{\text{err},\kappa} = \begin{cases} 0, & |\hat{e}_\theta| < \beta_{\text{err}}\sigma_{\hat{e}_\theta} \\ \alpha_{\text{err}}\left(|\hat{e}_\theta| - \beta_{\text{err}}\sigma_{\hat{e}_\theta}\right), & |\hat{e}_\theta| \geq \beta_{\text{err}}\sigma_{\hat{e}_\theta} \end{cases} , \tag{5.28}$$

where $\hat{e}_\theta$ is the estimated kinematic error, α_{err} is the correlation parameter, β_{err} is the parameter that scales the size of the interval $\beta_{\text{err}}\sigma_{\hat{e}_\theta}$, which represents the influence of the error estimate uncertainty, and $\sigma_{\hat{e}_\theta}$ is the error estimate SD.

Remark 5.4. As long as the absolute value of the estimated kinematic error $\hat{e}_\theta$ lies inside the interval $\beta_{\text{err}}\sigma_{\hat{e}_\theta}$, it does not result in a change in coactivation. As soon as it lies on or outside the bounds of this interval, it results in an increase in coactivation that is scaled by the correlation parameter α_{err}. Thus, the larger the error estimate SD $\sigma_{\hat{e}_\theta}$, the smaller the evoked increase in coactivation for a given estimated kinematic error $\hat{e}_\theta$.

During individual task execution with estimation of the state vector $\boldsymbol{\chi}$ based on visual information only, the individual error estimate SD $\sigma_{\hat{e}_\theta}$ is defined by

$$\sigma_{\hat{e}_\theta} = \sigma_{\nu_{\text{v}}} , \tag{5.29}$$

where $\sigma_{\nu_{\text{v}}}$ is the visual observation noise SD. During dyadic task execution with estimation of the state vector $\boldsymbol{\chi}$ based on both visual and haptic information due to the physical coupling with the partner, the dyadic error estimate SD $\sigma_{\hat{e}_\theta}$ is defined by

$$\sigma_{\hat{e}_\theta} = \sqrt{\frac{\sigma_{\nu_{\text{v}}}^2 \sigma_{\nu_{\text{h}}}^2}{\sigma_{\nu_{\text{v}}}^2 + \sigma_{\nu_{\text{h}}}^2}} , \tag{5.30}$$

which additionally includes the haptic observation noise SD $\sigma_{\nu_{\text{h}}}$.

Remark 5.5. The inclusion of the error estimate SD $\sigma_{\hat{e}_\theta}$ in the error function η_{err} ensures that not only the value of the estimated kinematic error $\hat{e}_\theta$, but also the corresponding level of uncertainty are incorporated. Furthermore, it ensures that the error function η_{err} is adapted to the decrease in uncertainty that results from the improvement in the estimation of the state vector $\boldsymbol{\chi}$ due to the exchange of haptic information with the partner.

5.3.2. Physical Interaction Function

For the interaction function η_{int}, we propose three different models. The first model assumes that, apart from its influence on the estimation of the state vector $\boldsymbol{\chi}$ and the implications on the error function η_{err}, the physical interaction with the partner does not result in any explicit change in coactivation. Thus, the interaction function $\eta_{\text{int},1}$ is given by

$$\eta_{\text{int},1,\kappa} = 0 . \tag{5.31}$$

Remark 5.6. With this model, the influence of the physical interaction with the partner is limited to the improvements in error estimate SD $\sigma_{\hat{e}_\theta}$ and estimated kinematic error $\hat{e}_\theta$.

The second model assumes that the interaction function η_{int} is correlated with the absolute value of the wrist angle difference $\tilde{\theta}_{\text{w}} - \theta_{\text{w}}$, which quantifies the exchange of interaction torque between the individuals. For this model, we evaluate two different variations. The respective interaction functions $\eta_{\text{int},2a}$ and $\eta_{\text{int},2b}$ are given by

$$\eta_{\text{int,2a},\kappa} = \alpha_{\text{int,2a}} |\tilde{\theta}_{\text{w},\kappa} - \theta_{\text{w},\kappa}| \ , \tag{5.32}$$

$$\eta_{\text{int,2b},\kappa} = -\alpha_{\text{int,2b}} |\tilde{\theta}_{\text{w},\kappa} - \theta_{\text{w},\kappa}| \ , \tag{5.33}$$

where $\alpha_{\text{int,2a}}$ and $\alpha_{\text{int,2b}}$ are the correlation parameters of the respective variations.

Remark 5.7. In the first variation (5.32), the exchange of interaction torque between the individuals results in a general increase in coactivation. In the second variation (5.33), it results in a general decrease in coactivation. Thus, with this model, the interaction behavior of the individuals is either governed by a general increase or a general decrease of the resistance towards the effects of the physical interaction with the partner.

The third model is similar to the second model in that it also assumes that the interaction function η_{int} is correlated with the absolute value of the wrist angle difference $\tilde{\theta}_{\text{w}} - \theta_{\text{w}}$. However, in this model, the algebraic sign and the magnitude of the correlation coefficient are influenced by the visual observation noise SD $\sigma_{\nu_{\text{v}}}$, which, in the context of the experiment, is defined by the visual feedback scenario and correlates with the tracking task performance. Thus, the respective interaction function $\eta_{\text{int},3}$ is given by

$$\eta_{\text{int},3,\kappa} = \left(-\alpha_{\text{int},3}\sigma_{\nu_{\text{v}}} + \beta_{\text{int},3}\right) |\tilde{\theta}_{\text{w},\kappa} - \theta_{\text{w},\kappa}| \ , \tag{5.34}$$

where $\alpha_{\text{int},3}$ and $\beta_{\text{int},3}$ are slope and intercept of the correlation characteristics, respectively.

Remark 5.8. In this model, an increase of the visual observation noise SD $\sigma_{\nu_{\text{v}}}$ results in a decrease of the correlation coefficient. This means that above a certain threshold of the visual observation noise SD $\sigma_{\nu_{\text{v}}}$, which depends on the parameters $\alpha_{\text{int},3}$ and $\beta_{\text{int},3}$, the algebraic sign of the correlation coefficient becomes negative. Thus, with this model, the change in resistance towards the effects of the physical interaction with the partner is influenced by the confidence in the individual contribution, which is assumed to be negatively correlated with the amount of visual noise in the visual feedback and the resulting tracking task performance. For increasing visual noise in the visual feedback, the change in coactivation decreases, ultimately yielding large decreases in coactivation for large amounts of visual noise.

5.4. Experiment

In this section, we focus on the experiment, in which two participants track pseudo-random movements of a shared target, either individually or while being physically coupled by a virtual spring, using wrist flexion/extension movements. Each participant is provided with distinct visual feedback, which includes the current wrist and target positions, and cannot see the partner's visual feedback. During the course of the experiment, the participants each experience two different levels of visual noise in their respective visual feedback.

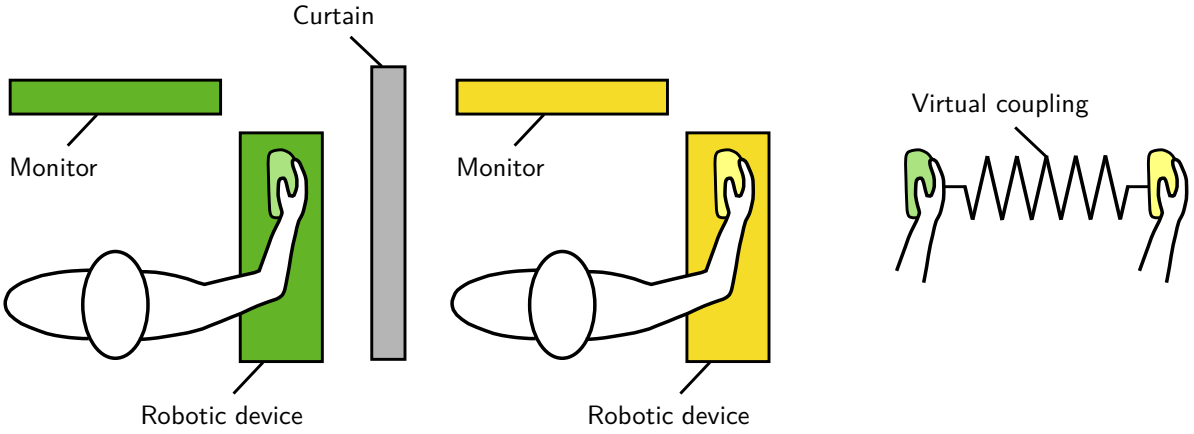

Figure 5.1.: Schematic representation of the dual robotic interface. It consists of two 1-DoF wrist interfaces, on which the participants can place their forearms to perform wrist flexion/extension movements. The participants can either perform the experiment individually or physically coupled by a virtual spring.

5.4.1. Apparatus

The apparatus comprises a 1-DoF dual robotic interface [147], which is shown schematically in Fig. 5.1. It consists of two wrist interfaces, on which the participants place their forearms in order to grasp a concavely shaped handle and perform wrist flexion/extension movements. Each interface is equipped with a DC motor that allows for application of external torques, e.g., in order to render a virtual coupling between the participants. The apparatus includes two monitors, each mounted in front of one of the interfaces, that enable presentation of distinct visual feedback. A curtain is drawn between the participants in order to prevent possible confounds from insights into the partner's visual feedback [148].

Each interface is equipped with a 5000 cpr differential encoder (*RI 58-O, Hengstler*) and a torque sensor (*TRT-100, Transducer Technologies*) with measurement range of $[0, 11.29]$ Nm. The DC motor (*MSS8, Mavilor*) can produce peak torque of 15 Nm and is current-controlled by a DC brush motor amplifier (*413C, Copley*). The muscle activation data of the wrist flexion/extension muscle pairs is obtained using a medically certified non-invasive 16-channel surface EMG device (*g.LADYBird, g.GAMMABox, g.BSamp, g.Tec*). The real-time system is run at a sample rate of 1 kHz using *Labview Real-time v10.0* (*National Instruments*) and the data is collected with a data acquisition card (*DAQ-PCI-6221, National Instruments*) at a downsampled rate of 0.1 kHz. All collected signals, including the surface EMG data, are filtered by a fifth order Savitzky-Golay filter with a cut-off frequency of 10 Hz [109].

5.4.2. Experiment Design

The experiment consists of a tracking task, in which the participants have to use wrist flexion/extension movements to follow the pseudo-random movements of a shared target as accurately as possible. The tracking task is either performed individually ("solo trials") or while being physically coupled with the partner by a virtual spring ("interaction trials").

Task Configuration

In order to achieve a hard virtual coupling, the virtual spring stiffness k_{VC} is set to a fixed value of 17.2 Nm/rad. The target trajectories are defined by a multi-sine function:

$$\theta_{\mathrm{t}}(t) = 0.3229 \sin(0.6464\pi t_{\mathrm{t}}) \sin(0.3478\pi t_{\mathrm{t}}) \text{ [rad]} , \tag{5.35}$$

with $t_{\mathrm{t}} = t_{\mathrm{t},0} + t$, where $t_{\mathrm{t},0}$ is the starting time. In order to prevent the participants from learning and adapting to the target movements, the starting time $t_{\mathrm{t},0}$ is selected randomly from $\{t_{\mathrm{t},0} \in [0, 20]\,\mathrm{s} \mid \theta_{\mathrm{t}}(t_{\mathrm{t},0}) = 0\,\mathrm{rad}\}$ according to a uniform distribution.

In order to enable the participants to accurately quantify their tracking performance, the root mean squared value of their kinematic error e_θ, which from this point on is referred to as tracking error e_θ, is presented to them on their respective monitor after each trial:

$$\mathrm{RMSE} = \sqrt{\frac{1}{h} \sum_{j=1}^{h} e_{\theta,j}^2} , \tag{5.36}$$

where h is the number of samples within the trial and the RMSE is presented in degrees.

Visual Feedback

The visual feedback includes the wrist angle θ_{w} and the target angle θ_{t}, but does not include the partner's wrist angle $\tilde{\theta}_{\mathrm{w}}$. It is presented on a black background that includes a grey dashed arc that indicates the possible 1-DoF wrist flexion/extension movements. The wrist angle θ_{w} is displayed in the form of a blue line cursor. The target angle θ_{t} is either displayed without visual noise ("clean scenario") or with visual noise ("noisy scenario"). In the clean scenario, it is displayed by a single red dot, and in the noisy scenario, it is displayed by a cloud of eight normally distributed red dots. Each of these dots is defined by three parameters, which are all randomly selected from independent Gaussian distributions: radial distance to the target position $\eta_1 \sim \mathcal{N}\left(\eta_1 \middle| 0, \sigma_{\eta_1}\right)$, angular distance to the target position $\eta_2 \sim \mathcal{N}\left(\eta_2 \middle| 0, \sigma_{\eta_2}\right)$, and angular velocity $\eta_3 \sim \mathcal{N}\left(\eta_3 \middle| 0, \sigma_{\eta_3}\right)$. The respective standard deviations $\sigma_{\eta_1} = 0.015$ m, $\sigma_{\eta_2} = 0.080$ rad, and $\sigma_{\eta_3} = 0.070$ rad/s are all constant and identical for all participants. In order to continuously change the shape of the cloud, every 100 ms one of the eight dots is replaced by a new dot. This means that each dot is visible for 800 ms. Fig. 5.2 shows exemplary illustrations of each of the two visual feedback scenarios.

EMG Calibration

Surface EMG data of the wrist flexion/extension muscle pairs is collected from the flexor carpi radialis (FCR) and extensor carpi radialis longus (ECRL) muscles. In order to be able to calibrate the obtained EMG data based on relationships between muscle activations and associated torques, an EMG calibration routine is performed. During this calibration routine, the participants are instructed to consecutively flex/extend their wrist in order to produce certain flexion/extension torques, which are indicated to them by a yellow target dot on their respective monitor. Each muscle activation lasts for 4 s and is followed by a 5 s rest period in order to avoid effects of muscle fatigue. The calibration procedure consists of four repetitions with flexion/extension torques of 1, 2, 3, and 4 Nm, respectively.

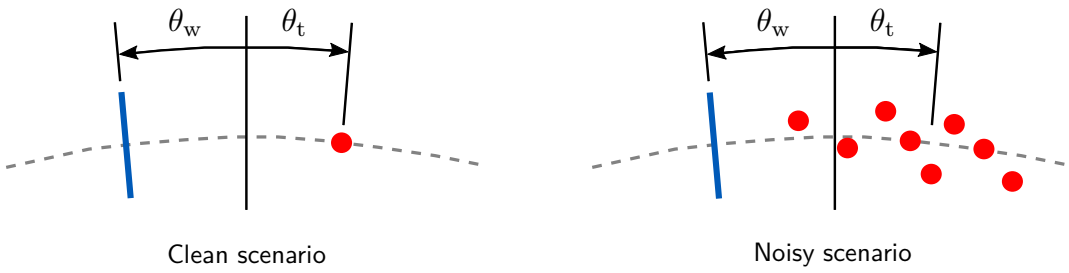

Figure 5.2.: Exemplary illustrations of the visual feedback scenarios. The grey dashed arc indicates the 1-DoF movements. The blue line cursor shows the wrist angle θ_w. The single red dot in the clean scenario and the cloud of red dots in the noisy scenario show the target angle θ_t. For clarity, the black background, on which the visual feedback is presented during the experiment, is omitted.

Linear regression of the measurements of the calibration routine yields the relationships between the muscle activations and the associated torques. These relationships are used to calculate the torque-calibrated muscle activations that correspond to the experimental EMG data [149]. Based on the resulting torque-calibrated muscle activations, the reciprocal activation a_{RA} and the coactivation a_{CA} are calculated as

$$a_{RA} = a_{FCR} + a_{ECRL} \ , \tag{5.37}$$

$$a_{CA} = \min\left(|a_{FCR}|, |a_{ECRL}|\right) \ , \tag{5.38}$$

where a_{FCR} and a_{ECRL} are the torque-calibrated muscle activations that correspond to the measurements obtained from the FCR muscle and the ECRL muscle, respectively.

5.4.3. Participants & Procedure

A total of 48 participants (14 male-male and 10 female-female pairs) with mean (SD) age of 25.29 (4.14) years volunteered to participate in this experiment. All participants were informed about the objectives and the procedure of the experiment, and provided written consent prior to participation. Handedness of the participants was assessed according to the Edinburgh Handedness Inventory [150]: 6 participants were left-handed, 40 participants were right-handed, and 2 participants did not specify handedness. The experiment was performed in the Human Robotics Group of Imperial College London according to the principles in the Declaration of Helsinki and approved by the institutional research ethics committee.

Remark 5.9. Due to torque sensor malfunctions, two of the acquired data sets needed to be removed from the analysis (dyad 1 and dyad 5). In the case of dyad 1, the torque sensor of the left participant provided implausibly large values that did not correlate properly with the corresponding kinematics. In the case of dyad 5, the torque sensor of the right participant completely stopped functioning. Due to the removal of these two data sets, the analysis of the experiment and the corresponding results include a total of 44 participants (14 male-male and 8 female-female pairs) with mean (SD) age of 25.41 (4.26) years. Of these remaining participants, 5 were left-handed, 37 were right-handed, and 2 did not specify handedness.

The experiment consists of 50 trials that each last 20 s. The first 5 trials are solo trials, in which the participants perform the tracking task individually and do not experience any visual noise in their visual feedback. These trials allow for familiarization with the apparatus and provide information on the individual motor behaviors. The following 40 trials are interaction trials, in which the participants perform the tracking task while being physically coupled with the partner. These 40 trials are divided into 4 blocks of 10 trials each, among which the 4 combinations of visual feedback scenarios are uniformly randomly distributed:

1) left clean - right clean ,

2) left clean - right noisy ,

3) left noisy - right clean ,

4) left noisy - right noisy .

These combinations of visual feedback scenarios provide information on how the different levels of visual noise, which correspond to different levels of tracking performance, influence the interaction behavior of the two participants. The last 5 trials are solo trials, which are identical to the first 5 trials. These trials provide information on the changes in the individual motor behaviors compared to the beginning of the experiment.

The participants were seated next to the interfaces, and instructed to place their right forearm on the interface and grasp the concavely shaped handle with their right hand. The forearm and the fingers were restrained by elastic straps in order to limit all possible movements to those of the wrist. The EMG electrodes were positioned on the FCR and ECRL muscles and tested for proper functionality. The participants were presented with exemplary illustrations of the different visual feedback scenarios, and were informed of the resulting possible combinations. Before the initialization of the encoders and torque sensors, the participants were asked to move their wrist to the position, in which they felt most relaxed and comfortable. After completion of these preparations, the curtain was drawn between the participants and they were instructed to not communicate verbally. The EMG calibration routine was performed and after its completion, the experiment was started. Verbal cues were provided by the experimenter, when the trial configuration changed from solo to interaction and vice versa. Visual cues were provided on the monitors, when the visual feedback scenarios changed betweens blocks of interaction trials. These visual cues indicated that a change would take place, but did not inform of the type of change.

5.4.4. Evaluation

The evaluation of the experiment is centered around the tracking error e_θ, the reciprocal activation a_{RA}, and the coactivation a_{CA}, with specific focus placed on relative within-subject differences in the coactivation a_{CA} between the different conditions. In order to be able to average and analyze these relative within-subject differences of the EMG data, we normalize the reciprocal activation a_{RA} and the coactivation a_{CA} for each participant:

$$a_{\mathrm{RA,n}} = a_{\mathrm{RA}} / a_{\mathrm{RA,max}} \ ,$$

$$a_{\mathrm{CA,n}} = a_{\mathrm{CA}} / a_{\mathrm{CA,max}} \ ,$$

where $a_{\mathrm{RA,n}}$ is the normalized reciprocal activation and $a_{\mathrm{CA,n}}$ is the normalized coactivation.

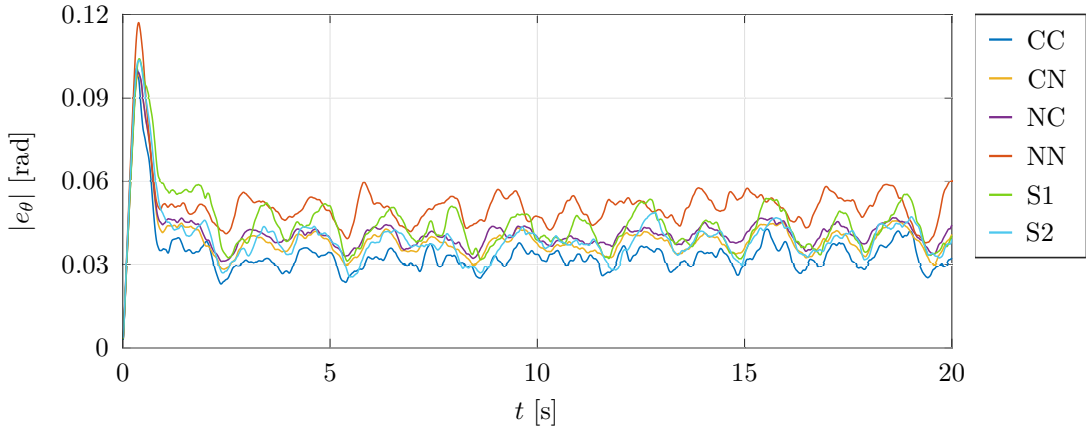

Figure 5.3.: Mean results of the absolute tracking error $|e_\theta|$, averaged over trials within conditions and participants (solo: 5 trials, interaction: 10 trials).

The corresponding normalizing values $a_{\mathrm{RA,max}}$ and $a_{\mathrm{CA,max}}$ are determined by first averaging the respective variables over time within trials and subsequently calculating the maximum values of the obtained averages. For simplicity, from this point on, we refer to the normalized variables $a_{\mathrm{RA,n}}$ and $a_{\mathrm{CA,n}}$ simply as reciprocal activation $a_{\mathrm{RA,n}}$ and coactivation $a_{\mathrm{CA,n}}$.

In order to be able to present the obtained results from a participant-specific perspective, the experimental conditions are converted into participant-specific conditions:

1) subject clean - partner clean (CC) ,

2) subject clean - partner noisy (CN) ,

3) subject noisy - partner clean (NC) ,

4) subject noisy - partner noisy (NN) .

Remark 5.10. During an experimental condition with different visual feedback scenarios, the participants are performing in different participant-specific conditions. For example, during the experimental condition *left clean - right noisy*, the left participant is performing in the participant-specific condition *subject clean - partner noisy* and the right participant is performing in the participant-specific condition *subject noisy - partner clean*.

For notational convenience, we define abbreviations for the participant-specific conditions that are listed in the enumeration above. Furthermore, we define abbreviations for the solo condition before interaction trials (S1) and the solo condition after interaction trials (S2). In the remainder of this section, we first analyze the absolute tracking error $|e_\theta|$ and then focus on the absolute reciprocal activation $|a_{\mathrm{RA,n}}|$, and the coactivation $a_{\mathrm{CA,n}}$.

Tracking Error

The absolute tracking error, averaged over trials within solo and interaction conditions and participants, is presented in Fig. 5.3. The temporal evolutions are similar for all conditions. At the beginning of the trial, the absolute tracking error rapidly increases and decreases to form a prominent spike with a substantially increased amplitude compared to the remainder

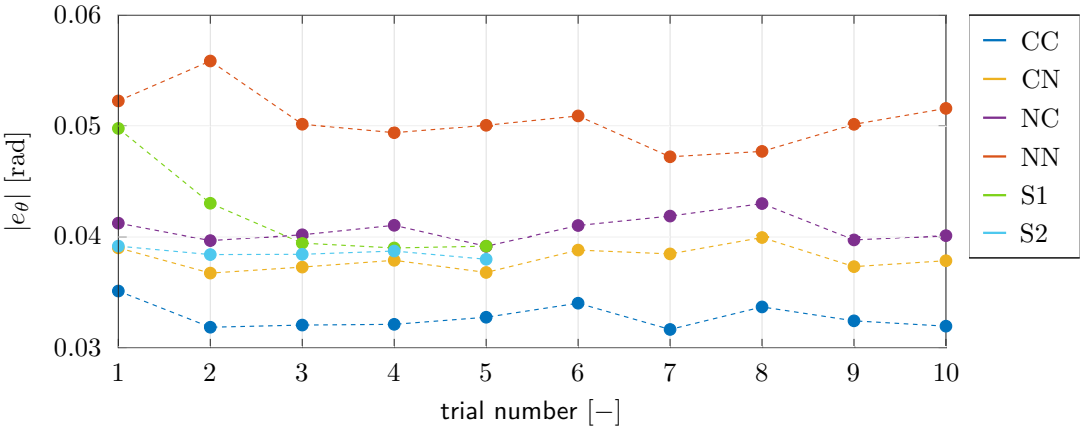

Figure 5.4.: Mean results of the absolute tracking error $|e_\theta|$, averaged over time within trials and participants ($t > 10$ s to avoid transient behavior).

of the trial. This sudden but short increase in amplitude could be caused by sensory delays of the participants. It could however also be caused by an adaptation process that takes place at the beginning of the trial. During the remainder of the trial, the absolute tracking error oscillates at a much lower level, inbetween condition-dependent lower and upper bounds.

In order to allow for quantitative assessment of these condition-dependent differences, Fig. 5.4 shows the absolute tracking error averaged over time within trials and participants. In order to avoid transient behavior during the first halves of the trials and only base the analysis on the steady-state behavior during the second halves of the trials, the averages are calculated for $t > 10$ s. In this figure, the differences between the conditions are more apparent. The absolute tracking error is the smallest in CC and by far the largest in NN. The mixed conditions lie inbetween, with the absolute tracking errors being slightly larger in NC than in CN. This small difference between the mixed conditions is caused by the fact that the virtual coupling is not rigid, i.e., the difference represents the deflection of the virtual spring. The differences in absolute tracking errors between the different conditions clearly illustrate the negative correlation between visual noise and tracking performance.

The absolute tracking error in S1 shows a steep learning curve that converges to absolute tracking errors similar to those in the mixed conditions. It seems that after completion of these solo trials, the participants are familiarized with the tracking task. The absolute tracking errors in S2 show no improvement compared to those in the last two trials of S1. This suggests that the physical interaction with the partner during the interaction trials does not results in perseverative improvement of the individual tracking performance.

Comparison of the absolute tracking errors in the last two trials of S1, i.e., after completion of familiarization with the tracking task, with those of CC shows that physical interaction with an equal partner results in mutual improvement of tracking performance. Comparison with the absolute tracking errors of CN demonstrates that even during physical interaction with an inferior partner, participants are able to adapt their motor behavior such that they achieve similar tracking performance as during individual task execution. These insights are similar to those observed in previous experiments [49, 144, 145].

The statistical analysis of the condition-dependent differences is performed based on the absolute tracking error averaged over time within conditions and participants, which is presented in Fig. 5.5. Analogous to the contents of Fig. 5.4, and for the same reasons,

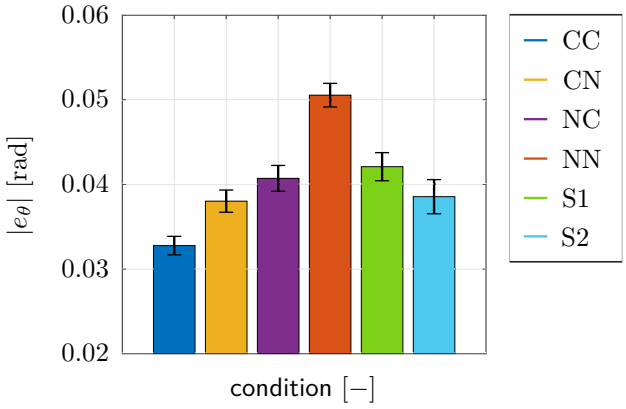

Figure 5.5.: Mean results of the absolute tracking error $|e_\theta|$, averaged over time within conditions and participants ($t > 10$ s to avoid transient behavior). Error bars represent ± standard error of the mean (SEM).

the averages presented in Fig. 5.5 are also calculated for $t > 10$ s. The statistical analysis of the differences between the interaction conditions is performed using a two-way repeated measures ANOVA with a 2x2 within-subject design, in which the independent variables are defined to be the subject's visual noise scenario (clean, noisy) and the partner's visual noise scenario (clean, noisy). Mauchly's test for sphericity indicates violation of the sphericity assumption ($\chi^2(5) = 20.68,\ p < 10^{-3}$). Thus, the results of the two-way repeated measures ANOVA are corrected using the Huynh-Feldt correction ($\epsilon = 0.808$). The corrected results indicate main effects of the subject's visual noise scenario ($F(1, 43) = 100.33,\ p < 10^{-12}$) and the partner's visual noise scenario ($F(1, 43) = 103.98,\ p < 10^{-12}$). The interaction effect between the subject's visual noise scenario and the partner's visual noise scenario is also statistically significant ($F(1, 43) = 16.75,\ p < 10^{-3}$). Post-hoc Bonferroni tests reveal the absolute tracking error to be significantly affected by the partner's visual noise scenario, independent of whether the subject is experiencing the clean scenario ($p < 10^{-6}$) or the noisy scenario ($p < 10^{-12}$). In summary, the results of the statistical analysis support the interpretations derived from the contents of Fig. 5.4 and Fig. 5.5. The absolute tracking error is not only significantly influenced by the subject's visual noise scenario and the partner's visual noise scenario, but also by the interaction between these two scenarios.

Muscle Activations

The absolute reciprocal activation and the coactivation, averaged over trials within solo and interaction conditions and participants, are presented in Fig. 5.6 and Fig. 5.7, respectively. At the beginning of the trial, the temporal evolutions are similar, with the absolute reciprocal activation and the coactivation increasing rapidly at similar rates. During the remainder of the trial, however, the temporal evolutions differ substantially.

While the absolute reciprocal activation shows only minor differences in average levels, the coactivation is governed by substantial differences, both in levels and convergence rates. Upon closer inspection, the levels in the absolute reciprocal activation are governed by similar tendencies to those in the coactivation. However, the differences are substantially less pronounced. This is partially due to the fact that the oscillation amplitudes are much larger in the absolute reciprocal activation than in the coactivation. The convergence rates

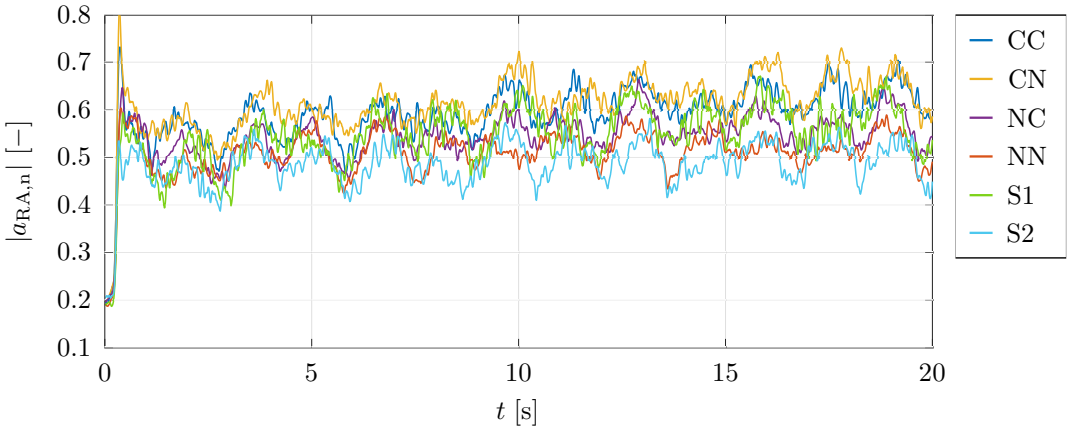

Figure 5.6.: Mean results of the absolute reciprocal activation $|a_{\mathrm{RA,n}}|$, averaged over trials within conditions and participants (solo: 5 trials, interaction: 10 trials).

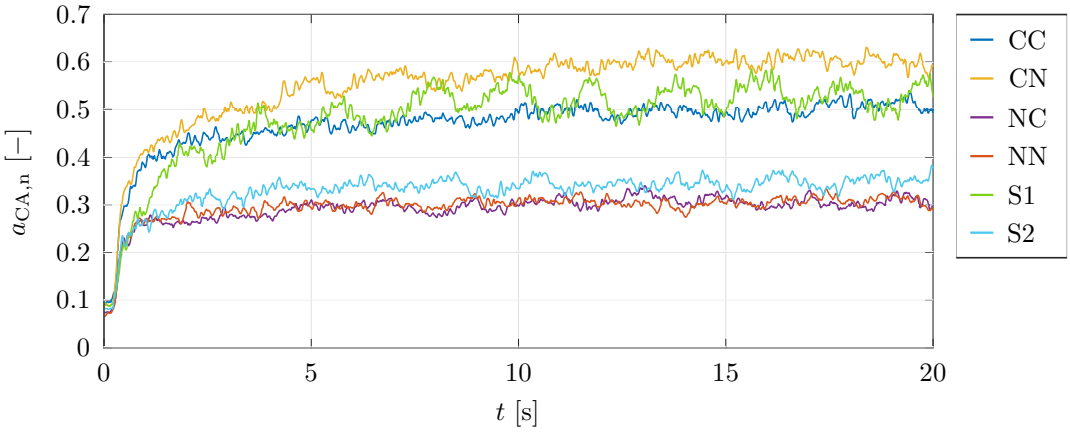

Figure 5.7.: Mean results of the coactivation $a_{\mathrm{CA,n}}$, averaged over trials within conditions and participants (solo: 5 trials, interaction: 10 trials).

of the coactivation seem to be negatively correlated with the respective levels. This could be the result of an analogous correlation with the occurrence of effects that are intended to be compensated by an increase in coactivation. These insights suggest that the differences in muscular effort observed in a previous experiment [49] largely originate from differences in coactivation, instead of reciprocal activation. Thus, for the remainder of this analysis, specific focus is placed on the condition-dependent differences in the coactivation.

In order to allow for quantitative assessment of these condition-dependent differences, Fig. 5.8 shows the coactivation averaged over time within trials and participants. In order to avoid transient behavior during the first halves of the trials and only base the analysis on the steady-state behavior during the second halves of the trials, the averages are calculated for $t > 10\,\mathrm{s}$. The differences between the conditions closely resemble the differences observed in Fig. 5.7. The coactivation is the largest in CN, followed by CC, and it is the smallest and similar in NC and NN. In the first two trials of NC, it is slightly larger than in NN. The differences between the conditions show that the coactivation is generally larger in subject clean conditions than in subject noisy conditions. In the subject noisy conditions, there is little difference between the interaction with a clean partner and the interaction with

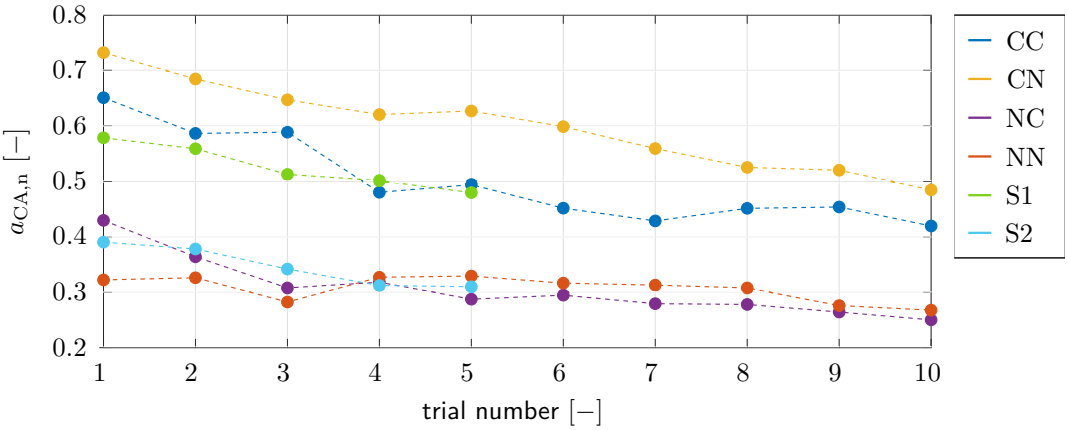

Figure 5.8.: Mean results of the coactivation $a_{\mathrm{CA,n}}$, averaged over time within trials and participants ($t > 10\,\mathrm{s}$ to avoid transient behavior).

a noisy partner. In contrast, in the subject clean conditions, the coactivation is substantially larger in the interaction with a noisy partner than it is in the interaction with a clean partner. The decrease in coactivation during the course of the conditions is largest and similar in the subject clean conditions and smallest and similar in the subject noisy conditions.

The coactivation in S1 is similar to that in CC, and the coactivation in S2 is similar to that in NC. The decrease in coactivation during the course of the solo trials is generally similar to the subject clean conditions and does not differ between S1 and S2. These correlations, in combination with the differences in decrease between the interaction conditions, suggest that the decrease is not only the result of effects of fatigue, but also results from effects of motor learning. During the first two trials of the subject noisy conditions, the coactivation and the decrease are larger for the condition with the clean partner than for the condition with the noisy partner. This indicates a more elaborate motor learning process at the beginning of these two conditions for the interaction with the clean partner.

The statistical analysis of the condition-dependent differences is conducted based on the coactivation averaged over time within conditions and participants, which is presented in Fig. 5.9. Analogous to the contents of Fig. 5.8, and for the same reasons, the averages presented in Fig. 5.9 are also calculated for $t > 10\,\mathrm{s}$. The statistical analysis of the differences between the interaction conditions is performed using a two-way repeated measures ANOVA with identical design to that of the absolute tracking error. Mauchly's test for sphericity does not indicate violation of the sphericity assumption ($\chi^2(5) = 8.66,\ p = 0.123$). The results indicate main effects of the subject's visual noise scenario ($F(1, 43) = 85.98,\ p < 10^{-11}$) and the partner's visual noise scenario ($F(1, 43) = 7.31,\ p = 0.010$). The interaction effect between the subject's visual noise scenario and the partner's visual noise scenario is also statistically significant ($F(1, 43) = 5.51,\ p = 0.024$). Post-hoc Bonferroni tests reveal that the coactivation is significantly affected by the partner's visual noise scenario, when the subject is experiencing the clean scenario ($p = 0.003$). In contrast, it is not significantly affected when the subject is experiencing the noisy scenario ($p = 0.980$). In summary, the results of the statistical analysis support the interpretations derived from the contents of Fig. 5.8 and Fig. 5.9. Most notably, the statistically significant interaction effect shows a significant correlation between the coactivation and the partner's visual noise scenario during execution of the clean scenario, but not during execution of the noisy scenario.

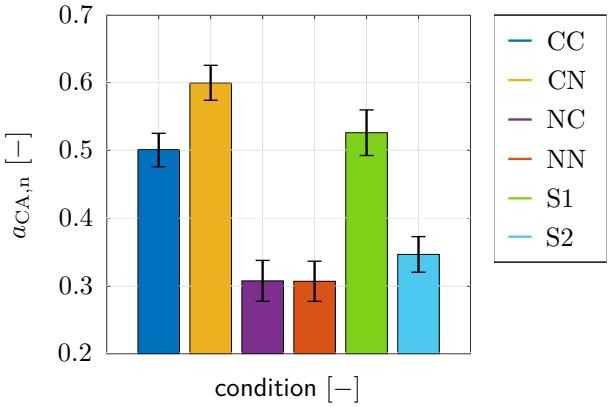

Figure 5.9.: Mean results of the coactivation $a_{\mathrm{CA,n}}$, averaged over time within conditions and participants ($t > 10\,\mathrm{s}$ to avoid transient behavior). Error bars represent ± standard error of the mean (SEM).

5.5. Simulation

In this section, we focus on the simulation, which we use to evaluate the different variations of the coactivation modulation model. In order to allow for more comprehensive evaluation, we additionally simulate solo trials with visual noise. The corresponding experimental data is generated based on the results of the visual tracking task control experiment in [146]. Analogous to the neuromechanical model presented in Section 5.2, the simulation is based on the simulation presented in [49], with the novelty lying in the differentiation of reciprocal activation and coactivation as well as the inclusion of the coactivation modulation model.

5.5.1. Implementation

The simulation is implemented according to the models in Section 5.2 and Section 5.3. It simulates individual and dyadic task execution, i.e., solo and interaction trials, with a sample rate of 200 Hz. In order to obtain similar tracking errors e_θ as in the experiment, the visual observation noise variances $\sigma^2_{\nu_\mathrm{v}}$ of the clean and noisy scenarios are defined based on a second order polynomial fit that describes the relationship between root mean squared values of tracking errors e_θ and respective visual observation noise SDs σ_v in solo trials. This polynomial fit is also used to define the virtual spring observation noise variance σ^2_{VC}, which represents the effects of the compliance of the coupling mechanics on the exchange of haptic information. The corresponding input value for the polynomial fit is set to 0.00763 rad, as determined in the analysis of the haptic tracking task experiment in [49].

The simulated data, which is used for the calculation of the polynomial fit, is generated by simulating a total of 50 solo trials with different visual observation noise SDs σ_v that are defined randomly within the interval $[0, 0.14]$ rad according to a uniform distribution. With the polynomial fit, the visual observation noise variances $\sigma^2_{\nu_\mathrm{v}}$ of the clean and noisy scenarios are determined based on the root mean squared values of the tracking errors e_θ of the respective solo trials in the experiment. The solo trials for the clean scenario are given by the combination of the solo trials before and after interaction. As our experiment does not include solo trials with visual noise for the noisy scenario, we generate the corresponding experimental data based on the results of the visual control experiment in [146].

The design of the visual control experiment in [146] is similar to that of our experiment. However, instead of multiple interaction conditions, it contains multiple solo conditions with different levels of visual noise. In one of these conditions, the parameterization of the visual noise is identical to that in our experiment. Thus, we calculate the ratio between the tracking errors e_θ of this condition and those of the condition without visual noise and use this ratio to generate the noisy scenario equivalents of the clean scenario tracking errors e_θ of our experiment. This procedure is executed analogously in order to obtain the noisy scenario equivalents of the clean scenario coactivation $a_{\mathrm{CA,n}}$ of our experiment.

The moment of inertia ι in the simulation, which represents the combined effects of the hand and the manipulandum of the wrist interface in our experiment, is set to 0.005 kgm^2, based on empirical values from the literature [151–154]. In order to ensure physiological plausibility of the motor behavior in our simulated data, we include a lower bound of the wrist stiffness k_{w} in the implementation of the coactivation modulation model. Based on empirical values of passive flexion/extension wrist stiffness from the literature, this lower bound of the wrist stiffness k_{w} is set to 2.0 Nm/rad [155–158].

Remark 5.11. In [151], the dynamics of the wrist are modeled as a second order system and the moment of inertia of the hand and the manipulandum is set to 0.005 kgm^2, based on experimental observations. In [152], the moment of inertia of the hand is reported to lie in the range of $0.0031 - 0.0037$ kgm^2. In [153], it is reported to be 0.0039 kgm^2. In [154], the moment of inertia of the hand and the manipulandum is reported to lie in the range of $0.0032 - 0.0054$ kgm^2, with an average value of 0.0047 kgm^2, of which the contribution of the manipulandum is reported to be 0.0013 kgm^2.

Remark 5.12. In [155] and [156], passive flexion/extension wrist stiffness is reported to lie in the approximate ranges of $0.7 - 1.2$ Nm/rad and $0.8 - 1.1$ Nm/rad, respectively. In [157], it is repeatedly estimated over a period of 11 days and continuously reported to be approximately 2.0 Nm/rad. In [158], passive flexion/extension wrist stiffness is estimated in constant load conditions and reported to lie in the approximate range of $2.0 - 3.0$ Nm/rad.

5.5.2. Simulation Design

The simulation is designed based on the design of our experiment presented in Section 5.4.2. The virtual spring stiffness k_{VC} is set to a fixed value of 17.2 Nm/rad. The target trajectories are defined by the multi-sine function (5.35) and the procedure for the random selection of the starting times $t_{\mathrm{t},0}$ is identical to that in our experiment. The visual observation noise ν_{v} and the haptic observation noise ν_{h} are generated by normally distributed random variables. In order to avoid bias due to these random definitions, each condition contains 50 trials. Analogous to the trials in our experiment, each of these 50 trials lasts 20 s.

According to a parameter sensitivity analysis conducted in [49], the predictive power of the simulation is relatively insensitive to changes in the process noise variance σ_ω^2 and the configuration of the LQR that determines the reciprocal activation torque τ_{RA}, i.e., the state weight matrix Q and the input weight r. In order to avoid increased spectral content for high frequencies, i.e., decreased physiological plausibility of the wrist movements, we define the process noise variance $\sigma_\omega^2 = 10$ $\mathrm{rad}^2/\mathrm{s}^4$. In order for the LQR to generate reciprocal activation torques τ_{RA} that are sufficiently small to necessitate contributions by coactivation torques τ_{CA}, the state weight matrix $Q = \mathrm{diag}\{1, 1\}$ and the input weight $r = 10$.

The parameters of the coactivation modulation model are defined heuristically to obtain values of the wrist stiffness k_{w} that are both similar to the results obtained in our experiment as well as plausible with respect to empirical values from the literature. For the model of the error function η_{err}, the correlation parameter $\alpha_{\mathrm{err}} = 2.5 \cdot 10^3$ Nm/rad^{2}s and the interval size parameter $\beta_{\mathrm{err}} = 0.2$. The metabolic cost parameter $\alpha_{\mathrm{meta}} = 3$ Nm/rads. The parameters of the different models of the interaction function η_{int} only influence the wrist stiffness k_{w} during interaction conditions. For the second model, the correlation parameters of the two model variations $\alpha_{\mathrm{int,2a}} = 100$ Nm/rad^{2}s and $\alpha_{\mathrm{int,2b}} = 500$ Nm/rad^{2}s. For the third model, the correlation characteristics slope parameter $\alpha_{\mathrm{int,3}} = 12 \cdot 10^3$ Nm/rad^{3}s and the intercept parameter $\beta_{\mathrm{int,3}} = 1.1 \cdot 10^3$ Nm/rad^{2}s. The plausibility of the obtained values of the wrist stiffness k_{w} with respect to empirical values from the literature is discussed in Section 5.6.

Remark 5.13. In order to exclude adaptation processes at the beginning of the experimental conditions, especially with respect to the solo trials before interaction, the first two trials of each condition are excluded in the calculation of the experimental data that is used for the comparison with the simulated data.

5.5.3. Evaluation

The evaluation of the simulated data is centered around the tracking error e_θ and the wrist stiffness k_{w}, with specific focus placed on the relative within-subject differences in the modulation of the wrist stiffness k_{w} and the comparison to the respective differences in the modulation of the coactivation $a_{\mathrm{CA,n}}$ in the experimental data. In order to be able to compare the data of the simulation and the experiment, we normalize the wrist stiffness k_{w} with the respective results of the clean scenario solo conditions:

$$k_{\mathrm{w,n}} = (k_{\mathrm{w}} / \overline{k}_{\mathrm{w}})\, \overline{a}_{\mathrm{CA,n}} \ ,$$

where $k_{\mathrm{w,n}}$ is the normalized wrist stiffness, $\overline{k}_{\mathrm{w}}$ is the overall mean of the wrist stiffness in the clean scenario solo condition in the simulated data, and $\overline{a}_{\mathrm{CA,n}}$ is the overall mean of the coactivation in the clean scenario solo condition in the experimental data. For simplicity, we refer to the resulting normalized wrist stiffness $k_{\mathrm{w,n}}$ simply as wrist stiffness $k_{\mathrm{w,n}}$.

Remark 5.14. The analysis of the simulation is based on mean results of the variables, either averaged over 1) trials within conditions, or 2) time within conditions. The corresponding experimental data is given by the mean results of the relevant variables, either averaged over 1) trials within conditions and participants, or 2) time within conditions and participants. For simplicity, from this point on, we refer to these mean results of the simulated and the experimental data simply as 1) temporal mean results and 2) overall mean results.

Remark 5.15. For clarity, the abbreviations for the conditions defined in Section 5.4.4 are extended by a subscript that indicates whether the abbreviation refers to the condition in the simulated data (S) or the experimental data (E), e.g., the abbreviation $\mathrm{CC_S}$ refers to the *subject clean - partner clean* condition in the simulated data. Furthermore, as we are not differentiating between solo trials before and after interaction anymore, but instead additionally considering the data of solo trials with visual noise, the conditions and respective abbreviations for the solo trials before interaction (S1) and after interaction (S2) are replaced by the solo clean trials (SC) and the solo noisy trials (SN).

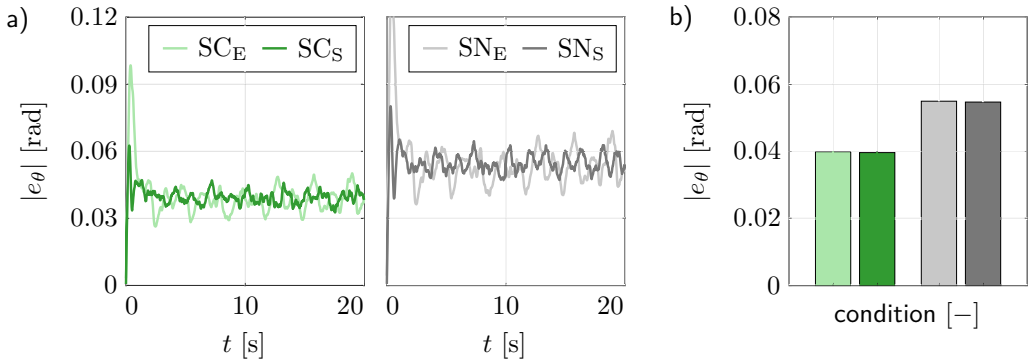

Figure 5.10.: Mean results of coactivation modulation model in solo conditions. Comparison of absolute tracking error $|e_\theta|$ in simulation and experiment data: a) temporal mean results, b) overall mean results.

In the remainder of this section, we first analyze the absolute tracking error $|e_\theta|$ and the wrist stiffness $k_{\mathrm{w,n}}$ produced by the coactivation modulation model for the solo conditions and subsequently we proceed analogously for the interaction conditions.

Solo conditions

In this section, we evaluate the coactivation modulation model by analyzing the results of the solo conditions in the simulated data and comparing them to the respective results in the experimental data. As the interaction function in the coactivation modulation model only contributes to the modulation of wrist stiffness during physical interaction with the partner, the results are presented without focus on the variations of the interaction model.

Fig. 5.10 shows the temporal and overall mean results of the absolute tracking error in the solo conditions. The temporal mean results in Fig. 5.10a show similar temporal evolutions for the simulated and the experimental data. In both conditions, the amplitude of the prominent spike at the beginning of the trial is substantially lower in the simulated data than it is in the experimental data. In the simulated data, the sudden but short increase in amplitude at the beginning of the trial is caused by the fact that it takes a certain amount of time for the wrist stiffness to be sufficiently large to allow for accurate tracking of the movements of the target. Once this sufficiently large wrist stiffness is reached, analogous to the experimental data, the absolute tracking error oscillates at a lower level, inbetween condition-dependent lower and upper bounds. Thus, this difference between the simulated and the experimental data suggests that the increase in amplitude at the beginning of the trial is not entirely caused by an adaptation process, but also partially caused by sensory delays of the participants, which are not explicitly incorporated in our implementation. The overall mean results in Fig. 5.10b demonstrate that, despite these minor differences, the definition of the visual observation noise variances based on the polynomial fit described in Section 5.5.1 produces absolute tracking errors in the simulated data that are extremely similar to those in the experimental data.

Remark 5.16. It should be noted, that the increased amplitude of the prominent spike in SN_E compared to that in SC_E could be an erroneous byproduct of the generation of the respective experimental data based on the results of the visual control experiment in [146].

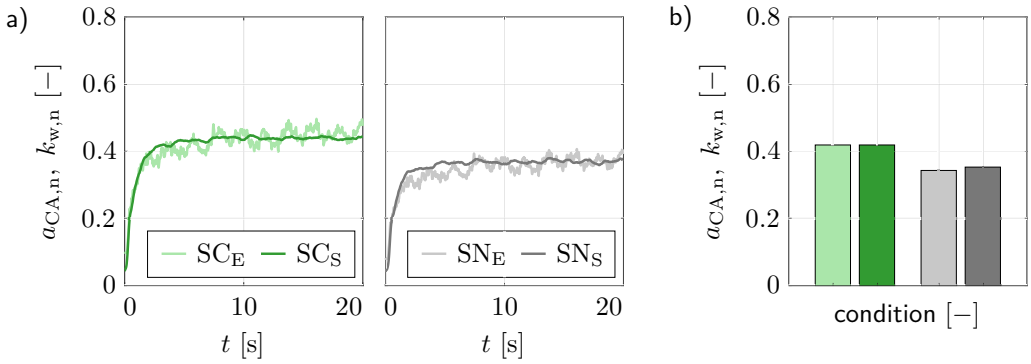

Figure 5.11.: Mean results of coactivation modulation model in solo conditions. Comparison of wrist stiffness $k_{w,n}$ in simulation data and coactivation $a_{CA,n}$ in experiment data: a) temporal mean results, b) overall mean results.

Fig. 5.11 presents the temporal and overall mean results of the wrist stiffness and the coactivation in the solo conditions. The temporal mean results in Fig. 5.11a show similar temporal evolutions for the simulated and the experimental data, with slightly increased amounts of noise in the experimental data of both conditions due to the generally noisy nature of EMG data. The temporal mean results demonstrate that the coactivation modulation model is able to reproduce the rapid increase at the beginning of the trial and the difference in levels between the two conditions. The rapid increase of the wrist stiffness at the beginning of the trial is caused by the large absolute tracking errors that are observable in the respective temporal mean results in Fig. 5.10a. With the increase in wrist stiffness, the absolute tracking errors decrease, until the interdependency of the effects of the tracking error and the minimization of the metabolic cost ultimately result in the convergence of the wrist stiffness to an approximately constant level. Due to the inclusion of the error estimate SD in the error function of the coactivation modulation model, this approximately constant level of convergence is influenced by the visual noise scenario. This influence is also clearly visible in the overall mean results in Fig. 5.11b, which demonstrate that the coactivation modulation model produces differences in levels of the wrist stiffness in the simulated data that are extremely similar to those of the coactivation in the experimental data.

Interaction conditions

In this section, we evaluate the coactivation modulation model by analyzing the results of the interaction conditions in the simulated data and comparing them to the respective results in the experimental data. As the interaction function in the coactivation modulation model now contributes to the modulation of wrist stiffness, the results are presented and evaluated individually for each of the different variations of the interaction model.

Fig. 5.12 shows the temporal and overall mean results of the absolute tracking error in the interaction conditions with interaction model 1. The general temporal characteristics in the temporal mean results in Fig. 5.12a are similar to those in the solo conditions, which are presented in Fig. 5.10a. However, in the interaction conditions, there are differences in levels between the simulated and the experimental data. These differences in levels are more apparent in the respective overall mean results in Fig. 5.12b, which show that the absolute tracking errors in the simulated data are generally decreased in comparison to those in the

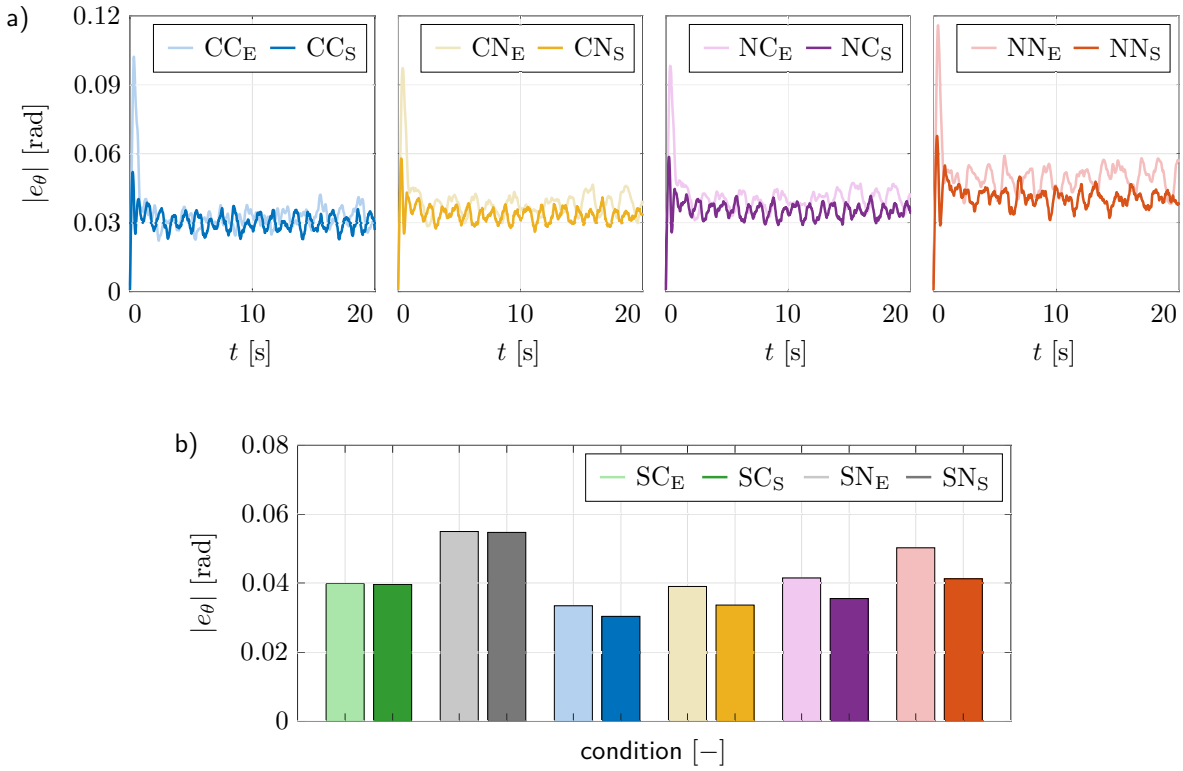

Figure 5.12.: Mean results of coactivation modulation model in interaction conditions with interaction function $\eta_{\text{int},1}$. Comparison of absolute tracking error $|e_\theta|$ in simulation and experiment data: a) temporal mean results, b) overall mean results (for comparison, including respective solo conditions).

experimental data. Despite this general decrease, the relative differences in levels between the different interaction conditions in the simulated data are nonetheless similar to those in the experimental data. Thus, while the general effect of mutual tracking performance improvement due to physical interaction with the partner is being simulated correctly, the extent of the improvement is being simulated incorrectly, resulting in larger improvement in the simulated data than in the experimental data.

Remark 5.17. The reason for this discrepancy is that the virtual spring observation noise variance is generated based on the analysis of the haptic tracking task experiment in [49]. This experiment does not contain the same target trajectories as our experiment and more importantly, the implementation of the simulation that is used in the analysis is not the same as our implementation. Thus, the resulting input value for the polynomial fit that generates the virtual spring observation noise variance is not equally valid for our implementation. The effects of a larger input value and virtual spring observation noise variance are analyzed and discussed in Section 5.6. For the remainder of this section, we focus on the modulation of the wrist stiffness in the different variations of the interaction model.

Fig. 5.13 presents the temporal and overall mean results of the wrist stiffness and the coactivation in the interaction conditions with interaction model 1. The general temporal characteristics in the temporal mean results in Fig. 5.13a are similar to those in the solo conditions, which are presented in Fig. 5.11a. However, in the interaction conditions, there

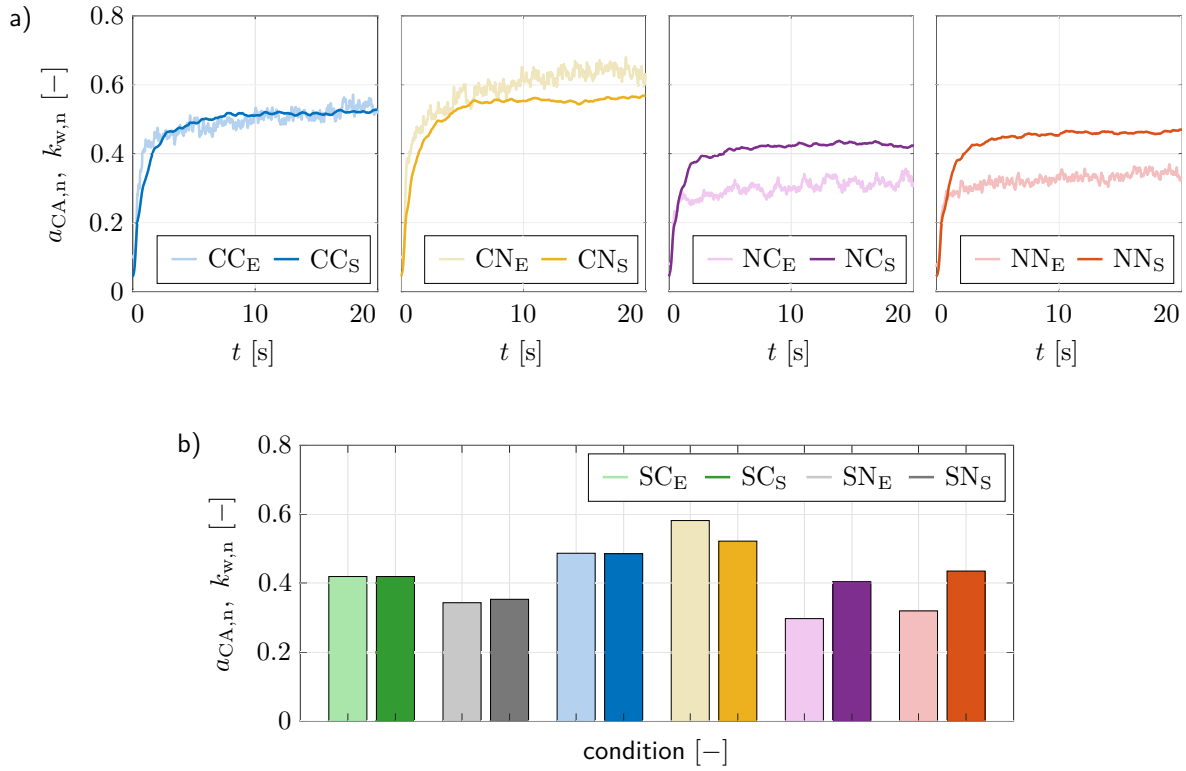

Figure 5.13.: Mean results of coactivation modulation model in interaction conditions with interaction function $\eta_{\text{int},1}$. Comparison of wrist stiffness $k_{\text{w,n}}$ in simulation data and coactivation $a_{\text{CA,n}}$ in experiment data: a) temporal mean results, b) overall mean results (for comparison, including respective solo conditions).

are significant differences in levels between the simulated and the experimental data. In CN, the wrist stiffness in the simulated data is decreased compared to the coactivation in the experimental data. In NC and NN, the wrist stiffness in the simulated data is substantially increased compared to the coactivation in the experimental data. CC is the only condition without significant differences in levels between the simulated and the experimental data. The overall mean results in Fig. 5.13b show that, in the simulated data, the wrist stiffness is generally increased in the interaction conditions compared to the respective solo conditions, i.e., it is increased both in CC_S and CN_S compared to SC_S as well as in NC_S and NN_S compared to SN_S.

Remark 5.18. The physical interaction with the partner results in an improved error estimate with decreased error estimate SD. The improved error estimate allows for mutual tracking performance improvement with decreased tracking errors, which are observable in the overall mean results in Fig. 5.12b. However, while decreased distance between estimated target angle and target angle results in similarly decreased tracking error, i.e., distance between wrist angle and target angle, it does not necessarily result in similarly decreased estimated tracking error, i.e., distance between wrist angle and estimated target angle. Thus, the combination of estimated tracking error and error estimate SD in the error function of the coactivation modulation model leads to a general increase in wrist stiffness due to physical interaction with the partner.

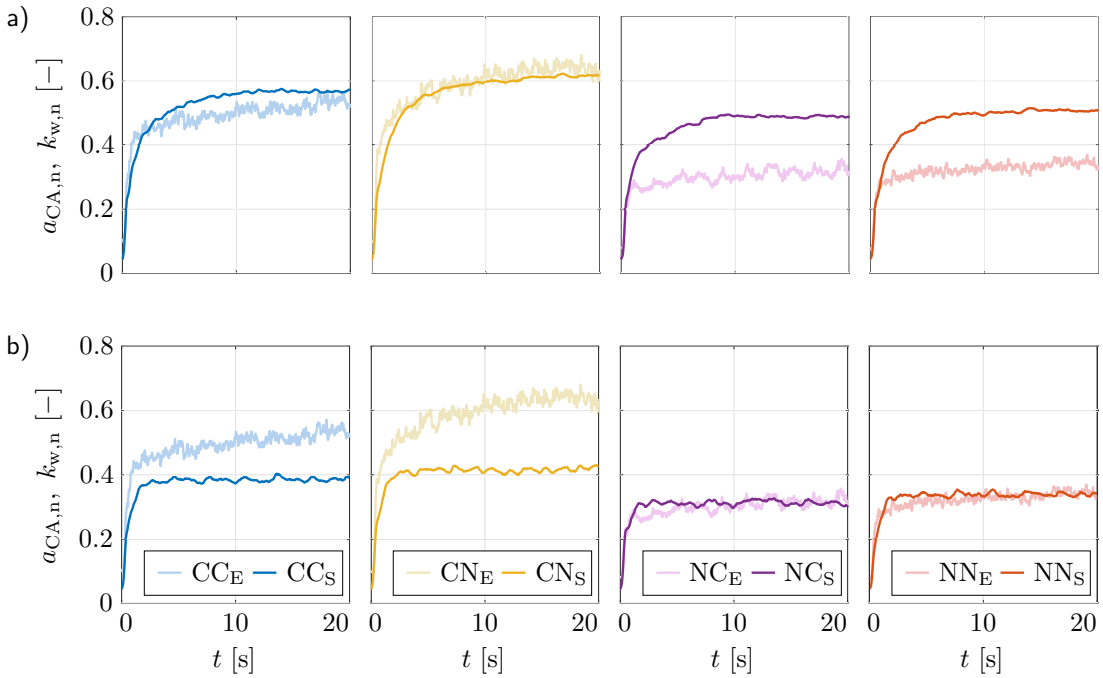

Figure 5.14.: Mean results of coactivation modulation model in interaction conditions with interaction function $\kappa_{\mathrm{int,2}}$. Comparison of wrist stiffness $k_{\mathrm{w,n}}$ in simulation data and coactivation $a_{\mathrm{CA,n}}$ in experiment data: a) variation 2a with interaction function $\kappa_{\mathrm{int,2a}}$, b) variation 2b with interaction function $\kappa_{\mathrm{int,2b}}$.

The temporal and overall mean results in Fig. 5.13 show that the coactivation modulation model with interaction model 1, i.e., without an explicit change in wrist stiffness due to physical interaction with the partner, is not able to accurately reproduce the modulation of the coactivation in the experimental data.

Fig. 5.14a presents the temporal mean results of the wrist stiffness and the coactivation in the interaction conditions with interaction model 2a (the respective overall mean results are omitted for brevity). The temporal mean results show that, compared to the respective results of interaction model 1 in Fig. 5.13a, CN is the only condition, in which a general increase in wrist stiffness results in a more accurate representation of the coactivation in the experimental data. In CC, the wrist stiffness in the simulated data is now increased compared to the coactivation in the experimental data. In NC and NN, the wrist stiffness in the simulated data is still increased compared to the coactivation in the experimental data, but with increased differences in levels.

The temporal mean results with interaction model 2b in Fig. 5.14b show that, compared to the respective results of interaction model 1 in Fig. 5.13a, NC and NN are the only conditions, in which a general decrease in wrist stiffness results in a more accurate representation of the coactivation in the experimental data. In CC and CN, the wrist stiffness in the simulated data is now substantially decreased compared to the coactivation in the experimental data. Thus, the temporal mean results in Fig. 5.14a and Fig. 5.14b show that the coactivation modulation model with interaction model 2a or model 2b, i.e., with a general increase or decrease in wrist stiffness due to physical interaction with the partner, are also not able to accurately reproduce the modulation of the coactivation in the experimental data.

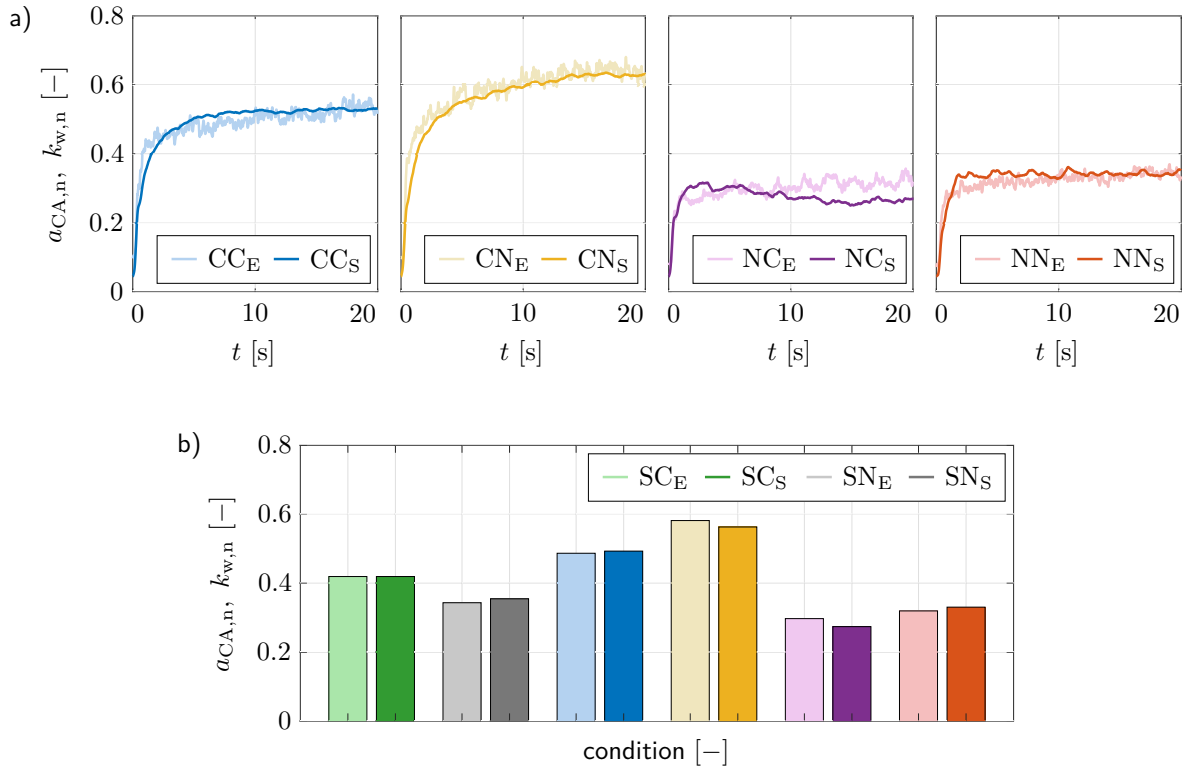

Figure 5.15.: Mean results of coactivation modulation model in interaction conditions with interaction function $\eta_{\mathrm{int},3}$. Comparison of wrist stiffness $k_{\mathrm{w,n}}$ in simulation data and coactivation $a_{\mathrm{CA,n}}$ in experiment data: a) temporal mean results, b) overall mean results (for comparison, including respective solo conditions).

Fig. 5.15 presents the temporal and overall mean results of the wrist stiffness and the coactivation in the interaction conditions with interaction model 3. The results show that, compared to the respective results of interaction model 1 in Fig. 5.13, the representation of the coactivation in the experimental data is either similarly accurate (CC) or substantially more accurate (CN, NC, NN). Apart from NC, the temporal mean results in Fig. 5.15a show extremely similar temporal evolutions for the simulated and the experimental data.

Remark 5.19. In $\mathrm{NC_S}$ and $\mathrm{NN_S}$, the large amount of visual noise in the visual feedback, which corresponds to low confidence in the individual contribution, results in a decrease in wrist stiffness due to the physical interaction with the partner. As this decrease in wrist stiffness in $\mathrm{NC_S}$ does not only resemble a decrease in resistance towards the effects of the physical interaction with the partner, but also a decrease in contribution to the overall movement torque of the dyad, it is compensated by an increase in wrist stiffness in $\mathrm{CN_S}$. The interdependency of these two effects is also the cause for the slight decrease in wrist stiffness after the rapid increase at the beginning of the trial in $\mathrm{NC_S}$.

The overall mean results in Fig. 5.15b show that, despite these minor differences between $\mathrm{NC_S}$ and $\mathrm{NC_E}$, the coactivation modulation model with interaction model 3, i.e., with a change in wrist stiffness due to physical interaction with the partner that is correlated with the visual noise in the visual feedback, is able to accurately reproduce the modulation of the coactivation in the experimental data.

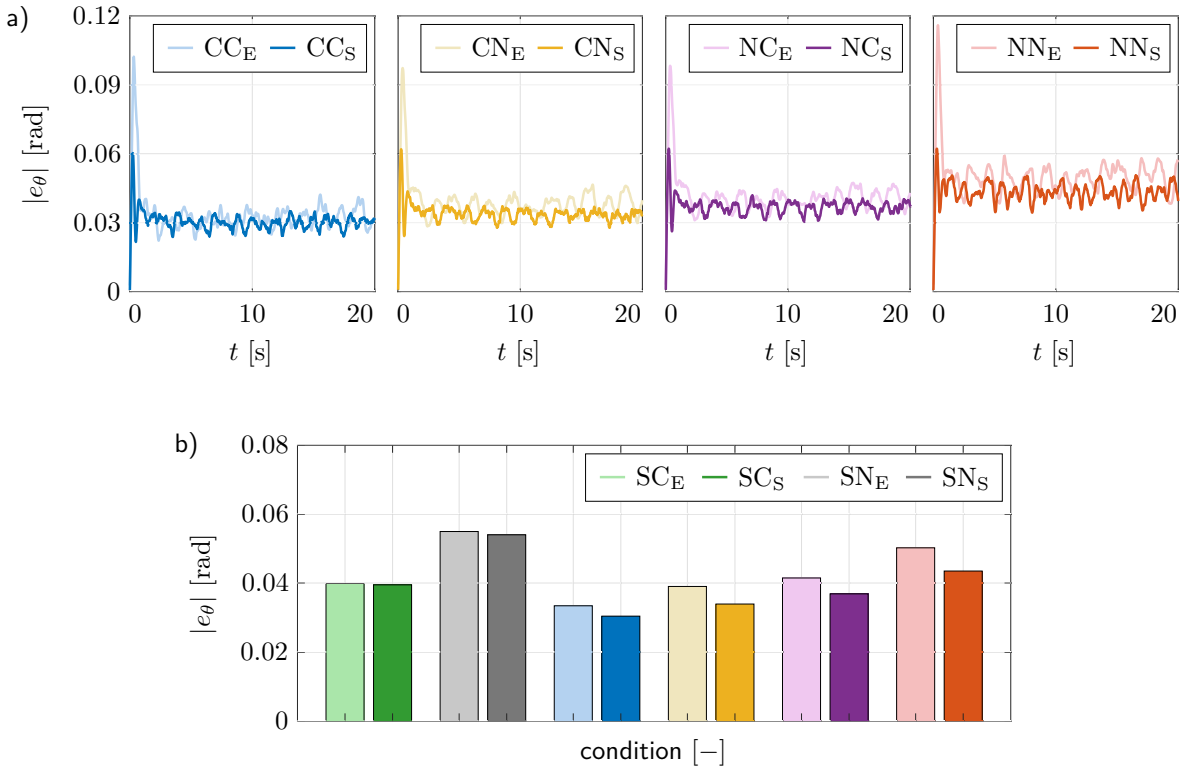

Figure 5.16.: Mean results of coactivation modulation model in interaction conditions with interaction function $\eta_{\text{int},3}$. Comparison of absolute tracking error $|e_\theta|$ in simulation and experiment data: a) temporal mean results, b) overall mean results (for comparison, including respective solo conditions).

Fig. 5.16 shows the temporal and overall mean results of the absolute tracking error in the interaction conditions with interaction model 3. The results look similar to those of interaction model 1 in Fig. 5.12. The only difference between the results is that the differences in levels between the simulated and the experimental data in NC and NN are marginally decreased. The corresponding increases in absolute tracking errors are caused by the decreases in wrist stiffness in NC_S and NN_S. These minor differences between the results show that the extent of the mutual tracking performance improvement is only slightly influenced by the wrist stiffness and predominantly depends on the definition of the virtual spring observation noise variance. Therefore, the effects of a larger virtual spring observation noise variance are analyzed and discussed in the next section.

5.6. Discussion

In order to analyze the effects of an increase of the virtual spring observation noise variance on the mutual tracking performance improvement due to physical interaction with the partner, we increase the associated input value for the second order polynomial fit to approximately three times its original value (from 0.4372 deg | 0.00763 rad to 1.50 deg | 0.02618 rad). The resulting temporal and overall mean results of the absolute tracking error for interaction model 3 in Fig. 5.17 show that the increase of the virtual spring observation noise variance results in substantially more accurate representations of the absolute tracking errors in the

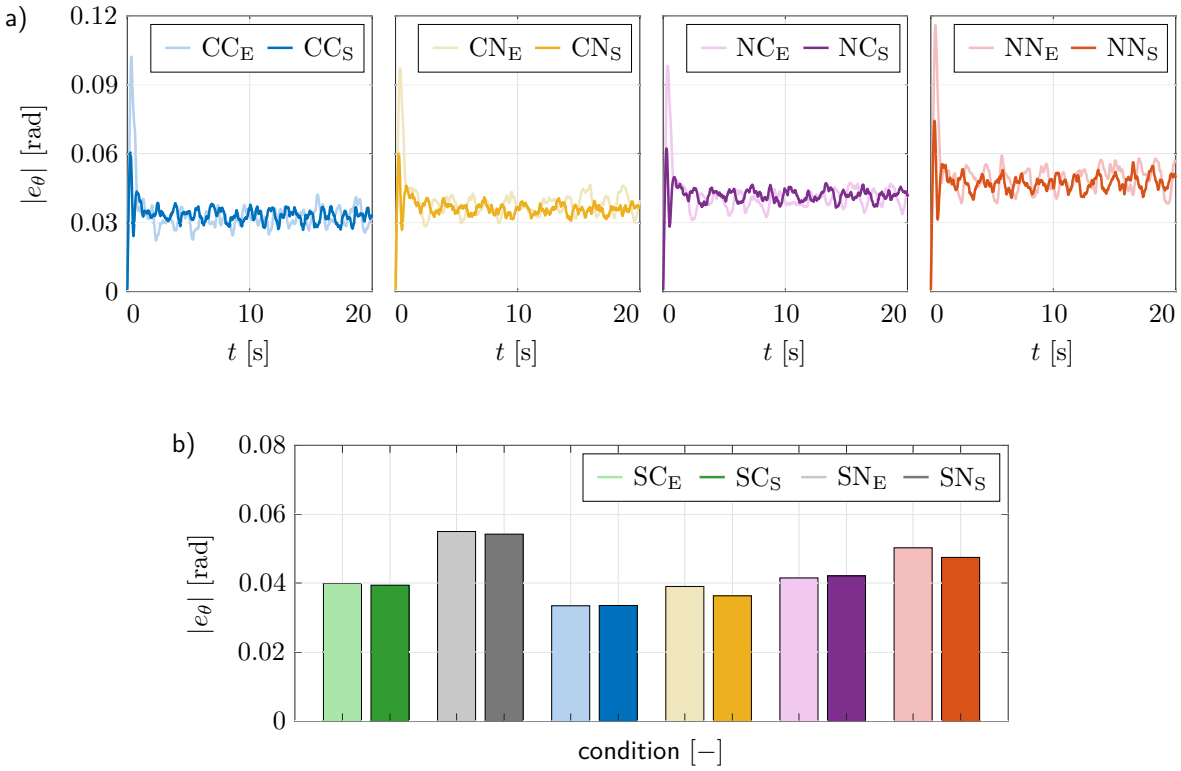

Figure 5.17.: Mean results of coactivation modulation model in interaction conditions with interaction function $\eta_{\text{int},3}$ and increased value of virtual spring variance σ^2_{VC}. Comparison of absolute tracking error $|e_\theta|$ in simulation and experiment data: a) temporal mean results, b) overall mean results (for comparison, including respective solo conditions).

experimental data. Fig. 5.18 shows the corresponding temporal and overall mean results of the wrist stiffness and the coactivation for interaction model 3. Compared to the respective results for interaction model 3 without increased virtual spring observation noise variance in Fig. 5.15, the wrist stiffness is similar in CC_S and NN_S, slightly increased in CN_S, and slightly decreased in NC_S. In CN_S and NC_S, the decrease in quality of the exchanged haptic information in the form of the increased uncertainty results in differently large increases of error estimate variance for the noisy participant and the clean participant. The increase of error estimate variance in NC_S is apparently so large, that the corresponding decrease in wrist stiffness requires compensation by an increase in wrist stiffness in CN_S.

The analysis of the effects of an increase of the virtual spring observation noise variance illustrates that the inclusion of the coactivation modulation model does not contradict the accurate representation of the mutual tracking performance improvement due to physical interaction with the partner. However, appropriate definition of the associated input value for the second order polynomial fit requires further analyses based on more comprehensive experimental data. This also applies to a more general definition of the parameters of the coactivation modulation model, which, in this work, are defined based on heuristics to obtain values of the wrist stiffness that are both similar to the results of the experiment and plausible with respect to empirical values from the literature. In future work, we aim to acquire more comprehensive experimental data that will allow for more general analysis and

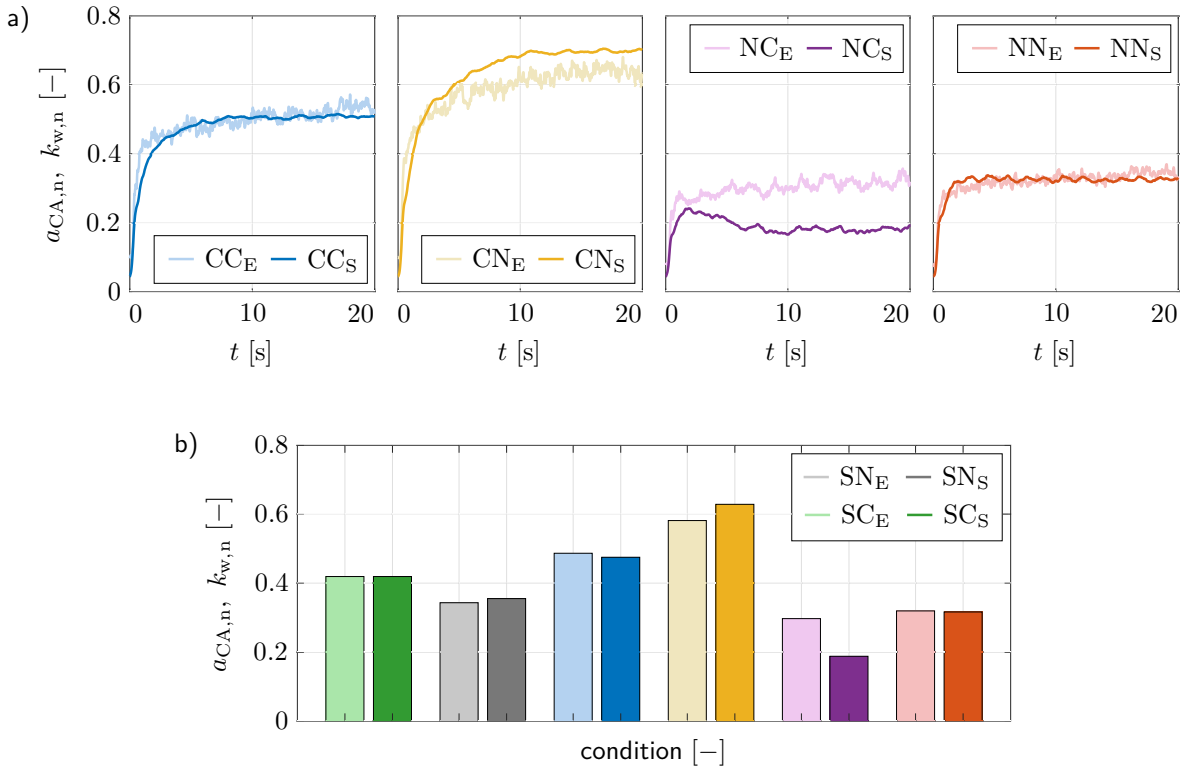

Figure 5.18.: Mean results of coactivation modulation model in interaction conditions with interaction function $\eta_{\mathrm{int,3}}$ and increased value of virtual spring variance σ^2_{VC}. Comparison of wrist stiffness $k_{\mathrm{w,n}}$ in simulation data and coactivation $a_{\mathrm{CA,n}}$ in experiment data: a) temporal mean results, b) overall mean results (for comparison, including respective solo conditions).

parameterization based on solo and interaction trials with multiple levels of visual noise in the visual feedback of the participants. This experimental data will also allow for elimination of the approximation of the noisy scenario solo trial data via calculation of equivalents of the clean scenario solo trial data based on the results of existing studies.

Despite the necessity of further analyses based on more comprehensive experimental data, we are able to demonstrate that the coactivation modulation model is capable of accurately reproducing modulation of coactivation, both during individual and dyadic execution of a shared tracking task. The analysis of the solo trials demonstrates that the inclusion of the error estimate variance in the error function of the coactivation modulation model provides accurate representations of the differences in levels between the different visual noise scenarios. The analysis of the interaction trials demonstrates that proper functionality of the coactivation modulation model requires the inclusion of an interaction function that models the explicit change in coactivation due to physical interaction with the partner and that correlation of this change with the visual noise in the visual feedback yields accurate representations of the modulation of the coactivation in the experimental data.

In order to assess the plausibility of the values of the wrist stiffness, we calculate the maximum values of the temporal mean results of the wrist stiffness in the simulated data of the coactivation modulation model with interaction model 3. The resulting maximum values range between 17.19 Nm/rad (SN) and 20.13 Nm/rad (SC) in the solo conditions

and 14.24 Nm/rad (NC) and 28.60 Nm/rad (CN) in the interaction conditions and are plausible with respect to empirical values from the literature. In [159], wrist stiffness is estimated during coactivation in an experiment, in which participants have to stabilize a mechanically unstable load with the characteristics of a negative spring. The resulting estimates of the wrist stiffness during coactivation are reported to lie in the approximate range of $8.0 - 32.0$ Nm/rad. In [160], wrist stiffness is estimated in non-ischaemic conditions with intact stretch reflex and in ischaemic conditions with abolished stretch reflex and the resulting estimates of the wrist stiffness are reported to be 12.0 Nm/rad with abolished stretch reflex and 25.8 Nm/rad with intact stretch reflex. In [161], wrist stiffness during flexion and extension is estimated in healthy sedentary subjects and in volleyball players. The resulting wrist stiffness estimates during flexion are reported in the approximate range of $4.0 - 37.0$ Nm/rad and the wrist stiffness estimates during extension are reported in the approximate range of $5.0 - 23.0$ Nm/rad. In [162], a realistic musculoskeletal model is used to simulate and investigate the change in wrist stiffness due to coactivation. The wrist stiffness simulated by the musculoskeletal model during coactivation is reported to lie in the approximate range of $5.0 - 42.0$ Nm/rad, with an average value of 28.7 Nm/rad.

The analysis of the absolute tracking error in the temporal mean results of the solo and the interaction conditions suggests that the increase in amplitude at the beginning of the trial is not entirely caused by an adaptation process of the wrist stiffness, but also partially caused by sensory delays of the participants. The effects of such sensory delays can be incorporated into the neuromechanical model and the corresponding implementation by firstly obtaining the estimated state vector for a delayed time step and subsequently using a forward model of the full state equation of the tracking dynamics to predict the estimated state vector for the current time step. For simplicity, in this work, we instead assume that the effects of sensory delays are sufficiently represented by the contents of the observation noise covariance matrix. In future work, we aim to explicitly incorporate sensory delays and examine their effects on the interaction behavior. Specifically, we aim to investigate the effects of physiologically accurate definitions of different sensory delays for the full state feedback control of the reciprocal activation and the impedance control of the coactivation, both on the mutual improvement of the tracking performance and on the modulation of the coactivation.

5.7. Summary

In this chapter, we examine modulation of muscle coactivation in cooperative physical HHI. We perform an experiment, in which two individuals use wrist flexion/extension movements to track pseudo-random movements of a shared target, while being physically coupled by a virtual spring and each experiencing two different levels of visual noise in their respective visual feedback. Consequently, we are able to observe how different levels of visual noise, which correspond to different levels of tracking performance, affect motor adaptation in the form of modulation of muscle coactivation in both individuals. In order to describe the motor behaviors of the two individuals, both during individual and dyadic task execution, we formulate a neuromechanical model that is based on the neuromechanical goal sharing model presented in [49], with the novelty lying in the differentiation of reciprocal activation and coactivation as well as the inclusion of a coactivation modulation model. We propose three different variations of the coactivation modulation model that differ in the definition of the interaction function. In order to enable functional assessment of the different variations,

we implement a simulation that emulates the conditions in our experiment. The evaluation of the experimental data demonstrates that the coactivation is generally larger in subject clean conditions than it is in subject noisy conditions. In the subject noisy conditions, there is little difference in coactivation between the interaction with a clean partner and the interaction with a noisy partner. In contrast, in the subject clean conditions, the coactivation is significantly larger in the interaction with a noisy partner than it is in the interaction with a clean partner. The evaluation of the simulated data demonstrates that the coactivation modulation model is able to accurately reproduce modulation of coactivation, both during individual and dyadic task execution. The analysis of the interaction trials demonstrates that proper functionality of the model requires the inclusion of an interaction function that models the explicit change in coactivation due to physical interaction with the partner and that correlation of this change with the amount of visual noise in the visual feedback yields accurate representations of the modulation of the coactivation in the experimental data.

6. Conclusions and Future Directions

Immediate robotic assistance through physical HRI necessitates control strategies that are designed to provide efficient and intuitive interaction. Furthermore, these control strategies must avoid instability, ill-defined robot behavior, and mismatched interaction behavior in order to guarantee safety and comfort of the human. The relevance of this scenario, today and in the near future, is motivated by the versatile capabilities of state-of-the-art robotics technology and substantiated by the numerous application domains, which range from agricultural and industrial manufacturing to medical and domestic service domains. All of these application domains of physical HRI have in common that due to the direct physical coupling of human and robot, development of suitable control strategies requires consideration of human motor behavior, especially the immediate feedback behavior in response to robot behavior. As this immediate feedback behavior is instantiated by human impedance control, the corresponding impedance characteristics represent an instrumental contribution for the control design process. The present thesis provides a comprehensive composition of instruments and insights to facilitate systematic and efficient consideration of human impedance characteristics in the control design process for physical HRI.

Summary of Contributions

In this thesis, we provide contributions for three crucial open challenges in the inclusion of human impedance control research in the development of safe and efficient physical HRI control strategies. We begin by enabling the information exploitation, i.e, the inclusion of a priori impedance knowledge within the context of human motor behavior modeling. Subsequently, we facilitate the information acquisition, i.e., the estimation of impedance components for realistic physical HRI. Finally, we investigate the information alteration, i.e., the impedance modulation strategies of human dyads during cooperative physical HHI.

Inclusion of impedance knowledge in human motor behavior modeling

In Chapter 3, we enable the information exploitation by presenting a method for modeling human motor behavior during physical and non-physical HRI that explicitly includes an impedance control model that compensates deviations from a desired trajectory. We adopt a Bayesian perspective by assuming GP priors for the desired trajectory as well as the impedance components. Based on these GP prior definitions, we derive compound kernels for the impedance and the interaction force. Together, these compound kernels form a multi-layered Bayesian human motor behavior model, which allows for the exploitation of a priori knowledge of human impedance characteristics for the regression of human motor behavior during physical and non-physical HRI. The regression of the human motor behavior

necessitates the inference of the human motor intention in the form of the desired trajectory. Consequently, the multi-layered Bayesian human motor behavior model is both a predictor of human motor behavior as well as an observer of human motor intention. Validation of the method with simulated data demonstrates superior prediction performance with respect to a naive GP prior for multiple parameterizations of the desired trajectory. As the validation in simulation reveals a dependency between prediction performance and the parameters of the GP priors, an overview of estimated human arm impedance characteristics is presented and implications for proper prior parameterization are discussed. Applicability of the method to real data as well as effects of training data sparsity are evaluated with experimental data. The results demonstrate that the generalization capabilities of the model allow for reliable human motor behavior predictions in previously unobserved regions of the input space.

Estimation of impedance components for realistic physical HRI

In Chapter 4, in order to facilitate the information acquisition, we present a method for the estimation of the impedance components in experiments that emulate realistic physical HRI scenarios. By incorporating dynamic regressor representation, we are able to formulate an impedance control model that is linear in all impedance components. By limiting the duration of the estimation interval to the minimum delay of voluntary feedback, we are able to ensure that the estimated impedance components do not contain contributions from voluntary feedback. In order to obtain estimates of the unperturbed states, we apply force perturbations that are designed such that the evoked feedback jerk frequency content can be isolated with a high pass filter. The impedance components are estimated in two separate tasks. We begin by estimating the inertial parameters in a static postural task and subsequently use them to estimate the damping and stiffness in a dynamic movement task. Validation of the method with simulated data shows that it provides superior estimation performance in comparison to the results obtained by application of existing impedance estimation methods within identical conditions. Analysis of the feedback jerk isolation for different movement velocities and variations of neural noise shows that it is able to provide superior estimation performance for movements with moderate to low velocities and is much less affected by an increase in movement variability. Applicability of the method to real data and plausibility of the estimation interval duration are evaluated with experimental data. The results demonstrate that the method allows for impedance estimation in experiments that emulate realistic physical HRI scenarios, without the need for assumptions concerning voluntary feedback behavior or inclusion of the do-not-intervene-voluntarily paradigm or comparable constraints within the respective dynamic movement tasks.

Analysis of impedance modulation strategies during physical HHI

In Chapter 5, we focus on the information alteration by investigating modulation of muscle coactivation during cooperative physical HHI. We perform an experiment, in which two individuals perform a tracking task, either individually or while being physically coupled. By including two different levels of visual noise in the respective visual feedbacks, we are able to observe how different levels of tracking performance affect motor adaptation in the form of modulation of muscle coactivation in both individuals. We describe the motor behaviors of the two individuals, both during individual and dyadic task execution, with a neuromechanical model that differentiates between reciprocal activation and coactivation.

It includes a coactivation modulation model, for which we propose three different variations that differ in the definition of the interaction function. The evaluation of the experimental data demonstrates that the coactivation is generally negatively correlated with the amount of visual noise in the visual feedback of the individual. Furthermore, it shows that, when the individual is not experiencing visual noise, the coactivation is significantly increased for the interaction with an equal partner without noise compared to an inferior partner with noise. The evaluation of the simulated data demonstrates that the coactivation modulation model is able to accurately reproduce modulation of coactivation, both during individual as well as dyadic task execution. Furthermore, the analysis of the interaction trials demonstrates that proper functionality of the model requires the inclusion of an interaction function that models the explicit change in coactivation due to physical interaction with the partner. Correlation of this interaction function with the amount of visual noise in the visual feedback of the individual allows for accurate representation of the experimental results. In summary, in this chapter, we present novel insights on modulation of coactivation during cooperative physical HHI and demonstrate that the involved uncertainties play essential roles in modeling modulation of coactivation during individual and dyadic task execution.

Outlook

Human impedance control plays an integral part in the control of motor behaviors and should play an equally integral part in the development of safe, intuitive, and efficient control strategies for physical HRI. Knowledge of the impedance components is not only crucial for stability assessment, it also enables approximation of the desired kinematic state, which represents the human motor intention and allows for improvement of performance through calculation of anticipatory control signals. In order to enable the exploitation of these advantageous aspects, this thesis provides a comprehensive composition of instruments and insights to facilitate systematic consideration of human impedance characteristics in the control design process for physical HRI. Although multiple challenges regarding human impedance control during physical interaction are addressed, several open research problems remain to be investigated in future works.

Online inference of human motor intention

In this thesis, the human motor behavior regression and intention inference capabilities of the Bayesian human motor behavior model in Chapter 3 are only applied offline. While an offline variation of the model is able to provide valuable insights and general predictions that can be incorporated in the design of future control strategies, it would nonetheless be beneficial to formulate an online variation of the model. Such a variation would be able to provide online estimations of the desired trajectory, which could be used to immediately and continuously adapt the robot behavior. Due to the computational complexity of the model, an online variation would likely require the integration of sparse or local approximations.

Impedance mappings including EMG capabilities

In Chapter 4, we assume the impedance components to be constant for the duration of the estimation interval. While this represents a valid approximation for the limited duration of the estimation interval, it would be beneficial to instead estimate general non-constant impedance functionals. With sufficient data, this would allow for the derivation of impedance mappings that span the entire workspace and provide estimates for different kinematic states. Such mappings could potentially be obtained by a variation of the Bayesian human motor behavior model in Chapter 3. Instead of including a priori impedance knowledge, one could include obtained estimates of the unperturbed states in order to estimate the conditional distributions of the impedance functionals. In addition to providing impedance estimations for previously unobserved regions of the input space and corresponding confidence levels, such an approach would also allow for the inclusion of EMG data. Therefore, the resulting impedance mappings would be able to provide impedance estimates for different kinematic states and also for different levels of muscle activation.

Optimal combination of error and interaction function

In Chapter 5, we demonstrate that, in order to accurately represent the modulation of the coactivation in the experimental data, the coactivation modulation model must include an interaction function that models the explicit change in coactivation due to the physical interaction with the partner. This represents an important insight into human motor control during physical HHI that lays the foundation for further research in this direction and more complex approaches to the coactivation modulation model. For example, it could be that the error function and the interaction function are in reality more interconnected than in the current model. Although they are not completely independent due to the inclusion of the error estimate SD and therefore also the influence of the physical interaction with the partner in the error function, they are currently not weighted in any way. It would be conceivable, that the contributions by these two functions are in reality combined in a similar way as the optimal combination of the visual and the haptic information in the iterative Kalman filter algorithm that is used to estimate the target position. Further analysis of these interdependencies requires additional experiments that provide more comprehensive data with multiple different levels of visual noise, both during solo and interaction trials.

Appendix

A.

A.1. Experiment Instructions

You will see the following image displayed on the screen in front of you during the experiment:

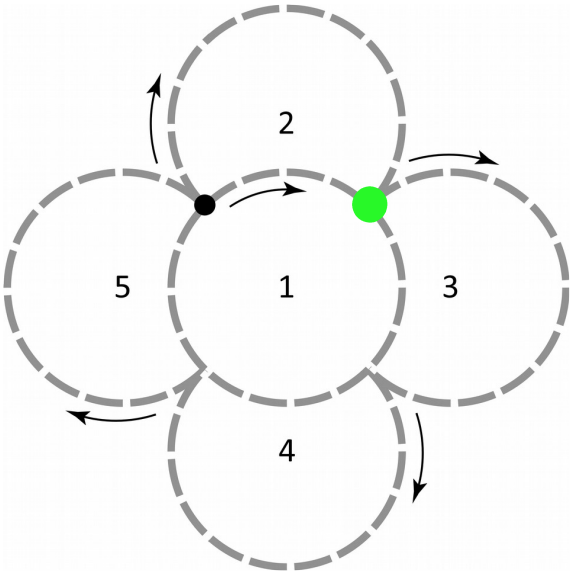

Your current position will be represented by the green dot. By moving the vertical handle on the cart in front of you, you are able to move the cart / the green dot in the 2D workspace.

Experimental procedure:

1) Move the green dot to the starting point, indicated by the black dot on the central circle.

2) Follow the reference trajectory at your own pace. The reference direction is indicated by the arrows and the reference execution order is indicated by the numbers 1-5.

3) Complete 15 repetitions of the reference trajectory without pause.

Figure A.1.: Experiment instructions for the experiment in Section 3.6.

Dear participants,
In this experiment, you will be interacting with the linear axes setup. You will be able to move the cart around in the two-dimensional workspace by applying horizontal forces to the vertical handle mounted on top of the cart. The dynamics of the cart will be rendered by an admittance that simulates a mass damper system. The position of the cart in the workspace is visualized by a dot on the screen behind the setup. During the experiment, the color of the dot will change: orange means the setup is turned off, red means the setup is turned on and the admittance is turned off (i.e. you are not able to move the cart), and green means the setup and the admittance are turned on (i.e. you are able to move the cart). Additionally, the workspace safety boundaries are visualized in the form of a boundary box. If you move across any of the four boundaries, the linear axes setup will immediately shut off. The same can be achieved by pushing the emergency shut off button, which will be located in the proximity of your left hand. In order to avoid misconfiguration of the force sensor, please do not grab the handle before the color of the dot has changed from orange to red. Furthermore, in order to minimize torques, please grab the handle at the lowest possible point.

During the experiment, in order to fix your shoulder position and limit all possible motions to those of your right arm, you will be sitting in a seat and your upper body will be restrained by a seat belt. Furthermore, in order to avoid any kind of wrist motion during the experiment, you will be wearing a wrist orthosis on your right hand. Finally, in order to constrain all possible motions to the horizontal plane and reduce effects of fatigue, your upper arm will be supported by a sling attached to the ceiling. Two passive motion tracking markers will be placed on your shoulder and elbow for measurement of position data.

Static Task

In the first part of the experiment, you will be performing a two-dimensional arm posture maintenance task. In this task, your objective is to maintain a defined arm posture within the two-dimensional workspace by naturally grasping the handle on top of the cart. As soon as the linear axes setup turns on (i.e. the color of the dot changes to red), the cart will automatically move to the first defined position, which is located at the bottom of the workspace. Once it has arrived there, please naturally grasp the handle. After a certain duration, a perturbation will deviate you from and return you to this position. During the perturbation, visualization of the current position will be deactivated (i.e. you will not see the red dot). After the perturbation, once the cart has returned to the defined position, the next trial will be initiated. After 20 trials, the defined position will be changed and the cart will automatically move to the next position. There are 5 positions (bottom, left, top, right, and center of the workspace) with 20 trials each. During this part of the experiment, the color of the dot will always be red, i.e., the admittance will always remain off and you will not be able to move the cart by applying forces to the handle. Your only objective in this task is to naturally grasp the handle on top of the cart. Please do not voluntarily react to the perturbations in any way. Furthermore, please do not prepare for the perturbations in any kind of preemptive manner.

Figure A.2.: Experiment instructions for the experiment in Section 4.6 (part 1).

Dynamic Task

In the second part of the experiment, you will be performing a two-dimensional point to point movement task. In this task, your objective is to move the cart from a defined starting position to a defined goal position in the two-dimensional workspace. This defined goal position will be displayed on the screen in front of you in the form of a gray dot, which will be located at the top of the workspace. In the beginning of the experiment, as soon as the linear axes setup turns on (i.e. the color of the dot changes to red), the cart will automatically move to the starting position, which is located at the bottom of the workspace. Once it has arrived there, please naturally grasp the handle. After a certain duration, the color of the dot will change to green. Once it is green, i.e., the admittance is turned on, your objective is to move the cart to the defined goal position. The duration of the movement should be approximately 2 seconds. In order to help you adjust your movement velocity accordingly, a beep sound will occur after 2 seconds. Once you have reached the goal position, the dot will turn back to red, the cart will automatically move back down to the starting position, and the next trial will be initiated. During some of the movements, a perturbation will deviate you from and return you to your trajectory. During the perturbation, visualization of your current position will be deactivated (i.e. you will not see the green dot).There are 60 trials and the perturbations are randomly distributed. This part of the experiment will be repeated 3 times. In this task, you are allowed to voluntarily react to the perturbations. However, analogous to the static task, please do not prepare for the perturbations in any kind of preemptive manner.

Figure A.3.: Experiment instructions for the experiment in Section 4.6 (part 2).

Experiment Instructions

In this experiment, you will be physically coupled and interacting with a human partner through wrist flexion and extension movements. You will be performing a trajectory tracking task, in which your shared goal consists of tracking a moving target as precisely as possible, i.e., minimizing the tracking error. In order to enable the assessment of your tracking performance, the tracking error will be displayed on screen at the end of each trial.

There will be two types of visual feedback: without noise and with noise. In the first scenario, the position of the tracking target is clearly visible, portrayed by a single red dot. In the second scenario, the position of the tracking target is not clearly visible, but approximated by a cloud of red dots.

It is important to note that in the scenario with visual noise: 1) none of the displayed dots represents the actual tracking target and 2) the mean of all displayed dots does not have to be identical to the actual tracking target.

Without visual noise

With visual noise

The experiment consists of four consecutive blocks of ten trials each. In each of these blocks, the two visual feedback conditions will be randomly distributed between you and your partner. This means that each of these four blocks will contain one of the following four scenarios:

Scenario	**Participant 1 (You)**	**Participant 2 (Your Partner)**
You: **without** visual noise Your partner: **without** visual noise	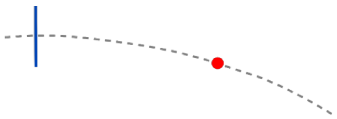	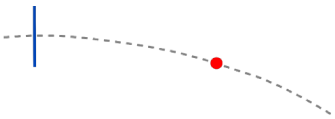
You: **with** visual noise Your partner: **without** visual noise	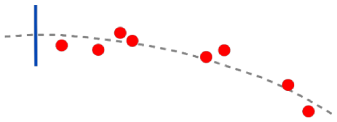	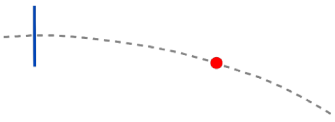
You: **without** visual noise Your partner: **with** visual noise	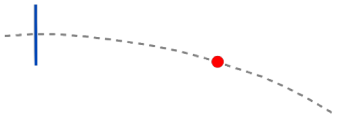	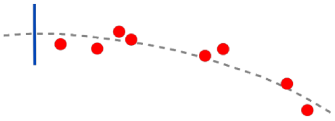
You: **with** visual noise Your partner: **with** visual noise	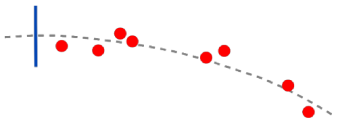	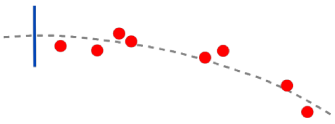

In each scenario, your only objective is to optimally cooperate with your partner in tracking the shared moving target as precisely as possible, i.e., minimizing the shared tracking error.

At the beginning of the experiment, you will perform an EMG calibration routine. Afterwards, you will perform five solo trials, in which you are not coupled to your partner, to familiarize yourself with the experimental setup. Next, you will experience the four consecutive physical interaction blocks. Finally, at the end of the experiment, you will perform another set of five solo trials. Thank you very much for participating in the experiment!

Figure A.4.: Experiment instructions for the experiment in Section 5.4.

List of Figures

List of Tables

Bibliography

[1] A. Mörtl, M. Lawitzky, A. Kucukyilmaz, M. Sezgin, C. Basdogan, and S. Hirche, "The role of roles: physical cooperation between humans and robots," *The International Journal of Robotics Research*, vol. 31, no. 13, pp. 1656–1674, 2012.

[2] V. Villani, F. Pini, F. Leali, and C. Secchi, "Survey on human–robot collaboration in industrial settings: Safety, intuitive interfaces and applications," *Mechatronics*, vol. 55, pp. 248–266, 2018.

[3] L. Marchal-Crespo and D. J. Reinkensmeyer, "Review of control strategies for robotic movement training after neurologic injury," *Journal of NeuroEngineering and Rehabilitation*, vol. 6, no. 1, p. 20, 2009.

[4] P. Beckerle, G. Salvietti, R. Unal, D. Prattichizzo, S. Rossi, C. Castellini, S. Hirche, S. Endo, H. B. Amor, M. Ciocarlie, F. Mastrogiovanni, B. D. Argall, and M. Bianchi, "A human–robot interaction perspective on assistive and rehabilitation robotics," *Frontiers in Neurorobotics*, vol. 11, p. 24, 2017.

[5] M. Spenko, H. Yu, and S. Dubowsky, "Robotic personal aids for mobility and monitoring for the elderly," *IEEE Transactions on Neural Systems and Rehabilitation Engineering*, vol. 14, no. 3, pp. 344–351, 2006.

[6] T. L. Chen, M. Ciocarlie, S. Cousins, P. M. Grice, K. Hawkins, K. Hsiao, C. C. Kemp, C.-H. King, D. A. Lazewatsky, A. E. Leeper, H. Nguyen, A. Paepcke, C. Pantofaru, W. D. Smart, and L. Takayama, "Robots for humanity: using assistive robotics to empower people with disabilities," *IEEE Robotics & Automation Magazine*, vol. 20, no. 1, pp. 30–39, 2013.

[7] A. Agah and K. Tanie, "Human interaction with a service robot: Mobile-manipulator handing over an object to a human," in *1997 IEEE International Conference on Robotics and Automation*, vol. 1. IEEE, 1997, pp. 575–580.

[8] R. Alami, A. Albu-Schäffer, A. Bicchi, R. Bischoff, R. Chatila, A. De Luca, A. De Santis, G. Giralt, J. Guiochet, G. Hirzinger, F. Ingrand, V. Lippiello, R. Mattone, D. Powell, S. Sen, B. Siciliano, G. Tonietti, and L. Villani, "Safe and dependable physical human-robot interaction in anthropic domains: State of the art and challenges," in *2006 IEEE/RSJ International Conference on Intelligent Robots and Systems*. IEEE, 2006, pp. 1–16.

[9] D. A. Rosenbaum, *Human motor control*. Academic press, 2009.

[10] K. P. Tee, E. Burdet, C.-M. Chew, and T. E. Milner, "A model of force and impedance in human arm movements," *Biological Cybernetics*, vol. 90, no. 5, pp. 368–375, 2004.

[11] M. Kawato, "Internal models for motor control and trajectory planning," *Current Opinion in Neurobiology*, vol. 9, no. 6, pp. 718–727, 1999.

[12] D. M. Wolpert and M. Kawato, "Multiple paired forward and inverse models for motor control," *Neural Networks*, vol. 11, no. 7-8, pp. 1317–1329, 1998.

[13] T. E. Milner and D. W. Franklin, "Impedance control and internal model use during the initial stage of adaptation to novel dynamics in humans," *The Journal of Physiology*, vol. 567, no. 2, pp. 651–664, 2005.

[14] N. Tomi, M. Gouko, and K. Ito, "Impedance control complements imcomplete internal models under complex external dynamics," in *2008 Annual International Conference of the IEEE Engineering in Medicine and Biology Society*. IEEE, 2008, pp. 5354–5357.

[15] C. M. Harris and D. M. Wolpert, "Signal-dependent noise determines motor planning," *Nature*, vol. 394, no. 6695, p. 780, 1998.

[16] A. A. Faisal, L. P. Selen, and D. M. Wolpert, "Noise in the nervous system," *Nature Reviews Neuroscience*, vol. 9, no. 4, pp. 292–303, 2008.

[17] F. Lacquaniti, F. Licata, and J. Soechting, "The mechanical behavior of the human forearm in response to transient perturbations," *Biological Cybernetics*, vol. 44, no. 1, pp. 35–46, 1982.

[18] E. Burdet, K. P. Tee, I. Mareels, T. E. Milner, C.-M. Chew, D. W. Franklin, R. Osu, and M. Kawato, "Stability and motor adaptation in human arm movements," *Biological Cybernetics*, vol. 94, no. 1, pp. 20–32, 2006.

[19] L. P. Selen, D. W. Franklin, and D. M. Wolpert, "Impedance control reduces instability that arises from motor noise," *Journal of Neuroscience*, vol. 29, no. 40, pp. 12 606–12 616, 2009.

[20] T. Flash and I. Gurevich, "Models of motor adaptation and impedance control in human arm movements," in *Advances in Psychology*. Elsevier, 1997, vol. 119, pp. 423–481.

[21] H. Gomi and R. Osu, "Task-dependent viscoelasticity of human multijoint arm and its spatial characteristics for interaction with environments," *Journal of Neuroscience*, vol. 18, no. 21, pp. 8965–8978, 1998.

[22] D. W. Franklin and D. M. Wolpert, "Computational mechanisms of sensorimotor control," *Neuron*, vol. 72, no. 3, pp. 425–442, 2011.

[23] B. Mehta and S. Schaal, "Forward models in visuomotor control," *Journal of Neurophysiology*, vol. 88, no. 2, pp. 942–953, 2002.

[24] E. Burdet, D. W. Franklin, and T. E. Milner, *Human robotics: neuromechanics and motor control*. MIT press, 2013.

[25] N. Hogan, "The mechanics of multi-joint posture and movement control," *Biological Cybernetics*, vol. 52, no. 5, pp. 315–331, 1985.

[26] D. Bennett, J. Hollerbach, Y. Xu, and I. Hunter, "Time-varying stiffness of human elbow joint during cyclic voluntary movement," *Experimental Brain Research*, vol. 88, no. 2, pp. 433–442, 1992.

[27] T. Tsuji, "Human arm impedance in multi-joint movements," in *Advances in Psychology*. Elsevier, 1997, vol. 119, pp. 357–381.

[28] J. M. Dolan, M. B. Friedman, and M. L. Nagurka, "Dynamic and loaded impedance components in the maintenance of human arm posture," *IEEE Transactions on Systems, Man, and Cybernetics*, vol. 23, no. 3, pp. 698–709, 1993.

[29] F. A. Mussa-Ivaldi, N. Hogan, and E. Bizzi, "Neural, mechanical, and geometric factors subserving arm posture in humans," *Journal of Neuroscience*, vol. 5, no. 10, pp. 2732–2743, 1985.

[30] N. Hogan, "Adaptive control of mechanical impedance by coactivation of antagonist muscles," *IEEE Transactions on Automatic Control*, vol. 29, no. 8, pp. 681–690, 1984.

[31] R. Osu, E. Burdet, D. W. Franklin, T. E. Milner, and M. Kawato, "Different mechanisms involved in adaptation to stable and unstable dynamics," *Journal of Neurophysiology*, vol. 90, no. 5, pp. 3255–3269, 2003.

[32] M. Darainy and D. J. Ostry, "Muscle cocontraction following dynamics learning," *Experimental Brain Research*, vol. 190, no. 2, pp. 153–163, 2008.

[33] R. Osu, D. W. Franklin, H. Kato, H. Gomi, K. Domen, T. Yoshioka, and M. Kawato, "Short-and long-term changes in joint co-contraction associated with motor learning as revealed from surface emg," *Journal of Neurophysiology*, vol. 88, no. 2, pp. 991–1004, 2002.

[34] D. W. Franklin, R. Osu, E. Burdet, M. Kawato, and T. E. Milner, "Adaptation to stable and unstable dynamics achieved by combined impedance control and inverse dynamics model," *Journal of Neurophysiology*, vol. 90, no. 5, pp. 3270–3282, 2003.

[35] D. W. Franklin, E. Burdet, K. P. Tee, R. Osu, C.-M. Chew, T. E. Milner, and M. Kawato, "Cns learns stable, accurate, and efficient movements using a simple algorithm," *Journal of Neuroscience*, vol. 28, no. 44, pp. 11 165–11 173, 2008.

[36] H. J. Huang and A. A. Ahmed, "Reductions in muscle coactivation and metabolic cost during visuomotor adaptation," *Journal of Neurophysiology*, vol. 112, no. 9, pp. 2264–2274, 2014.

[37] E. Burdet, R. Osu, D. W. Franklin, T. E. Milner, and M. Kawato, "The central nervous system stabilizes unstable dynamics by learning optimal impedance," *Nature*, vol. 414, no. 6862, pp. 446–449, 2001.

[38] C. Takahashi, R. A. Scheidt, and D. Reinkensmeyer, "Impedance control and internal model formation when reaching in a randomly varying dynamical environment," *Journal of Neurophysiology*, vol. 86, no. 2, pp. 1047–1051, 2001.

[39] R. Osu, N. Kamimura, H. Iwasaki, E. Nakano, C. M. Harris, Y. Wada, and M. Kawato, "Optimal impedance control for task achievement in the presence of signal-dependent noise," *Journal of Neurophysiology*, vol. 92, no. 2, pp. 1199–1215, 2004.

[40] D. R. Lametti, G. Houle, and D. J. Ostry, "Control of movement variability and the regulation of limb impedance," *Journal of Neurophysiology*, vol. 98, no. 6, pp. 3516–3524, 2007.

[41] P. L. Gribble, L. I. Mullin, N. Cothros, and A. Mattar, "Role of cocontraction in arm movement accuracy," *Journal of Neurophysiology*, vol. 89, no. 5, pp. 2396–2405, 2003.

[42] L. P. Selen, P. J. Beek, and J. H. Van Dieën, "Impedance is modulated to meet accuracy demands during goal-directed arm movements," *Experimental Brain Research*, vol. 172, no. 1, pp. 129–138, 2006.

[43] S. Crea, M. Cempini, M. Moise, A. Baldoni, E. Trigili, D. Marconi, M. Cortese, F. Giovacchini, F. Posteraro, and N. Vitiello, "A novel shoulder-elbow exoskeleton with series elastic actuators," in *2016 IEEE International Conference on Biomedical Robotics and Biomechatronics*. IEEE, 2016, pp. 1248–1253.

[44] J. C. Perry, J. Rosen, and S. Burns, "Upper-limb powered exoskeleton design," *IEEE/ASME Transactions on Mechatronics*, vol. 12, no. 4, pp. 408–417, 2007.

[45] B. Kim and A. D. Deshpande, "An upper-body rehabilitation exoskeleton harmony with an anatomical shoulder mechanism: Design, modeling, control, and performance evaluation," *The International Journal of Robotics Research*, vol. 36, no. 4, pp. 414–435, 2017.

[46] L. Peternel, N. Tsagarakis, and A. Ajoudani, "Towards multi-modal intention interfaces for human-robot co-manipulation," in *2016 IEEE/RSJ International Conference on Intelligent Robots and Systems*. IEEE, 2016, pp. 2663–2669.

[47] E. Gribovskaya, A. Kheddar, and A. Billard, "Motion learning and adaptive impedance for robot control during physical interaction with humans," in *2011 IEEE International Conference on Robotics and Automation*. IEEE, 2011, pp. 4326–4332.

[48] D. Mitrovic, S. Klanke, R. Osu, M. Kawato, and S. Vijayakumar, "A computational model of limb impedance control based on principles of internal model uncertainty," *Plos One*, vol. 5, no. 10, 2010.

[49] A. Takagi, F. Usai, G. Ganesh, V. Sanguineti, and E. Burdet, "Haptic communication between humans is tuned by the hard or soft mechanics of interaction," *Plos Computational Biology*, vol. 14, no. 3, p. e1005971, 2018.

[50] J. R. Medina, S. Endo, and S. Hirche, "Impedance-based gaussian processes for predicting human behavior during physical interaction," in *2016 IEEE International Conference on Robotics and Automation*. IEEE, 2016, pp. 3055–3061.

[51] J. R. Medina, H. Börner, S. Endo, and S. Hirche, "Impedance-based gaussian processes for modeling human motor behavior in physical and non-physical interaction," *IEEE Transactions on Biomedical Engineering*, vol. 66, no. 9, pp. 2499–2511, 2019.

[52] H. Gomi and M. Kawato, "Human arm stiffness and equilibrium-point trajectory during multi-joint movement," *Biological Cybernetics*, vol. 76, no. 3, pp. 163–171, 1997.

[53] M. S. Erden and A. Billard, "Hand impedance measurements during interactive manual welding with a robot," *IEEE Transactions on Robotics*, vol. 31, pp. 168–179, 2015.

[54] H. Börner, S. Endo, and S. Hirche, "Estimation of involuntary impedance in multi-joint arm movements," in *2018 IFAC Conference on Cyber-Physical & Human-Systems*. IFAC, 2018.

[55] H. Börner, S. Endo, and S. Hirche, "Estimation of involuntary components of human arm impedance in multi-joint movements via feedback jerk isolation," *Frontiers in Neuroscience*, vol. 14, 2020.

[56] H. Börner, G. Carboni, X. Cheng, A. Takagi, S. Hirche, S. Endo, and E. Burdet, "Physically interacting humans regulate muscle cocontraction to improve visuo-haptic perception," submitted to Science Advances.

[57] A. C. Lo, P. D. Guarino, L. G. Richards, J. K. Haselkorn, G. F. Wittenberg, D. G. Federman, R. J. Ringer, T. H. Wagner, H. I. Krebs, B. T. Volpe, C. T. Bever, D. M. Bravata, P. W. Duncan, B. H. Corn, A. D. Maffucci, S. E. Nadeau, S. S. Conroy, J. M. Powell, G. D. Huang, and P. Peduzzi, "Robot-assisted therapy for long-term upper-limb impairment after stroke," *New England Journal of Medicine*, vol. 362, no. 19, pp. 1772–1783, 2010.

[58] P. Maciejasz, J. Eschweiler, K. Gerlach-Hahn, A. Jansen-Troy, and S. Leonhardt, "A survey on robotic devices for upper limb rehabilitation," *Journal of NeuroEngineering and Rehabilitation*, vol. 11, no. 1, p. 3, 2014.

[59] N. Nordin, S. Q. Xie, and B. Wünsche, "Assessment of movement quality in robot-assisted upper limb rehabilitation after stroke: a review," *Journal of NeuroEngineering and Rehabilitation*, vol. 11, no. 1, p. 137, 2014.

[60] D. Shin, J. Kim, and Y. Koike, "A myokinetic arm model for estimating joint torque and stiffness from emg signals during maintained posture," *Journal of Neurophysiology*, vol. 101, no. 1, pp. 387–401, 2009.

[61] A. B. Slifkin and K. M. Newell, "Noise, information transmission, and force variability." *Journal of Experimental Psychology: Human Perception and Performance*, vol. 25, no. 3, p. 837, 1999.

[62] P. B. Matthews, "The human stretch reflex and the motor cortex," *Trends in Neurosciences*, vol. 14, no. 3, pp. 87–91, 1991.

[63] A. Thilmann, M. Schwarz, R. Töpper, S. Fellows, and J. Noth, "Different mechanisms underlie the long-latency stretch reflex response of active human muscle at different joints." *The Journal of Physiology*, vol. 444, no. 1, pp. 631–643, 1991.

[64] P. Merton and H. Morton, "Stimulation of the cerebral cortex in the intact human subject," *Nature*, vol. 285, no. 5762, p. 227, 1980.

[65] D. Lakatos, F. Petit, and P. Van Der Smagt, "Conditioning vs. excitation time for estimating impedance parameters of the human arm," in *2011 IEEE/RAS International Conference on Humanoid Robots*, 2011, pp. 636–642.

[66] E. J. Perreault, R. F. Kirsch, and P. E. Crago, "Effects of voluntary force generation on the elastic components of endpoint stiffness," *Experimental Brain Research*, vol. 141, no. 3, pp. 312–323, 2001.

[67] D. W. Franklin, E. Burdet, R. Osu, M. Kawato, and T. E. Milner, "Functional significance of stiffness in adaptation of multijoint arm movements to stable and unstable dynamics," *Experimental Brain Research*, vol. 151, no. 2, pp. 145–157, 2003.

[68] M. L. Latash and V. M. Zatsiorsky, "Joint stiffness: Myth or reality?" *Human Movement Science*, vol. 12, no. 6, pp. 653–692, 1993.

[69] M. L. Latash, "Reconstruction of equilibrium trajectories and joint stiffness patterns during single-joint voluntary movements under different instructions," *Biological Cybernetics*, vol. 71, no. 5, pp. 441–450, 1994.

[70] T. Zhou, V. M. Zatsiorsky, and M. L. Latash, "Unintentional changes in the apparent stiffness of the multi-joint limb," *Experimental Brain Research*, vol. 233, no. 10, pp. 2989–3004, 2015.

[71] V. Duchaine and C. Gosselin, "Safe, stable and intuitive control for physical human-robot interaction," in *2009 IEEE International Conference on Robotics and Automation*, 2009, pp. 3383–3388.

[72] T. Flash and N. Hogan, "The coordination of arm movements: an experimentally confirmed mathematical model," *Journal of Neuroscience*, vol. 5, no. 7, pp. 1688–1703, 1985.

[73] Y. Maeda, T. Hara, and T. Arai, "Human-robot cooperative manipulation with motion estimation," in *2001 IEEE/RSJ International Conference on Intelligent Robots and Systems*, vol. 4. Ieee, 2001, pp. 2240–2245.

[74] B. Corteville, E. Aertbeliën, H. Bruyninckx, J. De Schutter, and H. Van Brussel, "Human-inspired robot assistant for fast point-to-point movements," in *2007 IEEE International Conference on Robotics and Automation*. IEEE, 2007, pp. 3639–3644.

[75] S. Miossec and A. Kheddar, "Human motion in cooperative tasks: moving object case study," in *2008 IEEE International Conference on Robotics and Biomimetics*, 2009, pp. 1509–1514.

[76] A. Jha and S. S. Chiddarwar, "Robot programming by demonstration using teleoperation through imitation," *Industrial Robot*, vol. 44, no. 2, pp. 142–154, 2017.

[77] A. Billard, S. Calinon, R. Dillmann, and S. Schaal, "Robot programming by demonstration," *Handbook of Robotics*, vol. 59, 2008.

[78] C. K. Williams and C. E. Rasmussen, "Gaussian processes for regression," in *Advances in Neural Information Processing Systems*, 1996, pp. 514–520.

[79] C. E. Rasmussen, "Gaussian processes in machine learning," in *Advanced Lectures on Machine Learning*. Springer, 2004, pp. 63–71.

[80] S. M. Khansari-Zadeh and A. Billard, "Learning stable nonlinear dynamical systems with gaussian mixture models," *IEEE Transactions on Robotics*, vol. 27, no. 5, pp. 943–957, 2011.

[81] R. M. Neal, *Bayesian Learning for Neural Networks*. Berlin, Heidelberg: Springer-Verlag, 1996.

[82] J. Kocijan, A. Girard, B. Banko, and R. Murray-Smith, "Dynamic systems identification with gaussian processes," *Mathematical and Computer Modelling of Dynamical Systems*, vol. 11, no. 4, pp. 411–424, 2005.

[83] E. Solak, R. Murray-Smith, W. E. Leithead, D. J. Leith, and C. E. Rasmussen, "Derivative observations in gaussian process models of dynamic systems," in *Advances in Neural Information Processing Systems*, 2003, pp. 1057–1064.

[84] J. M. Wang, D. J. Fleet, and A. Hertzmann, "Gaussian process dynamical models for human motion," *IEEE Transactions on Pattern Analysis and Machine Intelligence*, vol. 30, no. 2, pp. 283–298, 2007.

[85] Z. Wang, M. P. Deisenroth, H. B. Amor, D. Vogt, B. Schölkopf, and J. Peters, "Probabilistic modeling of human movements for intention inference," *Robotics: Science and Systems, VIII*, 2012.

[86] M. A. Alvarez, D. Luengo, and N. D. Lawrence, "Linear latent force models using gaussian processes," *IEEE Transactions on Pattern Analysis and Machine Intelligence*, vol. 35, no. 11, pp. 2693–2705, 2013.

[87] L. Castellanos, V. Q. Vu, S. Perel, A. B. Schwartz, and R. E. Kass, "A multivariate gaussian process factor model for hand shape during reach-to-grasp movements," *Statistica Sinica*, vol. 25, no. 1, p. 5, 2015.

[88] J. R. Medina, D. Lee, and S. Hirche, "Risk-sensitive optimal feedback control for haptic assistance," in *2012 IEEE international Conference on Robotics and Automation*. IEEE, 2012, pp. 1025–1031.

[89] J. R. Medina, D. Sieber, and S. Hirche, "Risk-sensitive interaction control in uncertain manipulation tasks," in *2013 IEEE International Conference on Robotics and Automation*. IEEE, 2013, pp. 502–507.

[90] A. Van Der Vaart and H. Van Zanten, "Information rates of nonparametric gaussian process methods," *Journal of Machine Learning Research*, vol. 12, pp. 2095–2119, 2011.

[91] M. A. Álvarez and N. D. Lawrence, "Computationally efficient convolved multiple output gaussian processes," *Journal of Machine Learning Research*, vol. 12, pp. 1459–1500, 2011.

[92] Y. Tanaka, T. Tsuji, and M. Kaneko, "Task readiness impedance in human arm movements for virtual ball-catching task," in *2003 Annual Conference of the IEEE Industrial Electronics Society*, vol. 1. IEEE, 2003, pp. 478–483.

[93] T. Tsuji, Y. Takeda, and Y. Tanaka, "Analysis of mechanical impedance in human arm movements using a virtual tennis system," *Biological Cybernetics*, vol. 91, no. 5, pp. 295–305, 2004.

[94] J. E. Speich, L. Shao, and M. Goldfarb, "Modeling the human hand as it interacts with a telemanipulation system," *Mechatronics*, vol. 15, no. 9, pp. 1127–1142, 2005.

[95] M. J. Fu and M. C. Cavusoglu, "Human-arm-and-hand-dynamic model with variability analyses for a stylus-based haptic interface," *IEEE Transactions on Systems, Man and Cybernetics*, vol. 42, pp. 1633–1644, 2012.

[96] M. Álvarez and N. Lawrence, "Sparse convolved gaussian processes for multi-output regression," in *Advances in Neural Information Processing Systems*, 2009, pp. 57–64.

[97] E. Snelson, Z. Ghahramani, and C. E. Rasmussen, "Warped gaussian processes," in *Advances in Neural Information Processing Systems*, 2004, pp. 337–344.

[98] G. W. Bohrnstedt and A. S. Goldberger, "On the exact covariance of products of random variables," *Journal of the American Statistical Association*, vol. 64, no. 328, pp. 1439–1442, 1969.

[99] J. Shawe-Taylor and N. Cristianini, *Kernel methods for pattern analysis*. Cambridge university press, 2004.

[100] D. Duvenaud, J. Lloyd, R. Grosse, J. Tenenbaum, and G. Zoubin, "Structure discovery in nonparametric regression through compositional kernel search," in *2013 PMLR International Conference on Machine Learning*, 2013, pp. 1166–1174.

[101] T. Tsuji, P. G. Morasso, K. Goto, and K. Ito, "Human hand impedance characteristics during maintained posture," *Biological Cybernetics*, vol. 72, no. 6, pp. 475–485, 1995.

[102] P. K. Artemiadis, P. T. Katsiaris, M. V. Liarokapis, and K. J. Kyriakopoulos, "Human arm impedance: Characterization and modeling in 3d space," in *2010 IEEE/RSJ International Conference on Intelligent Robots and Systems*. IEEE, 2010, pp. 3103–3108.

[103] M. Dyck and M. Tavakoli, "Measuring the dynamic impedance of the human arm without a force sensor," in *2013 IEEE International Conference on Rehabilitation Robotics*, 2013, pp. 1–8.

[104] P. H. Chang, K. Park, S. H. Kang, H. I. Krebs, and N. Hogan, "Stochastic estimation of human arm impedance using robots with nonlinear frictions: An experimental validation," *IEEE/ASME Transactions on Mechatronics*, vol. 18, no. 2, pp. 775–786, 2012.

[105] S. Wang, G. Zuo, J. Xu, and H. Zheng, "Human hand impedance characteristics during reaching movements," in *2011 IEEE International Conference on Biomedical Engineering and Informatics*, vol. 3. IEEE, 2011, pp. 1282–1286.

[106] N. Srinivas, A. Krause, S. M. Kakade, and M. W. Seeger, "Information-theoretic regret bounds for gaussian process optimization in the bandit setting," *IEEE Transactions on Information Theory*, vol. 58, no. 5, pp. 3250–3265, 2012.

[107] T. Beckers, J. Umlauft, and S. Hirche, "Mean square prediction error of misspecified gaussian process models," in *2018 IEEE Conference on Decision and Control*. IEEE, 2018, pp. 1162–1167.

[108] D. H. Brainard, "The psychophysics toolbox," *Spatial Vision*, vol. 10, pp. 433–436, 1997.

[109] R. W. Schafer, "What is a savitzky-golay filter?" *IEEE Signal Processing Magazine*, vol. 28, no. 4, pp. 111–117, 2011.

[110] R. Osu and H. Gomi, "Multijoint muscle regulation mechanisms examined by measured human arm stiffness and emg signals," *Journal of Neurophysiology*, vol. 81, no. 4, pp. 1458–1468, 1999.

[111] J. Buzzi, G. Ferrigno, J. M. Jansma, and E. De Momi, "On the value of estimating human arm stiffness during virtual teleoperation with robotic manipulators," *Frontiers in Neuroscience*, vol. 11, no. 528, 2017.

[112] H. K. Kim, B. Kang, B. Kim, and S. Park, "Estimation of multijoint stiffness using electromyogram and artificial neural network," *IEEE Transactions on Systems, Man, and Cybernetics - Part A: Systems and Humans*, vol. 39, no. 5, pp. 972–980, 2009.

[113] D. Lakatos, D. Rüschen, J. Bayer, J. Vogel, and P. van der Smagt, "Identification of human limb stiffness in 5 dof and estimation via emg," in *International Symposium on Experimental Robotics*. Springer, 2013, pp. 89–99.

[114] A. Ajoudani, C. Fang, N. G. Tsagarakis, and A. Bicchi, "A reduced-complexity description of arm endpoint stiffness with applications to teleimpedance control," in *2015 IEEE/RSJ International Conference on Intelligent Robots and Systems*. IEEE, 2015, pp. 1017–1023.

[115] M. Darainy, N. Malfait, P. L. Gribble, F. Towhidkhah, and D. J. Ostry, "Learning to control arm stiffness under static conditions," *Journal of Neurophysiology*, vol. 92, no. 6, pp. 3344–3350, 2004.

[116] L. Masia and V. Squeri, "A modular mechatronic device for arm stiffness estimation in human-robot interaction," *IEEE/ASME Transactions on Mechatronics*, vol. 20, pp. 2053–2066, 2015.

[117] H. Patel, G. O'Neill, and P. Artemiadis, "On the effect of muscular cocontraction on the 3-d human arm impedance," *IEEE Transactions on Biomedical Engineering*, vol. 61, no. 10, pp. 2602–2608, 2014.

[118] E. J. Perreault, R. F. Kirsch, and P. E. Crago, "Multijoint dynamics and postural stability of the human arm," *Experimental Brain Research*, vol. 157, no. 4, pp. 507–517, 2004.

[119] J. J. Palazzolo, M. Ferraro, H. I. Krebs, D. Lynch, B. T. Volpe, and N. Hogan, "Stochastic estimation of arm mechanical impedance during robotic stroke rehabilitation," *IEEE Transactions on Neural Systems and Rehabilitation Engineering*, vol. 15, pp. 94–103, 2007.

[120] T. Wang, G. S. Dordevic, and R. Shadmehr, "Learning the dynamics of reaching movements results in the modification of arm impedance and long-latency perturbation responses," *Biological Cybernetics*, vol. 85, no. 6, pp. 437–448, 2001.

[121] H. M. Hondori and A. W. Tech, "Smart mug to measure hand's geometrical mechanical impedance," in *2011 Annual International Conference of the IEEE Engineering in Medicine and Biology Society*, 2011, pp. 4053–4056.

[122] E. Burdet, R. Osu, D. Franklin, T. Yoshioka, T. Milner, and M. Kawato, "A method for measuring endpoint stiffness during multi-joint arm movements," *Journal of Biomechanics*, vol. 33, no. 12, pp. 1705–1709, 2000.

[123] M. Darainy, F. Towhidkhah, and D. J. Ostry, "Control of hand impedance under static conditions and during reaching movement," *Journal of Neurophysiology*, vol. 97, no. 4, pp. 2676–2685, 2007.

[124] J. Wong, E. T. Wilson, N. Malfait, and P. L. Gribble, "Limb stiffness is modulated with spatial accuracy requirements during movement in the absence of destabilizing forces," *Journal of Neurophysiology*, vol. 101, no. 3, pp. 1542–1549, 2009.

[125] D. Piovesan, A. Pierobon, P. DiZio, and J. R. Lackner, "Experimental measure of arm stiffness during single reaching movements with a time-frequency analysis," *Journal of Neurophysiology*, vol. 110, no. 10, pp. 2484–2496, 2013.

[126] R. L. Sainburg, "Should the equilibrium point hypothesis (eph) be considered a scientific theory?" *Motor Control*, vol. 19, no. 2, pp. 142–148, 2015.

[127] M. Gautier and W. Khalil, "On the identification of the inertial parameters of robots," in *1988 IEEE Conference on Decision and Control*, 1988, pp. 2264–2269.

[128] W. Khalil and E. Dombre, *Modeling, identification and control of robots.* Butterworth-Heinemann, 2004.

[129] J. Klodmann, D. Lakatos, C. Ott, and A. Albu-Schäffer, "A closed-form approach to determine the base inertial parameters of complex structured robotic systems," *2015 IFAC Vienna International Conference on Mathematical Modelling*, vol. 48, no. 1, pp. 316–321, 2015.

[130] J. Y. Stein, *Digital signal processing: a computer science perspective.* John Wiley & Sons, Inc., 2000.

[131] T. Söderström and P. Stoica, *System identification.* Prentice-Hall, 1989.

[132] J. Wong, E. T. Wilson, N. Malfait, and P. L. Gribble, "The influence of visual perturbations on the neural control of limb stiffness," *Journal of Neurophysiology*, vol. 101, no. 1, pp. 246–257, 2009.

[133] R. Shadmehr and M. A. Arbib, "A mathematical analysis of the force-stiffness characteristics of muscles in control of a single joint system," *Biological Cybernetics*, vol. 66, no. 6, pp. 463–477, 1992.

[134] R. A. Horn and C. R. Johnson, *Matrix analysis*. Cambridge university press, 2012.

[135] K. P. Burnham and D. R. Anderson, *Model selection and multimodel inference: a practical information-theoretic approach*. Springer, 2002.

[136] E. Colgate, A. Bicchi, and M. A. Peshkin, "Safety for physical human-robot interaction," in *Handbook of Robotics*. Springer, 2008, pp. 1335–1348.

[137] P. Neranon, "Implicit force control approach for safe physical robot-to-human object handover," *Indonesian Journal of Electrical Engineering and Computer Science*, vol. 17, no. 2, pp. 615–628, 2020.

[138] R. Weitschat, J. Ehrensperger, M. Maier, and H. Aschemann, "Safe and efficient human-robot collaboration part i: Estimation of human arm motions," in *2018 IEEE International Conference on Robotics and Automation*. IEEE, 2018, pp. 1993–1999.

[139] S. Haar, O. Donchin, and I. Dinstein, "Individual movement variability magnitudes are explained by cortical neural variability," *Journal of Neuroscience*, vol. 37, no. 37, pp. 9076–9085, 2017.

[140] M. Deng, A. Inoue, H. Gomi, and Y. Hirashima, "Recursive filter design for estimating time varying multijoint human arm viscoelasticity." *International Journal of Signal and Imaging Systems Engineering*, vol. 7, no. 1, pp. 2–18, 2006.

[141] T. Asao, S. Suzuki, and K. Kotani, "Estimation of driver's steering intention by using mechanical impedance," in *2013 HCI International Conference on Human Interface and the Management of Information*. Springer, 2013, pp. 3–11.

[142] L. Roveda, F. Vicentini, and L. M. Tosatti, "Deformation-tracking impedance control in interaction with uncertain environments," in *2013 IEEE/RSJ International Conference on Intelligent Robots and Systems*. IEEE, 2013, pp. 1992–1997.

[143] J. L. Emken, R. Benitez, A. Sideris, J. E. Bobrow, and D. J. Reinkensmeyer, "Motor adaptation as a greedy optimization of error and effort," *Journal of Neurophysiology*, vol. 97, no. 6, pp. 3997–4006, 2007.

[144] G. Ganesh, A. Takagi, R. Osu, T. Yoshioka, M. Kawato, and E. Burdet, "Two is better than one: physical interactions improve motor performance in humans," *Scientific Reports*, vol. 4, p. 3824, 2014.

[145] A. Takagi, G. Ganesh, T. Yoshioka, M. Kawato, and E. Burdet, "Physically interacting individuals estimate the partner's goal to enhance their movements," *Nature Human Behaviour*, vol. 1, no. 3, pp. 1–6, 2017.

[146] G. Carboni, T. Nanayakkara, A. Takagi, and E. Burdet, "Adaptive visuo-haptic perception through muscle coactivation," submitted to Scientific Reports.

[147] A. Melendez-Calderon, L. Bagutti, B. Pedrono, and E. Burdet, "Hi5: A versatile dual-wrist device to study human-human interaction and bimanual control," in *2011 IEEE/RSJ International Conference on Intelligent Robots and Systems*. IEEE, 2011, pp. 2578–2583.

[148] A. Takagi, C. Bagnato, and E. Burdet, "Facing the partner influences exchanges in force," *Scientific Reports*, vol. 6, p. 35397, 2016.

[149] A. Melendez-Calderon, V. Komisar, and E. Burdet, "Interpersonal strategies for disturbance attenuation during a rhythmic joint motor action," *Physiology & Behavior*, vol. 147, pp. 348–358, 2015.

[150] R. C. Oldfield *et al.*, "The assessment and analysis of handedness: the edinburgh inventory," *Neuropsychologia*, vol. 9, no. 1, pp. 97–113, 1971.

[151] T. E. Milner, "Adaptation to destabilizing dynamics by means of muscle cocontraction," *Experimental Brain Research*, vol. 143, no. 4, pp. 406–416, 2002.

[152] M. Lakie, E. G. Walsh, and G. Wright, "Measurements of inertia of the hand, and the stiffness of the forearm muscles using resonant-frequency methods, with added inertia or position feedback," vol. 310, no. 1, pp. P3–P4, 1981.

[153] S. Lehman and B. Calhoun, "An identified model for human wrist movements," *Experimental Brain Research*, vol. 81, no. 1, pp. 199–208, 1990.

[154] M. J. Grey, "Viscoelastic properties of the human wrist during the stabilization phase of a targeted movement," Ph.D. dissertation, School of Kinesiology, Simon Fraser University, 1997.

[155] D. Formica, S. K. Charles, L. Zollo, E. Guglielmelli, N. Hogan, and H. I. Krebs, "The passive stiffness of the wrist and forearm," *Journal of Neurophysiology*, vol. 108, no. 4, pp. 1158–1166, 2012.

[156] A. L. Pando, H. Lee, W. B. Drake, N. Hogan, and S. K. Charles, "Position-dependent characterization of passive wrist stiffness," *IEEE Transactions on Biomedical Engineering*, vol. 61, no. 8, pp. 2235–2244, 2014.

[157] A. B. Leger and T. E. Milner, "Passive and active wrist joint stiffness following eccentric exercise," *European Journal of Applied Physiology*, vol. 82, no. 5-6, pp. 472–479, 2000.

[158] S. De Serres and T. Milner, "Wrist muscle activation patterns and stiffness associated with stable and unstable mechanical loads," *Experimental Brain Research*, vol. 86, no. 2, pp. 451–458, 1991.

[159] T. E. Milner, C. Cloutier, A. B. Leger, and D. W. Franklin, "Inability to activate muscles maximally during cocontraction and the effect on joint stiffness," *Experimental Brain Research*, vol. 107, no. 2, pp. 293–305, 1995.

[160] T. Sinkjær and R. Hayashi, "Regulation of wrist stiffness by the stretch reflex," *Journal of Biomechanics*, vol. 22, no. 11-12, pp. 1133–1140, 1989.

[161] C. Cornu, O. Maietti, and I. Ledoux, "Muscle elastic properties during wrist flexion and extension in healthy sedentary subjects and volley-ball players," *International Journal of Sports Medicine*, vol. 24, no. 04, pp. 277–284, 2003.

[162] A. Zonnino and F. Sergi, "Model-based analysis of the stiffness of the wrist joint in active and passive conditions," *Journal of Biomechanical Engineering*, vol. 141, no. 4, 2019.